IntechOpen

# Antennas and Wave Propagation

*Edited by Pedro Pinho*

# ANTENNAS AND WAVE PROPAGATION

Edited by **Pedro Pinho**

**Antennas and Wave Propagation**
http://dx.doi.org/10.5772/intechopen.71178
Edited by Pedro Pinho

**Contributors**

Jan M. Kelner, Cezary Ziółkowski, Thomas Vaupel, Saeed Ahmed, Karlo Queiroz Costa, Hoi Shun Lui, Faisal Aldhubaib, Stuart Crozier, Nicholas Shuley, Nurhan Turker Tokan, Sultan Aldirmaz, Gregory Mitchell, Wojciech Jan Krzysztofik, Susana Mota, Armando Rocha

© **The Editor(s) and the Author(s) 2018**
The rights of the editor(s) and the author(s) have been asserted in accordance with the Copyright, Designs and Patents Act 1988. All rights to the book as a whole are reserved by INTECHOPEN LIMITED. The book as a whole (compilation) cannot be reproduced, distributed or used for commercial or non-commercial purposes without INTECHOPEN LIMITED's written permission. Enquiries concerning the use of the book should be directed to INTECHOPEN LIMITED rights and permissions department (permissions@intechopen.com).
Violations are liable to prosecution under the governing Copyright Law.

Individual chapters of this publication are distributed under the terms of the Creative Commons Attribution 3.0 Unported License which permits commercial use, distribution and reproduction of the individual chapters, provided the original author(s) and source publication are appropriately acknowledged. If so indicated, certain images may not be included under the Creative Commons license. In such cases users will need to obtain permission from the license holder to reproduce the material. More details and guidelines concerning content reuse and adaptation can be foundat http://www.intechopen.com/copyright-policy.html.

**Notice**

Statements and opinions expressed in the chapters are these of the individual contributors and not necessarily those of the editors or publisher. No responsibility is accepted for the accuracy of information contained in the published chapters. The publisher assumes no responsibility for any damage or injury to persons or property arising out of the use of any materials, instructions, methods or ideas contained in the book.

First published in London, United Kingdom, 2018 by IntechOpen
eBook (PDF) Published by IntechOpen, 2019
IntechOpen is the global imprint of INTECHOPEN LIMITED, registered in England and Wales, registration number: 11086078, The Shard, 25th floor, 32 London Bridge Street
London, SE19SG – United Kingdom
Printed in Croatia

British Library Cataloguing-in-Publication Data
A catalogue record for this book is available from the British Library

Additional hard and PDF copies can be obtained from orders@intechopen.com

Antennas and Wave Propagation
Edited by Pedro Pinho

p. cm.

Print ISBN 978-1-78923-624-8

Online ISBN 978-1-78923-625-5

eBook (PDF) ISBN 978-1-83881-530-1

# We are IntechOpen, the world's leading publisher of Open Access books

## Built by scientists, for scientists

**3,700+**
Open access books available

**116,000+**
International authors and editors

**119M+**
Downloads

Our authors are among the

**151**
Countries delivered to

**Top 1%**
most cited scientists

**12.2%**
Contributors from top 500 universities


WEB OF SCIENCE™

Selection of our books indexed in the Book Citation Index in Web of Science™ Core Collection (BKCI)

Interested in publishing with us?
Contact book.department@intechopen.com

Numbers displayed above are based on latest data collected.
For more information visit www.intechopen.com

# Meet the editor

Pedro Pinho was born in Vale de Cambra, Portugal, in 1974. He received *Licenciado* and Master's degrees in Electrical and Telecommunications Engineering, and a Ph.D. degree in Electrical Engineering from the University of Aveiro in 1997, 2000, and 2004, respectively. He is currently an assistant professor in the Electronics, Telecommunications and Computers Engineering Department in Instituto Superior de Engenharia de Lisboa and a senior member of the research staff in Instituto de Telecomunicações, Aveiro, Portugal. Dr. Pinho is also a senior member of the IEEE, serves on the technical program committee in several conferences, and is a reviewer of several IEEE journals. He has authored or co-authored one book, 10 book chapters, and more than 100 papers for conferences and international journals. He participated as principal investigator or coordinator in projects with scientific and/or industry focus, both at a national and international level. To date he has led and leads five Ph.D. students and 42 M.Sc. students. His current research interest is antennas and radio propagation.

# Contents

# Preface

Over the past few years, wireless data traffic has drastically increased due to a change in the way today's society creates, shares, and consumes information, causing profound changes in our world and in our ways of life. This rapid increase in mobile data growth and the use of smartphones are creating unprecedented challenges, and new frequency bands are needed to explore and support new wireless systems architectures. Millimeter-wave and terahertz band communications are now being investigated by major research institutions and industry. In this context, new challenges in antennas and radio propagation modeling fields have started to meet the expected need for higher data rates for the future. Considering all this, one can say that there are endless possibilities for wireless communications.

This book aims to introduce and treat a series of advanced and emerging topics in the field of antennas and radio propagation. One of the main subjects of this book is related to the trend to use higher frequencies, and an increasing demand for much higher-speed wireless communication anywhere and anytime. Consequently, new spectral bands will be required to support these extremely high data rates and new transceivers are necessary. Moreover, some aspects related to radio propagation modeling are presented; in addition, teaching transmission line propagation and a software tool for plane wave reflection are shown.

The book is organized into nine chapters. In the first chapter, a broadband dipole-loop graphene antenna for terahertz band communication is presented. The second chapter is dedicated to the characterization of substrate-integrated waveguide components and antennas to implement applications with low losses using standard printed board technologies. The third chapter presents a time domain analysis of modified Vivaldi antennas. Besides frequency analysis, a time domain analysis is required to characterize the transient behavior of ultra-wideband antennas (UWB) for pulsed operations, since pulse distortion of the UWB antenna reduces the system performance and decreases the signal-to-noise ratio of the UWB communication system.

Teaching transmission line and wave propagation is a challenging task because it involves quantities that are not easily observable and because the underlying mathematical equations involve time and distance variables and complex numbers. In such a context, the fourth chapter presents a set of tools with a strong visualization and easy student interaction, which can improve the learning outputs.

The fifth chapter presents state-of-the-art radio network planning and propagation models for urban and indoor wireless communication networks. The sixth chapter presents a geometric-statistical propagation model that defines three groups of received signal components: direct path, delayed, and local scattering components. The multielliptical propagation model, which represents the geometry of scatterer locations, is the basis for determining the

delayed components. In the seventh chapter, a review of the background and state of the art of resonance-based target recognition is introduced. This chapter covers recent developments in using a polarimetric signature for target recognition, as well as using natural resonant frequencies for subsurface sensing applications. The chapter concludes with some highlights of the ongoing challenges in the field.

The eighth chapter is dedicated to anisotropic propagation of electromagnetic waves. Engineered anisotropic media provide unique electromagnetic properties, including a higher effective refractive index, high permeability with relatively low magnetic loss tangent at microwave frequencies, and lower density and weight when compared with traditional media.

The last chapter covers the diffraction problem in detail and investigates magnetic line source diffraction by a perfect electromagnetic conductor (PEMC) step for a lossy medium. The PEMC step is assumed to be placed in lossy medium.

The editor and authors would like to express their gratitude to the publisher for the assigned time, invaluable experience, efforts, and staff who successfully contributed toward enriching the final overall quality of the book.

To Carla Lourenço, Íris Pinho and Petra Pinho.

**Professor Pedro Pinho**
Assistant Professor
Electronics, Telecommunications and Computers Engineering Department
Instituto Superior de Engenharia de Lisboa
Lisbon, Portugal

Senior Member
Instituto de Telecomunicações
Aveiro, Portugal

Section 1

# Antennas and Wave Propagation

Chapter 1

# Numerical Analysis of Broadband Dipole-Loop Graphene Antenna for Applications in Terahertz Communications

Costa Karlo Queiroz da,
Sousa Gleida Tayanna Conde de,
Gabriel Silva Pinto and Andrey Viana Pires

Additional information is available at the end of the chapter

http://dx.doi.org/10.5772/intechopen.74936

**Abstract**

Graphene possesses good properties as unusually high electron mobility, atomic layer thickness, and unique mechanical flexibility, which made it one promising material in the design of terahertz antennas. In this book chapter, we present a numerical analysis of a broadband dipole-loop graphene antenna for application in terahertz communications. The bidimensional method of moments (MoM-2D), with equivalent surface impedance of graphene, is used for numerical analysis. First, we review the principal characteristics of the conventional rectangular graphene dipole. Then, we consider the broadband graphene antenna, composed by one rectangular dipole placed near and parallel to a circular-loop graphene element, where only the dipole is feed. In this analysis, we investigated the effects of the geometrical parameters and the chemical potential, of the graphene material, on the overall characteristics of the compound antenna. Some results are compared with simulations performed with software based on finite element method. The results show that this simple compound graphene antenna can be used for broadband communications in the terahertz band.

**Keywords:** graphene antenna, broadband dipole-loop antenna, terahertz radiation, method of moment (MoM), graphene surface impedance

## 1. Introduction

Over the last few years, wireless data traffic has drastically increased due to a change in the way today's society creates, shares, and consumes information. This change has been accompanied

IntechOpen

© 2018 The Author(s). Licensee IntechOpen. This chapter is distributed under the terms of the Creative Commons Attribution License (http://creativecommons.org/licenses/by/3.0), which permits unrestricted use, distribution, and reproduction in any medium, provided the original work is properly cited. CC BY

by an increasing demand for a much higher speed wireless communication anywhere, anytime. Advanced physical layer solutions and, more importantly, new spectral bands will be required to support these extremely high data rates [1].

In this context, terahertz (THz) band communication [2–8] is envisioned as a key wireless technology to satisfy this demand; it is an alternative to spectrum demand and capacity limitations of current wireless systems, allowing multitude of applications. The THz band is the spectral band that spans the frequencies between 0.1 and 10 THz. While the frequency regions immediately below and above this band (the microwaves and the far infrared, respectively) have been extensively investigated, this is still one of the least-explored frequency bands for communication [1].

Therefore, there is a need to develop new transceiver antennas that are able to operate in THz frequencies in a very large operating bandwidth. Different technologies are actually in development in literature. In this chapter, we focus on graphene technology for the design of broadband terahertz antennas.

Graphene is a monolayer of carbon atoms arranged in a two-dimensional hexagonal honeycomb lattice [9]. The exceptional properties of graphene like unusually high electron mobility, atomic layer thickness, and possibility of miniaturizing antennas based on this material and many other properties made it one promising material in many areas ranging from solar cells [10] to ultra-high-speed transistors [11].

Significant benefits can be obtained for graphene antennas in telecommunications applications such as monolithic integration with nanoelectronic graphene radio frequency (RF), efficient dynamic adjustment through chemical potential, relatively low loss in the band of terahertz (THz), and the possibility of miniaturization of antennas due to common plasmon effect in metamaterials [12, 13]. On the other side, there are few alternatives and works in literature about broadband graphene antennas [14, 15].

In this chapter, a theoretical analysis was made in a broadband graphene antenna composed by a rectangular dipole and a circular loop. The analysis is made using the two-dimensional method of moments (MoM 2D) with surface impedance [15, 16]. It was calculated by input impedance, reflection coefficient, and bandwidth from antennas with different geometrical parameters and values of chemical potential in the range of 0.5–2 THz. Some results were obtained by finite element method (FEM) with the Comsol software for comparison [17].

## 2. Antenna geometry

**Figure 1** shows the geometry of the proposed broadband graphene antenna. This antenna is composed of two elements: a rectangular planar dipole with dimensions $L$ and $W$, with same values used in [13] for comparison, and a circular passive ring (or circular loop) with inner radius R1 and outer radius R2. The environment in which the elements are inserted has a relative permittivity $\varepsilon_r = 2.4$, which is the average of air and substrate permittivity used in [13], where in this reference, the substrate is in $z < 0$. In other words, here we use an equivalent effective permittivity for the whole medium, which is considered homogeneous with no substrate.

http://dx.doi.org/10.5772/intechopen.74936

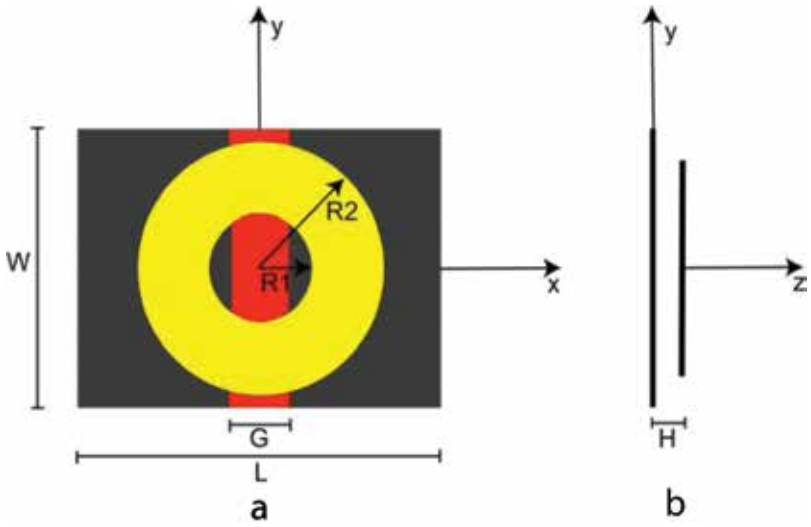


**Figure 1.** Geometry of the rectangular planar dipole graphene coupled to a circular-loop antenna of the same material: (a) top view and (b) side view.

The two elements are separated by a height *H*, as shown in **Figure 1**. In the analysis, the geometry of antennas was maintained fixed, that is, the dipole's dimensions and the values of ring's radii (R1 and R2) and height (*H*) between antennas were fixed, and the chemical potential of graphene circular loop was changed to obtain a broadband operation.

The size of the dipole graphene has only one planar dimension (e.g., *W* and *L*) because the graphene thickness is considered very small. This antenna is fed by an equivalent ideal voltage source called photomixer [13] with width *W* and gap length *G* in the middle of the dipole shown in **Figure 1**. In MoM, we call it voltage source and, in FEM, we used a lumped port [17].

## 3. Theoretical development

In this section, the model used for the surface conductivity of graphene, a summary of the MoM-2D model used in the analysis, and details of the Comsol model are presented.

### 3.1. Graphene surface conductivity

The experimental results show that edge effects on the graphene conductivity can be disregarded in the micrometer scale [15]. Therefore, one can use the electrical conductivity model developed for infinite graphene sheet. In this chapter, we use the Drude model for graphene surface conductivity in the range of 0.5–2 THz

$$\sigma(\omega) = \frac{2e^2 k_B T}{\pi h^2} \ln\left[2\cosh\left(\frac{\mu_C}{2k_B T}\right)\right] \frac{-j}{\omega - j\tau^{-1}} \tag{1}$$

where $\tau = 10^{-12}$ s is the relaxation time, $T$ is the temperature, and $\mu_C$ is the chemical potential, which is a function, for example, of a DC voltage applied in graphene sheet [18]. **Figure 2** shows examples of $\sigma$ for different values of chemical potential with $T = 300$ K.

### 3.2. Method of moment model

The boundary condition on the antenna surface produces the following integral equation of electric field in frequency domain with temporal dependence $\exp(j\omega t)$:

$$\left[\left(\bar{E}_S + \bar{E}_i\right) \cdot \bar{a}_t\right] \bar{a}_t = Z_S \bar{J} \tag{2}$$

where $\bar{E}_s$ (V/m) is the scattering field from the antenna, $\bar{E}_i$(V/m) is the incident electric field from the voltage source, $\bar{a}_t$ is a unitary vector tangential to the antenna's surface, $\bar{J}$(A/m) is the surface current density of the antenna, and $Z_S = 1/\sigma$ is the surface impedance of graphene. The scattered field is

$$\bar{E}_S = -j\omega\mu_0 \iint_S \bar{J} \frac{e^{-jkR}}{4\pi R} ds' + \nabla\left[\frac{1}{j\omega\varepsilon_0} \iint_S \nabla \cdot \bar{J} \frac{e^{-jkR}}{4\pi R} dS'\right] \tag{3}$$

where $j$ is the imaginary unit, $k = \omega(\mu_0\, \varepsilon_r\, \varepsilon_0)^{1/2}$, $\omega$ is the angular frequency (rad/s), $\mu_0$ and $\varepsilon_0$ are the magnetic permeability and electrical permittivity, respectively, in free space, $\varepsilon_r = 2.4$ in the present analysis, and $R$ is the distance between source points and observation points, both on the antenna surface $S$.

The numerical solution of Eq. (2) by MoM consists in to approximate the surface current on the antenna by a linear combination in a given set of basis function and performs the conventional test procedure with a given set of test function [16]. With this approximation, we transform the integral Eq. (2) in an algebraic linear system which is numerically solved.

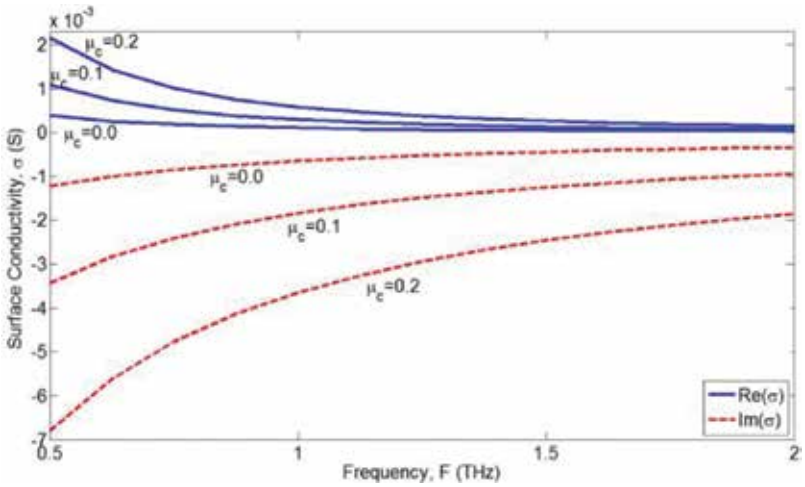


**Figure 2.** Surface conductivity of graphene versus frequency for different values of $\mu_C$, with $T = 300$ K.

### 3.3. Finite element method model

The Comsol software [17], which is based on the finite element method, was used to simulate examples of graphene antennas to compare our MoM model. The graphene sheet is modeled by an equivalent volumetric electrical conductivity, where it is defined by the surface conductivity (1) divided by the graphene thickness, which was considered finite in the Comsol model $\sigma_V(\omega) = \sigma(\omega)/\Delta$, where $\Delta$ is the thickness of the antenna. The domain used is a spherical volume with $\varepsilon_r = 2.4$, where a perfect matched layer (PML) is placed in the outer boundary to absorb the radiated waves. In this model, the dipole is excited by a voltage source with a lumped port element.

## 4. Numerical results

In this section, we first present the results of two examples of conventional graphene dipole with different sizes. The principal characteristics of this antenna are reviewed. The results are obtained by MoM and FEM models and compared with data of literature [13]. After that, we present the results for the broadband graphene dipole loop. In this case, we analyze the dependence of the radiation and broadband properties of this antenna as a function of the geometry and chemical potential of the loop.

### 4.1. Conventional graphene dipole

For comparison of our models, this section presents the analysis of the two graphene antennas of the study [13]. The parameters of these antennas are presented in **Table 1**, where we named them Antennas 1 and 2. These two antennas were simulated by MoM and Comsol. The discretization details used in these models are shown in **Figure 3**, where **Figure 3a** and **b** show the meshes used in the MoM method and **Figure 3c** and **d** show the meshes used in the FEM. Note that the meshes in MoM method are only in the surface's antennas, while in the FEM, the meshes are also in a spherical volume around the antennas. This is why the MoM method presents small number of unknowns than the FEM, and consequently, the MoM method requires a smaller computational cost than the FEM.

The input impedance obtained for both antennas is presented in **Figure 4** and the results of input resistance $R_{in}$ and input reactance $X_{in}$ between MoM, simulation Comsol and data from [12] are compared. In general, a good agreement of the results is observed in these figures; the little differences are due to the differences in models and discretizations. The antennas present dipolar resonances similar to conventional RF-microwave antennas, where the fundamental

| Antenna | $\mu_c$ | $L$ | $W$ |
|---|---|---|---|
| 1 | 0.13 $e$V | 17 $\mu$m | 10 $\mu$m |
| 2 | 0.25 $e$V | 23 $\mu$m | 20 $\mu$m |

**Table 1.** Parameters of conventional graphene dipole antennas.

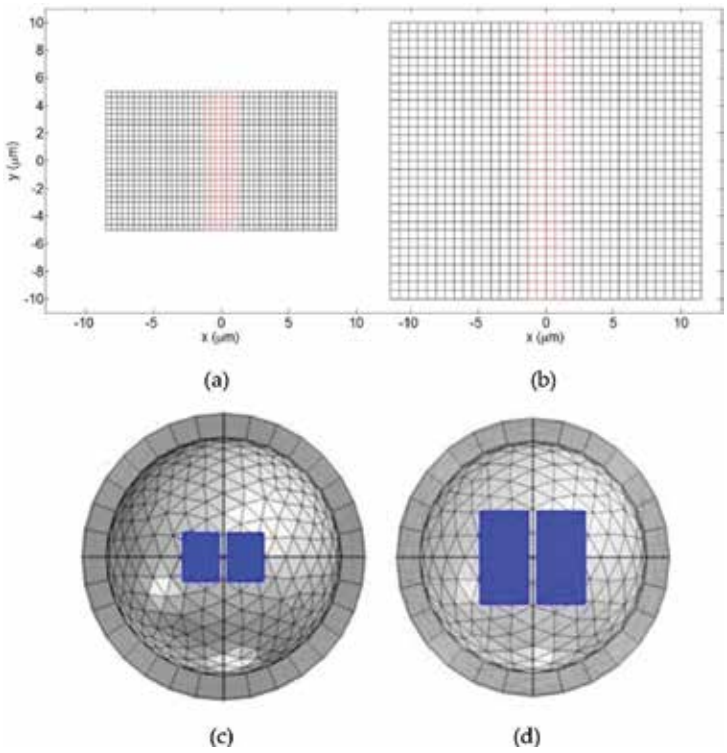


**Figure 3.** Discretization mesh of graphene antenna used in simulations. (a) Antenna 1—MoM model. (b) Antenna 2—MoM model. (c) Antenna 1—Comsol model. (d) Antenna 2—Comsol model.

resonance is dipolar $\lambda/2$ with lower $R_{in}$ and the second resonance is $\lambda$ with higher $R_{in}$. The values of these resonant frequencies are presented in **Table 2**. Antenna 1 possesses a smaller length $L$ than Antenna 2 but the resonances of Antenna 2 are higher than those of Antenna 1; this occur because the chemical potential of Antenna 2 is higher than that of Antenna 1 and this parameter shifts the input impedance to higher frequencies.

**Figure 5** shows the reflection coefficient of Antennas 1, when this antenna is matched with a transmission line with characteristic impedance of $Z_c = 100\ \Omega$. In this case, the fractional bandwidth is $B = 11.44\%$, for a reference reflection level of −10 dB. For Antenna 2, this fractional bandwidth is $B = 8.88\%$. These results show that conventional graphene dipoles possess a smaller bandwidth. The next sections present the analysis of broadband graphene dipoles with bandwidths higher than those presented in this section.

### 4.2. Graphene dipole loop

In this section, we present the numerical results for the broadband graphene dipole-loop antennas of **Figure 1**. First, we make a parametric analysis of geometry and then the effect of chemical potential of loop on the bandwidth and radiation characteristics. The results presented are input impedance, reflections coefficient, bandwidth, and radiation diagram.

http://dx.doi.org/10.5772/intechopen.74936

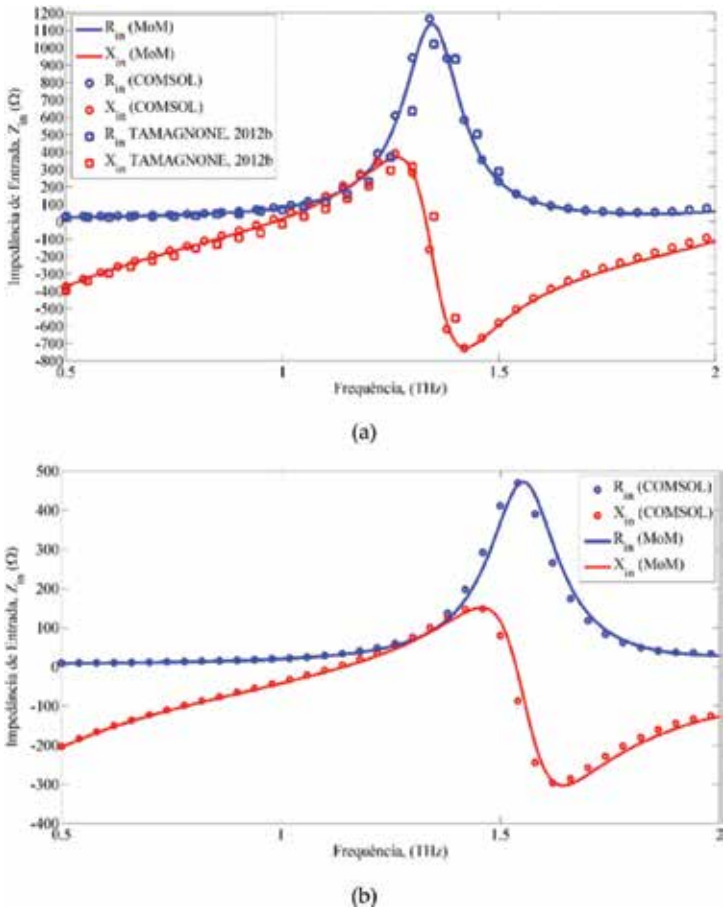


**Figure 4.** Input impedance: (a) Antenna 1 and (b) Antenna 2.

| | First resonance | Second resonance |
|---|---|---|
| MoM | F1 = 0.89 THz | F2 = 1.34 THz |
| Comsol | F1 = 0.97 THz | F2 = 1.33 THz |
| Tamagnone [13] | F1 = 1.02 THz | F2 = 1.35 THz |

**Table 2.** Resonant frequencies of Antennas 1 and 2 calculated by different methods.

### *4.2.1. Parametric analysis with geometry*

A parametric analysis of graphene dipole loop of **Figure 1** is presented in this section. We investigate the variation of the characteristics of antenna as a function of the loop's geometry element. In all the analysis, we fixed the size and chemical potential of the dipole with those values of Antennas 1 presented in **Table 1**. In addition, we varied the following parameters of loop element: inner radius R1, outer radius R2, and distance H.

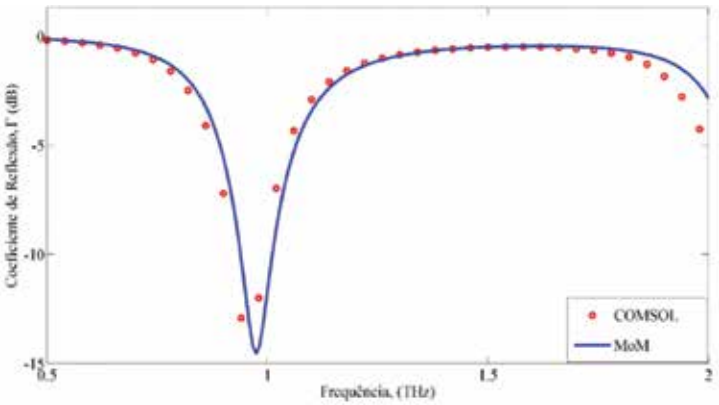


**Figure 5.** Reflection coefficient of Antenna 1 matched with an impedance feed of $Z_c$ = 100 Ω.

The values of H are varied from 1 to 5 $\mu$m. The outer radius R2 presents eight values from 3 to 10 mm, and the inner radius R1 with three fractions of R2, that is, R1 = 0.4 × R2, R1 = 0.6 × R2, and R1 = 0.8 × R2. A total of 120 simulations were done with the MoM code developed. For both elements (dipole and loop), we fixed the potential of $\mu_C$ = 0.13 eV (**Table 1**). **Figure 6** shows some examples of graphene dipole loop analyzed with different loop's size and the correspondent mesh used in the MoM model.

For each simulation, we plot the input impedance $Z_{in}$ of the antenna. First, we noted that for higher values of H and R1, the electromagnetic coupling between the dipole and the loop element is smaller. Therefore, the parameters where we obtained best coupling and matching bandwidth are H = 1 mm and R1 = 0.4 × R2. The geometries for some of these cases are presented in **Figure 5d–f**. **Figure 7** shows the input impedances for these cases R2 equal to 3, 4, 5, and 6 $\mu$m, and **Figure 8** the $Z_{in}$ for the cases 7, 8, 9, and 10 $\mu$m.

In these figures, we can see the effect of the loop and the dipole in the total input impedance. For example, for the case of R2 = 9 mm in **Figure 9**, the resonances of the loop and the dipole are approximately in 0.75 and 1.0 THz, respectively. Also, the loop resonance is shifted to lower frequencies for higher values of R2, and the dipole resonance remains approximately constant. This happens because we are varying only the size of the loop in these simulations, and this size modifies the loop's resonance more strongly.

This behavior of multi-resonance is common for antennas with multiresonant elements coupled electromagnetically, which is the case of the dipole-loop antenna. This analysis of **Figures 7** and **8** shows that we can control the total input impedance so that it presents a broadband characteristic. For this purpose, we choose the loop's size in such a way as to couple the loop and the dipole resonance near to each other to obtain a broader resonance.

To observe this statement, we plot the reflection coefficient of these antennas when they are connected to a transmission line impedance characteristic of $Z_c$ in **Figure 9**. This parameter is calculated by $\Gamma = |(Z_{in}-Z_c)/(Z_{in}+Z_c)|$. A wider bandwidth was obtained when we choose $Z_c$ = 80 Ω for the cases R2 = 3, 4, 5 and 6 $\mu$m, and $Z_c$ = 150 Ω for the cases R2 = 7, 8, 9 and 10 $\mu$m.

http://dx.doi.org/10.5772/intechopen.74936

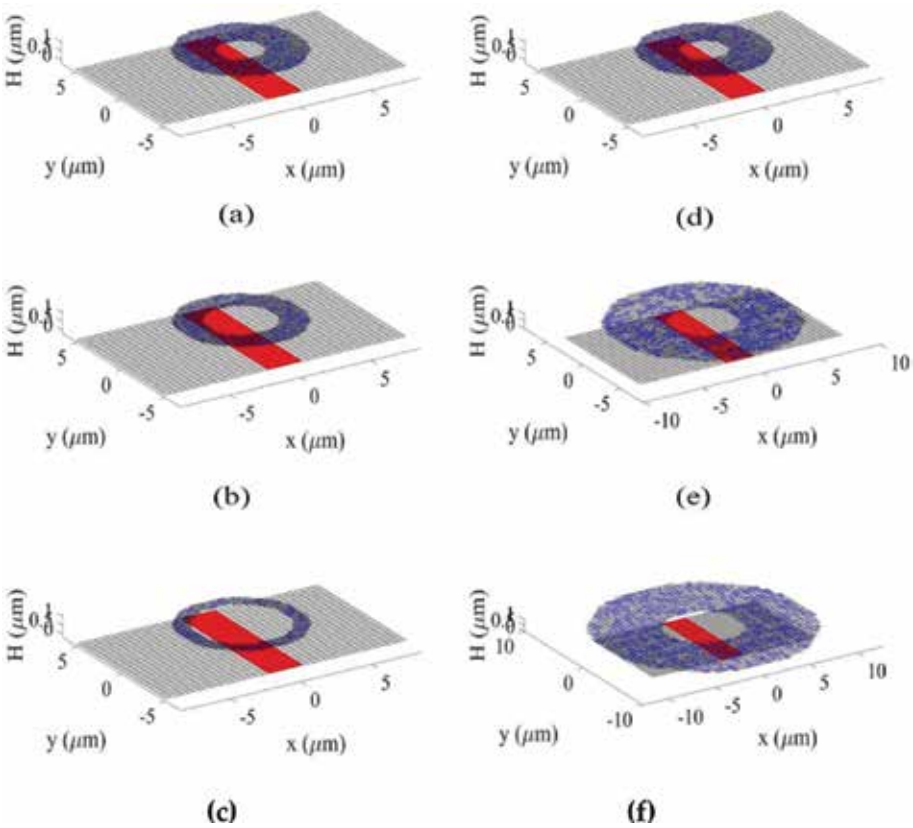


**Figure 6.** Geometry and mesh of some analyzed examples of graphene dipole-loop antenna with different values of inner radius R1: (a) R1 = 0.4 × R2, (b) R1 = 0.6 × R2, and (c) R1 = 0.8 × R2, and with different values of outer radius R2, where R1 = 0.4 × R2: (d) R2 = 4 μm, (e) R2 = 7 μm, and (f) R2 = 10 μm.

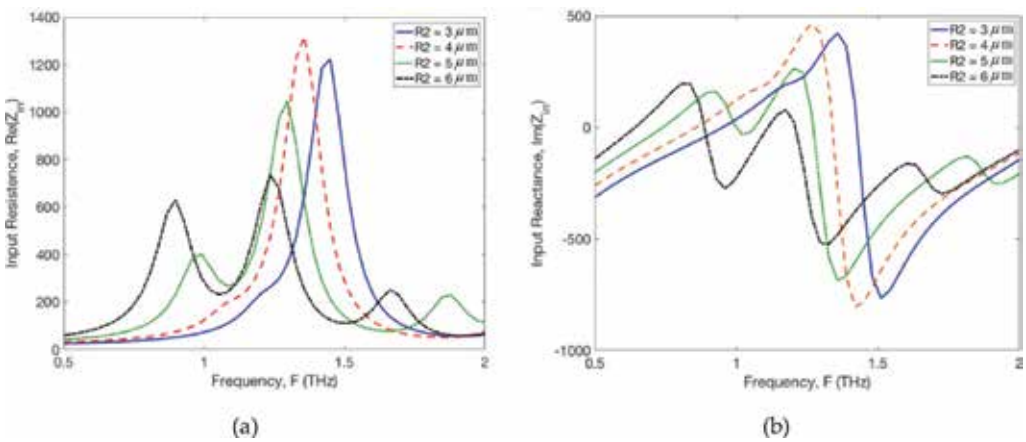


**Figure 7.** Input impedance for antennas with H = 1 $\mu$m, where R1 = 0.4 × R2, R2 = 3, 4, 5, and 6 $\mu$m: (a) input resistance ($Re(Z_{in})$) and (b) input reactance ($Im(Z_{in})$).

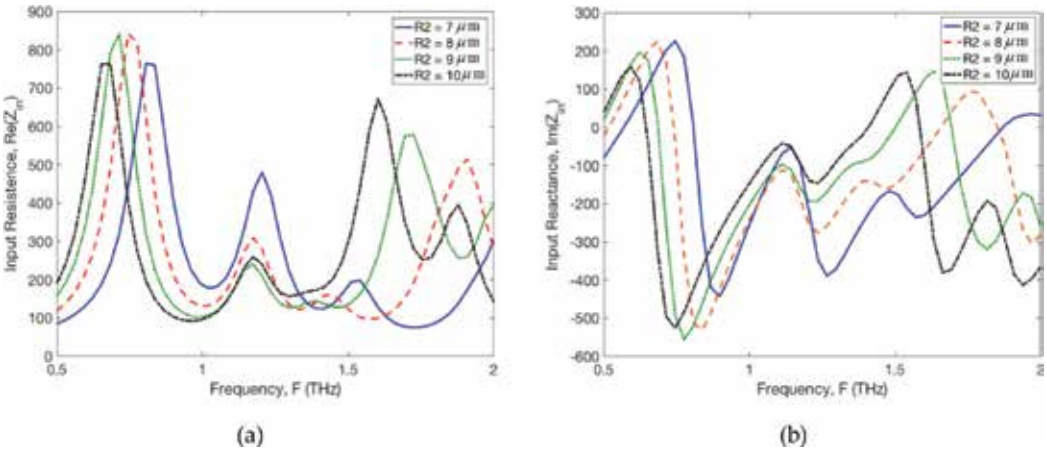


**Figure 8.** Input impedance for antennas with H = 1 $\mu$m, where R1 = 0.4 × R2, R2 = 7, 8, 9, and 10 $\mu$m: (a) input resistance (Re($Z_{in}$)) and (b) input reactance (Im($Z_{in}$)).

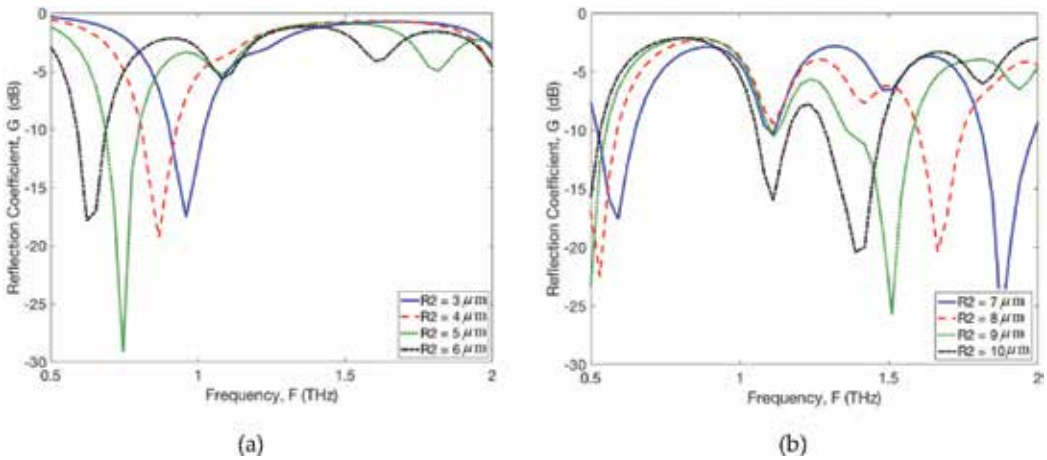


**Figure 9.** Reflection coefficient of antennas of **Figures 6** and **7**. (a) R2 = 3, 4, 5, and 6 $\mu$m ($Z_c$ = 80 Ω). (b) R2 = 7, 8, 9, and 10 $\mu$m ($Z_c$ = 150).

To compare the bandwidth of these antennas, we calculated the fractional bandwidth defined by $B(\%) = 200 \times (f_H - f_L)/(f_H + f_L)$, where $f_H$ and $f_L$ are the superior and inferior, respectively, limits of the band for a level of −10 dB. The results are presented in **Table 3**, where the fractional bandwidth for all simulations for the case H = 1 mm is presented. We observe that the best case is R2 = 7 mm with R1 = 0.4 × R2, where $B$ = 21.7%.

For the case with broad bandwidth of **Table 3** (R1 = 0.4 × R2 and R2 = 7 $\mu$m), we plot the normalized radiation diagram at F = 0.56 THz in the middle of the bandwidth in **Figure 10**. The diagram is an asymmetric version of that diagram of an isolated dipole. The asymmetry is due to the asymmetric geometry of the antenna in the $xz$ plane. This diagram radiates more energy in the –z direction, where in this case, the loop acts as a reflector element.

| **Fractional bandwidth, *B*(%)** | | | |
|---|---|---|---|
| | R1 | | |
| R2 | 0.4 × R2 | 0.6 × R2 | 0.8 × R2 |
| 3 μm | 12.1 | 14.7 | 11.2 |
| 4 μm | 13.7 | 10.7 | 10.7 |
| 5 μm | 15.4 | 6.9 | 10.1 |
| 6 μm | 15.4 | 4.6 | 10.2 |
| 7 μm | 21.7 | 11.7 | 15.3 |
| 8 μm | 9.0 | 12.6 | 14.4 |
| 9 μm | 2.2 | 18.7 | 14.5 |
| 10 μm | 9.9 | 17.7 | 14.6 |

**Table 3.** Fractional bandwidth of dipole-loop antennas with H = 1 $\mu$m.

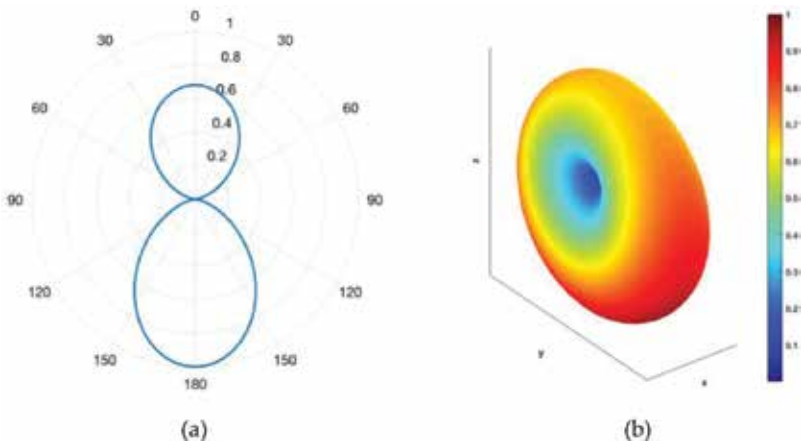


**Figure 10.** Normalized radiation diagram of antennas with a higher bandwidth (R2 = 7 μm, R1 = 0.4 × R2) at F = 56THz, in the middle of the bandwidth. (a) 2D diagram at plane *xz*. (b) 3D diagram.

### *4.2.2. Effect of chemical potential*

In this section, we present the variation of the characteristic of the antennas as a function of the chemical potential of the loop. The dimensions of the loop and the dipole were fixed as $W = 17\ \mu$m, $L = 10\ \mu$m, $H = 1\ \mu$m, R2 = 5 $\mu$m, and R1 = 0.4 × R2. The chemical potential of the dipole is $\mu_C = 0.13$ eV and the loop is varied $\mu_C = 0$, 0.03, 0.07, 0.1 and 0.13 eV. **Figure 11** shows the geometry and MoM mesh for this antenna.

**Figures 12** and **13** show the input impedance and reflection coefficient obtained, respectively. In **Figure 13**, we used $Z_c = 300\ \Omega$, for $\mu_C = 0$, 0.07, 0.1, and 0.13 eV, and for $\mu_C = 0.03$ eV, we used $Z_c = 150\ \Omega$. These values of the Zc produce a better bandwidth.

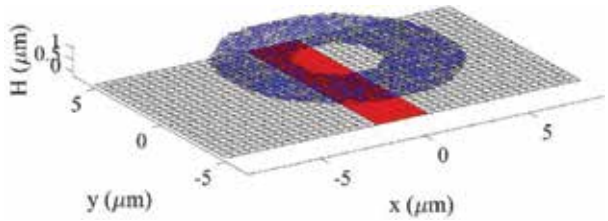


**Figure 11.** Geometry and MoM mesh of dipole-loop antenna with 17 $\mu$m, $L = 10$ $\mu$m, $H = 1$ $\mu$m, R2 = 5 $\mu$m, and R1 = 0.4 × R2.

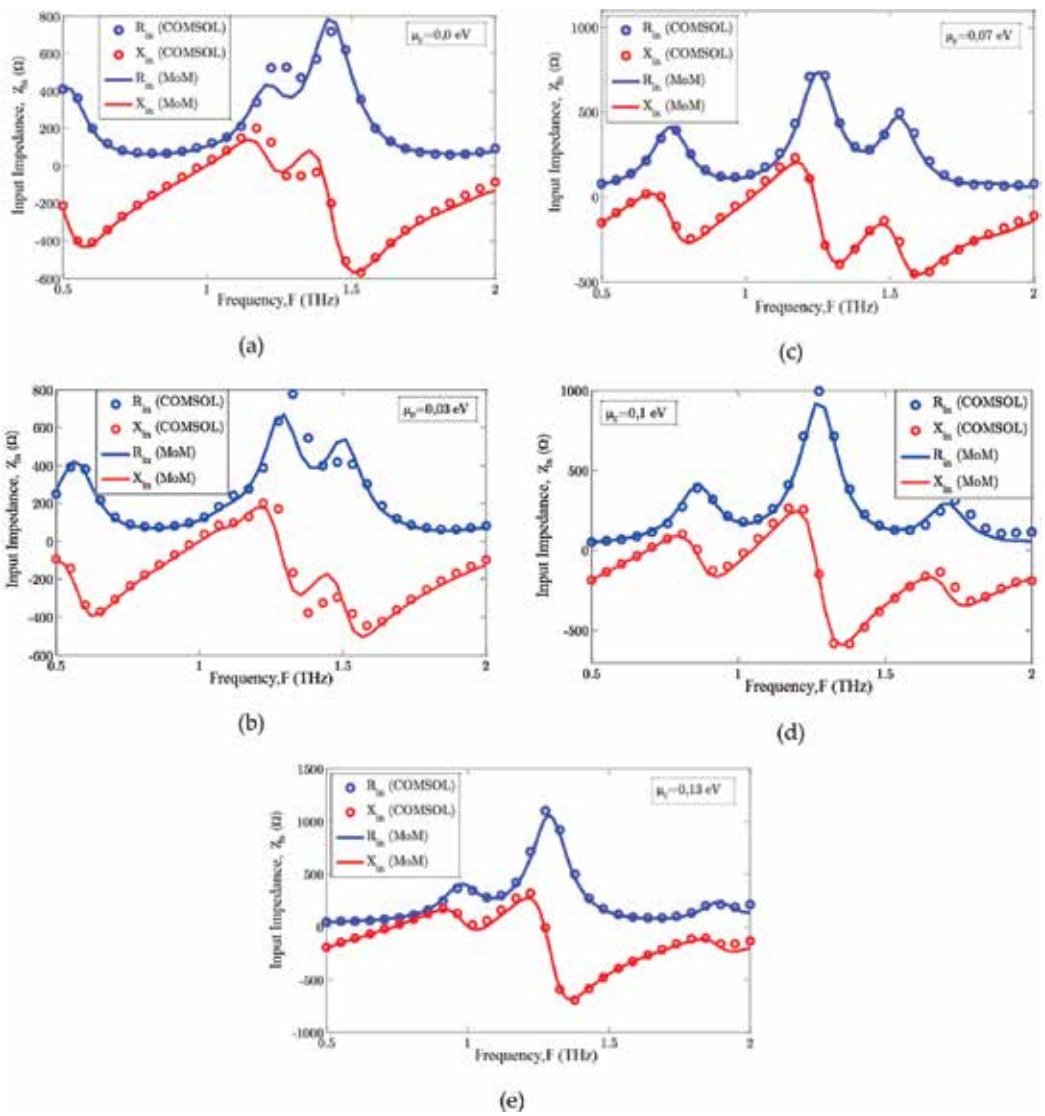


**Figure 12.** Input impedance variation with the chemical potential of loop. Geometry of dipole-loop antenna is $W = 17$ $\mu$m, $L = 10$ $\mu$m, $H = 1$ $\mu$m, R2 = 5 $\mu$m, and R1 = 0.4 × R2 ($\mu_C = 0.13$ eV for dipole). Chemical potential of loop are: (a) $\mu_C = 0.0$ eV; (b) $\mu_C = 0.03$ eV; (c) $\mu_C = 0.07$ eV; (d) $\mu_C = 0.1$ eV; and (e) $\mu_C = 0.13$ eV.

http://dx.doi.org/10.5772/intechopen.74936

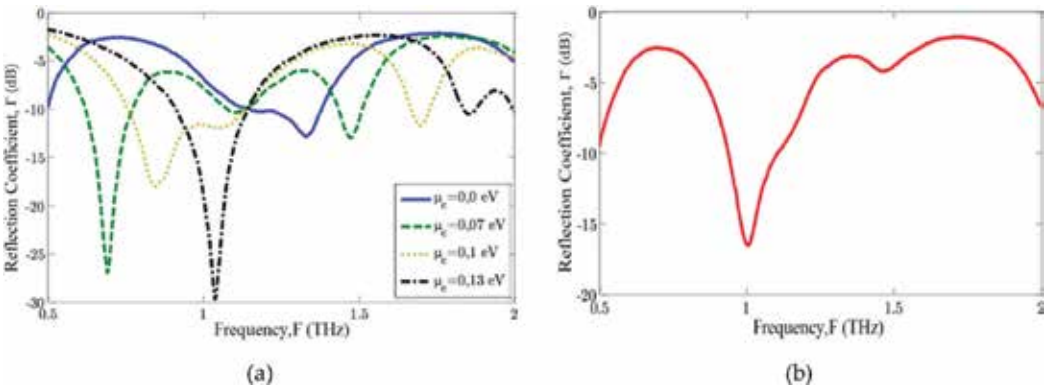


**Figure 13.** Variation of reflection coefficient with loop's chemical potential. Data of dipole-loop antenna: $W$ = 17 $\mu$m, $L$ = 10 $\mu$m, $H$ = 1 $\mu$m, R2 = 5 $\mu$m, and R1 = 0.4 × R2 ($\mu_C$ = 0.13 eV for dipole), chemical potential of loop (a) $\mu_C$ = 0.0, 0.07, 0.1, and 0.13 eV ($Z_c$ = 300 Ω), and (b) $\mu_C$ = 0.03 eV ($Z_c$ = 150 Ω).

| **Fractional bandwidth *B*(%)** | | | | | |
|---|---|---|---|---|---|
| $\mu_C$ (eV) | 0.0 | 0.03 | 0.07 | 0.1 | 0.13 |
| *B* (%) | 22.4 | 16.9 | 21.5 | 43.5 | 26.8 |

**Table 4.** Fractional bandwidth for the antennas of **Figure 13**.

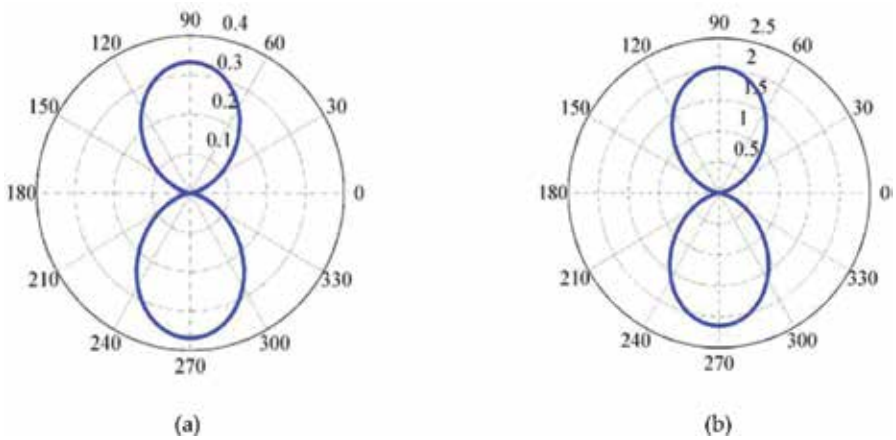


**Figure 14.** 2D radiation diagram of gain at plane $xy$ and in frequencies (a) F = 0.69 THz (first resonance) and (b) F = 0.85 THz (second resonance). Data of antenna: $W$ = 17 $\mu$m, $L$ = 10 $\mu$m, $H$ = 1 $\mu$m, R2 = 5 $\mu$m, and R1 = 0.4 × R2, $\mu_C$ = 0.13 eV (for dipole) $\mu_C$ = 0.1 eV (for loop).

First, we observe a better agreement between MoM and Comsol. Also, we note that we can control the effect of the loop in the total input impedance by varying its chemical potential.

We observe in **Figure 12** that only the resonance of loop is modified with chemical potential. For example, in **Figure 12c**, the loop resonance is near F = 0.75 THz, and in **Figure 12d**, it is near F = 0.8 THz.

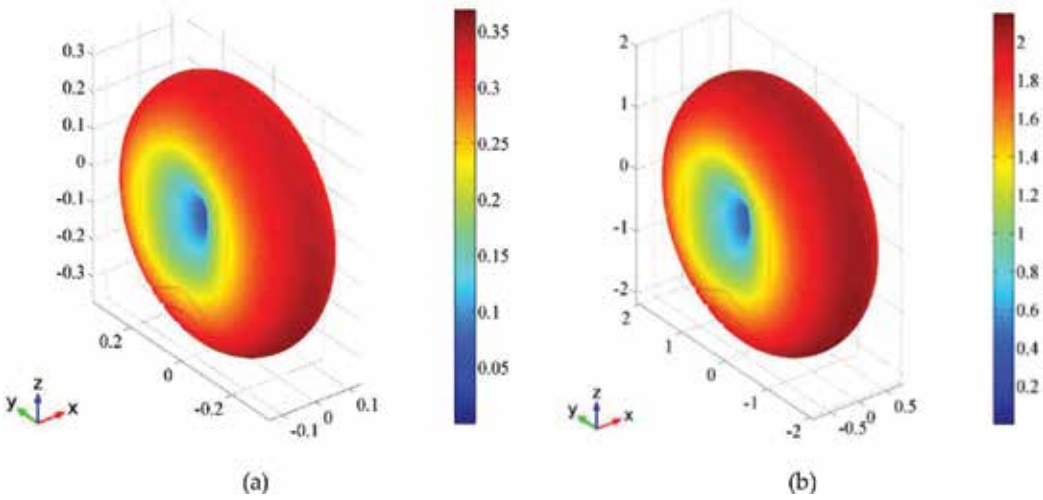


**Figure 15.** 3D radiation diagram of gain at frequencies (a) F = 0.69 THz (first resonance) and (b) F = 0.85 THz (second resonance). Data of antenna: $W$ = 17 $\mu$m, $L$ = 10 $\mu$m, $H$ = 1 $\mu$m, R2 = 5 $\mu$m, and R1 = 0.4 × R2, $\mu_C$ = 0.13 eV (for dipole) $\mu_C$ = 0.1 eV (for loop).

The results of **Figure 13** were obtained for $Z_c$ = 300 Ω; however for the case of $\mu_C$ = 0.03 eV, we used $Z_c$ = 150 Ω. These values of $Z_c$ presented a better bandwidth. The bandwidth obtained are presented in **Table 4**, where the broad bandwidth was found for the case with $\mu_C$ = 0.7 eV.

The resonant frequencies for the best bandwidth ($\mu_C$ = 0.1 eV) are F = 0.69 and 0.85 THz, as can be seen in **Figure 12d**, where the reactance is null. The radiation diagrams in these frequencies are presented in **Figures 14** and **15**. We observe that these diagrams are more symmetrical and similar to that of isolated dipole. This is because the size of the loop element is smaller than that of **Figure 10**; therefore, the effect of their surface current to produce far field is smaller.

## 5. Conclusions

In this book chapter, we presented a numerical analysis of a broadband graphene dipole-loop antenna for terahertz application. In this antenna, only the dipole element is fed by a voltage source, while the loop element is electromagnetically coupled to the dipole. The bidimensional method of moment, with an equivalent surface impedance of graphene, was used for numerical calculations, and some results are obtained by finite element method for comparison. A good agreement between these two methods was obtained, but the method of moment is faster than the finite element method. In the results, we first presented a review of the principal characteristics of the conventional graphene dipole antenna. Then, we analyzed the broadband characteristics of the graphene dipole-loop antenna as a function of geometry and chemical potential of the loop. The results show that these parameters can be used to enhance the fractional bandwidth of this antenna, where a combination of these two parameters in the optimization process produces better results than one alone. The best antenna obtained presented a fractional bandwidth of 43.5% with a radiation diagram with linear polarization and good symmetry properties.

## Acknowledgements

The authors would like to thank the Mr. Mauro Roberto Collatto Junior Chief Executive Officer of the Junto Telecom Company for the financial and emotional support to this project.

## Conflict of interest

The authors declare that there is no conflict of interest regarding the publication of this work.

## Author details

Karlo Queiroz da Costa[1]*, Gleida Tayanna Conde de Sousa[2], Gabriel Silva Pinto[2] and Andrey Viana Pires[2]

*Address all correspondence to: karlo@ufpa.br

1 Department of Electrical Engineering, Federal University of Para, Tucuruí-PA, Brazil

2 Department of Electrical Engineering, Federal University of Para, Belém-PA, Brazil

## References

[1] Akyildiz IF, Jornet JM, Han C. Terahertz band: Next frontier for wireless communications. Physics Communications. 2014;**12**:16-32

[2] Koch M. Terahertz communications: A 2020 vision. In: Miles R, Zhang XC, Eisele H, Krotkus A, editors. Terahertz Frequency Detection and Identification of Materials and Objects, NATO Security through Science Series. Vol. 19. Springer; 2007. pp. 325-338

[3] Piesiewicz R, Kleine-Ostmann T, Krumbholz N, Mittleman D, Koch M, Schoebel J, Kurner T. Short-range ultra-broadband terahertz communications: Concepts and perspectives. IEEE Antennas and Propagation Magazine. 2007;**49**(6):24-39

[4] Federici J, Moeller L. Review of terahertz and subterahertz wireless communications. Journal of Applied Physics. 2010;**107**(11):111101

[5] Huang K-C, Wang Z. Terahertz terabit wireless communication. IEEE Microwave Magazine. 2011;**12**(4):108-116

[6] Kleine-Ostmann T, Nagatsuma T. A review on terahertz communications research. Journal of Infrared, Millimeter and Terahertz Waves. 2011;**32**:143-171

[7] Song H, Nagatsuma T. Present and future of terahertz communications. IEEE Transactions on Terahertz Science and Technology. 2011;**1**(1):256-263

[8] Kürner T, Priebe S. Towards THz communications-status in research, standardization and regulation. Journal of Infrared, Millimeter and Terahertz Waves. 2014;**35**(1):53-62

[9] Geim A, Novoselov K. The rise of graphene. Nature Materials. March 2007;**6**(3):183-191

[10] Fang Z et al. Graphene-antenna sandwich photodetector. Nano Letters. June, 2012: 3808-3813

[11] Schwierz F. Graphene transistors. Nature Nanotechnology. May 2010

[12] Perruisseau-Carrier J. Graphene for antenna applications–Opportunities and challenges from microwaves to THz. Loughborough Antennas & Propagation Conference, UK. 2012

[13] Tamagnone M, Gómez-Díaz JS, Mosig JR, Perruisseau-Carrier J. Analysis and design of terahertz antennas based on plasmonic resonant graphene sheets. Journal of Applied Physics. December 2012;**112**

[14] Zhang H, Jiang Y, Wang J. A broadband terahertz antenna using graphene. 11th International Symposium on Antennas, Propagation and EM Theory (ISAPE), Antennas, Propagation and EM Theory (ISAPE), Guilin, China. 18-21 October 2016

[15] da Costa KQ, Dimitriev V, Nascimento CM, Silvano GL. Theoretical analysis of graphene nanoantennas with different shapes. Microwave and Optical Technology Letters. May 2014;**56**(5)

[16] da Costa KQ, Dimitriev V. Planar monopole UWB antennas with cuts at the edges and parasitic loops. InTech: Ultra Wideband Communications: Novel Trends—Antennas and Propagation, 1st ed., pp. 143-145, 2011

[17] COMSOL Multiphysic 4.4, COMSOL Inc., http://www.comsol.com

[18] Hanson GW. Dyadic Green's functions and guided surface waves for a surface conductivity model of Graphene. Journal of Applied Physics. 2008;**103**:064302

Chapter 2

# A Combined Electric/Magnetic Field Surface Volume Integral Equation Approach for the Fast Characterization of Microstrip/Substrate Integrated Waveguide Structures and Antennas

Thomas Vaupel

Additional information is available at the end of the chapter

http://dx.doi.org/10.5772/intechopen.75062

**Abstract**

In this contribution, a combined electric field/magnetic field surface/volume integral equation approach is presented with special features for the characterization of substrate integrated waveguide (SIW) components. Due to the use of a parallel-plate waveguide Green's function, only a small number of volume current basis functions are necessary to model the vias of the SIW sidewalls. The focal point is set on the specification of microstrip-SIW transitions using a via and a pad/antipad configuration for the coupling between the microstrip parts and the SIW and transitions with a two-stage ridged substrate integrated waveguide (SIW) where the SIW has a very thick substrate with regard to the microstrip line making it well suited for the design of a new class of compact end-fire SIW antennas for phased array applications which are partly characterized with CST Microwave Studio. An effective S-parameter extraction is used with both microstrip and special SIW waveguide ports.

**Keywords:** integral equation, surface/volume discretization, microstrip-SIW transitions, S-parameter extraction, via and slot modeling, horn, slot/leaky wave antennas

## 1. Introduction

Due to the trend to higher frequencies, substrate integrated waveguide (SIW) components and antennas are once more well-suited building blocks to realize applications with low losses and compact design. A SIW consists of two periodic rows of metallic vias connecting metallic strips (or ground planes) on top and bottom of a dielectric substrate as a quasi-planar structure and

IntechOpen

© 2018 The Author(s). Licensee IntechOpen. This chapter is distributed under the terms of the Creative Commons Attribution License (http://creativecommons.org/licenses/by/3.0), which permits unrestricted use, distribution, and reproduction in any medium, provided the original work is properly cited. CC BY

can thus very easily integrated and fabricated together with other microstrip/coplanar components using standard printed circuit board technologies and can be considered as a filled rectangular waveguide with the via rows as sidewalls [3]. Therefore, SIWs have the same low loss properties and first designs can be made using tools for the calculation of rectangular waveguide components. Thus, SIWs are increasingly used for antenna feeding networks with power dividers, filters, resonators, couplers, and phase shifters in micro- and mm-wave applications. For the full-wave characterization of such components, frequently mode matching techniques are proposed, but they are typically restricted to the modeling of the SIW components itself but without considering transitions to a microstrip/coplanar environment or radiating slot elements [2]. At the moment a strong interest is set on compact broadband horn-like SIW antennas with end-fire radiation characteristic [10, 11]. However, to reach the desired broadband properties with compact dimensions suited for phased array applications, SIWs on a thick substrate are needed. Simple microstrip-SIW transitions or interconnects like in [3, 6] cannot be used for the excitation of such thick SIWs; in this context, tapered transitions in vertical and lateral direction are proposed in [4]. In contrast to this, we have presented a two-stage transition based on a Chebychef design in [5]. Since the fabrication of the ridged-SIW structures is quite elaborate, we have also investigated transitions using a shorted via between the microstrip line and the bottom of the SIW as given in [6]. Such structure can be easily fabricated, but the bandwidth becomes small using thicker substrates. For thick substrates we investigate transitions where the length of the coupling via is smaller than the SIW thickness like the typical probes in standard rectangular waveguides. For the characterization of these structures, we have extended an integral equation approach [7] with special features for the effective characterization of SIWs. Based on the Green's functions of multilayered media, a substrate-filled parallel-plate medium can be used in many cases; thus together with volume basis functions for vertical currents, only the vias of the SIWs must be discretized. The microstrip parts are modeled with electric surface currents, whereas the antipads and other apertures are modeled with magnetic surface currents allowing the characterization of a class of leaky wave antennas [8] with very low computational effort. A further task was the careful S-parameter determination comprising both microstrip- and SIW waveguide ports.

## 2. Formulation with first applications

The round vias of SIW structures with diameter $d_{circ}$ can be replaced for the simulations by quadratic vias with the side length $l_{square}$ with typically high accuracy using the formula [1]:

$$l_{square} = \frac{d_{circ}}{2}\left(1 + \frac{1}{\sqrt{2}}\right) \tag{1}$$

The vias are then modeled with quadratic volume current basis functions (piecewise constant current in height) connecting the corresponding metallic sheets of one SIW waveguide with typically only one basis function per via. For multilayer microstrip-SIW transitions and other SIW components and circuits, we use a very effective modeling and discretization strategy [7].

http://dx.doi.org/10.5772/intechopen.75062

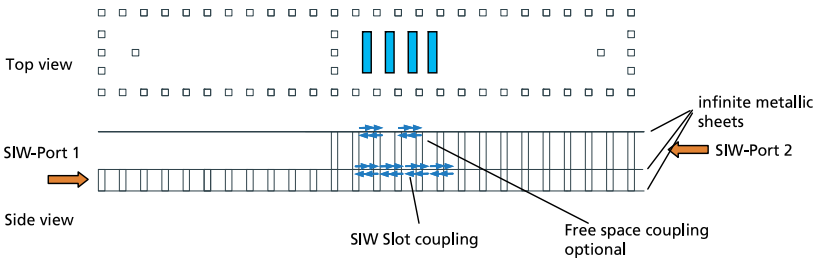


**Figure 1.** Structure with SI waveguides and ports on different levels with slot coupling as well as free space coupling (or a further stratified halfspace).

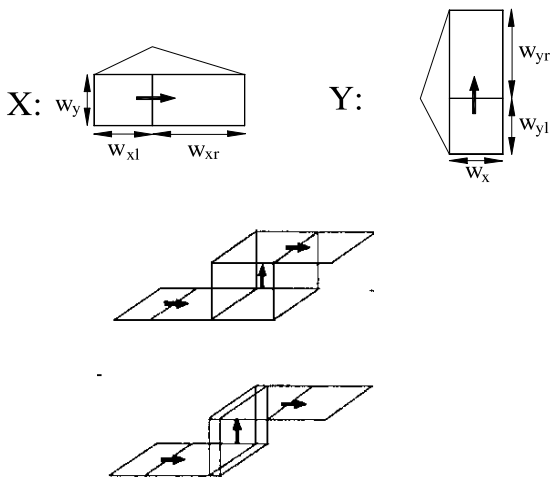


**Figure 2.** Used basis functions. Top: Planar (asymmetric) rooftop functions for electric and magnetic surface currents (x- and y-orientation). Bottom: z-directed volume currents attached to x-directed surface currents.

The SIWs are modeled with parallel-plate media where the metallic plates are connected by the vias of the SIW. A typical scheme, here with SIW waveguide ports, is given in **Figure 1**. It consists of two SI waveguides on different levels and SIW ports with a slot coupling (blue) and optional slots for the radiation in the upper half space, which can be free space or a complex stratified medium. As indicated in the side view, the slots are modeled with corresponding magnetic surface currents (also in blue) at the upper and lower side of the corresponding metallic sheet with opposite signs leading to a magnetic field integral equation for the magnetic currents. A sketch of the used basis functions is given in **Figure 2**.

For the matrix entries in the method of moments concerning magnetic surface current functions $n$ and $m$ on one level $lb$, we get a spectral admittance representation:

$$Y_{nm}(lb,lb) = \int_{k_x}\int_{k_y} \overleftrightarrow{G}^{H}_{M,\,lb,\,comp}\left(k_x,k_y,z_{lb}\right)\cdot\vec{F}_{lb,\,m}\left(k_x,k_y\right)\cdot\vec{F}^{*}_{lb,\,n}\left(k_x,k_y\right)dk_x dk_y \tag{2}$$

with the composite Green's function:

$$\overleftrightarrow{G}^{H}_{M,\,lb,\,comp}\left(k_x,k_y,z_{lb}\right)=\overleftrightarrow{G}^{H}_{M,\,lb}\left(k_x,k_y,z_{lb}\right)+\overleftrightarrow{G}^{H}_{M,\,lb-1}\left(k_x,k_y,z_{lb}\right)$$

which is the sum of the Green's functions $\overleftrightarrow{G}^{H}_{M,\,lb}$ above (radiation into a half-space or another parallel-plate medium) and below the metallic sheet *lb* (parallel-plate medium) $\overleftrightarrow{G}^{H}_{M,\,lb-1}$ and $\vec{F}_{lb,\,m,\,n}\left(k_x,k_y\right)$ the Fourier transforms of the basis functions. For the couplings between volume currents, we get a combined space/spectral impedance expression:

$$Z_{nk}\left(lv,lv^{'}\right)=\int_{k_x}\int_{k_y}\int_{z'}\int_{z}\overleftrightarrow{G}^{E}_{J,\,lb}\left(k_x,k_y,z^{'},z\right)\cdot\vec{F}_{lv,k}\left(k_x,k_y,z^{'}\right)\cdot\vec{F}^{*}_{lv,\,n}\left(k_x,k_y,z\right)dz\,dz^{'}\,dk_x dk_y \tag{3}$$

with a complete analytical treatment of the space-domain integrations, and for couplings between magnetic and volume currents, we get a matrix entry without dimension, denoted with *ZY*:

$$ZY_{nk}(lv,lb)=\int_{k_x}\int_{k_y}\int_{z'}\overleftrightarrow{G}^{E}_{J,\,lb}\left(k_x,k_y,z_{lb},z^{'}\right)\vec{F}_{lv,k}\left(k_x,k_y,z^{'}\right)\cdot\vec{F}^{*}_{lb,\,n}\left(k_x,k_y,z_{lb}\right)dz^{'}\,dk_x dk_y \tag{4}$$

The spectral domain integrations are carried out with two different strategies depending on the lateral distance of the basis functions.

A structure well suited for testing of different features of the method is given in **Figure 3**. At the right, we apply a SIW port 2 or a SIW absorber consisting of only five volume functions connected by lumped resistors with the metallic sheets.

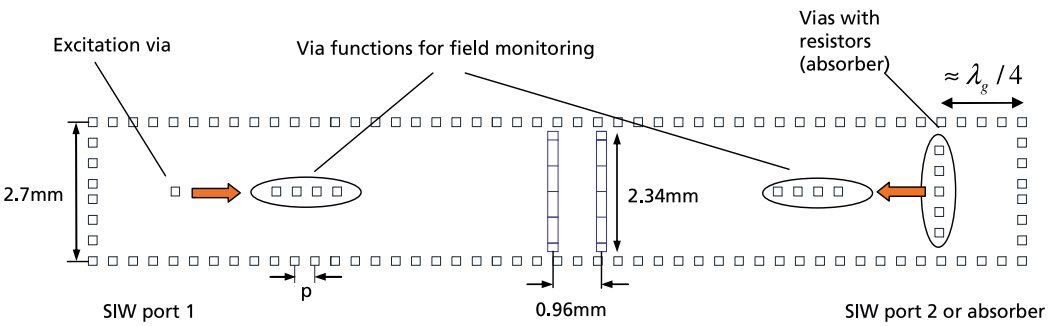


**Figure 3.** Structure for testing of SIW ports and absorbers combined with a reflection-canceling slot pair. Via side length 0.17 mm and via distance p = 0.4 mm, $\varepsilon_r = 3.0 - j0.003$, and h = 0.254 mm.

The SIW ports consist of an excitation via and four via (volume) functions here only used for field (voltage) monitoring in the center of the SIW to extract the forward and backward waves in the SIW for S-parameter calculation.

To compute the voltages at the field monitoring vias, at first the complete coupling matrix with all via functions is computed. Afterward the matrix is compressed by deleting the matrix columns related to the monitor functions and by taking out the related line entries stored for later reuse and the voltage computation. |S11|,tl and |S12|,tl are the results for the homogeneous through line with nearly an ideal matching and transmission showing the good performance of the SIW port model and S-parameter extraction.|S11|,abs shows the broadband matching with the 5-via absorber at the right using 240 Ohm resistors connecting the vias to the ground plane. Such an absorber can be used as an effective numerical broadband-matched termination of a SIW, but it should also be possible to manufacture it using SMD resistors connecting the vias with the ground planes.

For another test the SIW is fitted with two slots of length 2.34 mm in the middle. The separation and length of the slots are chosen in such a way that we get a so-called reflection-canceling slot pair. |S11|,ds denotes the matching with the additional reflection-canceling slot pair showing a quite good matching around 36–37 GHz.

A good test for the reliability of the numerical solutions and to get a detailed insight into the power flow of a structure is the computation of the power balance. Thus the input power at the excitation via (**Figure 3**) is

$$P_{IN} = \frac{1}{2}\mathrm{Re}\{U \cdot I^*\} \tag{5}$$

The absorbed energy within the $N_{abs}$ resistors with resistance $R$ amounts to

$$P_{abs} = \frac{1}{2}\sum_{n=1}^{N_{abs}} R|I_n|^2 \tag{6}$$

And the radiated space wave energy into the upper halfspace is determined with the help of the saddle point method leading to the integral

$$P_{Rad} = \left| \frac{jk_m \cos\vartheta_r}{2\pi r} \int_{\vartheta_r=0}^{\pi/2} \int_{\varphi_r=0}^{2\pi} e^{jk_{xr} r \sin\vartheta_r \cos\varphi_r} e^{jk_{yr} r \sin\vartheta_r \sin\varphi_r} \overleftrightarrow{G}_M^{E,FF}(k_{xr}, k_{yr}) \sum_{n=1}^{N_s} I_n \vec{F}_n\,(k_{xr}, k_{yr})\, r \sin\vartheta_r \, d\varphi_r d\vartheta_r \right|^2 \tag{7}$$

with the wavenumbers $k_{xr} = -k_m \sin\vartheta_r \cos\varphi_r$ and $k_{yr} = -k_m \sin\vartheta_r \sin\varphi_r$. Here $k_m$ is the wavenumber of the topmost layer $m$ and $\overleftrightarrow{G}_M^{E,FF}$ is the far-field evaluation of the Green's function for the electric field of magnetic (surface) currents radiating into layer $m$.

If the structures are analyzed with infinite low dielectric and metallic losses,

$$P_{IN} = P_{Rad} + P_{Abs} \tag{8}$$

must hold. The results for the SIW with the absorber and the slot pair are given in **Figure 4**, right. It can be seen that the radiation power is below 20 percent up to about 37 GHz (the frequency band with good matching) with only one slot pair, whereas about 80 percent is converted in the absorber. If the input power according to Eq. (5) is normalized to 100 percent, then the sum in Eq. (8) leads to the red curve in **Figure 4**, right. Except some small deviation in the region 40–42 GHz, the 100 percent are met with good accuracy. However, for this accuracy the number of sampling points for the numerical integration must be quite high.

For an improved computational performance, a general coupling integral reads

$$V_{nm} = \int_{k_x}\int_{k_y} \left[ I\overleftrightarrow{G}\left(k_x, k_y, z_m, z_n\right) - I\overleftrightarrow{G}^{Asy}\left(k_x, k_y, z_m, z_n\right)\right] \cdot \vec{F}_{m0}\left(k_x, k_y.z_m\right) \cdot \vec{F}^{*}_{n0}\left(k_x, k_y, z_n\right) e^{jk_x\Delta x_{nm}} e^{jk_y\Delta y_{nm}} dk_x\, dk_y$$
$$+ \int_{k_x}\int_{k_y} I\overleftrightarrow{G}^{Asy}\left(k_x, k_y, z_m, z_n\right) \cdot \vec{F}_{m0}\left(k_x, k_y.z_m\right) \cdot \vec{F}^{*}_{n0}\left(k_x, k_y, z_n\right) e^{jk_x\Delta x_{nm}} e^{jk_y\Delta y_{nm}} dk_x\, dk_y \tag{9}$$

where $I\overleftrightarrow{G}$ is a general Green's function tensor where all analytical space-domain integrations with regard to $z$ and $z'$ are already incorporated. The $\vec{F}_{m,n0}$ are the Fourier transforms of the basis functions in the origin of the coordinate system; thus, the $\Delta x_{nm}$ and $\Delta y_{n,m}$ are the lateral separations of the basis functions with regard to $x$ and $y$. **Figure 5** shows the different integration areas with the integrand behavior in the inner area $A_{In}$ and the used simultaneous integration path deformations (for both wavenumbers $k_x$ and $k_y$) in this area.

For basis functions with very small lateral separations or overlapping functions and self-couplings, an asymptotic representation $I\overleftrightarrow{G}^{Asy}$ for $k_\rho = \sqrt{k_x^2 + k_y^2} \to \infty$ is subtracted, leading to

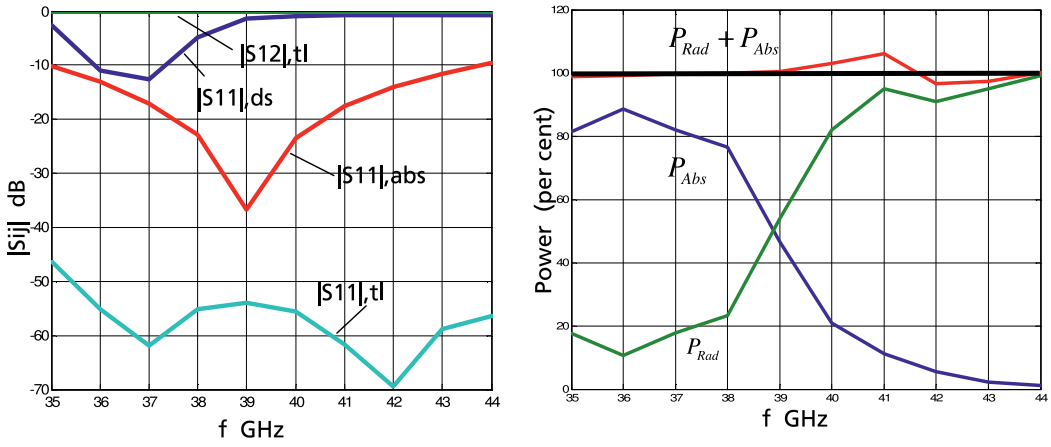


**Figure 4.** Left: S-parameter extraction results for the SIW through line (tl), with absorber (abs) and additional double slot (ds), h = 0.254 mm. Right: power balance.

an overall integrand with an exponential decay with regard to $k_\rho$. The contribution with this asymptotic representation is then added in Eq. (9) with the second integral, which can be evaluated completely analytically for all kinds of involved basis functions. In the inner area, pole rings due to surface wave and/or parallel-plate waves can occur; furthermore the inner area contains all wavenumbers related to radiating space waves. The wavenumbers in the outer areas $A_{out1}$, $A_{out2}$, and $A_{out3}$ are mainly related to evanescent waves. However, if we have only SIW structures and components like in **Figure 3** without any radiating slots, we have only a contribution of a parallel-plate wave pole ring in the inner area for the coupling integrals of vias Eq. (3), whereas with a radiation by slots or other radiating elements into the upper (layered) halfspace, a branch point occurs as further singularity as well as possible surface wave poles in the integrands of the coupling integrals Eq. (2) and Eq. (4). All these

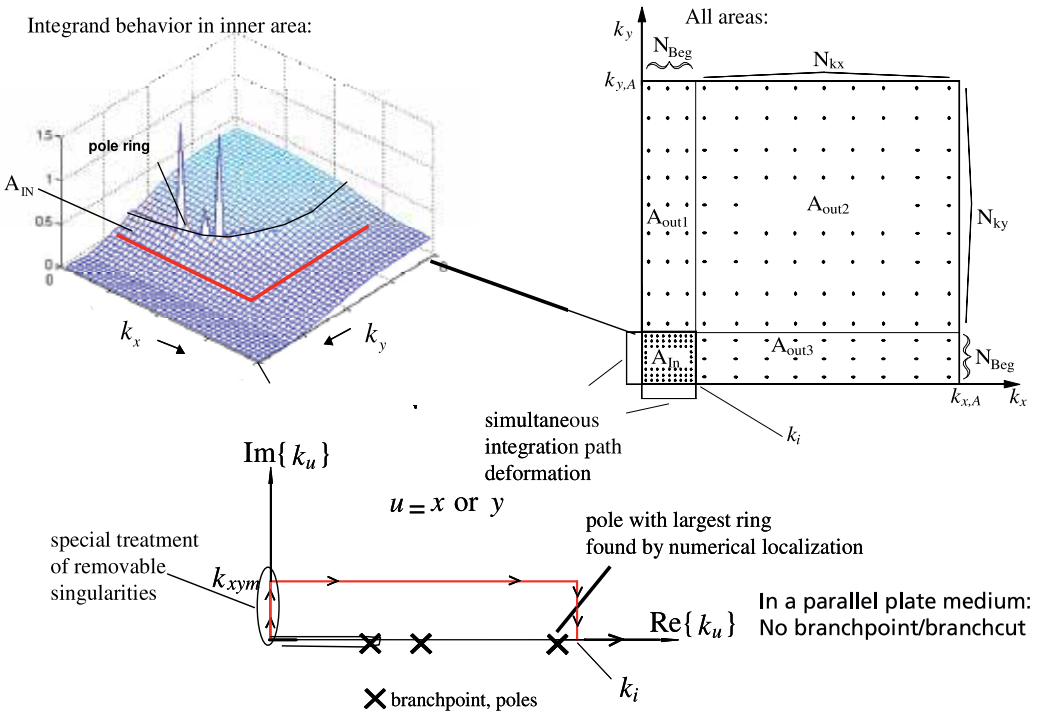


**Figure 5.** Top left: Typical integrand behavior in the inner integration area with pole rings. Right: First quadrant with all integration areas. Bottom: Simultaneous integration path deformations in the inner area.

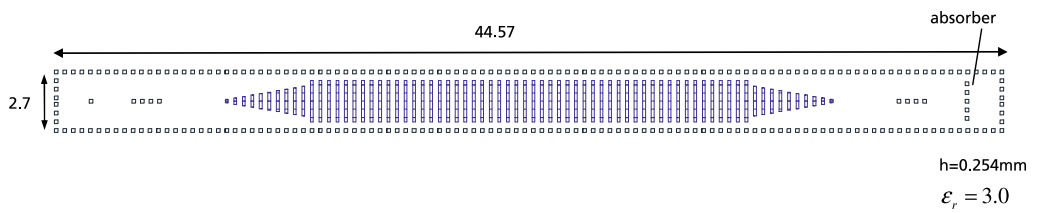


**Figure 6.** A leaky wave antenna with slots in the cover for end-fire radiation with the same SIW as in **Figure 3**. Slot separation 0.4 mm.

singularities are circumvented with the red integration path applied for both wavenumbers $k_x$ and $k_y$(**Figure 5**, bottom). Since the only contribution in Eq.(3) for vias within the parallel plates comes from the parallel-plate wave pole, the number of integration sampling points in the inner area must be chosen significantly higher than typical microstrip and slot/coplanar

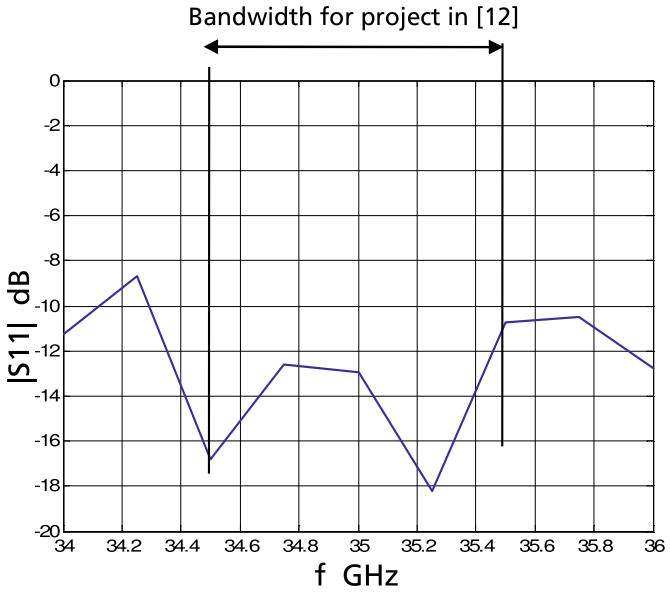


**Figure 7.** Matching behavior of the structure in **Figure 6**.

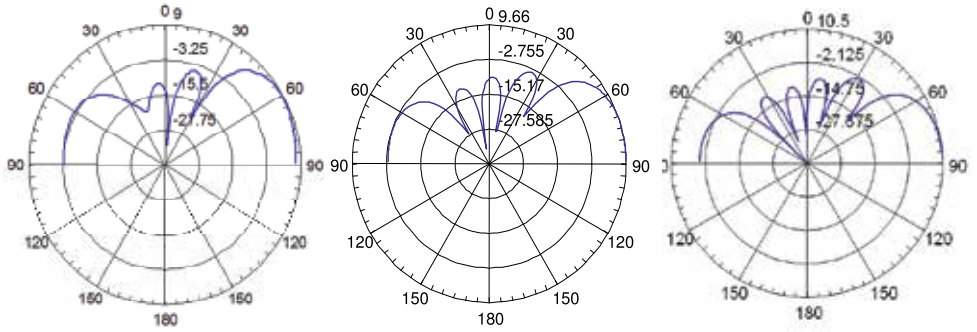


$P_{Abs} = 47.6\%$ $P_{Abs} = 52.0\%$ $P_{Abs} = 60.7\%$

$P_{Rad} = 49.6\%$ $P_{Rad} = 45.5\%$ $P_{Rad} = 36.45\%$

$P_{Rad} + P_{Abs} = 97.2\%$ $P_{Rad} + P_{Abs} = 97.5\%$ $P_{Rad} + P_{Abs} = 97.2\%$

**Figure 8.** Radiation patterns and power balance of the leaky wave antenna in **Figure 6**.

structures. For the structure in **Figure 3** with slots and absorber, 16 sampling points must be applied for both $k_x$ and $k_y$ wavenumbers on the horizontal path to reach the power balance accuracy in **Figure 4**, right. On the vertical paths, two sampling points for each path are sufficient. For the numerical integration, composite Legendre-Filon quadrature techniques are used.

A leaky wave antenna for end-fire radiation is given in **Figure 6** applying slots with constant length (l = 1.9 mm) in the middle and additional tapered slot areas at the ends for better matching. The simulated matching behavior is given in **Figure 7** together with the desired bandwidth for the MIMO radar project in [12].

A good test for the reliability of the results is to compute the sum of the absorbed power $P_{abs}$ and the radiated power $P_{rad}$ without dielectric losses. Thus we get for $P_{abs} + P_{rad}$ nearly constant values around 97.5% if the integration accuracy for Eqs. (2)–(4) is sufficient. This is outlined in **Figure 8** for three frequencies together with the antenna elevation patterns.

## 3. Microstrip to SIW transitions

For the connection of structures like in **Figure 6** to a microstrip circuitry, a microstrip-SIW transition like in **Figure 9** is well suited, consisting of a microstrip line with width $w_{mic}$ (0.33 mm) on a substrate with the height $h_{Mic}$ (here 0.13 mm). The energy of the microstrip line is then coupled by the via (with distance $d$ to the left wall, here 1.49 mm) through the antipad (blue, side length 0.42 mm) into the SIW with the height $h_{SIW}$ (0.75 mm) and width $w_{SIW}$ (4.29 mm).

The permittivity for both the microstrip line and the SIW is $\varepsilon_r = 3.0$. The incident ($i_i$) and backward ($i_b$) current waves on the microstrip line are extracted by means of the complex amplitudes of four current basis functions. The voltage waves in the SIW $u_i$ and $u_b$ are extracted by means of four electric field monitors in the same way as in **Figure 3**.

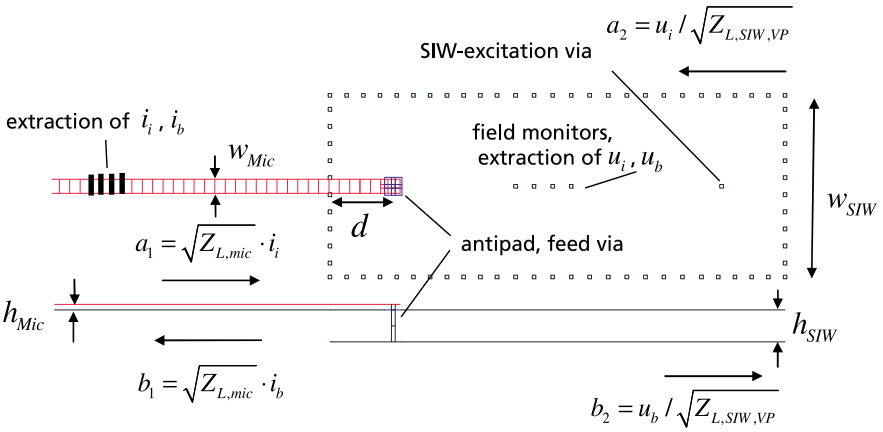


**Figure 9.** Extraction of the S-parameter for a microstrip-SIW transition.

For the consistent evaluation of the wave quantities $a_1, b_1, a_2, b_2$, it is necessary to use the voltage-power definition for the characteristic impedance for the microstrip line and especially for the SIW. With the help of the equivalent width of a SIW:

$w_{eq} = w_{SIW} - \frac{d_{circ}^2}{0.95\,p}$ (see, e.g. [3] and $d_{circ}$ from Eq. (1)) and p the center to center distance of the vias we get for the characteristic impedance:

$$Z_{L,\,SIW,\,VP} = 2\frac{h_{SIW}}{w_{eq}}\frac{\mu_0\omega}{\sqrt{k^2 - \left(\frac{\pi}{w_{eq}}\right)^2}} = \frac{|U|^2}{2P_{w,\,a,\,b}} \tag{10}$$

**Figure 10** shows the results with the own IG-approach and with the time domain approach of CST Microwave Studio both with a very similar behavior. The green curve for $|S_{11}|$ in the own IG-approach is for a finer vertical discretization (three volume basis functions), whereas the other curves are computed with two volume basis functions showing already a stable solution behavior for this configuration. For $|S_{22}|$ we get nearly the same results as for $|S_{11}|$ as expected due to the very low dielectric losses considered for the simulation in contrast to the results with CST MWS. Structures like in **Figure 9** with a small thickness of the SIW can be designed with the formulas, e.g., in [6]. For the input resistance, we get

$$R_{in} = 2 \cdot \frac{k_0\ h_{SIW}\ Z_0}{w_{eq}\ \beta_{10}} \sin^2(\beta_{10}\,d) \sin^2\left(\frac{\pi x}{w_{eq}}\right) \tag{11}$$

with $k_0$ and $Z_0$ the free space wave number and wave impedance, respectively, and $\beta_{10}$ the propagation constant in the filled equivalent rectangular waveguide. Typically, the feed via is centered in the SIW, i.e., $x = w_{eq}/2$ and $d$ is around a quarter of a guided wavelength and $h_{SIW}$ should be much smaller than a quarter of a guided wavelength to guarantee a nearly constant current distribution on the feed via. In contrast to the formula in [6], Eq. (11) has an additional

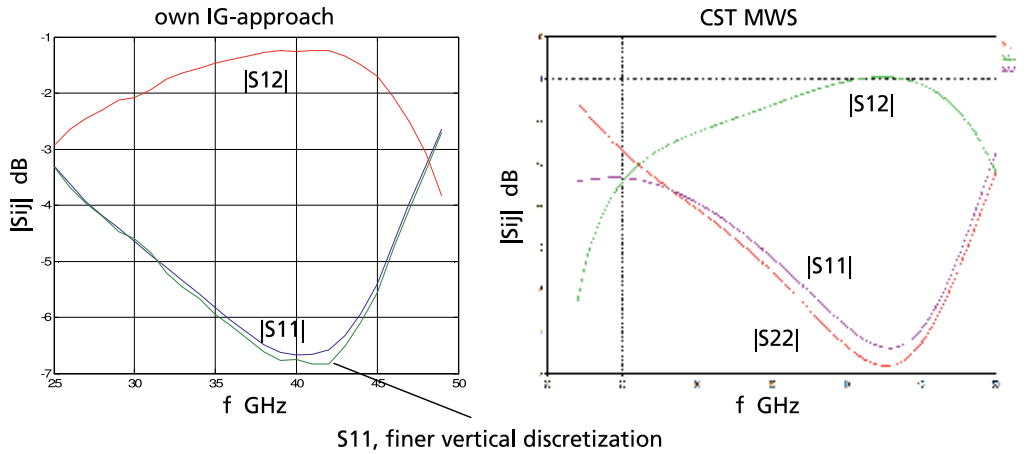


**Figure 10.** Results for the structure in **Figure 9**. Left: With own IG-approach. Right: With CST Microwave Studio (time domain).

factor of 2 due to a mistake during the derivation in [6]. For small values of $h_{SIW}$, the structure in **Figure 9** can be further optimized, and a broadband matching can be achieved with a microstrip circuitry as shown in the following structure. For larger values $h_{SIW}$, the structure in **Figure 11** is much better suited for broadband operation.

In this case the feed via has only a length of 1.0 mm within the SIW with a height of 2.5 mm. Again the permittivity for both the microstrip line and the SIW is $\varepsilon_r = 3.0$. Such a structure is similar to a coaxial probe feed in a rectangular waveguide; thus, a start design can be made with solution methods like in [6], modified for filled waveguides. However, the influence of the antipad and optional pad structure typically has a significant influence on the overall impedance seen from the microstrip line. Therefore we started directly with numerical tests using typical values for pad and antipad size as well as for the length and the side length (here 0.43 mm) of the feed via. The other vias have a side length of 0.26 mm with a separation of 1 mm. This leads for the configuration in **Figure 11** (without the matching stubs) in a short time to a design with the behavior in **Figure 12**, left. For the structure in **Figure 11**, only 311 basis functions are needed with a computation time of about 1 minute for 34 frequency points (AMD Phenom II X4 965 Quadcore processor). For the vertical discretization, six volume basis functions are used for each via of the SIW and the feed via to achieve stable results.

In this case, an additional pad did not show a further improvement, but with the shape of the antipad (blue), a further slight optimization could be performed, leading to a length of 0.9 mm and a width of 0.7 mm. However, with these specifications, we not yet achieve a matching below −10 dB in the desired frequency range from 30 to 40 GHz, but we get a flat curve between −7 and − 8 dB for $|S_{11}|$. Based on this behavior, a further matching with two additional microstrip stubs leads to the behavior in **Figure 12**, right, now showing a good matching from less than 30 GHz to more than 40 GHz. **Figure 13** shows the matching with a SIW absorber at the right end of the SIW in **Figure 11**. In this case the absorber has a slightly smaller bandwidth than the transition.

Besides this kind of transition, we have also specified transitions with a stepwise ridged waveguide. These structures are similar than the proposed transitions in [4], but we do not need the quite complex tapered shapes described in [4]. Our design is based on a two-stage Chebychef approach which can handle also much higher transform ratios than the designs in [6].

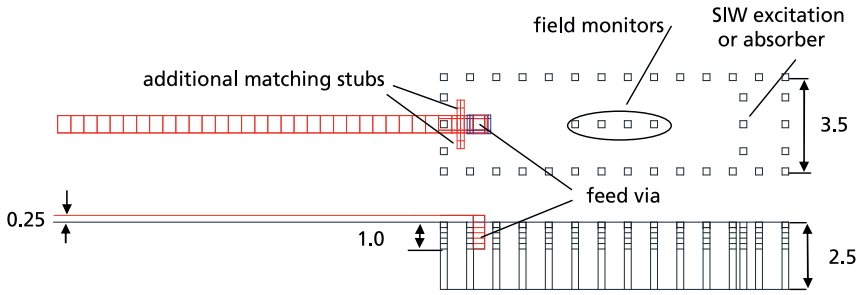


**Figure 11.** Broadband microstrip-SIW transition for SIWs with larger thickness.

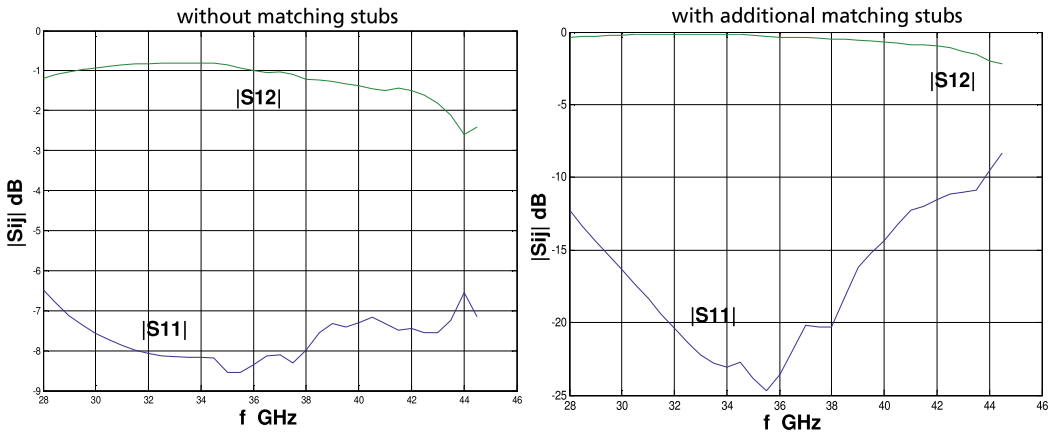


**Figure 12.** Results for the structure in **Figure 11** with microstrip port to the left and SIW port to the right. Left: Without matching stubs. Right: With additional matching stubs.

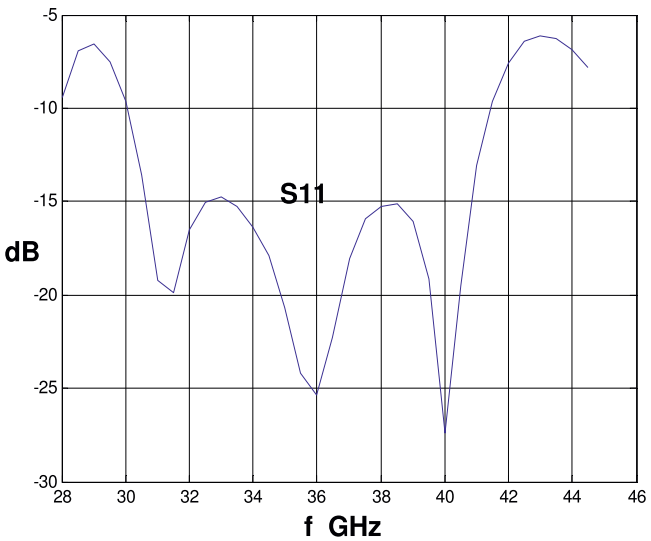


**Figure 13.** Result for the structure in **Figure 11** with SIW absorber to the right.

A typical design with our approach is given in **Figure 14**. Here, the transform ratio with the definition

$$\alpha = \frac{\text{hrw-hmic}}{\text{hrw}}$$

amounts to 7, whereas in [4], only a structure with a transform ratio of 4 was designed. **hrw** is the height of the standard SIW (or rectangular waveguide to the right) and **hmic** is the height of the microstrip line to the left.

http://dx.doi.org/10.5772/intechopen.75062

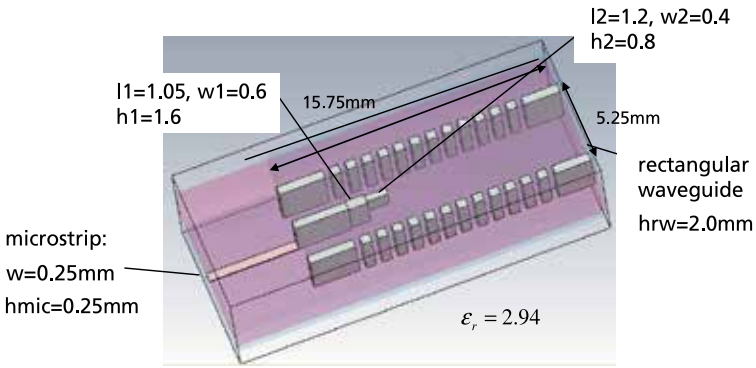


**Figure 14.** Design of a microstrip-SIW transition with two-stage ridged waveguide. Dimensions in mm.

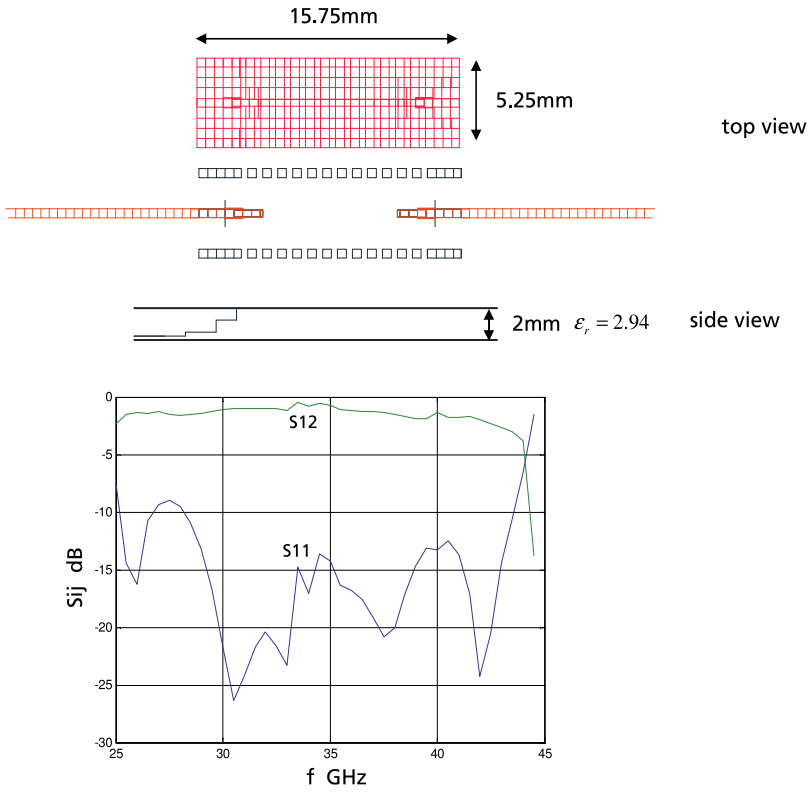


**Figure 15.** Microstrip to SIW transition with two-stage ridged waveguide. Top: Back-to-back arrangement with discretization. Bottom: S-parameter (absolute values).

For the design of the transition, a quantity

$$\sec\Theta_m = \cosh\left(\frac{1}{2}\cosh^{-1}\left|\frac{\ln(Z_{SIW}/Z_{mic})}{2\cdot a_{rip}}\right|\right)$$

is computed, where $Z_{SIW}$ is the characteristic impedance of the SIW or the equivalent rectangular waveguide, here the voltage-power definition Eq. (10) should be used, and $Z_{mic}$ the characteristic impedance of the microstrip line. With this quantity, two reflection factors are computed with

$$\Gamma_0 = \frac{a_{rip}}{2}\sec^2(\Theta_m), \quad \Gamma_1 = a_{rip}\left(\sec^2(\Theta_m) - 1\right)$$

where $a_{rip}$ is the tolerated intensity of the ripples in the passband, e.g., for 10 percent, $\alpha_{rip} = 0.1$. With $Z_{SIW} = 258$ Ohm and $Z_{mic} = 47$ Ohm, we get $\sec\Theta_m = 2.18$. With the reflection factors, we can compute the characteristic impedances for the ridged waveguide sections:

$$Z_1 = Z_{mic} \cdot e^{2\Gamma_0}, \quad Z_2 = Z_1 \cdot e^{2\Gamma_1}$$

leading here to $Z_1 = 74.45$ Ohm and $Z_2 = 161$ Ohm. To determine the corresponding ridged waveguide dimensions, we have used CST MWS to compute the voltage from the ridge to the lower ground for a given power. This leads to the dimensions **l1**, **w1,** and **h1** for length, width, and height of the first section and **l2**, **w2,** and **h2** for the second section as also given in **Figure 14**. For the section which is connected with the microstrip line, we have chosen the same width as for the microstrip line because the differences of the characteristic impedances remain small. Of course a further adjustment of this width can be done. **Figure 15**, top, shows the transition in a back-to-back arrangement together with the discretization for our integral equation approach (side view shows only the first transition). In this case, we have modeled the cover of the SIW as a finite structure, whereas the bottom ground plane remains infinite.

## 4. SIW horn antenna elements

**Figure 15**, bottom, shows the matching behavior of this arrangement. The reflection factor remains mainly below −15 dB; the structure may be a good alternative to the transition in **Figure 11**. The back-to-back structure was also built and measured successfully and was then combined with two radiating apertures shown in **Figure 16**. On the left the transition is combined with a simple open SIW and a short parallel-plate section. On the right an additional stepwise widening is applied. This is realized with two dielectric bars which are glued on the top and bottom side of the parallel-plate section where the metallization was removed before at these areas. As shown in the inset in **Figure 16**, the upper dielectric bar is metallized at the top and at the left side and analogously the lower bar to get a symmetric aperture with a height of 3.5 mm.

For the characterization of such structures with an end-fire radiation, we use CST Microwave Studio (time domain solver) at the moment, because it is still difficult with our integral equation framework to handle structures with finite dielectric layers to one side [5].

**Figure 17** shows left the simulated matching behavior of the two structures. With the simple open SIW, the matching is still very poor as expected (blue line), whereas with the additional widening, the reflection factor remains below −10 dB for a large frequency range. However, despite of the additional widening, we still get a rather strong backward radiation as illustrated

http://dx.doi.org/10.5772/intechopen.75062

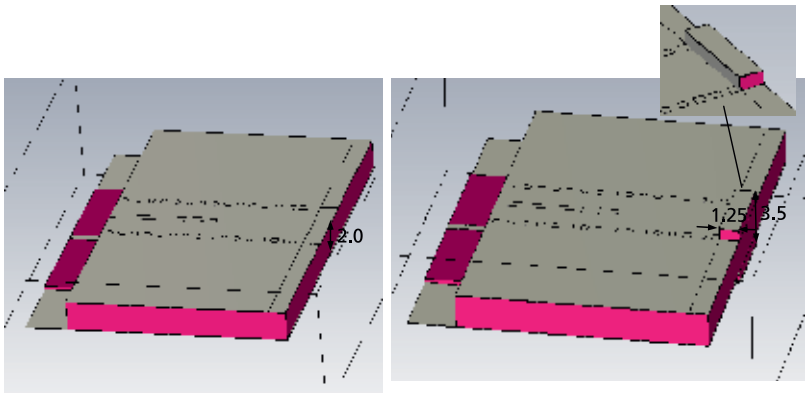


**Figure 16.** Combinations of the transition in **Figure 15** with two radiating apertures. Left: Open SIW with short parallel-plate section. Right: With a stepwise widening at the end.

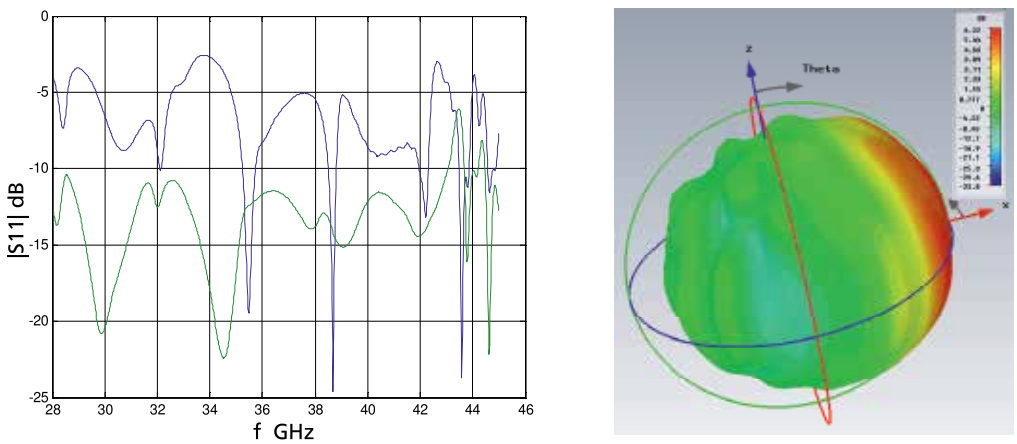


**Figure 17.** Left: Matching behavior of the structures in **Figure 16**. Blue: Open SIW and parallel-plate section. Green: With widening. Right: Antenna pattern (gain) of the structure with widening. Simulations with CST MWS.

in **Figure 17**, right. The structures were manufactured and measured afterward showing the matching behavior in **Figure 18** with the screenshots of the network analyzer. Similar as the simulated results, the simple structure with open SIW shows a poor matching around −5 dB up to the dip around 33.8 GHz, whereas the structure with widening shows a good matching mainly below −10 dB over the whole measured frequency range. Despite of the good matching behavior and further options to reduce the backward radiation, the stepwise widening is difficult to fabricate, even in the case it is designed with via wholes like the feeding SIW.

SIW horn antennas have already been studied for a longer time; typically they suffer from the substrate to the air transition which leads to larger reflections and backside radiation especially with thin substrates as we have seen with the open SIW aperture in **Figure 16**. In [9], a better matching and bandwidth enhancement of such kind of antennas is achieved with several parallel-plate sections in front of the origin antenna. However, the problem with the large

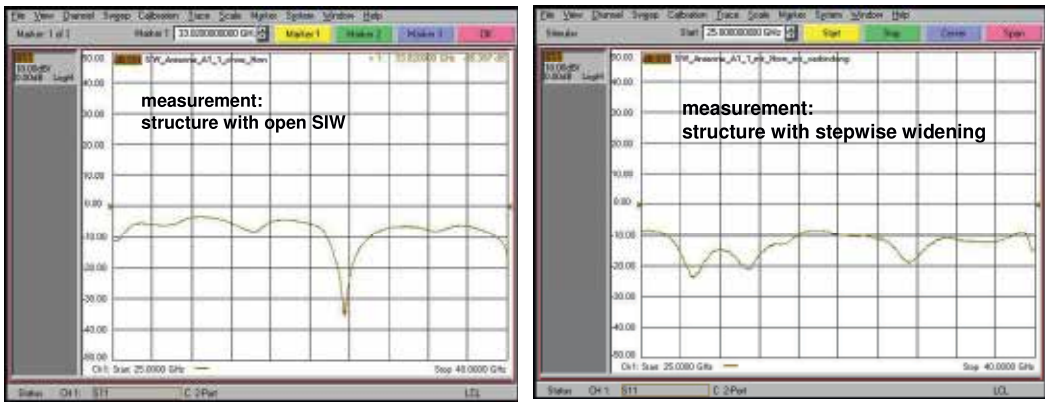


**Figure 18.** Measured matching behavior of the structures in **Figure 16**. Left: Open SIW and parallel-plate section. Right: With widening.

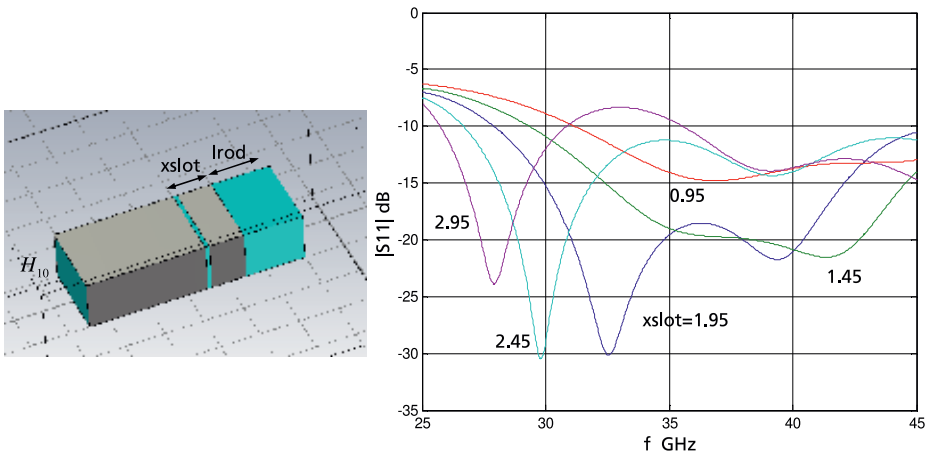


**Figure 19.** Left: Rectangular waveguide with ringslot and dielectric rod. Right: Matching behavior of the left structure in dependence of **xslot** (in mm) and **lrod** fixed to 2.5 mm (CST MWS).

backside radiation is only slightly reduced or not at all; typically, a good matching is achieved but simultaneously with a large backside radiation and vice versa. Some further improvements are made in [10] using transitions with a saw-tooth geometry. But for a good performance, the aperture width must be typically larger than one free space wavelength; thus, an application within a typical phased array arrangement requiring an element distance around $\lambda_0/2$ is not possible.

In contrast to the parallel-plate configurations in [9, 10] or the widening in **Figure 16**, right, for a better matching of SIW horn antennas, we use in a further study a (rectangular) ringslot to improve the matching behavior and bandwidth together with a reduction of the backside radiation. **Figure 19** shows the structure with the rectangular ringslot located with the distance **xslot** apart from the right metallic edge of the rectangular waveguide and a dielectric extension with the length **lrod** (fixed to 2.5 mm). The width of the waveguide and dielectric is set to 4.0 mm, the height to 2.0 mm. This means that the width is only slightly higher than $\lambda_0/2$ at

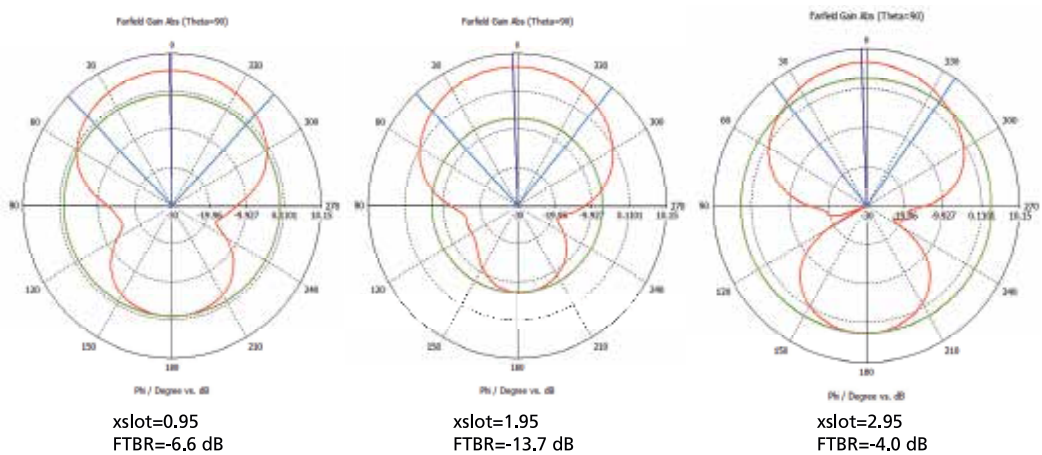


**Figure 20.** Azimuth diagrams at 35 GHz and FBTR for three values of **xslot**.

35 GHz. At the right the matching behavior of the structure with $H_{10}$wave excitation and variation of **xslot** is illustrated. With a desired center frequency of 35 GHz and a bandwidth with a range of 30 to 40 Ghz at least, a value of 1.95 mm for **xslot** is best suited in this context.

The dependence of the matching behavior with regard to **lrod** and the slot width is much lower; in this case, a slot width of 0.2 mm was used. **Figure 20** shows the azimuth diagrams for three values of **xslot** together with the forward-to-backward ratio (FTBR). It can be observed that the best value is reached for xslot = 1.95 mm, which also leads to the best matching behavior.

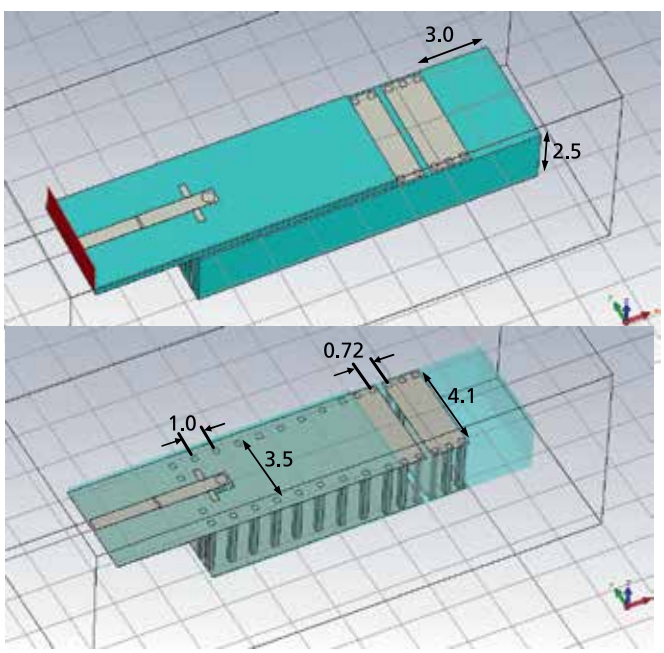


**Figure 21.** Complete antenna element in SIW technology. Top: Representation with hidden components. Bottom: With transparent substrates. Dimensions in mm.

The structure in **Figure 19** has then been transformed into SIW technology and combined with the microstrip to SIW transition of **Figure 11** with the substrate thickness 2.5 mm. This leads to the structure in **Figure 21**. The slot width in the lower and upper metallization amounts to 0.3 mm; the via separation near the slot was reduced to 0.72 mm. In the region of the feeding via, the SIW has a width of 3.5 mm as in **Figure 11** (center to center of the vias) and is then increased by a smooth taper to 4.1 mm.

The vias close to the slot are modeled with a round cross section, but the differences compared with a quadratic cross section are negligible.

**Figure 22** shows the matching behavior simulated with CST. We can see that the reflection factor is even below −15 dB in the range from 30 to 40 GHz.

Finally, **Figure 18** shows the antenna patterns derived with CST MWS. Especially by hands of the 3D pattern, we can observe that the overall backside radiation is very low. A similar antenna element like in **Figure 21** was already built, but in the microstrip-to-SIW transition, the feeding via is connected with the bottom ground plane like in **Figure 9** leading therefore to a (desired) smaller bandwidth of about 2 GHz around the center frequency 35 GHz well suited for the project in [12] mentioned in context with the leaky wave antenna in **Figures 6** and **7**. The fabricated elements show a similar antenna pattern than in **Figure 23** and are already tested in a phased array arrangement.

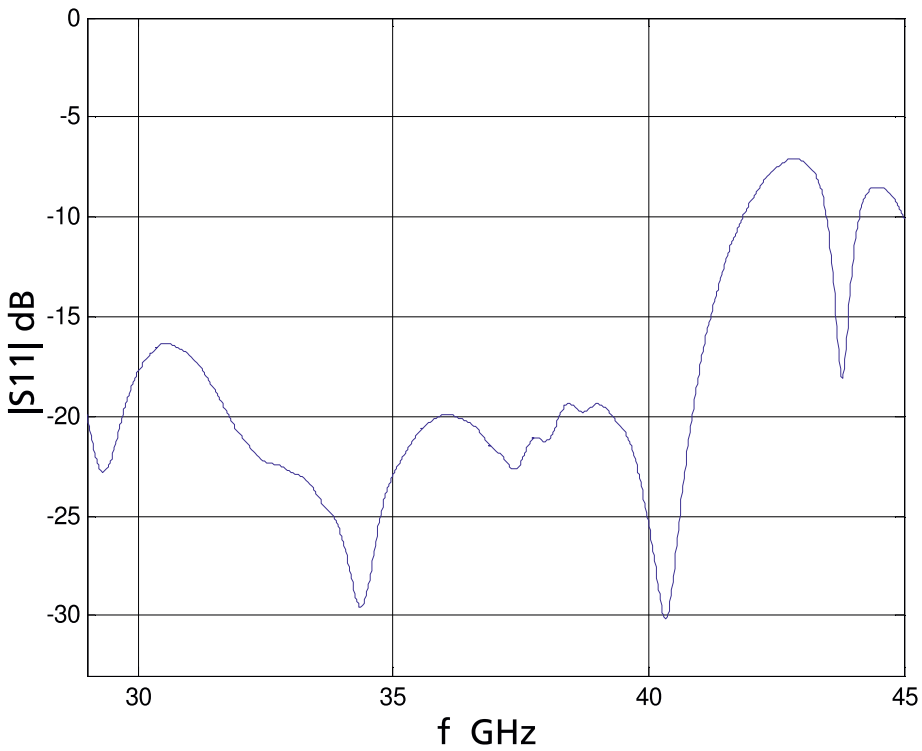


**Figure 22.** Left: Matching behavior of the complete antenna element in **Figure 21** (CST MWS). Right: Fabricated element (here for the project in [12]), top view with microstrip line and matching stubs and bottom view with 1 Euro coin.

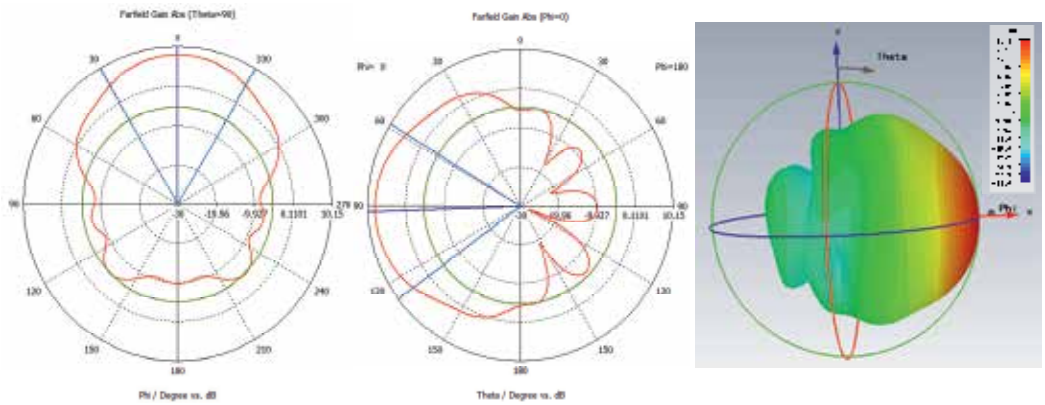

**Figure 23.** Azimuth, elevation, and 3D antenna pattern of the antenna element in **Figure 21** at 35 GHz.

## 5. Conclusions

This chapter comprises the application of an integral equation framework to the analysis and design of substrate integrated waveguide (SIW) components and antennas. For SIW circuits, microstrip to SIW transitions, and slot antennas, only the vias must be considered for the discretization of the SIWs in many cases, whereas radiating slots or antipads are modeled with magnetic surface currents. The computational performance and accuracy are significantly improved by a subdivision of the Cartesian wavenumber plane, integration path deformations, an asymptotic subtraction technique, as well as extended quadrature methods. The introduction of special SIW ports, field monitoring, and compact SIW absorbers allows an effective S-parameter extraction and power balance control also in combination with microstrip ports. For SIWs with larger thickness, broadband microstrip-to-SIW transitions have been designed based on a feed via with pad/antipad combination and a two-stage ridged-SIW structure. The latter was combined with an end-fire horn antenna based on a stepwise widening and was successfully built and measured. But the best radiation properties could be obtained with a combination of a SIW with a rectangular ringslot and a dielectric rod showing both broadband behavior and a small backward radiation. This structure is already tested within different array arrangements for a MIMO radar using a transition with feed via connected to the lower ground and smaller bandwidth, whereas a broadband version is used in near future for an airborne synthetic aperture radar.

## Author details

Thomas Vaupel

Address all correspondence to: thomas.vaupel@fhr.fraunhofer.de

Fraunhofer Institute for High Frequency Physics and Radar Techniques FHR, Wachtberg, Germany

## References

[1] Buchta M, Heinrich W. On the equivalence between cylindrical and rectangular via-holes in electromagnetic modeling. In: Proceedings of the 37th EuMC. Oct. 2007:142-145

[2] Caballero ED, Esteban H, Belenguer A, et al. Efficient analysis of substrate integrated waveguide devices using hybride mode-matching between cylindrical and guided modes. IEEE Transactions on Microwave Theory and Techniques. Feb. 2012;**60**(2):232-243

[3] Kumar H, Jadhav R, Ranade S. A review on substrate integrated waveguide and its microstrip interconnect. IOSR Journal of Electronics and Communication Engineering. Sep-Oct. 2012;**3**(5):36-40

[4] Ding Y, Wu K. Substrate integrated waveguide-to-microstrip transition in multilayer substrate. IEEE Transactions on Microwave Theory and Techniques. Dec. 2007;**55**(12):2839-2844

[5] Vaupel T. Design of end-fire substrate integrated waveguide antenna elements using in-house planar-3D integral equation frameworks and commercial full-3D methods. In: 8th European Conference on Antennas and Propagation. Netherlands: The Hague; 2014:2512-2515

[6] Yau CK, Huang TY, Shen TM, et al. Design and modelling of microstrip line to substrate integrated waveguide transitions. In: Zhurbenko V, editor. Passive Microwave Components and Antennas. InTechOpen. April 2010:225-246. Chapter 11. DOI: 10.5772/9418 ISBN: 978-953-307-083-4

[7] Vaupel T. A MFIE/Volume integral equation approach with minimum discretization effort for substrate integrated waveguide structures and leaky wave/slot antennas. IEEE APS Symposium. Fajardo, Puerto Rico; 2016:1327-1328

[8] Liu J, Jackson D, Long Y. Substrate integrated waveguide (SIW) leaky-wave antenna with transverse slots. IEEE Transaction on Antennas and Propagation. Jan 2012;**60**(1):20-29

[9] Esquis-Morote M, Fuchs B, Zürcher J-F, Mosig JR. A printed transition for matching improvement of SIW horn antennas. IEEE Transactions on Antennas and Propagation. April 2013;**61**(4):1923-1930

[10] Esquis-Morote M, Fuchs B, Zürcher J-F, Mosig JR. Novel thin and compact H-Plane SIW horn antenna. IEEE Transactions on Antennas and Propagation. June 2013;**61**(6):2911-2920

[11] Vaupel T, Eibert TF, Hansen V. Spectral domain analysis of large (M)MIC-structures using novel quadrature methods. International Journal of Numerical Modelling: Electronic Networks, Devices and Fields. Jan-Feb. 2005;**18**:23-38

[12] Panhuber R, Klenke R, Biallawons O, Klare J. System concept for the Imaging MIMO Radar of the radar warning and information System RAWIS. In: Proceedings of EUSAR 2016: 11th European Conference on Synthetic Aperture Radar. Hamburg, Germany. 2016:1-4

Chapter 3

# Time-Domain Analysis of Modified Vivaldi Antennas

Sultan Aldırmaz Çolak and Nurhan Türker Tokan

Additional information is available at the end of the chapter

http://dx.doi.org/10.5772/intechopen.74945

**Abstract**

In the ultra-wideband (UWB) application frequency domain parameters such as gain, group delay isn't sufficient to demonstrate the performance of the antenna. Besides frequency domain analysis, a time-domain analysis is required to characterize the transient behavior of UWB antennas for pulsed operations since pulse distortion of the UWB antenna reduces the system performance and decreases the signal to noise ratio (SNR) of the UWB communication system. Vivaldi antenna is a widely used UWB antenna, especially in microwave imaging applications. Performance of Vivaldi antennas is enhanced by adding corrugation on the edge of exponential flaring and/or grating elements on the slot area. From the measured scattering parameters of modified Vivaldi antennas, pulse preserving capabilities are observed. Pulse width extension and fidelity factor parameters are used to define the similarity between the transmitted and received pulse. The analysis is performed with angular dependence with respect to the signal transmitted at the main beam direction.

**Keywords:** UWB antenna, Vivaldi antenna, time domain, pulse distortion, fidelity analysis, corrugation

## 1. Introduction

Ultra-wideband (UWB) systems have been used in various applications that range from deep space investigation to commercial telecommunication links and radars with high spatial resolutions [1–3]. Due to its low complexity, small physical size, low manufacturing cost, low interference and high time-domain resolution, it is widely used in communication systems, microwave imaging, remote sensing and radar.

In 2012, federal communications commission (FCC) has allocated 7.5 GHz-wide frequency band that ranges from 3.1 to 10.6 GHz for UWB applications [4]. In UWB systems, antennas

IntechOpen

© 2018 The Author(s). Licensee IntechOpen. This chapter is distributed under the terms of the Creative Commons Attribution License (http://creativecommons.org/licenses/by/3.0), which permits unrestricted use, distribution, and reproduction in any medium, provided the original work is properly cited.

can be considered as the key component that affects the system performance. The performance and quality of UWB antennas are mostly analyzed in the frequency domain. For narrow-band systems, traditional frequency domain parameters (such as gain, group delay time, etc.) are enough to assess the performance of the antenna. However, in the ultra-wideband applications, these parameters are not sufficient to demonstrate the performance of the antenna. Besides frequency domain analysis, a time-domain analysis is required to characterize the transient behavior of UWB antennas for pulsed operations [5]. The antenna's transient response is the quantity for the characterization of the signal distortion and correlation of the radiated pulse in the time domain [6–7]. The time-dispersion characteristic of the antenna is one of the most important factors that should be considered in ultra-wideband applications since antennas with smaller time dispersion will have a better energy-focusing property and anti-interference performance. Antenna with larger dispersion leads to a less stable phase center and increases the interference in UWB communications based on pulse radio [8]. Consequently, this will result in time spreading of pulses and make signal transmission less predictable and less reliable in sensor system. Thus, it is necessary to investigate the antenna and radio propagation performance. This analysis should be performed not only in the main beam direction of the antenna but also in an arbitrary angular direction. By calculating the correlation between the transmitted signal and radiated signal in an arbitrary angular direction, the angular region where the pulse is preserved can be determined.

In order to radiate a short pulse with low distortion, the antenna needs to efficiently operate over a broad bandwidth and be non-dispersive, with a stable phase center at all frequencies. One of the most widely employed solutions for broadband planar, directive antenna is tapered slot antenna. With its relatively small physical size, low cost, easy integration with the circuit board and almost stable radiation properties within its band, exponentially tapered slot antenna, which is also known as Vivaldi antenna, became a good candidate for UWB communication, radar and microwave imaging applications [9–10]. Recent works have aimed to increase its radiation performance by physically modifying its structure. A parasitic elliptical patch is inserted in the slot aperture for radiation stability and directivity improvement at high frequencies [11]. In [12], to reduce side- and back-lobe levels, extend the bandwidth and increase the main lobe gain, an exponential slot edge is added to the structure. In [13], a double slot structure is proposed in the Vivaldi antenna, to enhance the directivity and radiation performance, whereas double antipodal structure having corrugated edges and the semicircle director is presented in [14] for the same purpose. Vivaldi antenna is modified by incorporating corrugations on the edges of the exponential tapered slots and periodic grating elements consisting of metallic strips on the slot area in [15] to increase gain, especially at the lower end of the frequency band.

Time-domain characteristics of standard Vivaldi antennas are investigated and proved to be weakly dispersive in [16]. In [17], the time-domain radiation properties of the Vivaldi antenna are analyzed with angular dependence with respect to the signal transmitted at the main beam direction. In literature, time-domain characteristics of the modified Vivaldi antennas are not considered so far. With this work, effects of the physical modification on the Vivaldi structure will be observed in the time domain. If the modifications made to improve frequency-domain parameters would benefit time-domain parameters, they will be investigated, and potentials of these antennas to be used as basic element for non-distorted radiated link are discussed.

http://dx.doi.org/10.5772/intechopen.74945

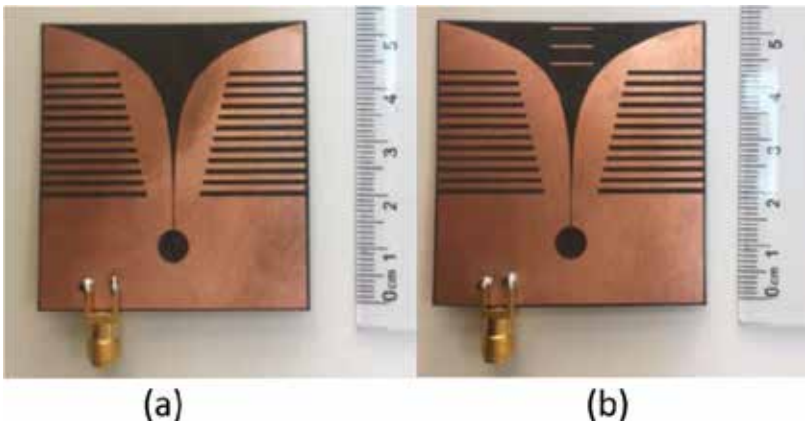


**Figure 1.** Modified Vivaldi antennas with (a) corrugation and (b) corrugation and strip.

Pulse-preserving capabilities of modified Vivaldi antennas given in **Figure 1** are measured in terms of two parameters: the pulse width extension and the fidelity factor. In addition, the results are compared with that of the standard Vivaldi antennas. Their time-domain performance is quantified by their respective standard deviations from the width of the ideal signal that has constant value. Standard Fourier transform relationship is used to recover time-domain waveforms. Although this chapter concentrates on Vivaldi structures operating in 3.1–10.6 GHz, the analysis is also applicable to any UWB antenna.

This chapter is organized as follows: In the next Section, time-domain analysis and the procedure for the analysis of the angular distortion of radiated pulses are presented. In Section 3, the modified Vivaldi antennas are introduced and their frequency-domain performance is demonstrated. Measurement setup and time-domain analysis results of the antennas are given in Section 4. Section 5 concludes the whole chapter.

## 2. Time-domain analysis

Despite the wide frequency of the radiation, the transmitted UWB waveform is dispersive. This is one major difference from narrow-band circumstances. When the signal is transmitted through a UWB antenna, the antenna output signal contains the input signal and its derivatives with varying delays, caused mainly by the resonances in the radiator structure. Frequency-dependent variations of antenna characteristics and reflection coefficients, and RF circuitry, are considered as the sources of waveform dispersion [18]. When $S_{21}$ parameter of the link in the frequency domain presents linear phase variation which results as non-dispersive radiation and constant amplitude which results as no amplitude distortion, the time-domain pulse is not distorted.

Impulse response of a link, $S_{21}(t, \theta, \varphi)$, can be derived by taking the inverse Fourier transform of $S_{21}(\omega, \theta, \varphi)$:

$$S_{21}(t, \theta, \varphi) = IFT\left\{S_{21}(\omega, \theta, \varphi)\right\} \tag{1}$$

where the angle $\theta$ starts from the positive $z$-axis and the angle $\phi$ starts from the positive $x$-axis. $\omega$ refers to angular frequency, whereas $t$ denotes time. Pulse distortion in the time domain can be observed from the difference between the received and transmitted UWB pulse in shape.

### 2.1. Time-domain parameters

The main parameters for the evaluation of the pulse characteristics in the time domain are obtained from the transient response of the antenna [5]. The peak value of the antenna impulse response, $P(\theta, \varphi)$, is expressed in Eq. (2):

$$P(\theta, \varphi) = max\left|S_{21}(t, \theta, \varphi)\right| \tag{2}$$

The angular dependency of $P$ is the result of angular-dependent impulse response. Most energy is contained around the peak of the impulse response. The higher values of $P(\theta, \phi)$ demonstrates lower loss of the link. The pulse width is the width of the time window that contains a certain percentage of the total energy. Half-power width, $\tau$, is a parameter used to define the broadening of the signal:

$$\tau = t_2\big|_{|S_{21}(t,\theta,\varphi)|=0.7\,P_{nor,max}(\theta,\varphi)} - t_1\big|_{t_1<t_2,\,|S_{21}(t,\theta,\varphi)|=0.7\,P_{nor,max}(\theta,\varphi)} \tag{3}$$

where $P_{nor,max}$ is the maximum value of the normalized version of the antenna impulse response. $t_2$ and $t_1$ are the instants when half power width occurs, after and before the maximum, respectively. Time difference between the half power width of the received signal and the reference signal describes the broadening of the transmitted pulse. Thus, when there is no distortion, $\tau$ of the received pulse is equal to the $\tau$ of the transmitted pulse. This is the ideal case. However, mostly the link is distorted and the widening affects the communication quality. Ringing duration parameter, $\tau_r$, given in Eq. (4), defines the oscillations in the antenna impulse response:

$$\tau_r = t_r\big|_{|S_{21}(t,\theta,\phi)|=RP(\theta,\varphi)} - t_P\big|_{t_P<t_r,\ |S_{21}(t,\theta,\varphi)|=P(\theta,\varphi)} \tag{4}$$

$R$ is a coefficient that is used to define the instant of the ringing. $t_p$ and $t_r$ are the instants when the pulse has its maximum and first ringing, respectively. Although these parameters are widely used to quantify the time-domain signal, correlation between the transmitted and received pulse should be observed as well. Besides, due to the angular variation of the transmitted signal, cross-correlation between the transmitted and received signals should be investigated and quantified not only at the main beam direction but also with angular dependence as given in [19].

### 2.2. Fidelity analysis

The correlation coefficient between the received pulse and transmitted pulse demonstrates the amount of pulse distortion which the antenna induced. The fidelity factor, *FF*, is a parameter used to quantify the similarity between transmitted and received signal [16]:

$$FF = max_{\tau} \frac{\int_{-\infty}^{+\infty} S_{ref}(t)\, S_{21}(t-\tau)\, dt}{\sqrt{\int_{-\infty}^{+\infty} |S_{ref}(t)|^2 dt} \sqrt{\int_{-\infty}^{+\infty} |S_{21}(t)|^2 dt}} \quad (5)$$

where $S_{ref}(t)$ and $S_{21}(t)$ are the transmitted and received signals, respectively. If the transmitted and received signals are exactly same, *FF* coefficient has its maximum of 1. When *FF* coefficient is 1, input signal isn't distorted by the antenna. Fidelity depends on the spatial radiation characteristics of the antenna. Thus, angular variation of the *FF* coefficient should also be observed. Because of the normalization procedure, fidelity factor cannot provide information about the amplitudes of signals.

## 3. Modified Vivaldi antennas

### 3.1. Antenna design

The Vivaldi antenna is one of the classical ultra-wideband antennas with many applications [8]. It is a traveling-wave, end-fire antenna and due to its completely planar structure, it can be easily integrated in UWB sensor circuit. It has almost symmetric radiation patterns in the E and H planes. Theoretically, with its exponentially tapered slot, the Vivaldi antenna has an unlimited range of operating frequencies. However, in practice, it is constrained by the physical dimensions such as taper dimensions, the slot line width and transition from the feed line.

The structure of the standard Vivaldi antenna together with its dimensions is shown in **Figure 2a**. The proposed Vivaldi antenna consists of a microstrip feed line, microstrip line to slot line transition and the radiating structure. It is designed to operate efficiently as the transmitter and receiver in the unlicensed band of 3.1–10.6 GHz (7.5 GHz bandwidth). The slot curve of the Vivaldi antenna is the exponential function, which is expressed as $S(z) = (W_{slot}/2)\, e^{az}$ where $a = 0.165$ and $W_{slot} = 0.25$ mm. A quarter wavelength open circuit stub is used for wideband matching. The aperture coupling is optimized for the frequency range from 3.1 to 10.6 GHz. The size of the Vivaldi antenna is 50 × 50 mm. Its dimensions are given in **Figure 2a**. Rogers RT/Duroid 5870 with 0.51-mm dielectric thickness and 17.5-um copper is chosen for the design. The dielectric constant of the dielectric material is $\varepsilon_r = 2.33$.

One of the bottlenecks of the conventional Vivaldi antenna is its relatively low directivity, especially at lower frequencies of the band. The lower frequency response of Vivaldi antennas with satisfactory impedance match and effective radiation is usually improved by increasing the aperture size. Another solution is introducing variable length slots to effectively increase the aperture of the antenna [15, 20]. It is shown that by incorporating a corrugated profile on the sides of exponential flaring, more suitable characteristics, especially for microwave imaging applications (i.e., higher gain, broader bandwidth), can be obtained compared to standard Vivaldi designs [21].

Performance of these antennas is widely discussed in the frequency domain. Time-domain analysis of these antennas is also needed since these antennas are considered as a good choice for microwave imaging applications [21]. With this aim, Vivaldi antenna with corrugations is designed to operate at UWB frequencies. It has the same size and uses the same material as

the standard Vivaldi. The dimensions of the Vivaldi with corrugations are given in **Figure 2b**. The edge of Vivaldi is symmetrically corrugated by slots along the y-axis. The corrugations are rectangular slots with varying lengths. Design parameters of the corrugations are the distance between slots, the width of slots and the length of slots. The width of slots and distance between the rectangular slots of corrugation remain same. The length of the slots decreases gradually toward the flaring. Simulations proved that increasing the number of slots improves the radiation characteristics of the designed antenna by triggering extra resonances and modifying the direction of the current on the edges. The corrugations on the edges of the flaring act like a resistive loading. These corrugations are useful to concentrate the wave toward the slot area and contribute to the end-fire radiation patterns. The design parameters of the corrugation are optimized as 1 mm, 1 and 20–14.5 mm, respectively.

Besides adding corrugations on the edges of the flaring, adding grating elements on the slot area in the direction of the antenna axis is another technique to enhance the gain of the antenna. These elements work as directive elements and contribute to the radiation in the end-fire direction. With the combination of both the corrugations and grating elements, the gain of the antenna increases significantly in the end-fire direction [15].

The third design for the Vivaldi antennae is achieved by adding three metallic strips on the slot area as demonstrated in **Figure 2c**. Design parameters of the grating elements that are

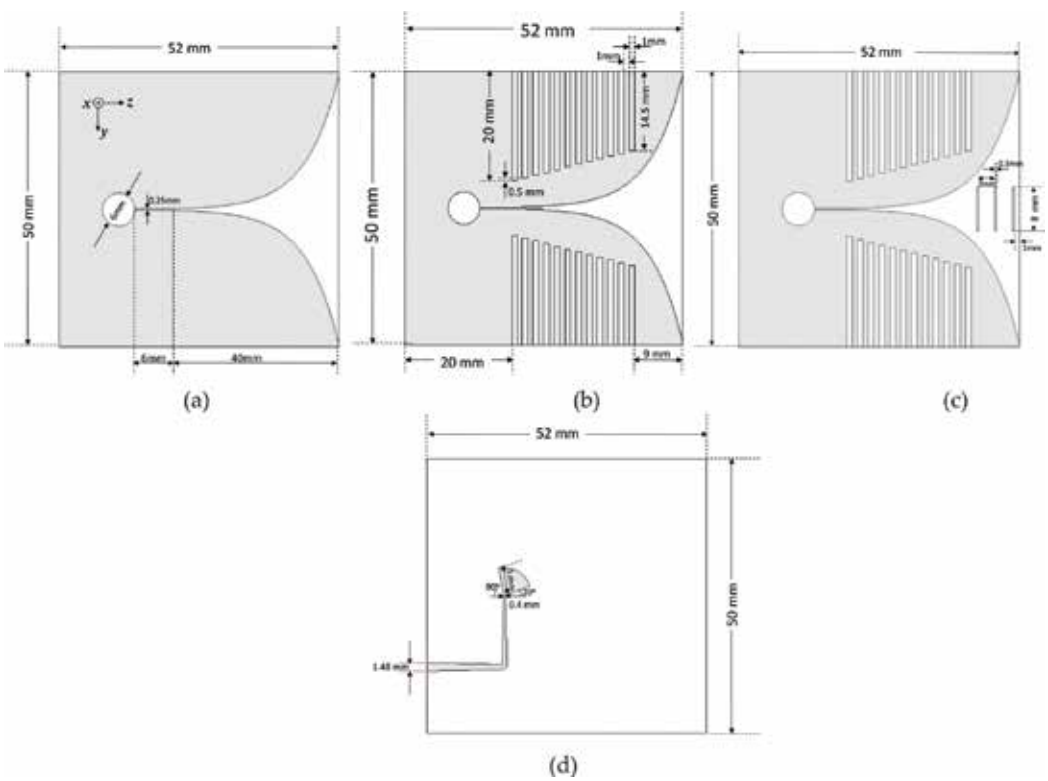


**Figure 2.** UWB Vivaldi antennas with its dimensions: (a) top view of Vivaldi; (b) top view of Vivaldi with corrugation; (c) top view of Vivaldi with corrugation and strip; (d) bottom view.

located to the flaring are the distance between strips, the width of strips and the length of strips. They are optimized as 3, 0.3 and 8 mm, respectively. All of the three Vivaldi designs use the same exponential tapering and balun. To match the antenna over a wide frequency band, a microstrip line to slot line transition and feed balun is designed as shown in **Figure 2d**. The selected reference axis system is also presented. The overall size of the antenna is not affected by the techniques used to increase the gain and improve the radiation patterns of the antenna in bore sight direction; therefore, the overall size of the antenna remains compact.

### 3.2. Antenna performance

To demonstrate the pulse distortion properties of the modified Vivaldi antennas, the prototypes have been manufactured with printed circuit board technology. The prototypes are shown in **Figures 1** and **3** (Vivaldi with corrugation and Vivaldi with corrugation and strip in **Figure 1**, standard Vivaldi in **Figure 3**). The scattering parameters of the antenna are measured using an Agilent vector network analyzer. The reflection behavior of each antenna has been investigated in terms of $S_{11}$. The measured return loss variation of the antennas is given in **Figure 4**. Simulations performed with a commercial finite integration technique-based software package computer simulation technology (CST) microwave studio, not reported for brevity, are in excellent agreement with the measurement results.

Simulated gain variations of the antennas are given in **Figure 5**. The realized gain of the modified antennas improves significantly throughout the frequency band compared to standard Vivaldi. Existence of the corrugations and grating elements maximizes the radiation in the bore sight direction. With the corrugations added, at the lower frequencies of the band, both of the modified Vivaldi antennas have higher gain compared to standard Vivaldi antenna. Moreover, Vivaldi with corrugation and strip has a 0.2 dB more gain than Vivaldi with corrugation at the whole frequency band. With these results, the positive effect of the existence of corrugation and metallic strips is observed in the frequency domain. However, since the antennas are aimed to be used for UWB applications, their time-domain performance should also be investigated.

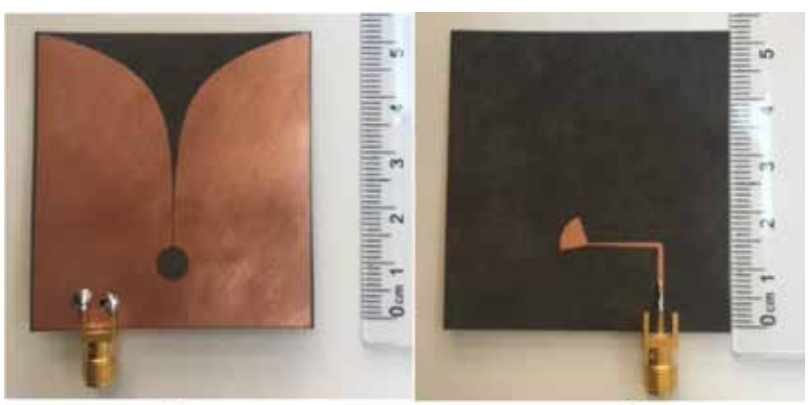


**Figure 3.** Fabricated Vivaldi antenna (a) top view; (b) back view.

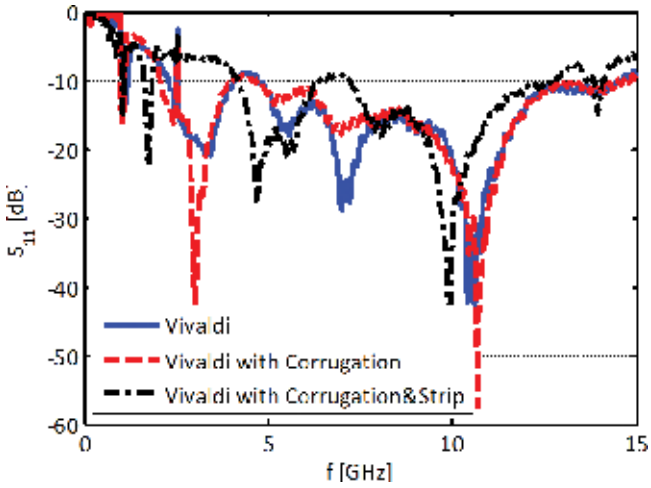


**Figure 4.** Measured return loss of Vivaldi antennas.

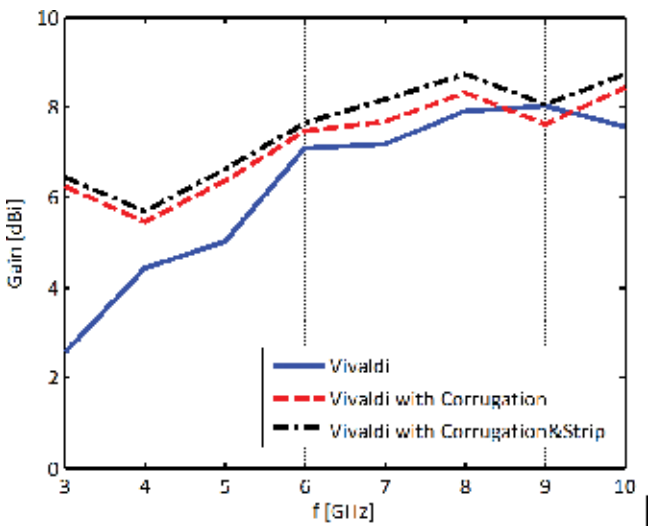


**Figure 5.** Simulated gain variations of Vivaldi antennas.

## 4. Time-domain analysis of modified Vivaldi antennas

### 4.1. Measurement setup

Time-domain analysis of modified Vivaldi antennas is performed and compared with that of standard Vivaldi antenna. A link composed of two identical Vivaldi antennas has been experimentally characterized. The measurements were performed with the same setup. The transmit-receive antenna link measurement setup demonstration for E-plane is shown in **Figure 6**.

The antennas were placed at about 20 cm of distance. In **Figure 7**, measurement setup is shown for E and H planes. In **Figure 8**, the amplitudes of $S_{21}$ parameters at $\theta = 0^{\circ}$ are plotted as the function of the frequency in the range 0–12 GHz.

The procedure for the measurement of $S_{21}(\omega, \theta, \varphi)$ with angular variation can be summarized as follows: The measurements are performed by shifting one of the antennas in the range of $-90^{\circ} \leq \theta \leq 90^{\circ}$ with $5^{\circ}$ steps in E- ($\varphi = 90^{\circ}$) and H-planes ($\varphi = 0^{\circ}$) and measuring $S_{21}(\omega, \theta, \varphi)$. Afterward, the impulse response of the link with angular variation is derived by means of inverse Fourier transform of the measured $S_{21}$ as shown in the next section.

### 4.2. Time-domain analysis

#### *4.2.1. Pulse comparison*

The link between the transmitting and receiving antennas can be characterized in terms of its complex transfer function:

$$H(\omega) = U_{RX}(\omega)/U_{TX}(\omega) \tag{6}$$

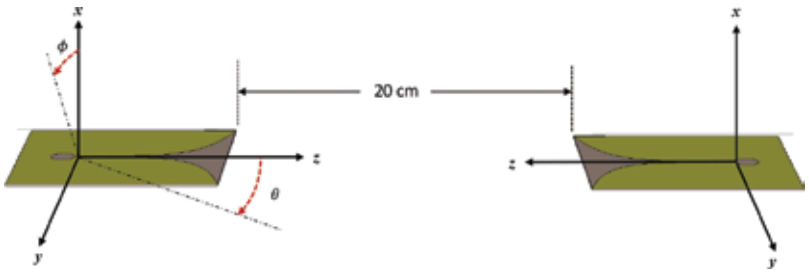


**Figure 6.** Demonstration of the measurement setup.

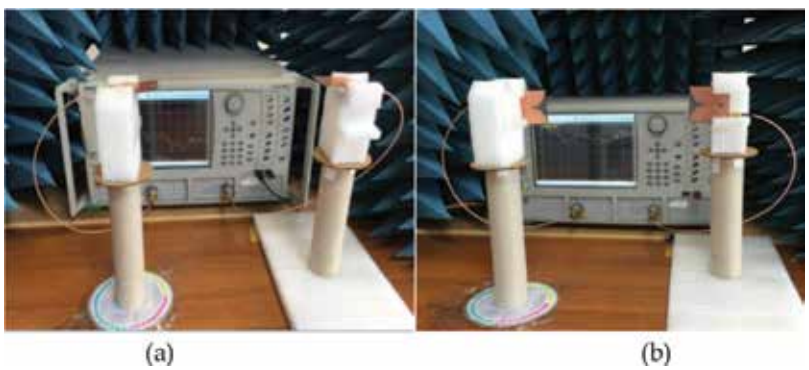


**Figure 7.** Measurement setup for the characterization of the antenna link (a) E-plane; (b) H-plane.

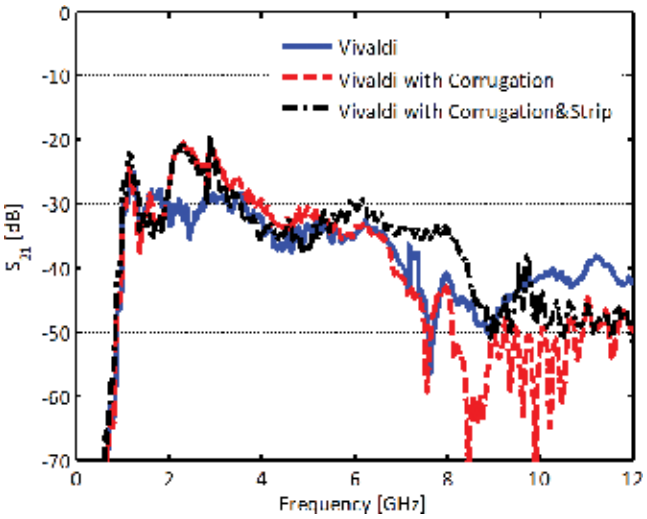


**Figure 8.** Measured insertion loss of the antennas.

where $U_{RX}(\omega)$ and $U_{TX}(\omega)$ are the spectra of the received and transmitted voltages, respectively. The coupling parameter between the antennas is related with the complex transfer function of the antennas as [22]:

$$S_{21}(\omega) = H_{TX}(\omega)\, H_{RX}(\omega)\, \frac{j\omega}{2\pi r c}\, e^{-j\omega r/c} \tag{7}$$

where $H_{TX}(\omega)$ and $H_{RX}(\omega)$ are the transfer functions of transmit and receive antenna. $r$ is the distance between the antennas. The impulse response of the links is derived over 7.5 GHz bandwidth, from 3.1 to 10.6 GHz, by means of the inverse fourier transform (IFT) of the measured $S_{21}(\omega)$. In the application of time-domain analysis, the reference signal $S_{ref}(t)$ will be a sinc pulse associated with the mentioned 7.5 GHz band, which can be expressed as:

$$S_{ref}(t) = IFT\left\{S_{ref}(\omega)\right\} = \frac{1}{2\pi}\int_{\omega_1}^{\omega_2} e^{-j\omega t}\, d\omega \tag{8}$$

where $\omega_1 = 2\pi f_1$ and $\omega_2 = 2\pi f_2$ . In **Figure 9a–d**, a comparison between the response of the antenna link in time domain and the reference signal delayed to the present maximum in correspondence of the main peak of the link's impulse response is shown for $\theta = 0, 10, 30, 45^{\circ}$ in the E-plane ($\varphi = 90^{\circ}$). The green dash-dot line is the ideal delayed pulse obtained by Eq. (8). Blue solid, red-dashed and black dash-dot lines belong to impulse response of the Vivaldi, Vivaldi with corrugation and Vivaldi with corrugation and strip, respectively. For a rigorous comparison, path loss effect is removed by scaling the received pulse amplitude to the transmitted amplitude. Thus, in the time-domain representations, the amplitude of the $S_{21}$ parameter measured with the setup in **Figure 7** is normalized to its maximum. The length of the coaxial cables used between the connector of the antenna and network analyzer

port is 50 cm. The Teflon coaxial cables for the transmitter/receiver antennas correspond to 4.83 ns of propagation time. The signal path in the microstrip antenna is 65.2 mm. With an effective dielectric constant of 1.97 at 5 GHz, the propagation time inside transmitter/receiver antennas are calculated approximately as 0.61 ns. A total of 20 cm free space propagation corresponds to 0.666 ns of propagation time. When the 2 cm adapters used at the network analyzer ports are added, total propagation time of the signal can be calculated as approximately 6.3 ns. This is observed from the time-domain representations obtained from the measurement results as well. The main peak of the signal arrives to the receiver after approximately 6.3 ns.

The half power width of the reference signal is 0.119 ns. When the antenna is at bore sight, half power width of the pulse for standard Vivaldi is measured as 0.011 ns wider than that of the reference signal. Similarly, the pulse is 0.076 and 0.03 ns wider for Vivaldi with

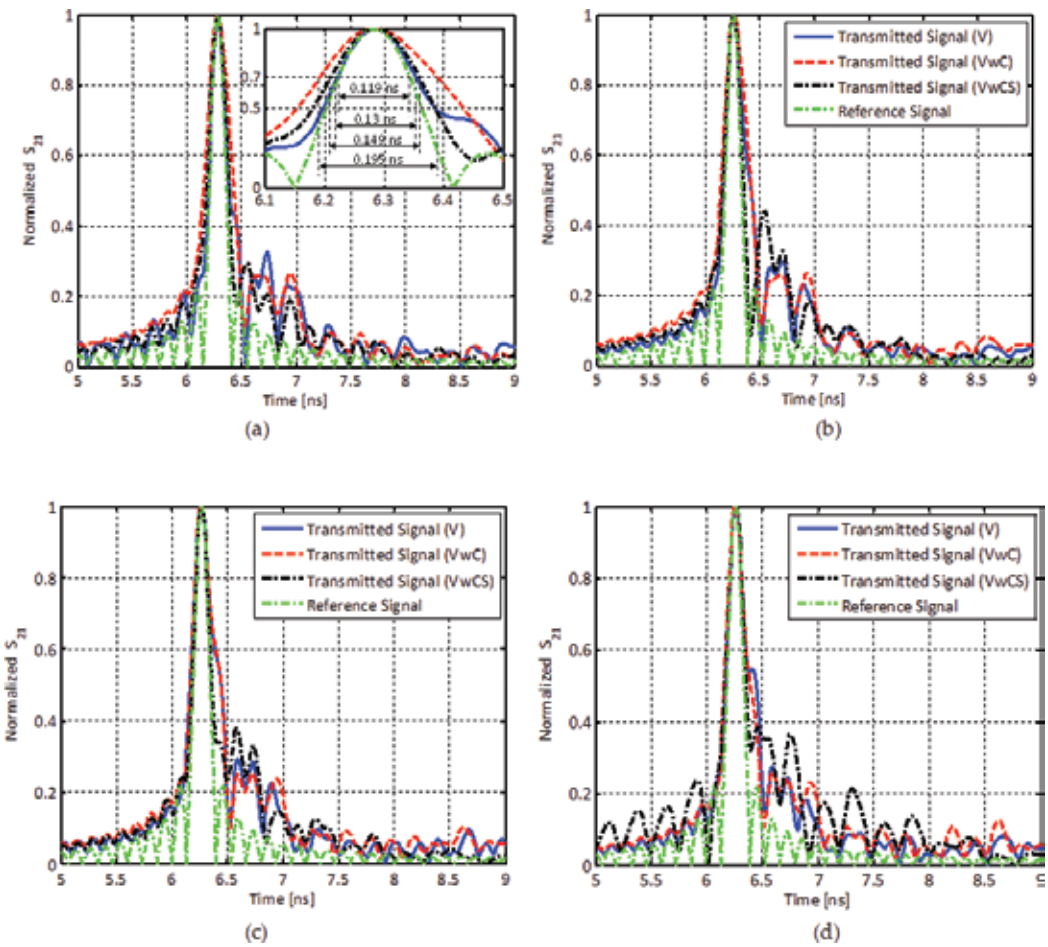


**Figure 9.** Comparison between the impulse response and an ideal delayed pulse in E-plane (a) $\theta = 0°$; (b) $\theta = 10°$; (c) $\theta = 30°$; (d) $\theta = 45°$.

corrugation and Vivaldi with corrugation and strip, respectively. The pulse is visible in the inset (**Figure 9a**). The pulses widen for larger values of $\theta$. This is observed in **Figure 9b–d**. When $\theta = 0^\circ$ in E-field, the shape of the transmitted pulse is close to that of standard Vivaldi and Vivaldi with corrugation and strip. As theta gets larger, the pulses widen. This is observed at $\theta = 10^\circ$ given in **Figure 9b**. At $10^\circ$ the main beam of Vivaldi with corrugation and strip pulse is similar to the main beam of reference pulse but secondary pulses are generated. A very similar case occurs at $\theta = 30^\circ$. At $\theta = 45^\circ$, secondary pulse of the standard Vivaldi is also generated.

Similarly, a comparison in H-plane ($\varphi = 0^\circ$) between the time-domain response of the antenna link that consists of standard Vivaldi and modified Vivaldi antennas and the reference signal, delayed by 6.3 ns to present the maximum in correspondence of the main peak of the link impulse response, is shown in **Figure 10**. In H-plane, pulse characteristics are different than the E-plane. Clearly, the pulse-preserving capability of Vivaldi with corrugation and strip is

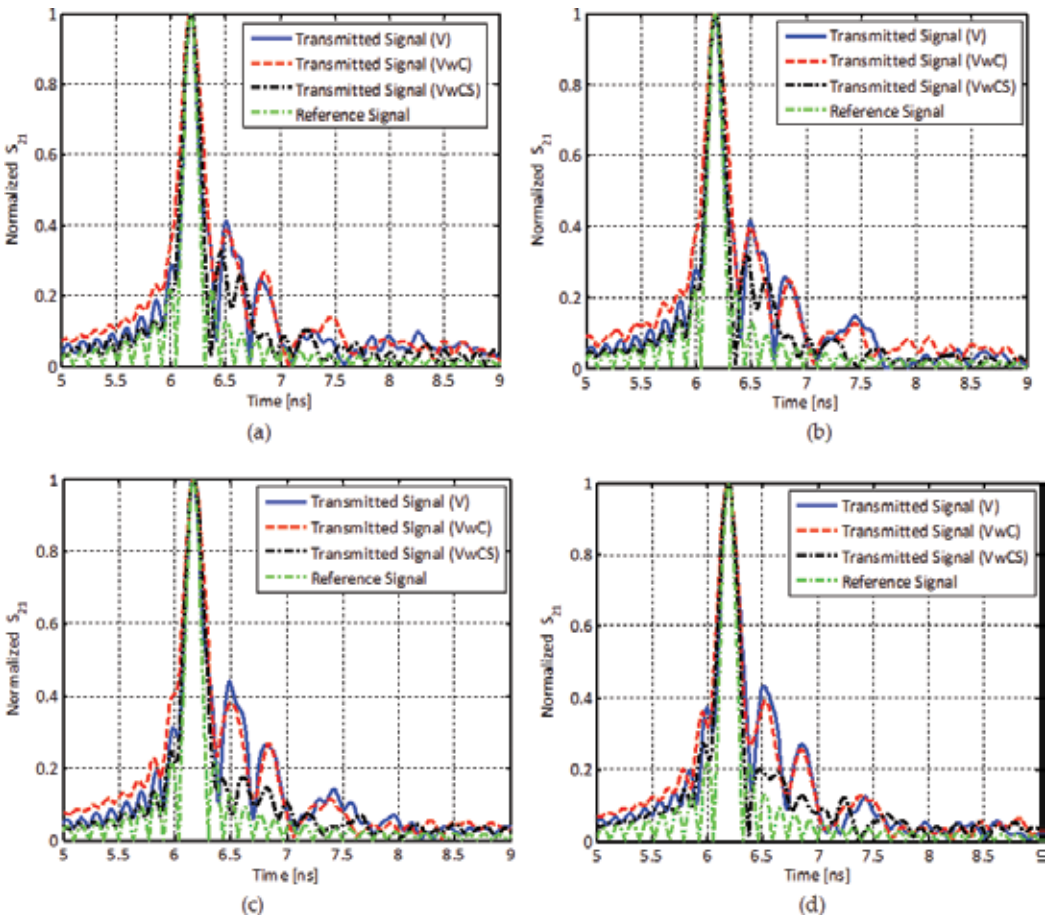


**Figure 10.** Comparison between the impulse response and an ideal delayed pulse in H-plane (a) $\theta = 0^\circ$; (b) $\theta = 10^\circ$; (c) $\theta = 30^\circ$; (d) $\theta = 45^\circ$.

better than the other Vivaldi antennas. Although only the measurement results are shared in this communication, simulations performed with CST, not reported for brevity, are in very good agreement with the measured results.

*4.2.2. Pulse analysis*

Based on the comparison between the impulse response of link and ideal delayed signal, one can clearly establish the presence of pulse widening. To quantify the amount of widening, pulse analysis with respect to $\theta$ in E- and H-planes are performed using the definition given in Eq. (3). In **Figure 11(a)** and **(b)**, half power width of the impulse response, $\tau$ is demonstrated in E- and H-planes, respectively. The green dotted line shows the width of the reference pulse which is equal to 0.119 ns.

Secondary pulse signal that has its maximum reach to half power of the main beam is generated by the link after $65^\circ$ in E-plane and $70^\circ$ in H-plane. As a result, pulse width is observed between $-65^\circ \leq \theta \leq 65^\circ$ for E-plane and $-70^\circ \leq \theta \leq 70^\circ$ in H-plane. Based on the pulse width results, it can be concluded that the width of the pulse that belongs to Vivaldi with corrugation widens more than the standard and corrugation and strip Vivaldi. This is valid both in E- and in H-planes. This result is even more obvious when the pulse width is compared to that of the reference signal. In **Figure 12**, pulse extension ratio of the measured pulse is given. It is calculated by the following expression:

$$Pulse\ Extension\ Ratio\ = \frac{\tau_{pulse} - \tau_{reference\ pulse}}{\tau_{reference\ pulse}} \tag{9}$$

The pulse extension ratio of Vivaldi with corrugation is below 65% in $-60^\circ \leq \theta \leq 60^\circ$. It goes above 100% afterward. Pulse width ratio of Vivaldi and Vivaldi with corrugation and strip is more stable than Vivaldi with corrugation. Based on pulse analysis results, one can accept the standard Vivaldi to have the best pulse distortion performance in the time

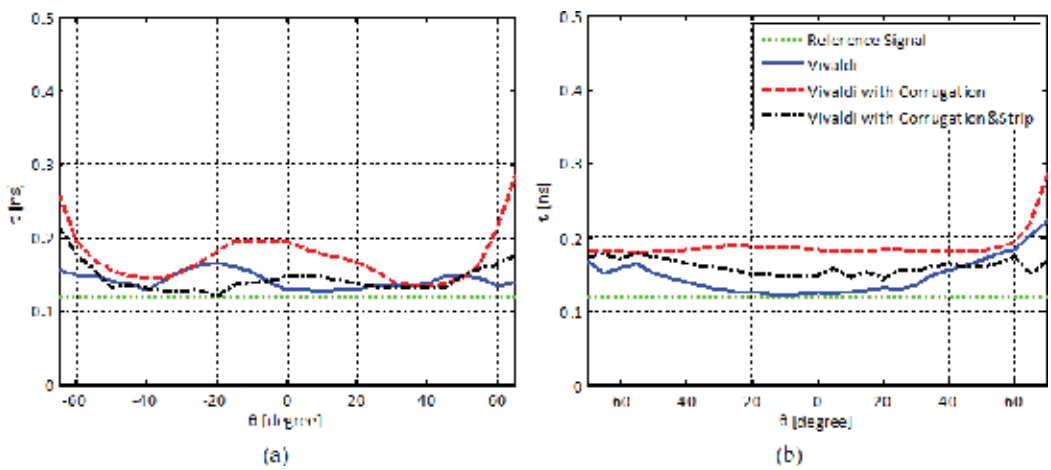


**Figure 11.** Half power width of the measured pulse (a) E-plane; (b) H-plane.

domain. Although, these results give an idea about the pulse distortion introduced by the Vivaldi antennas, to more rigorously quantify the pulse, distortion fidelity analysis should be performed.

*4.2.3. Fidelity analysis*

Most of the energy carried by the pulse is stored around the peak of the impulse. The correlation coefficient between the received pulse and transmitted pulse quantifies the similarity between transmitted and received signal. For the 3.1–10.6 GHz band, the fidelity factor of the link between two identical antennas is shown in **Figure 13** for E- and H-planes. The fidelity variation obtained from the measured $S_{21}$ has unexpected pits at some angles. This may be due to the structure of the antenna profile. The fidelity values in E-plane are mostly close to 0.9 in

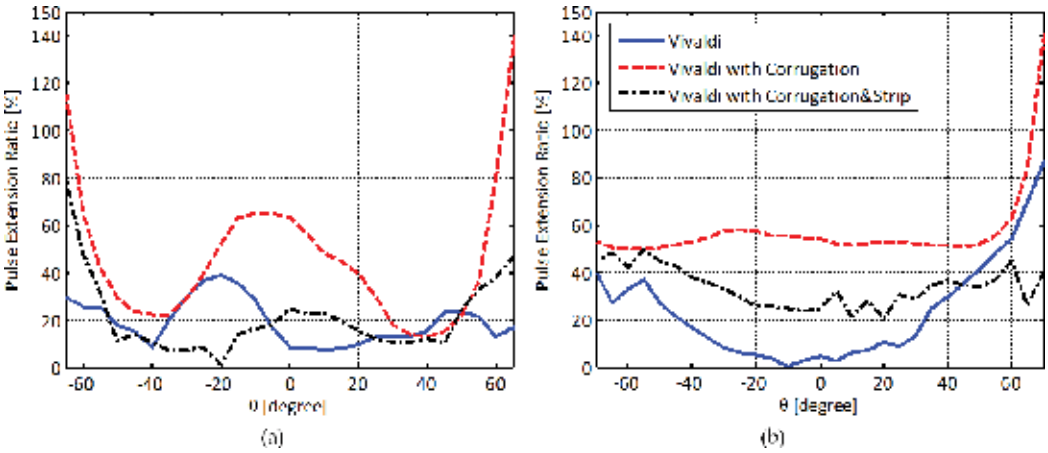


**Figure 12.** Pulse extension ratio of the measured pulse in (a) E-plane; (b) H-plane.

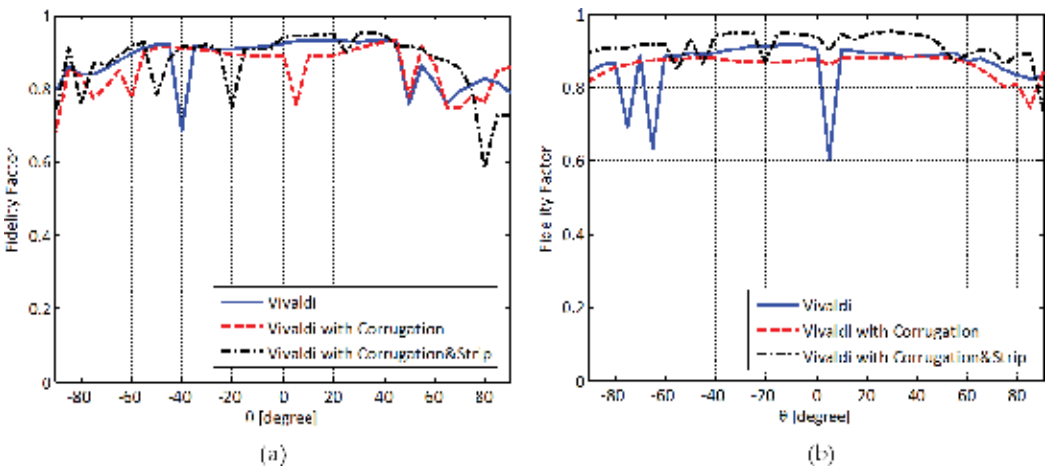


**Figure 13.** Fidelity factor variations of the pulses (a) E-plane; (b) H-plane.

for $-45^{\circ} \leq \theta \leq 45^{\circ}$. It has a lower value for the angles greater than $45^{\circ}$. In H-plane, Vivaldi with corrugation and strip has clearly a higher fidelity value than the others. Although standard Vivaldi was considered to have better impulse response in terms of pulse widening, fidelity analysis results represent Vivaldi with corrugation and strip to have the highest similarity between the transmitted and received signal. A good antenna performance requires simultaneously both a high fidelity and small pulse extension ratio of the impulse response. Thus, the modified version of Vivaldi antenna having corrugation and strip is a good candidate for UWB applications with its higher gain and wider bandwidth in the frequency domain and better pulse-preserving properties in the time domain.

## 5. Conclusion

In this chapter, the analysis procedure for the pulse-preserving properties of impulse-radiating antennas is defined. The analysis procedure is applied to a widely used UWB antenna, namely Vivaldi antenna. Vivaldi antennas are popular in UWB applications due to its complete planar structure which enables it to be easily integrated to UWB sensor circuit. However, Vivaldi antenna has relatively low directivity, especially at lower frequencies of the band. The lower frequency response of Vivaldi antennas may be improved by increasing the aperture size of the antenna. In the cases where physical size matters slots are added on the edges of exponential flaring to effectively increase the aperture of the antenna. The corrugated profile results in more suitable characteristics (i.e., higher gain, higher directivity, broader bandwidth). Besides adding slots on the edges of the flaring, adding grating elements on the slot area in the direction of the antenna axis is another technique to enhance the gain of the antenna. With the combination of both the corrugations and grating elements, the gain of the antenna increases significantly in the end-fire direction. Although these modified Vivaldi antennas are used in many UWB applications, their time-domain performance is not observed. With this contribution, pulse-preserving capabilities of modified Vivaldi antennas based on measurements are observed. Two parameters are used to quantify the capability of the antenna. First one is the pulse width extension that defines the broadening of the signal at its half power. Since most of the energy is stored around the peak of the pulse, this parameter is useful to demonstrate the pulse-preserving capability of the antenna but not sufficient. The second parameter is the fidelity factor that measures the correlation between the transmitted and received pulse. The performance of the modified Vivaldi antennas is also analyzed in different angular directions with respect to the main beam. Among the Vivaldi structures observed, Vivaldi antenna with corrugation and strip is proved to be potentially suited for both pulsed and harmonic broadband instruments.

## Acknowledgements

This work was supported by Research Fund of the Yıldız Technical University (Project Number: FBA-2017-3071).

## Author details

Sultan Aldırmaz Çolak[1] and Nurhan Türker Tokan[2]*

*Address all correspondence to: nurhanturker@gmail.com

1 Department of Electronics and Communications Engineering, Kocaeli University, Kocaeli, Turkey

2 Department of Electronics and Communications Engineering, Yildiz Technical University, Istanbul, Turkey

## References

[1] Schwarz U, Thiel F, Seifert F, Stephan R, Hein MA. Ultrawideband antennas for magnetic resonance imaging navigator techniques. IEEE Transactions on Antennas and Propagation. 2010;**58**:2107-2112. DOI: 10.1109/TAP.2010.2046848

[2] Chahat N, Zhadobov M, Sauleau R, Ito KA. Compact UWB antenna for on-body applications. IEEE Transactions on Antennas and Propagation. 2011;**59**:1123-1131. DOI: 10.1109/TAP.2011.2109361

[3] Ardenne A, Smolders B, Hampson G. Active adaptive antennas for radio astronomy; results of the initial R&D program toward the square kilometer array. In: Proceedings of the SPIE Conference 4015 Radio Telescope, Munich; March 27-30 2000

[4] "First report and order," Revision of Part 15 of the Commission's Rules Regarding Ultra-Wideband Transmission Systems Federal Communications Commission; 2002

[5] Pancera E, Zwick T, Wiesbeck W. Spherical fidelity patterns of UWB antennas. IEEE Transactions on Antennas and Propagation. 2011;**59**:2111-2119. DOI: 10.1109/TAP.2011.2143666

[6] Shlivinsky A, Heyman E, Kastner R. Antenna characterization in the time domain. IEEE Transactions on Antennas and Propagation. 1997;**45**:1140-1149. DOI: 10.1109/8.596907

[7] Wiesbeck W, Adamiuk G, Sturm C. Basic properties and design principles of UWB antennas. Proceedings of the IEEE. 2009;**97**:372-385

[8] Yang Y, Wang BZ, Ding S. Performance comparison with different antenna properties in time reversal ultra-wideband communications for sensor system applications. Sensors, Sensors. 2018;**18**:88. DOI: 10.3390/s18010088

[9] Gibson PJ. The Vivaldi aerial. In: Proceedings of 9th European Microwave Conference, Brighton; September 17-20, 1979. pp 101-105

[10] Tokan NT. Performance of Vivaldi antennas in reflector feed applications. Applied Computational Electromagnetics Society Journal. 2013;**8**:802-808

[11] Nassar IT, Weller TM. A novel method for improving antipodal Vivaldi antenna performance. IEEE Transactions on Antennas and Propagation. 2015;**63**:3321-3324

[12] Oliveira AMD, Perotoni MB, Kofuji ST, Justo JF. A palm tree antipodal Vivaldi antenna with exponential slot edge for improved radiation pattern. IEEE Antennas and Wireless Propagation Letters. 2015;**14**:1334-1337. DOI: 10.1109/LAWP.2015.2404875

[13] Wang YW, Wang GM, Zong BF. Directivity improvement of Vivaldi antenna using double-slot structure. IEEE Antennas and Wireless Propagation Letters. 2013;**12**:1380-1383. DOI: 10.1109/LAWP.2013.2285182

[14] Zhang Y, ChaoWang EL, Guo G. Radiation enhanced Vivaldi antenna with double-antipodal structure. IEEE Antennas and Wireless Propagation Letters. 2017;**16**:561-564. DOI: 10.1109/LAWP.2016.2588882

[15] Pandey GK, Singh HS, Bharti PK, Pandey A, Meshram MK. High gain Vivaldi antenna for radar and microwave imaging applications. International Journal of Signal Processing Systems. 2015;**3**:35-39. DOI: 10.12720/ijsps.3.1.35-39

[16] Mehdipour A, Mohammadpour-Aghdam K, Faraji-Dana R. Complete dispersion analysis of Vivaldi antenna for ultra wide band applications. Progress in Electromagnetics Research. 2007;**77**:85-96. DOI: 10.2528/PIER07072904

[17] Pancera E. Strategies for time domain characterization of UWB components and systems [Thesis] Universität Karlsruhe (TH) Fakultät für Elektrotechnik und Informationstechnik, Germany; 2009

[18] Do-Hoon K. Effect of antenna gain and group delay variations on pulse-preserving capabilities of ultra wideband antennas. IEEE Transactions on Antennas and Propagation. 2006;**54**(8):2208-2215. DOI: 10.1109/TAP.2006.879189

[19] Tokan NT, Neto A, Tokan F, Cavallo D. Comparative study on pulse distortion and phase aberration of directive ultra-wide band antennas. IET Microwaves, Antennas and Propagation. 2013;**7**(12):1021-1026. DOI: 10.1049/iet-map.2013.0032

[20] Gopikrishnan G, Akhterand Z, Jaleel Akhtar M. A novel corrugated four slot Vivaldi antenna loaded with metamaterial cells for microwave imaging. In: Proceeding of the Asia-Pacific Microwave Conference (APMC), New Delhi; 2016. pp. 1-4

[21] Abbak M, Akıncı MN, Çayören M, Akduman L. Experimental microwave imaging with a novel corrugated Vivaldi antenna. IEEE Transactions on Antennas and Propagation. 2017;**65**:3302-3307. DOI: 10.1109/TAP.2017.2670228

[22] Neto A. UWB, non dispersive radiation from the planarly fed leaky lens antenna. Part 1: Theory and design. IEEE Transactions on Antennas and Propagation. 2010;**58**:2238-2247

Chapter 4

# Teaching Transmission Line Propagation and Plane Wave Reflection Using Software Tools

Susana Mota and Armando Rocha

Additional information is available at the end of the chapter

http://dx.doi.org/10.5772/intechopen.74937

**Abstract**

Teaching transmission lines and wave propagation is a challenging task because it involves quantities not easily observable and also because the underlying mathematical equations—functions of time, distance and using complex numbers—are not prone to an easy physical interpretation in a frequent framework of a superposition of traveling waves in distinct directions. In such a context, tools with a strong visualization and easy student interaction can improve the learning outputs. We describe here a few tools and give basic exercises to address the main learning topics.

**Keywords:** telegrapher's equation, transmission line equations, input impedance, impedance matching, plane wave reflection and transmission

## 1. Introduction

The subject of propagation in transmission lines is a very important topic in analog microwave and high-speed digital circuits design. The full understanding of the circuit that models the transmission line, the line voltage and current equations, the input impedance of a transmission line and matching circuits is a basic background for any engineer dealing with circuits having sizes from an order of magnitude less than the wavelength. The wireless communications require a basic understanding of the multipath propagation channel whose basic models imply the understanding of plane wave reflection at the boundary between two infinite mediums. The phenomena described above are addressed here with very easy to use interactive tools developed in Matlab and that can assist teachers lecturing on these subjects and may also be used by the students as a virtual home laboratory. The first tools were already described in detail in [1] and made available and in http://bit.ly/2m8oBoe, whereas a new one

IntechOpen

© 2018 The Author(s). Licensee IntechOpen. This chapter is distributed under the terms of the Creative Commons Attribution License (http://creativecommons.org/licenses/by/3.0), which permits unrestricted use, distribution, and reproduction in any medium, provided the original work is properly cited. CC BY

on plane waves that is available in http://bit.ly/2m9TvMY is now presented and comprehensively described here.

## 2. Transmission line model: TLM.m

An ideal transmission line is made of a pair of conductors that carries a signal along a path length $\ell$ with only a delay $\tau$. Supposing a very high frequency and that any perturbation travels at finite speed we cannot assume that the voltage and current are constant along the line. Assuming two narrow parallel conducting strips of length $\ell$ = 1 m the image of a capacitor, with capacitance Ct(F), materializes immediately: an input voltage at one end will trigger a current to charge the capacitor. However, the two strips carrying the current can be seen also as a single rectangular turn of an inductor with inductance $L_t$(H): the current rate of change is limited. The equivalent circuit emerges as a series inductor followed by a capacitor to the ground.

This section addresses the response of a cascade of infinitesimal ladder circuits with length $\Delta x$, consisting of a series inductor with inductance $L\Delta x$ and a capacitor to the GND with capacitance $C\Delta x$, where L (H/m) and C (F/m) are, respectively, a distributed inductance and a distributed capacitance.

### 2.1. The TLM script description and objectives

The TLM.m script analyses the frequency response of a chosen number of N cascaded cell circuits (i.e., a discretized transmission line) terminated by an arbitrary resistance $R_L$. The total inductance and capacitance correspond to that of a 1 m commercial coaxial cable with a characteristic impedance of $Z_0$ = 50 Ω. The frequency response of the 1 m line is also calculated and depicted together with that of the discretized line, for comparison purposes.

The tool interface is shown in **Figure 1** depicting a simulation from DC to 1 GHz with 4 cells and $Z_L$ = 50 Ω. All the simulations are made assuming L = 189 nH/m, C = 76 pF/m and a generator with an internal impedance $R_g$ = 50 Ω. The main components of the tool and corresponding objectives are:

- Frame (1) shows the ladder circuit transfer function—the amplitude in dB (blue line) and the unwrapped phase in rad (green line)—and the transfer function of the ideal transmission line in the same format (black dotted line for the amplitude and red dotted line for the phase). The outputs intend to show that by increasing the number of cells the response of the discrete ladder circuit becomes close to that of the transmission line.
- Frame (2) shows the ladder circuit and the transmission line input resistance and input reactance using the same trace and color codes. The bottom slider is used to select a particular frequency and to highlight the ladder circuit response, in all the graphs, with a square marker. These values are also given in a table at the right of the slider. Additionally, the particular points of the frequency response can be examined.

http://dx.doi.org/10.5772/intechopen.74937

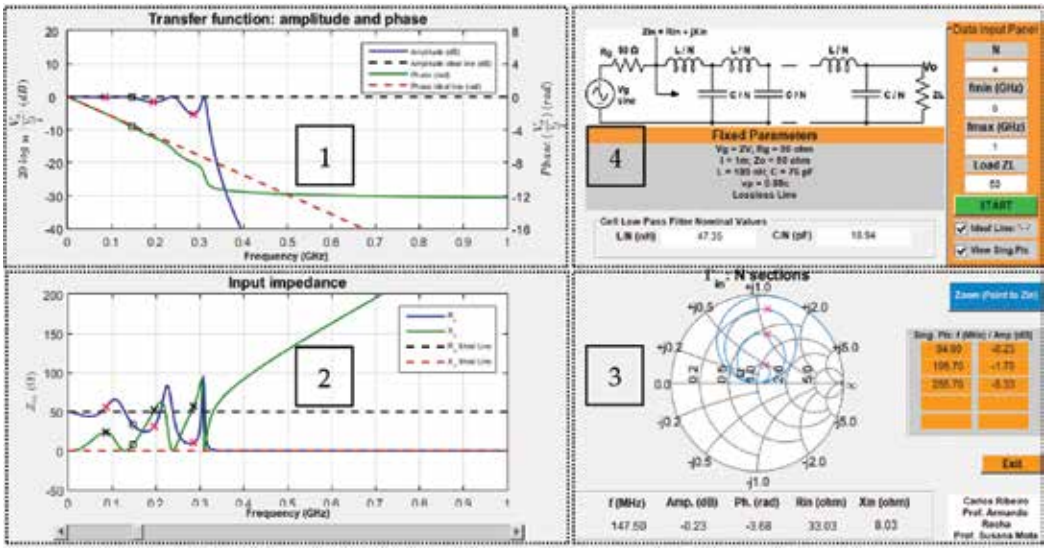


**Figure 1.** TLM Matlab tool aspect: frame description is given below.

- Frame (3) shows a Smith chart with the impedance of the ladder circuit and optionally, by activating an upper button, with the singular points at frequencies for which the transfer function is minimal. This output intends to show the trend of the discretized line input impedance in a Vector Network Analyzer (VNA) format.
- Frame (4) shows the schematics with the circuit parameters beneath. At the right, there is the input area allowing changing the simulation conditions (i.e., the frequency, number of cells and $Z_L$).

### 2.2. A few exercises

Run the script with N = 1 and the frequency range up to 1.5 GHz. Observe the results in **Figure 2** (left). Check if the single cell circuit is a low-pass filter whose impedance becomes purely reactive (inductive more specifically) and tends to an infinite value.

By increasing N = 5 the filter bandwidth becomes larger and the impedance starts to exhibit a real part close to 50 Ω and an imaginary part still inductive, but, at some frequencies is null: resonances are occurring and the input impedance is $Z_{in}$ = 50 Ω. The response amplitude is 0 dB at these last frequencies with others exhibiting some local minima. The Smith chart and the numerical outputs allow the identification of these points easily. The trend of $Z_{in}$ with frequency is an infinite inductive reactance: the first input cell dominates always the full circuit at a sufficiently high frequency that is related with N.

Increasing further the number of cells allows observing that the input resistance remains close to the 50 Ω and the input reactance remains close to 0 Ω for an increased bandwidth. Therefore, the circuit becomes an all pass filter with a delay, as can be observed from the linear phase exhibited by the frequency response of the circuit, approaching that of the ideal transmission line.

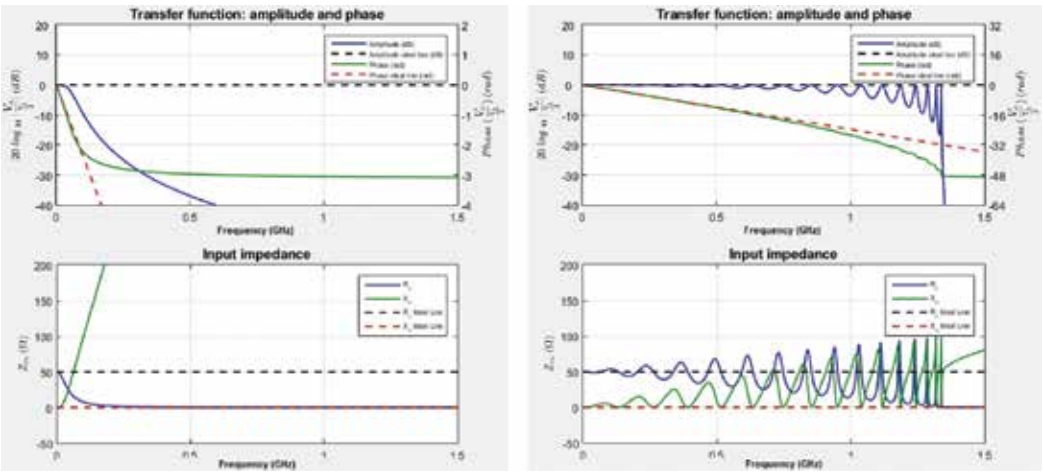


**Figure 2.** Transfer function and input impedance: N = 1 (left) and N = 16 (right).

### 2.3. Laboratory experiment

A laboratory prototype with N = 6 sections was implemented as can be observed in **Figure 3(a)**. The ladder circuit uses inductors with an average $L_1$ = 36.7 nH and capacitors with an average $C_1$ = 16.0 pF, ($\sqrt{LC^{-1}} \cong 50\Omega$). Furthermore, a lumped low-pass L-C circuit, with the integrated

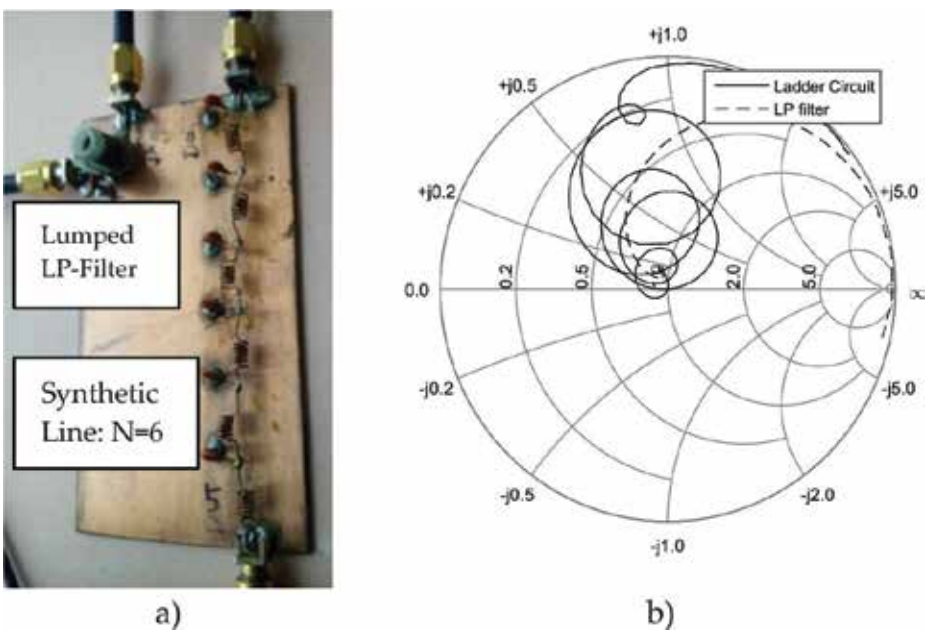


**Figure 3.** (a) Synthetic line with N = 6 and a lumped low-pass L-C circuit; (b) $Z_{in}$ measured with a VNA up to 400 MHz.

http://dx.doi.org/10.5772/intechopen.74937

inductance and capacitance of the ladder circuit elements, was added to the PCB for comparison purposes. The impedance of both circuits was measured with a VNA and is presented in **Figure 3(b)**.

As can be observed, the ladder circuit impedance follows in major lines the expected behavior, including the trend with the frequency to become a very high inductive impedance, in spite of some noticeable deviation at higher frequencies and not the perfect "ties" in general. The global similarity can be tested with TLM.m simulations using N = 6. On the other hand, the LP filter shows the expected trend: the input impedance becomes a very high inductive value at an early frequency if compared to the ladder circuit. In fact, the impedance even becomes capacitive: the anomaly is due to the non-ideality of the components, namely the serial resonance of the inductor.

In spite of the non-ideality of the frequency response of the components and other implementation difficulties, the prototype is very promising as a pedagogical tool to teach the circuit model of transmission line: it represents the telegrapher's equation physical model. Eventually, having a single L-C circuit, a circuit with N = 2 and another one with N = 4 may be recommended. The hardware implementation requires the use of high quality inductors and capacitors (high self-resonance frequency: small nominal values are recommended), equalization of the nominal values and a careful layout of the inductors to minimize mutual inductance.

Another interesting and easy exercise for the student is to compute, himself, the input impedance of the circuit with N cascaded cells, by using the recursive equation:

$$Z_n = j\omega L_1 + \frac{Z_{n-1}}{1 + jZ_{n-1}\omega C_1} \tag{1}$$

where n goes from 1 to N and the starting condition is $Z_{n-1} = Z_L$, for n = 1. With a little effort Eq. (1) can be implemented and computed in Matlab for any range of frequencies, an arbitrary number N of sections or even load impedances (other details, such as how to compute the transfer function, can be found in [1]).

## 3. Transmission line input impedance: Zin.m

Wave propagation—voltage and current—in transmission lines is usually handled by employing phasor analysis. In this context, it is crucial to understand that, in general, there are two waves traveling in opposite directions and that their relative phase changes along the line. Consequently, a standing wave is produced for voltage and current. The Zin tool explores the characteristics of the line input impedance by displaying simultaneously the amplitudes of the voltage and current standing waves and the corresponding phasors. Therefore, the relative amplitude and phase between them may be associated with the standing waves. The input impedance may be observed at any arbitrary point in a line of one-wavelength long, enabling this way, the perception of the impedance periodic behavior for lossless lines.

### 3.1. Description and objectives

The application assumes a transmission line with $Z_0 = 50\ \Omega$ and a generator with an amplitude of 2 V and internal impedance of 50 Ω. The tool interface is depicted in **Figure 4** and its description is as follows:

- On the top, it is shown the line circuit schematic, and on its right, there is a small area for entering the simulation parameters: the load impedance and the attenuation coefficient may be introduced. Above the schematic, there is an *information area* for results output, displaying the VSWR, the maximum and the minimum values of the resistance and reactance along the line. These results are updated every time any input is changed.
- Below the schematic, there is a rectangular graph where the normalized voltage phasor, 1+Γ(d), and the normalized current phasor, 1-Γ(d), are represented (in blue and red, respectively) at one point *d* of the line, which is chosen by actuating on the slider below this diagram. Furthermore, the voltage and current amplitudes along the line are also shown. Closely, on the right of this graph there is a new area for results output, presenting the reflection coefficient in the chosen point of the line, using rectangular and polar coordinates. At the rightmost side, the reflection coefficient, along the line, is also presented graphically in polar coordinates.
- At the bottom left, there is another rectangular graph exhibiting the observed resistance and reactance along the line (in blue and red, respectively). In addition, at the bottom rightmost side, the impedance along the line is represented again, this time in the complex plane. Below this representation, there is one more area for results output displaying the resistance and reactance at the selected line point.

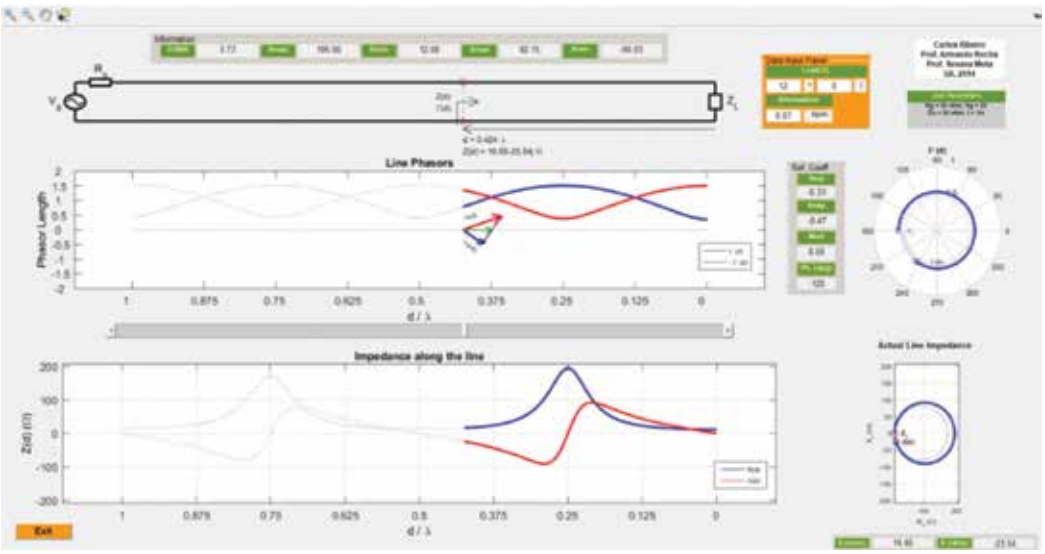


**Figure 4.** The interface of the input impedance demonstrator.

The picture of the reflection coefficient in a polar representation, as it is usually measured in laboratory using VNAs, intends to introduce or reinforce, in a straightforward way, the "Towards generator" or "Towards load" concepts, facilitating the understanding and use of the Smith chart. The impedance graph aims to establish the relationship between the type of impedance (with inductive or capacitive reactance) and the quadrant where the complex coefficient is represented and to establish also that the reflection coefficient and the corresponding impedance both describe a circumference (i.e., there is a conformal transformation between both).

### 3.2. A few exercises

Consider the lossless line with a resistive load impedance being two to five times smaller (or larger) than the characteristic impedance, for example, as 12 Ω.

- Observe the fluctuations on the voltage and current amplitudes along the line, the resulting input impedance, by inspecting both representations (the rectangular and complex plane graphs) and the refection coefficient. Notice that the impedance at $d = 0.25\lambda$ is again purely resistive (but greater than the characteristic impedance), whereas at $d = 0.5\lambda$ it is exactly equal to the load impedance again.
- Also, analyze the behavior of the input impedance at the standing wave maxima and minima points, and notice that the impedance nature (capacitive/inductive) changes, that is, at these points, the line behaves as a resonant circuit. Try to identify the type of resonance (series/parallel) exhibited at each of these points. Hint: consider a small increase/reduction in the frequency (i.e., a small reduction/increase of the wavelength) and compare with the lumped resonant circuits.
- Within the first line section of $0.5\lambda$ length, closer to the load, locate two points where the resistance of the observed impedance is equal to the line characteristic impedance and annotate the corresponding reactance. Explain how this reactance could be canceled by using, for example, a lumped element.

Maintaining the lossless line, study other loads as the *short-circuit* (SC), *open-circuit* (OC) and purely reactive impedances. In addition to $d = 0.25\lambda$ and $d = 0.5\lambda$, considered previously, also observe the line impedance at $d = 0.125\lambda$.

Consider now a lossy line and repeat the simulations with the loads suggested in the previous paragraphs. The results presented in **Figure 4** refer to a 12 Ω load and those in **Figure 5** refer to the SC. In both cases, it was considered a transmission line with an attenuation coefficient of 0.07 Np/m. Notice that voltage and current phase relations are maintained, but their amplitude fluctuations are more significant near the load. On the other hand, near the line input (generator) these fluctuations tend to vanish, particularly for highly attenuating lines (to better observe this effect, it is advisable to increase the attenuation coefficient). As a result, both the reflection coefficient and the input line impedance trace a spiral converging to the line characteristic impedance.


**Figure 5.** Input impedance of a lossy transmission line terminated in SC.

### 3.3. Laboratory experiment

**Figure 6** displays experimental results obtained for a microstrip line terminated in SC whose length is 6.2 cm, which equals one wavelength at about 2.73 GHz.

The reflection coefficient, presented in **Figure 6(b)**, was measured using a VNA, from 500 kHz (almost DC) up to 2 GHz. This line may be considered as a practical implementation for the input parameters used in **Figure 5**, even though, the measurements were acquired in the frequency domain, not along the line as shown by the demonstrator. In fact, it is possible to

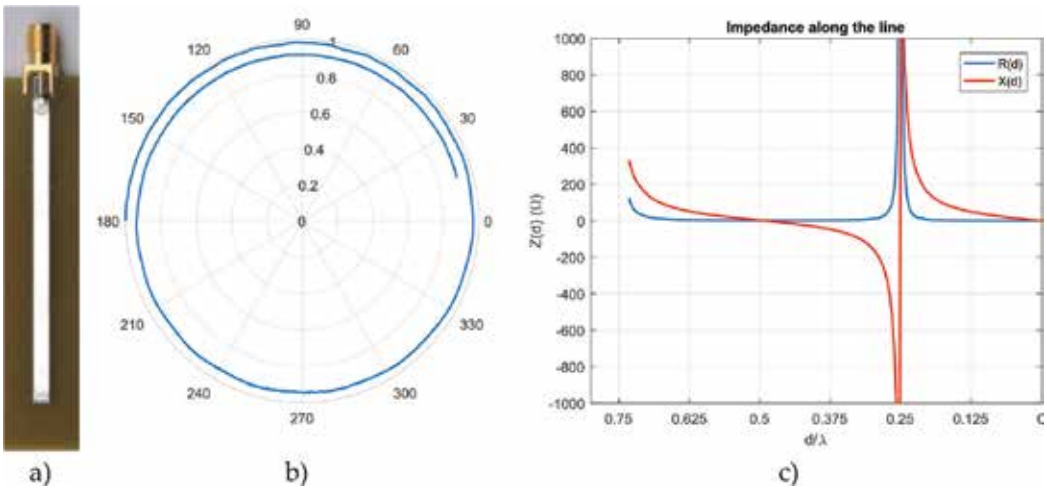


**Figure 6.** (a) Microstrip line terminated in SC; (b) the input reflection coefficient measured from 500 kHz up to 2 GHz; and (c) the corresponding input impedance.

http://dx.doi.org/10.5772/intechopen.74937

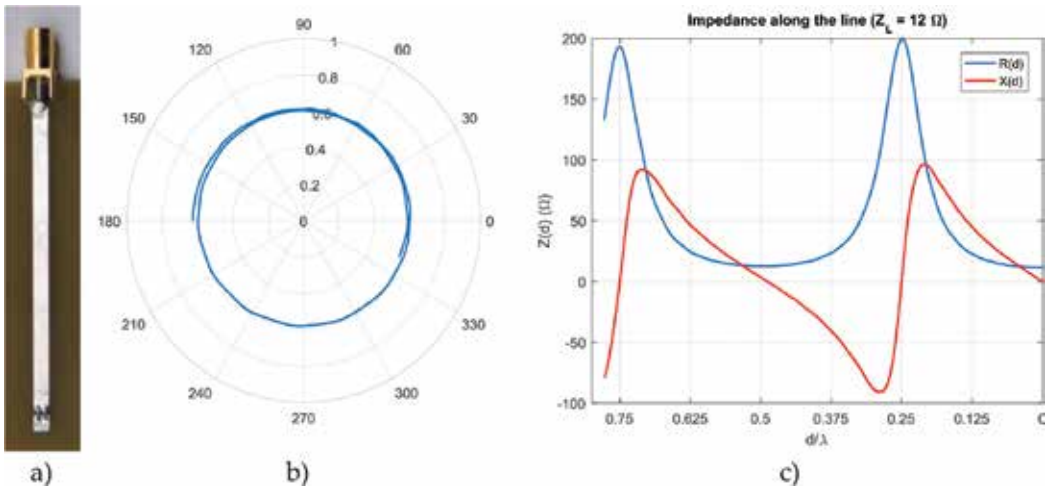


**Figure 7.** (a) Microstrip line terminated with $Z_L = 12\ \Omega$; (b) the input reflection coefficient measured from 500 kHz up to 2 GHz; and (c) the corresponding input impedance.

achieve quite consistent results, because, the demonstrator considers an increasing distance to the load, while, the measurements include an increasing attenuation coefficient with frequency for a constant line length.

The resistance and reactance of the impedance along the line are also presented in **Figure 6(c)**. In order to make the comparison with the results from the demonstrator easier (**Figure 5**), the frequency axis has been translated into electrical distance by using the frequency for which the line length equals one wavelength.

**Figure 7** displays the same type of experimental results obtained for a microstrip line with the same physical properties and terminated with $Z_L = 12\ \Omega$. This line may be viewed as a practical implementation for the input parameters used in **Figure 4**. In this case, similarly to the line-terminated SC, the reflection coefficient starts with an angle of 180° and its angular excursion should be the same, since the physical properties of the two lines are identical. However, the reflection coefficient in **Figure 7(b)** presents a larger angular excursion, suggesting a longer line or, in alternative, a load with a small inductive element. In fact, this can be due to the small patch used for welding the load to the ground plane below the substrate or the non-ideality of the resistor. Therefore, the frequency for which the line length appears to be one wavelength decreased to 2.57 GHz, which is about 6% less than that of the SC. Consequently, by using this value to obtain the electrical distance, for the abscissa axis in **Figure 7(c)**, results in an apparently longer transmission line.

## 4. Impedance matching: Matching.m

This application helps to find a matching solution expending a single series or parallel element. The solution is not given immediately; instead, it is intended to be found by experimentation,

using the properties of the transmission line impedance, that is, the user must find an appropriate distance to the load where to insert a susceptance (parallel) or a reactance (series) and the corresponding length (for a stub) or the nominal component value (if a lumped element is used).

The demonstrator shows the transmission line together with the stub or the lumped component, and uses the Smith chart so that the user is able to evaluate the outcome of all the inputs or changes introduced, by displaying the input impedance or admittance on the Smith chart and also, numerically, next to the circuit schematic. Furthermore, assuming that the reactance of the load does not change with frequency, the circuit frequency response is presented on the Smith chart and, in addition, on one rectangular graph window (return loss, VSWR or transmission loss can be represented).

### 4.1. Description and objectives

The tool assumes a generator with internal impedance of 50 Ω and a lossless transmission line with characteristic impedance of 50 Ω, with a length that is 0.5λ at the chosen frequency. The user interface is depicted in **Figure 8** and its description is as follows:

- On the upper left side it is shown the circuit schematic and, on its right there is an area for entering the parameters, where the user can specify the load impedance, the project frequency ($f_p$), the type of matching network (series or parallel) and the type of the matching element (inductor, capacitor or OC/SC terminated stub). Any of these options may be set and changed at any time by the user.
- Below the circuit schematic, there is a slider allowing the user to choose where to place the matching component and, below the slider, a Smith chart is displayed. As the slider is moved, the line impedance for series arrangements (or admittance for parallel arrangements) is displayed on the Smith chart using a blue line. Simultaneously, the corresponding numerical values are given next to the slider.
- The matching element (stub or lumped component) may be adjusted using another slider inside the area for parameter inputs. The resulting impedance (or admittance) is immediately shown on the Smith chart using a green line. At the same time, numerical values are also displayed near this slider: stub length (or nominal value of the lumped component), corresponding reactance (or susceptance in absolute value), position of the matching network, and the VSWR achieved.
- At the bottom right side, a rectangular window presents the return loss, transmission loss or the VSWR: the user can choose one of the three which is displayed as a function of the frequency from $f_p/2$ to $10f_p$. In addition, a "check box" allows, at any moment, to visualize also the impedance frequency response on the Smith chart (or remove it).

### 4.2. A few exercises

Consider $Z_L$ = 12 Ω and $f_p$ = 700 MHz. Start by introducing a series network using a lumped component:

http://dx.doi.org/10.5772/intechopen.74937

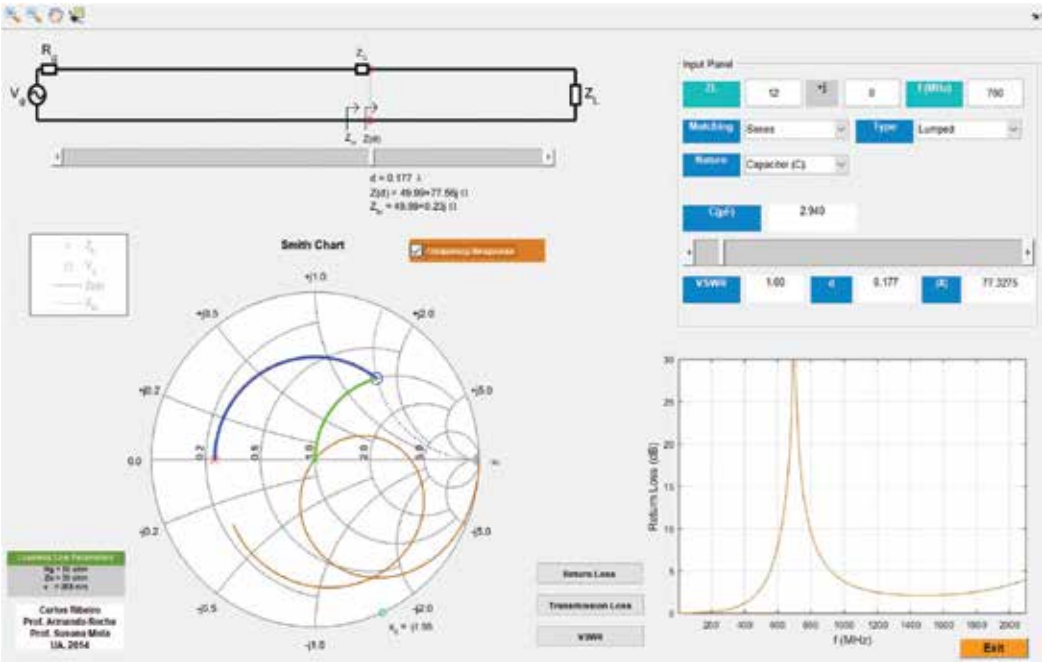


**Figure 8.** The interface of the matching demonstrator.

- By actuating in the slider below the circuit schematic locate the first point in line (as close to the load as possible) where the real part of Z(d) is about 50 Ω. Then move the other slider inside the parameter input panel and try to reach the center of the Smith chart. This is the solution depicted in **Figure 8**. Confirm that only one of the available components (inductor or capacitor) allows matching the transmission line.
- Locate a second point in the line where the real part of Z(d) is again 50 Ω, and find the lumped component which matches the system. Verify whether there is an alternative position on the line (different from those found previously) where a match can be achieved. Observe the input impedance, the VSWR and the return loss as a function of the frequency. Try to explain the behavior of the return loss when the frequency tends to infinity.
- Summarize all solutions found: two possible points per half wavelength to insert the component and, that for each position, only one type of lumped component (inductor or capacitor) offers a solution to the problem.

Consider now $Z_L = 12.5\ \Omega$, $f_p = 650$ MHz and achieve the matching using a parallel stub:

- Move the slider below the schematic and find one first position on the line (as close to the load as possible) where the real part of Y(d) is about 1/50 S and notice that at this location, the equivalent impedance, $Z_{in}$, involves a 50 Ω resistor in parallel with a certain reactance. Then, move the slider inside the parameter input panel and try to reach the center of the

Smith chart. Annotate the corresponding stub lengths for OC and SC terminations. **Figure 9** presents the solution using a stub in OC.

- Observe that, at certain frequency, the return loss reaches the worst value of 0 dB (meaning that the reflection coefficient touches somewhere the outer circle of the Smith chart, that is, $|\Gamma| = 1$). Try to explain this observation.
- Repeat this last exercise using lumped elements and notice that for each of the above positions (those where it is possible to match the line impedance with parallel stubs) there is only one lumped element that allows to match the line.

### 4.3. Laboratory experiment

**Figure 10(a)** shows a practical implementation of the solution given in **Figure 8**. Its input impedance was measured, from 500 kHz up to 2 GHz, using a VNA and is represented in **Figure 10(b)**. The corresponding return loss is presented in **Figure 10(c)**. The best return loss value (highlighted by an asterisk in the figure) is slightly better than 15 dB and it is achieved at nearly the project frequency (698 MHz).

Furthermore, **Figure 11(a)** depicts a practical implementation of the solution found in **Figure 9**. In the same way, **Figure 11(b)** and **(c)** show, respectively, the measured input impedance and the corresponding return loss. At the project frequency (650 MHz) the return loss measured is about 20.4 dB (the best return loss value is about 21 dB achieved at 637 MHz).

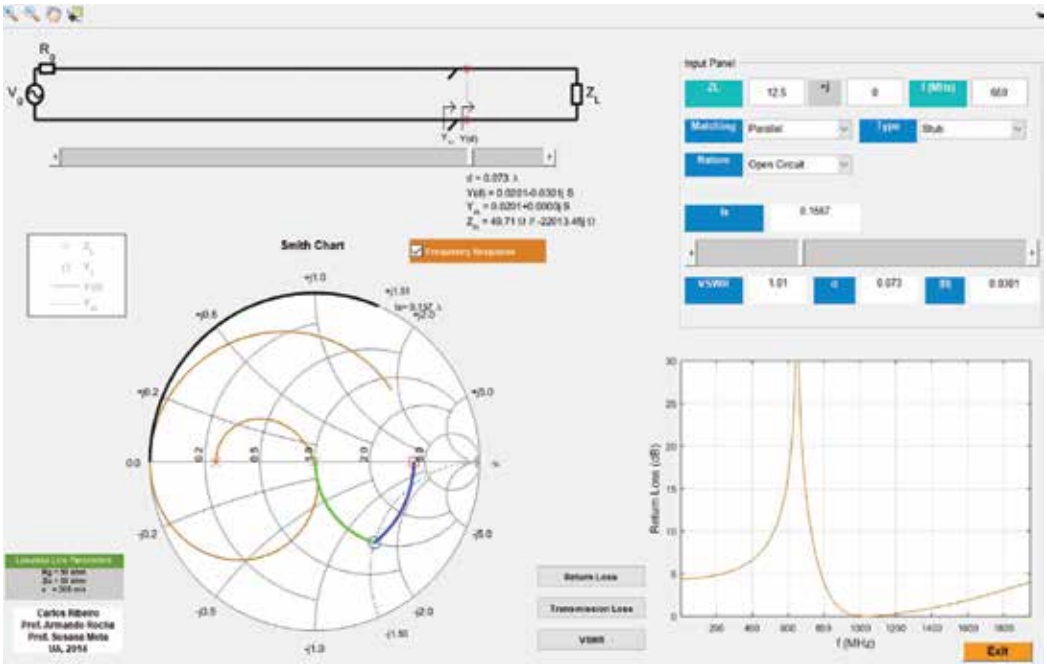


**Figure 9.** Matching $Z_L = 12.5\ \Omega$ at $f_p = 650$ MHz with a parallel stub in OC.

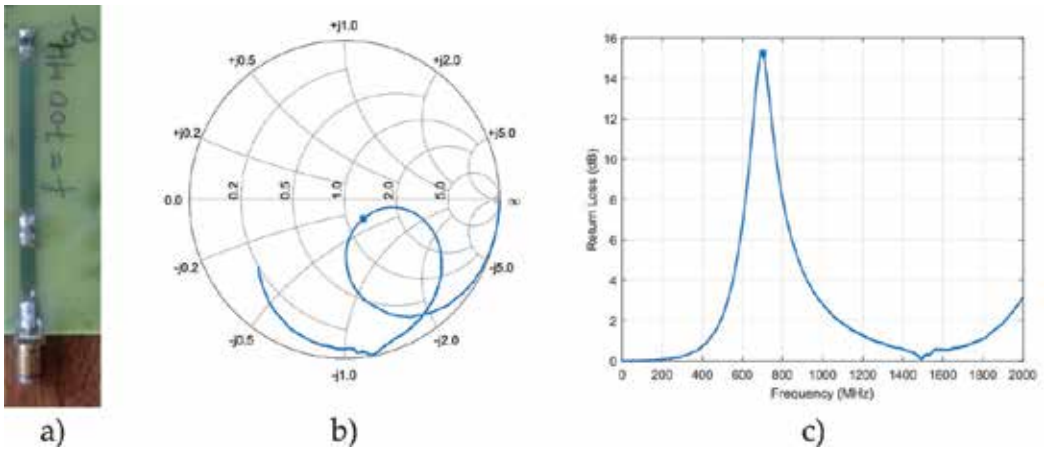


**Figure 10.** (a) Matching $Z_L$ = 12 Ω at $f_p$ = 700 MHz using a series capacitor, (b) the measured input impedance, and (c) measured return loss.

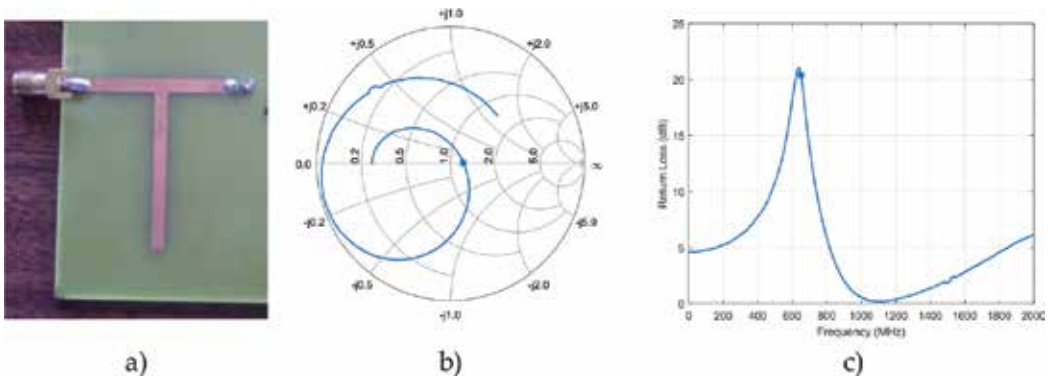


**Figure 11.** (a) Matching $Z_L$ = 12.5 Ω at $f_p$ = 650 MHz, with a parallel OC stub, (b) the measured input impedance, and (c) measured return loss.

In both cases, the results displayed by the demonstrator are generally in good agreement with those from the measurements.

## 5. Electromagnetic waves: EM.m

The reflection and transmission of electromagnetic plane waves is a fundamental resource to understand wireless multipath propagation channel models and to introduce basic concepts concerning propagation phenomena in optical fibers. Teaching this matter is even more difficult than the transmission lines one. To justify we can point out the following reasons: the phenomenon depends on the wave polarization; vectors should be used to represent electromagnetic fields (3-D visualization or similar is mandatory); the superposition of incident and

reflected fields is more complex, because, waves do not travel in the same direction; and finally, there are particular cases, such as, the total transmission (Brewster angle) and the total reflection (above a critical angle), of incident plane waves.

### 5.1. The EM.m script description and objectives

Let us assume an electromagnetic plane wave traveling in a medium 1 impinging on a plane infinite boundary (from now on called *reflection plane*) between two lossless mediums: medium 1 and medium 2, having, respectively, a dielectric permittivity $\varepsilon_1$ and $\varepsilon_2$. Both mediums are non-magnetic, that is, $\mu_1 = \mu_2 = \mu_0$, with $\mu_0$ being the vacuum permeability. The dielectric permittivity, $\varepsilon$, can be written using the relative permittivity, $\varepsilon_r$, as $\varepsilon = \varepsilon_r \varepsilon_0$, with $\varepsilon_0$ being the free space permittivity.

The impedance of a medium is given by.

$$\eta = \frac{120\pi}{\sqrt{\varepsilon_r}} \ (\Omega) \tag{2}$$

and the wavenumber (or phase constant) is given by:

$$\beta = \frac{2\pi\sqrt{\varepsilon_r}}{\lambda_0} \ (\text{rad/m}) \tag{3}$$

with $\lambda_0$ being the free space wavelength. The *angle of incidence*, $\theta_i$, is defined as the angle between the direction of propagation, $\widehat{k}_i$, and the normal to the reflection plane (please see **Figure 12**). The *incidence plane* is the plane defined by the direction of propagation and the normal to the reflection plane (XoZ plane). The incident wave causes a reflected wave, having an angle of reflection equal to the angle of incidence, and a transmitted wave propagating on medium 2, having an angle of transmission, $\theta_t$, given by:

$$sen\,\theta_t = \sqrt{\frac{\varepsilon_{r1}}{\varepsilon_{r2}}} sen\,\theta_i \tag{4}$$

Two distinct linearly polarized incident plane waves, **Figure 12**, can be identified:

- A polarization with the electric field parallel to the incidence plane, $E_{\parallel}$, having components along z and x. The orthogonal magnetic field, $H_{\parallel}$, has a component along y.
- A polarization with the electric field perpendicular to the incidence plane, $E_{\perp}$. The orthogonal magnetic field, $H_{\perp}$, has components along z and x.

The reflection coefficient, $\Gamma$, and the transmission coefficient, T, for the parallel polarization, are given by:

$$\Gamma_{\parallel} = \frac{\sqrt{\left(1 - \frac{\varepsilon_{r1}}{\varepsilon_{r2}} sen^2\,\theta_i\right)} - \sqrt{\frac{\varepsilon_{r2}}{\varepsilon_{r1}}}\cos\,\theta_i}{\sqrt{\left(1 - \frac{\varepsilon_{r1}}{\varepsilon_{r2}} sen^2\,\theta_i\right)} + \sqrt{\frac{\varepsilon_{r2}}{\varepsilon_{r1}}}\cos\,\theta_i} \qquad T_{\parallel} = \left(1 + \Gamma_{\parallel}\right)\frac{\cos\,\theta_i}{\cos\,\theta_t} \tag{5}$$

http://dx.doi.org/10.5772/intechopen.74937

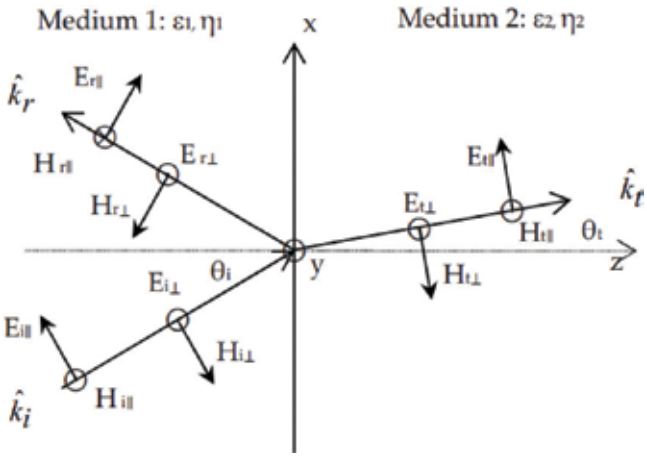


**Figure 12.** Plane wave incidence (plane XoY): 'i', 'r' and 't' means incident, reflected and transmitted waves, the unit vector along the incident, reflected and transmitted waves direction of propagation are $\hat{k}_i, \hat{k}_r, \hat{k}_t$, the symbol ⊙ means vector pointing to the reader and ⊗ pointing downwards.

with $\theta_t$ given by Eq. (4) and, for the perpendicular polarization, are given by:

$$\Gamma_{\perp} = \frac{\cos\theta_i - \sqrt{\frac{\varepsilon_{r2}}{\varepsilon_{r1}} - sen^2\,\theta_i}}{\cos\theta_i + \sqrt{\frac{\varepsilon_{r2}}{\varepsilon_{r1}} - sen^2\,\theta_i}} \qquad T_{\perp} = 1 + \Gamma_{\perp} \tag{6}$$

It can be shown that, for parallel polarization, there is an angle of incidence, $\theta_{iB}$, called *Brewster angle* at which the reflection coefficient becomes null. This angle is given by:

$$\theta_{iB} = sin^{-1}\sqrt{\frac{\varepsilon_{r2}}{\varepsilon_{r1} + \varepsilon_{r2}}} \tag{7}$$

In addition, regardless the wave polarization there is an angle of incidence, for the case of incidence in a less dense medium, which turns the absolute value of the reflection coefficient unitary. This is the *critical angle*, $\theta_{ic}$, given by:

$$\theta_{ic} = \sin^{-1}\left(\sqrt{\frac{\varepsilon_{r2}}{\varepsilon_{r1}}}\right) \tag{8}$$

For the parallel polarization, the following set of electric and magnetic fields equations can be derived using Eqs. (2)–(5):

$$\vec{\mathbf{E}}_i\,(x,z) = \mathbf{E}_{io}(\hat{x}\,\cos\theta_i - \hat{z}\,sen\theta_i)\,e^{-j\beta_1\,(x\,sen\,\theta_i + z\,\cos\,\theta_i)} \tag{9}$$

$$\vec{\mathbf{H}}_i\,(x,z) = \hat{y}\,\frac{\mathbf{E}_{io}}{\eta_1}\,e^{-j\beta_1\,(x\,sen\,\theta_i + z\,\cos\,\theta_i)} \tag{10}$$

$$\vec{\mathbf{E}}_r\,(x,z) = \Gamma_{\parallel}\mathbf{E}_{io}\,(\hat{x}\,\cos\theta_i + \hat{z}\,sen\theta_i)\,e^{-j\beta_1\,(x\,sen\,\theta_i - z\,\cos\,\theta_i)} \tag{11}$$

$$\vec{\mathbf{H}}_r\,(x,z) = -\widehat{y}\,\Gamma_{\parallel}\,\frac{\mathbf{E}_{io}}{\eta_1}\,e^{-j\beta_1\,(x\,sen\,\theta_r - z\,\cos\,\theta_r)} \tag{12}$$

$$\vec{\mathbf{E}}_t\,(x,z) = T_{\parallel}\mathbf{E}_{io}\,(\widehat{x}\,\cos\theta_t - \widehat{z}\,sen\theta_t)e^{-j\beta_2\,(x\,sen\,\theta_t + z\,\cos\,\theta_t)} \tag{13}$$

$$\vec{\mathbf{H}}_t\,(x,z) = \widehat{y}\,T_{\parallel}\,\frac{\mathbf{E}_{io}}{\eta_2}\,e^{-j\beta_2\,(x\,sen\,\theta_t + z\,\cos\,\theta_t)} \tag{14}$$

with $\mathbf{E}_{io}$ being a reference incident electric field amplitude.

Similarly, using Eqs. (2)–(4) and (6) the following equations can be derived for the perpendicular polarization:

$$\vec{\mathbf{E}}_i\,(x,z) = \widehat{y}\,\mathbf{E}_{io}\,e^{-j\beta_1\,(x\,sen\,\theta_i + z\,\cos\,\theta_i)} \tag{15}$$

$$\vec{\mathbf{H}}_i\,(x,z) = \frac{\mathbf{E}_{io}}{\eta_1}\,(-\widehat{x}\,\cos\,\theta_i + \widehat{z}\,sen\,\theta_i)\,e^{-j\beta_1\,(x\,sen\,\theta_i + z\,\cos\,\theta_i)} \tag{16}$$

$$\vec{\mathbf{E}}_r\,(x,z) = \widehat{y}\,\Gamma_{\perp}\mathbf{E}_{io}\,e^{-j\beta_1\,(x\,sen\,\theta_i - z\,\cos\,\theta_i)} \tag{17}$$

$$\vec{\mathbf{H}}_r\,(x,z) = \frac{\Gamma_{\perp}\mathbf{E}_{io}}{\eta_1}\,(\widehat{x}\,\cos\,\theta_i + \widehat{z}\,sen\,\theta_i)\,e^{-j\beta_1\,(x\,sen\,\theta_i - z\,\cos\,\theta_i)} \tag{18}$$

$$\vec{\mathbf{E}}_t\,(x,z) = \widehat{y}\,T_{\perp}\mathbf{E}_{io}\,e^{-j\beta_2\,(x\,sen\,\theta_t + z\,\cos\,\theta_t)} \tag{19}$$

$$\vec{\mathbf{H}}_t\,(x,z) = \frac{T_{\perp}\mathbf{E}_{io}}{\eta_2}\,(-\widehat{x}\,\cos\,\theta_t + \widehat{z}\,sen\,\theta_t)\,e^{-j\beta_2\,(x\,sen\,\theta_t + z\,\cos\,\theta_t)} \tag{20}$$

The interpretation of Eqs. (5) and (6) and the fields given from Eqs. (9)–(20) as a function of $\theta_i$ is difficult. The EM.m script addresses this problem by depicting the reflection coefficients and all the set of fields in three separate figures. A screenshot of the tool interface, that follows a similar but more complete approach of the one described in [2], is presented in **Figure 13**.

The interface is divided in four graphs (left part) and an input data/output area (right part). The numbered areas contain:

1. The fields with a single Cartesian component along $\widehat{y}$: $E_{i\perp}$, $E_{r\perp}$, or the total field $E_{1\perp} = E_{i\perp} + E_{r\perp}$ in medium 1 and $E_{t\perp}$ in medium 2 for the perpendicular polarization; $H_{i\parallel}$, $H_{r\parallel}$, or the total field $H_{1\parallel} = H_{i\parallel} + H_{r\parallel}$ in medium 1 and $H_{t\parallel}$ in medium 2 for the parallel polarization. The representation contains also the directions of the incident, reflected and transmitted waves (represented by segments as in **Figure 12**) and the wavelength in medium 1 and 2 and along the $\widehat{x}$ and $\widehat{z}$ axis (written equations).
2. The fields along the $\widehat{z}$ axis: $H_{iz\perp}$, $H_{rz\perp}$, or the total field $H_{tz\perp} = H_{iz\perp} + H_{rz\perp}$ in medium 1 and $E_{tz\perp}$ in medium 2 for the perpendicular polarization; $E_{iz\parallel}$, $E_{rz\parallel}$, or the total field $E_{1\parallel} = E_{iz\parallel} + E_{rz\parallel}$ in medium 1 and $E_{tz\parallel}$ in medium 2 for the parallel polarization.
3. The fields along the $\widehat{x}$ axis (as described above).

4. The amplitude of the reflection and transmission coefficients and their respective phase. The slider can be used to change the angle of incidence.

5. The interaction tools to choose the incident polarization, the angle of incidence, the dielectric constants, the angle of incidence and the waves to be displayed (i, r or t).

6. The numerical outputs: reflection and transmission coefficients, angle of transmission and the critical or Brewster angle (if they exist).

The simulations are made for a normalized electric field amplitude of 1 V/m, a free space wavelength $\lambda_0 = 1$ m and the z and x axis ranges are fixed to $4\lambda_0$. All the magnetic fields are multiplied by the impedance of medium 1, $\eta_1$, to have all the values in the same range for a convenient pseudo-color graph with a color code around the black color. The graphs are time animated by depicting successively several snapshots within one period.

### 5.2. A few exercises

The first exercise is made with $\varepsilon_{r1} = 1$ and $\varepsilon_{r2} = 4$ and normal incidence ($\theta_i = 0°$) for perpendicular polarization. **Figure 13** depicts some results shown for this case. Check the reflection and transmission coefficients (similar to a transmission line terminated by a resistive load). Verify

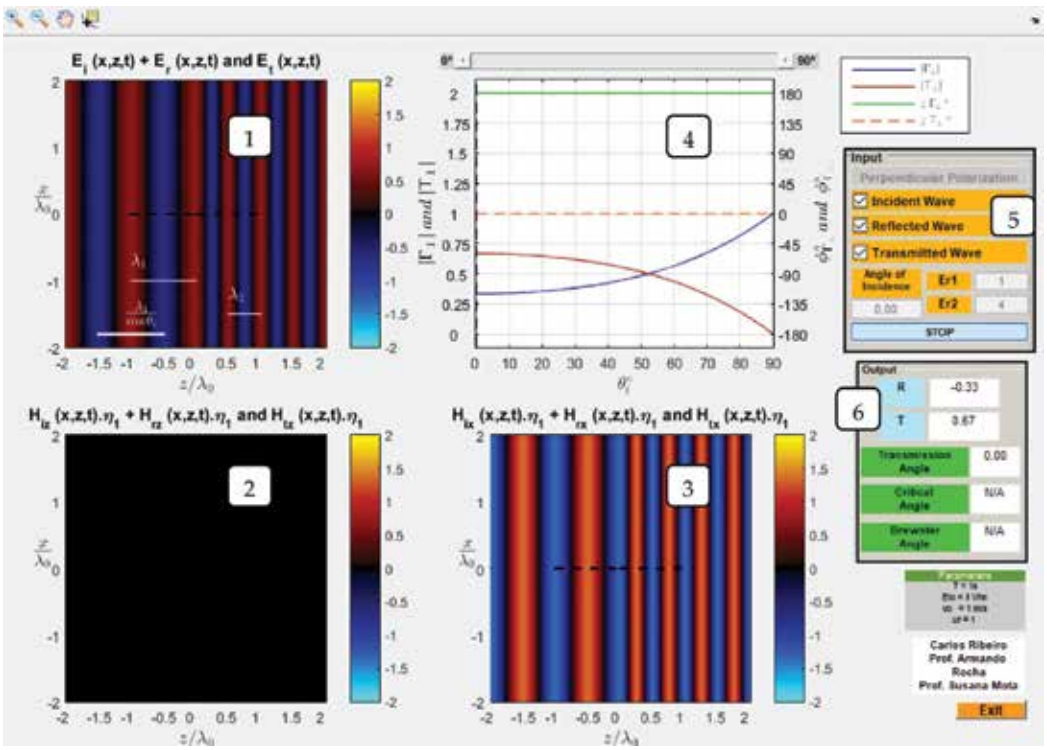


**Figure 13.** EM.m tool screen shot: frame description is given below.

that they are the same for the parallel polarization and also that $\Gamma_\perp$ increases monotonically from $\theta_i = 0°$ to 90° up to 1 (text frame (3)).

Observe the incident, the reflected and total fields and the standing waves in medium 1. The minima (black stripes) and the maxima (more hot colors and cold colors) occur always at planes parallel to the reflection plane, in spite of a travel in time being observed (left side of text frames (1): electric field $E_y$ and (3): magnetic field $H_x$). Also the distance between maxima and minima is a quarter of the wavelength. In medium 2 the wave is traveling to the right and has half of the wavelength of that in medium 1, due to the higher dielectric constant (right side of text frames (1) and (3)). No interference is observed because only one traveling wave exists. The component of the magnetic field (text frame (2)) along z-axis does not exist for this particular geometry as can be confirmed by checking **Figure 12**.

The diectric constant for medium 2 can be increased to observe a larger standing wave amplitude (on the limit an infinite dielectric constant mimics a perfectly conducting medium). There is no perceived advance in medium 2 and the standing wave is depicted as flashing stripes alternating between a light blue and yellow colors. The physical situation is similar to an ideal ressonant circuit where energy is being transferred between the inductor (magnetic field) and the capacitor (electric field) with no dissipated power (transmitted).

The second exercise uses the same configuration but considering $\theta_i = 45°$ and the results are presented in **Figure 14**. Observe the interference in medium 1: the distances of the maxima and minima are now longer and the interference is more "intense", due to a higher amplitude of the reflected wave. There is a perception of the wave in medium 1 traveling along x and the interference occurring along $z^-$. The wave in medium 2 moves away along the direction $\theta_t$.

The third exercise ($\varepsilon_{r1} = 1$ and $\varepsilon_{r2} = 4$) uses parallel polarization and incidence with the Brewster angle, $\theta_i = 63.43°$ (Eq. (7)) and the results are depicted in **Figure 15**. The reflection coefficient is null and, as in other cases, increases again up to 1 for tangential incidence after changing sign at the Brewster angle. By observing the total field, check that there is no reflected wave and consequently no interference in medium 1. This means that all the incident power at this polarization and angle of incidence is entirely transmitted to medium 2: an incident circular polarization would give a reflected wave with linear polarization. In addition, it is

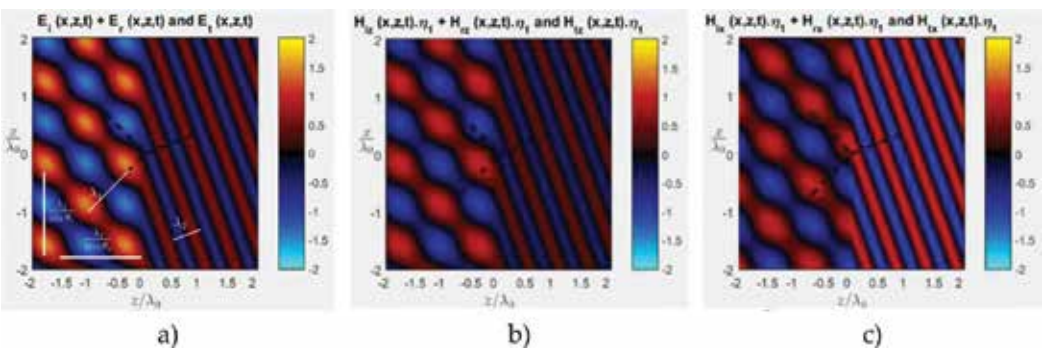


**Figure 14.** Incidence: $\theta_i = 45°$ (a) electric field $E_y$ (b) magnetic field $H_z$ and (c) magnetic field $H_x$.

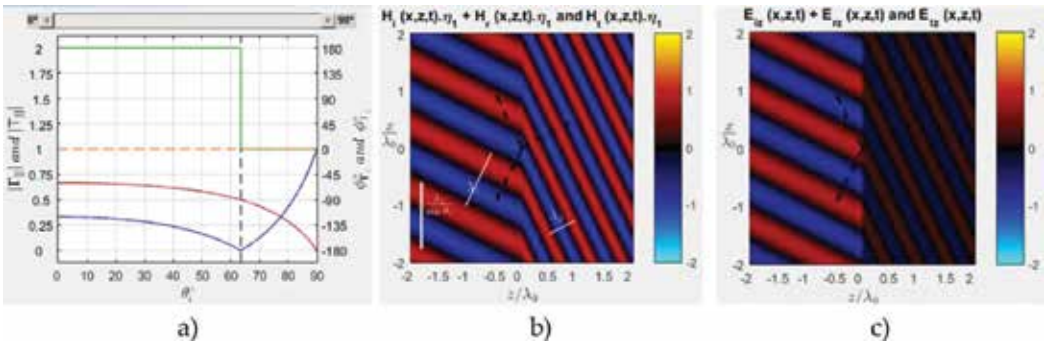


**Figure 15.** (a) $\Gamma_{\parallel}$ and $T_{\parallel}$ (b) magnetic field $H_y$ and (c) electric field $E_z$.

interesting to observe the discontinuity of the electric field, $E_z$, at the interface between the two mediums (see **Figure 15(c)**), as it is expected from the boundary conditions. It is worthwhile to verify that the Brewster angle does not exist for the perpendicular polarization.

The fourth exercise ($\varepsilon_{r1} = 4$ and $\varepsilon_{r2} = 1$) uses parallel polarization and illustrates the incidence above the critical angle $\theta_{ic} = 30°$ (Eq. (8)). Start by an angle of incidence a few degrees below $\theta_{ic}$ and check that the angle of transmission is close to 90°. Increasing the angle of incidence a few degrees past $\theta_{ic}$ allows to observe the results of **Figure 16**: the reflection coefficient becomes real and unitary (full reflection) at $\theta_{ic}$ and complex (but unitary) at higher angles.

The fields inside medium 2 assume a tooth-like shape along the z-axis, the amplitude decreases with the distance z from the reflection plane and the wave travels along x. By increasing angle of incidence, the fields become closer to the reflection plane. That is, there is no power transferred to medium 2 and the wave is contained in medium 1 by a dielectric based "container". The angle $\theta_t$ becomes complex, Eq. (4), and an attenuation constant emerges from the exponentials in Eqs. (13), (14), (19) and (20).

Check that the phenomena occurs for both parallel and perpendicular polarization and only when medium 1 is more "dense" ($\varepsilon_{r1} < \varepsilon_{r2}$).

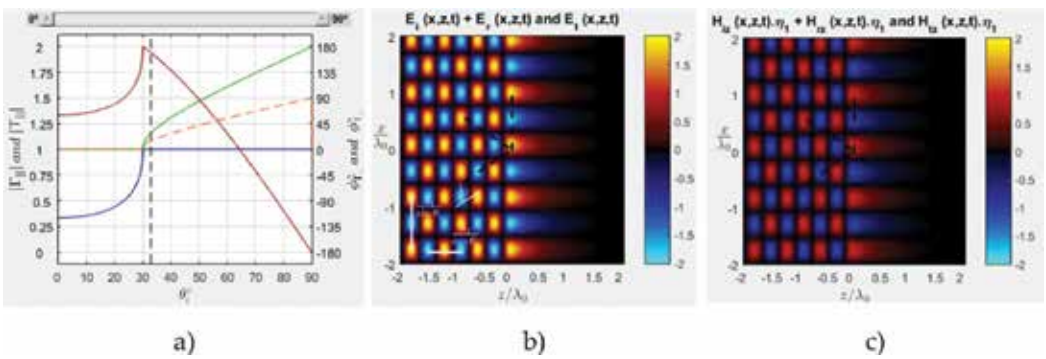


**Figure 16.** Incidence above $\theta_{ic}$: (a) $\Gamma_{\perp}$ and $T_{\perp}$ (b) electric field $E_y$ and (c) magnetic field $H_z$.

## 6. Conclusions

Simulation tools, to explore the basic concepts about transmission line propagation and about reflection and transmission of plane waves, were described. Moreover, some theoretical exercises were given and, in addition, a few laboratory prototypes measurements depicting the theoretical exercises were presented, thus, highlighting the usefulness of the tools, as well as, the need to complement the learning by using simulations with practical laboratory experiences.

## Acknowledgements

The authors are grateful to the Department of Electronics, Telecommunications and Informatics for the opportunity of teaching this subjects and using the RF equipment to perform the laboratory measurements. They are also grateful to the former MSc student, C. Ribeiro, for the intense brainstorming with them and for the implementation of the simulation tools.

## Author details

Susana Mota* and Armando Rocha

*Address all correspondence to: smota@ua.pt

Departamento de Eletrónica, Telecomunicações e Informática, Instituto de Telecomunicações, Aveiro, Portugal

## References

[1] Rocha A, Mota S, Ribeiro C. Software tools for teaching wave propagation in transmission lines [education corner]. IEEE Antennas and Propagation Magazine. 2017;**59**(3):118-127

[2] Trintinalia LC. Simulation tool for the visualization of EM wave reflection and refraction. IEEE Antennas and Propagation Magazine. 2013;**55**(1):203-211

Chapter 5

# Radio Network Planning and Propagation Models for Urban and Indoor Wireless Communication Networks

Wojciech Jan Krzysztofik

Additional information is available at the end of the chapter

http://dx.doi.org/10.5772/intechopen.75384

**Abstract**

As the growing demand for mobile communications is constantly increasing, the need for better coverage, improved capacity, and higher transmission quality rises. Thus, a more efficient use of the radio spectrum and communication systems availability are required. This chapter presents EM propagation models most commonly used for the design of wireless communication systems, computer networks WLAN and WPAN for urban and/or in indoor environments. The review of commercial or University computer codes to assist design of WLAN and WPAN networks were done. An example of computer design and simulation of indoor Bluetooth and WLAN communication systems, in the building of Wroclaw University of Science and Technology, Wroclaw, Poland is shown in Chapter 8.

**Keywords:** EM wave propagation, urban, outdoor, indoor, deterministic model, empirical model, one-slop, multi-wall, ray tracing, ray lunching, dominant path, mobile communication system, WLAN, Wi-Fi, Bluetooth

## 1. Introduction

In recent years, a substantial increase in the development of broadband wireless access technologies for evolving wireless Internet services and improved cellular systems has been observed. Because of them, it is widely foreseen that in the future an enormous rise in traffic will be experienced for mobile and personal communications systems. This is due to both an increased number of users and introduction of new high bit rate data services. This trend is observed for third-generation systems, and it will most certainly continue for fourth- and fifth-generation systems.

Wireless communication systems, as opposed to their wireline counterparts, pose some unique challenge:

IntechOpen

© 2018 The Author(s). Licensee IntechOpen. This chapter is distributed under the terms of the Creative Commons Attribution License (http://creativecommons.org/licenses/by/3.0), which permits unrestricted use, distribution, and reproduction in any medium, provided the original work is properly cited. CC BY

**a.** allocated spectrum limitation results in a limited levels of system capacity;

**b.** radio propagation environment and the mobility of users give rise to signal fading and spreading in time, space, and frequency; and

**c.** expired battery life at the mobile device poses DC power constraints.

In addition, cellular wireless communication systems have to cope with interference due to frequency reuse. Research efforts investigating effective technologies to mitigate such effects have been going on for the past years, as wireless communications are experiencing rapid growth.

The rise in traffic will put a demand on both manufacturers and operators to provide sufficient capacity in the networks. This becomes a major challenging problem for the service providers to solve, since there exist certain negative factors in the radiation environment contributing to the limit in capacity.

A major limitation in capacity is co-channel interference caused by the increasing number of users. The other impairments contributing to the reduction of system performance and capacity are multipath fading and delay spread caused by signals being reflected from structures (e.g., buildings and mountains) and users traveling on vehicles (**Figure 1**).

To aggravate further the capacity problem, in 1990s, the Internet gave the people the tool to get data on-demand (e.g., stock quotes, news, weather reports, e-mails, etc.) and share information in real time. This resulted in an increase in airtime usage and in the number of subscribers, thus saturating the systems' capacity.

Wireless carriers have begun to explore new ways to maximize the spectral efficiency of their networks and improve their return on investment. Research efforts investigating methods of improving wireless systems performance are currently being conducted worldwide.

In the design of wireless networks for companies and institutions, there is no room for chance. Failure to even potentially the smallest factor can cause errors that will make our project become useless. To organize the design process, the concept of splitting the process into three phases is introduced [1]: *initial phase*—collects information about the requirements and expectations of the client; *design phase*—identifying the best access point, AP, location by application of simulation based on the EM wave propagation models; and *measurement phase*—implementation of the project and the introduction of any amendments arising from the difference between the results of measurements (the real behavior of the network), and simulation.

In the circumstances in which radio waves are many phenomena, the designation of a useful signal level is extremely complex and requires the introduction of appropriate propagation models. Such model is a collection of mathematical expressions, graphs, and algorithms used to produce propagation characteristics of EM waves in chosen environment. Propagation models can be divided into empirical (statistical) such as One-Slope (O-S), Multi-Wall (M-W)—linear and nonlinear, dominant path model (DPM), etc., the deterministic (e.g., Ray Tracing, RT, Intelligent Ray Tracing, IRT, Ray Lunching, RL, etc.). There are also models which are a combination of both of these types.

http://dx.doi.org/10.5772/intechopen.75384

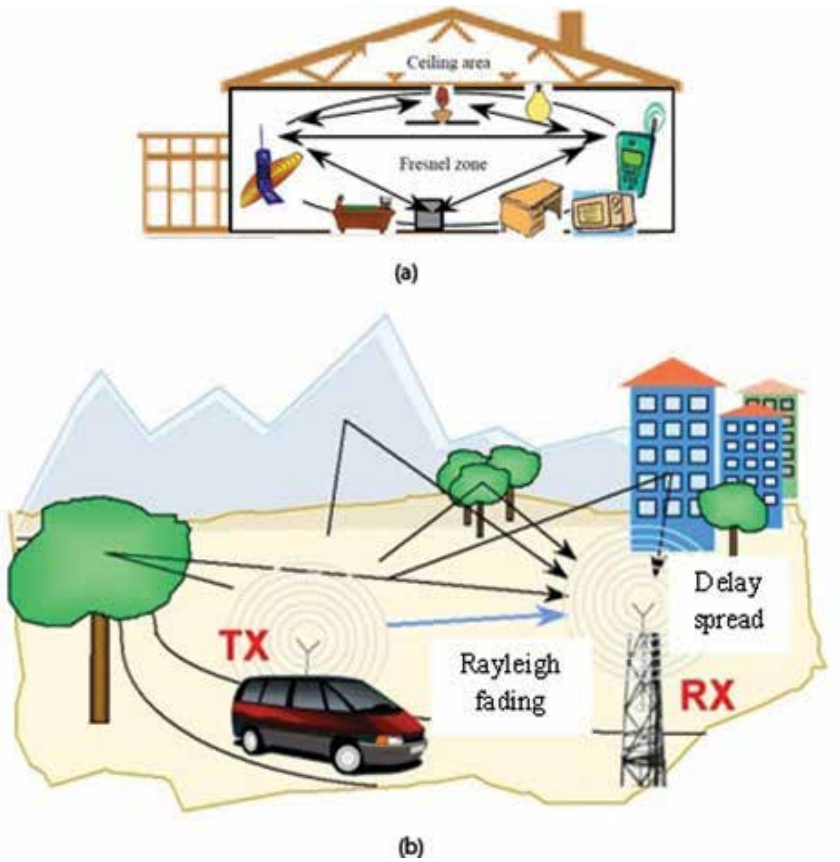


**Figure 1.** Wireless systems impairments in: indoor (a) and outdoor (b) environments.

Presented models allow streamlining the design process for wireless networks. On the market, there are a lot of solutions, commercial computer codes, based on these concepts.

## 2. Radio link budget

Wireless network design requires that you specify the size and shape of the areas covered by the access points. To this end, the link budget is performed:

$$P_{Rx} = P_{Tx} + G_{Tx} + G_{Rx} - (L_{Tx} + L_{Rx} + L) \tag{1}$$

where $P_{Rx}$ is the received power (dBm), $P_{Tx}$ is the broadcast power (dBm), $G_{Tx}$ is the power gain of transmitting antenna (dB), $G_{Rx}$ is the power gain of receiving antenna (dB), $L_{Tx}$ is transmitting antenna cable attenuation, $L_{Rx}$ is receiving antenna cable attenuation, and $L$ is the route of EM wave propagation attenuation (dB).

The most difficult to determine the part of the link budget is the attenuation loss $L$ of the propagation route. Typical wireless systems environment is located inside the buildings filled with walls, furniture, peoples, and other objects. In such conditions, the mechanism of propagation of the EM waves is very complex. A number of EM waves distributed inside buildings belong to different physical phenomena [2]:

- ***Diffraction***: when signal encounters on the road, an impermeable barrier, whose dimensions are larger than the wavelength. At the edges of the obstacles is the deflection of the wave causing the attenuation, dispersion, and a change in the direction of EM wave propagation,
- ***Dispersion***: when on the road the wave contains obstacles, whose dimensions are comparable to the wavelength. In this case, the radio waves are directed in more directions, which is difficult to predict and model,
- ***Reflection***: when radio wave on the way encounters an obstacle, whose dimensions are much larger than the wavelength of the incident EM wave, they reflect itself from the obstacle. In cases when at the receiving end, there are many of reflected waves signal can be very unstable,
- ***Penetration over obstacles***: when radio wave encounters an obstacle, which is to some extent transparent for radio waves, allowing the reception of radio signals inside buildings (waves penetrate through walls and ceilings),
- ***Absorption***: caused by the appearance of the plants on the propagation route, peoples with high absorption capacity. Radio waves are absorbed also by other obstacles, such as walls, furniture, and painting of the walls, curtains on the windows, etc.,
- ***Running along the tunnels and corridors***: guided wave phenomenon can be dealt with as a special mechanism to describe the propagation in tunnels or corridors, arising as a result of multiple reflections and interference of the EM waves along the route.

The designation of the attenuation of a route in such conditions is extremely difficult. Having regard to these mechanisms of propagation, the propagation models have been developed. The propagation model is an algorithm to analyze the propagation of radio waves in the environment taking into account the mechanisms described above. The algorithm described it in the proper order by means of the specified mathematical expressions, charts, and tables of some coefficients, and they are most frequently served in the form of recommendations of the ITU, IEEE and others worldwide standardizing institutions.

The propagation models permit to determine the average value of the propagation loss in a proper place. For the complete modeling of the propagation environment, the statistics of the received signal should be provided, which lets you include slowly variable and quick-exchange of signal dropouts. The slowly variable dropouts are understood as fluctuations in the average value of a signal over a distance of several wavelengths. Studies have shown that the lognormal distribution with standard deviation of values $\sigma = 2.7/5.3$ dB is the best model of the phenomenon of slow signal fade [8]:

http://dx.doi.org/10.5772/intechopen.75384

$$p(x) = \frac{1}{x \cdot \sigma \cdot \sqrt{2 \cdot \pi}} \cdot e^{\frac{-(\log x - \log m)^2}{2 \cdot \sigma^2}} \tag{2}$$

where $p(x)$ is the probability of the appearance of the signal with a value of $x$, $\sigma$ is the standard deviation of the distribution, and $m$ is the mean value of the signal.

The quick-exchange dropouts shall be understood as fluctuations in the average value of the signal caused by changes in the propagation environment, for example, the movement of people in the building. These fluctuations at the small number of moving people best describes the Rice distribution with a value of $\sigma = 7/14$ dB [8]:

$$p(x) = \frac{x}{\sigma^2} \cdot e^{\frac{-\left(x^2 + A^2\right)^2}{2 \cdot \sigma^2}} \cdot I_0\left(\frac{A \cdot x}{\sigma^2}\right) \tag{3}$$

where $p(x)$ is the probability of the appearance of the signal with a value of $x$, $\sigma$ is the standard deviation of the lognormal distribution with mean value $m$, and $A$ is the strongest signal component amplitude, $I_0$ is a modified Bessel function of the first kind of order 0.

In order to facilitate the description of the Rice distribution, the $k$ parameter is used [8]:

$$k = 10\log\frac{A^2}{2 \cdot \sigma^2} \tag{4}$$

In the case of a large movement of people in buildings, it is advisable to use the Rayleigh distribution [8]:

$$p(x) = \frac{x}{\sigma^2} \cdot e^{\left(\frac{-x^2}{2 \cdot \sigma^2}\right)} \tag{5}$$

where $p(x)$ is the probability of the appearance of the signal with a value of $x$ and $\sigma$ is the standard deviation of the lognormal distribution with mean value $m$.

Analysis of the introduced distributions has allowed determining that the value of the signal exceeded at a given point in the 90% of the time in the conditions inside the building is smaller by about 6 dB from the mean value.

## 3. Empirical models

Empirical models are based on measurements and observations made under different conditions. Their accuracy depends not only on the results of measurements but also from the similarity of the present environment and the environment in which the modeling measurements were conducted. The propagation environments inside buildings are strongly differentiated. The use of empirical models in such conditions can lead to less accurate results relative to other promotional environments. Therefore, for indoor environments, more accurate models are considered to be deterministic models. Despite this, the easy implementation and fast calculation time that empirical models are not lost in popularity [8].

### 3.1. The one-slope model

The one-slope model is the simplest model used in the indoor environment. It does not take into account the details of the structure of the building but only the distance and $n$ parameter describing an environment [8]:

$$L = L_0 + 10 \cdot n \cdot \log(d) \tag{6}$$

where $L_0$ is the attenuation at a distance of 1 m, $n$ is the coefficient of the power distribution, and $d$ is the distance between the transmitter and the receiver.

The parameters of the $L_0$ and $n$ are empirical parameters assigned to the specified environment. By appropriate selection of their values, we can adjust the model to a specific type of building, for which we design a wireless network. Examples of model values for different propagation environments are shown in **Table 1.**

Building 1 represents buildings introducing the large attenuation (with high density of users, furniture, walls, and other obstacles). Building 2 represents the typical office buildings of medium attenuation. Building 3 represents the big empty spaces of exhibition halls, warehouses, and large offices with a small amount of furniture and other obstacles of the generally small damping. Parameter $n$ in the case of propagation in the corridor is only 1, 2—what is apparent from the account of the phenomenon of driving in the tunnel (waveguide), which amplifies the signal. Due to the small accuracy of the model O-S has been used in a small number of computer tool applications: I-PROP (Technical University of Prague) and WinProp (AWE).

| f, GHz | $L_0$, dB | n | Application |
|---|---|---|---|
| 2.45 | 40 | 3.5 | Building 1 |
| 2.45 | 40 | 4.5 | Building 2 |
| 2.45 | 40 | 2 | Building 3 |
| 2.45 | 40 | 1.2 | Corridor in the building |
| 5.25 | 46.8 | 3.5 | Building 1 |
| 5.25 | 46.8 | 4.5 | Building 2 |
| 5.25 | 46.8 | 2 | Building 3 |
| 5.25 | 46.8 | 1.2 | Corridor in the building |

**Table 1.** Sample parameters of the one-slope model.

### 3.2. The multi-wall model

The most popular models of empirical studies to take into account the effect of the walls and ceilings are multi-wall models. Linear multi-wall model (also called the Motley-Keenan model) specifies the attenuation on the direct route between transmitter and receiver, taking into account the attenuation by walls and ceilings of the building [8]:

$$L = L_0 + 10 \cdot n \cdot \log(d) + \sum_{i=1}^{I} N_{wi} \cdot L_{wi} + \sum_{j=1}^{J} N_{fj} \cdot L_{fj} \tag{7}$$

where $L_0$ is the attenuation at distance of 1 m, $n$ is the index that depends on the adopted model, $d$ is the distance between the transmitter and receiver, $N_{wi}$ is the number of walls of equal attenuation value, $N_{fj}$ is the number of floors with equal attenuation values, $L_{wi}$ is the attenuation of the $i$-th walls- kind, and $L_{fj}$ is the attenuation of j-th ceilings value.

Based on measurements, the parameter values are designated as [8]: $L_0$ = 37 dB, $L_f$ = 20 dB (for typical slabs thickness < 30 cm), $L_w$ = 3.5 dB (for plaster walls), and 7 dB (for concrete walls), $n$ = 2.

Conditions of the propagation inside the building more accurately reflects, so called, nonlinear model of multi-walls, which was developed within the framework of the European project COST 231 and approved by the ITU as recommended for third generation of cellular mobile systems projects. Attenuation of radio link referred to the model is given by following equations [4]:

$$L = L_{FS} + L_0 + \sum_{i=1}^{I} N_{wi} \cdot L_{wi} + N_f^{\left(\frac{N_f+2}{N_f+1}-b\right)} \cdot L_f \tag{8}$$

$$L_{FS} = 32,4 + 20\log\left(f_{[MHz]}\right) + 20\log\left(d_{[km]}\right) \tag{9}$$

where $L_{FS}$ is the free space loss, $L_0$ is the attenuation at distance of 1 m, $N_{wi}$ is the number of $i$-type walls on the propagation route, $N_f$ is the number of floors on the propagation route, $L_{wi}$ is the attenuation of the $i$-type walls, $L_f$ is the slab attenuation, $b$ is the empirical parameter, $f$ is the channel center frequency (MHz), and $d$ is the distance between the transmitter and the receiver (km).

Some of model parameters were determined empirically [4]: $L_0$ = 37 dB, $L_f$ = 18.3 dB (for ceilings constructed of reinforced concrete with a thickness < 30 cm), $L_{w1}$ = 3.4 dB (for plaster walls with lots of window openings), $L_{w2}$ = 6.9 dB (for concrete walls and constructed from bricks, perforated in the form of holes in their design), and $b$ = 0.46.

The M-W models are used in computer programs (commercial and academic). Examples of computer codes are: WinProp (AWE Communication), ACTIX Analyzer, and I-Prop (University of Prague). **Figure 2** shows a comparison of the simulation results obtained in the building type 1 by applying the model of one-slope (b) and nonlinear model of multi-walls (c).

Simulations were made using the demo version of the I-Prop program for the transmitter with a power of 10 dBm and at a frequency of 2.45 GHz [3]. The M-W model in indoor environments takes into account the impact of the walls on the suppression of radio wave but only on the direct of transmission transmitter to receiver route. As mentioned earlier, the specificity of phenomena in indoor environments causes if a direct signal is often not the

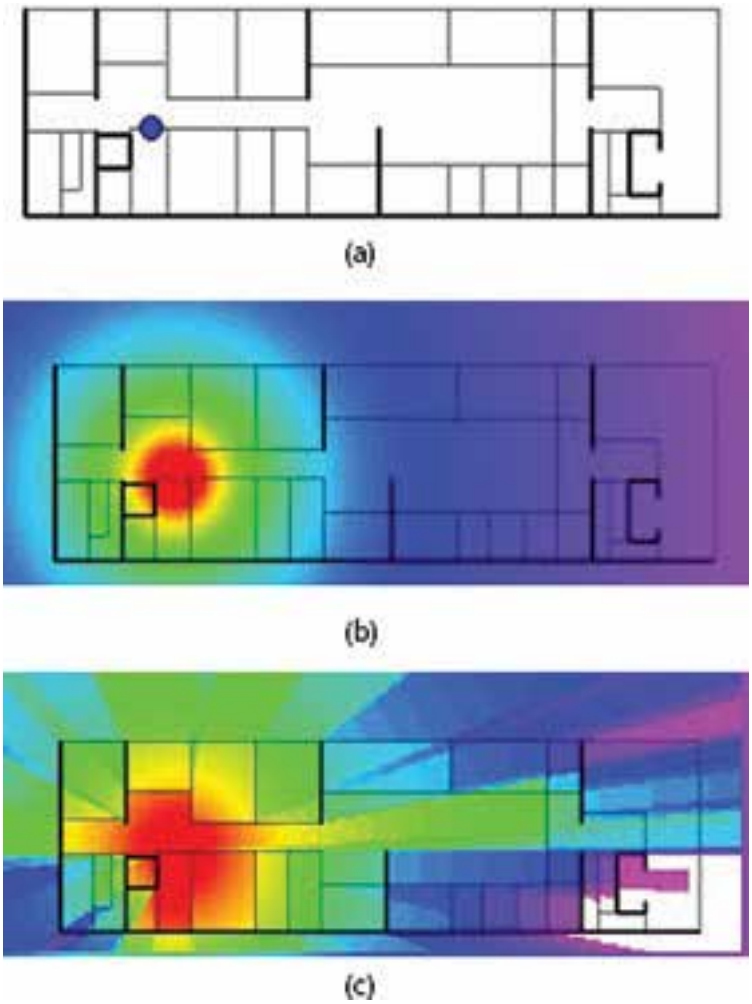


**Figure 2.** The projection of floors and location of the access point (a), the distribution of the signal for one-slope model (b), and for nonlinear model of multi-walls (c) [3].

strongest one. In that cases in the received signal the reflected as well as the diffraction rays should also be considered [4].

### 3.3. Dominant path model

In the dominant path model (D-P), the losses shall be determined for several wave propagation routes. As shows experience, in most cases, only two or three rays carry more than 95% of the signal energy. Analysis of the results of measurements also showed that the adjacent rays decompose the same phenomena and are almost identical. This fact was used in the D-P model, which is looking for the routes with the smallest attenuations. In **Figure 3**, the concept of the D-P model is shown.

http://dx.doi.org/10.5772/intechopen.75384

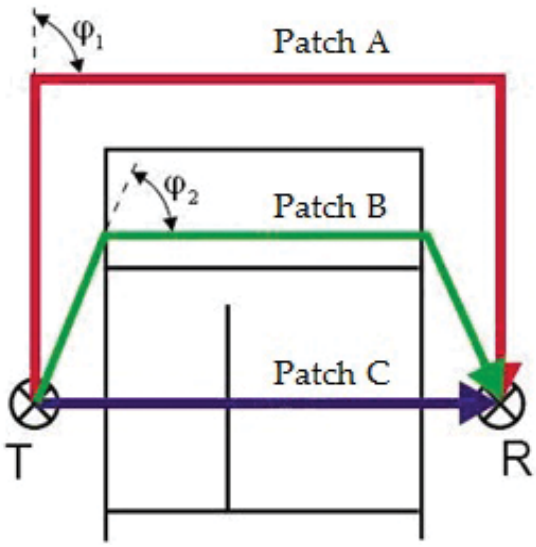


**Figure 3.** Routes of the wave propagation in dominant path model [5].

The losses on selected routes shall be, according to [5]:

$$L = 20 \cdot n \cdot \log(d) + \sum_{i=1}^{I} f(\varphi_i, i) + \sum_{j=1}^{J} L_j - W \tag{10}$$

where $n$ is the factor depending on propagation conditions for direct radius, $d$ is the length of the propagation route, $W$ is the factor of the conduct of wave which grows for the smaller distance between the faces on the propagation route, $f(\varphi_i,i)$ is the function determining the loss depending on the number of phenomena, $i$ specifies the following phenomena, $\varphi_i$ is the angle between the new and the previous direction of propagation, and $L_j$ is the attenuation caused by the transition of the wave by $j$-wall (or ceiling).

The D-P model allows you to take into account the situation, when the dominant radius is not the dominant one, it means the attenuation of EM waves is not lowest one. So, on the beginning the attenuations for some few routes are determined, for which are expected to be the smallest. On further analysis, only those routes have been taken into account. It is important that the exact designation of the losses is associated with some encountered phenomena (reflection and diffraction) and strengthening related to the phenomenon of the driving waves in the corridors (the waveguide effect). The designation of a wave driving factor $W$ and suppression caused by diffraction and reflection can greatly vary depending on the type of building. For each environment before the calculations, it is recommended that measurements should be arranged, the results of which will allow for the designation of a function $f(\varphi_i, i)$ and parameter $W$. Parameter $W$ that specifies the contribution to the phenomenon of the conduct of the wave in the D-P model depends on: the width of the corridor/tunnel, the material from which the walls are built, the walls' orientation relative to the designated path, and the continuity of the phenomenon of the conduct of the wave.

Determination of the coefficient $W$ starts the analysis of three parameters for each of the walls and at the point of $x$. The factor $w_i(x)$ that represents the interim impact of the $i^{th}$ wall on the conduct of the wave at the point $x$, can be appointed from [5]:

$$w_i(x) = A_i \cdot D_i(x) \cdot L_i \tag{11}$$

$$A_i = \begin{cases} 1 - \left(\varphi_i / 45^{\circ}\right) & 0 \le \varphi \le 45^{\circ} \\ 0 & \varphi > 45^{\circ} \end{cases} \tag{12}$$

$$D_i(x) = \begin{cases} 1 - (d_i(x)/3m) & 0 \le d_i \le 3m \\ 0 & d_i > 3m \end{cases} \tag{13}$$

$$L_i = \begin{cases} 1 - (L_{Ri}/10dB) & 0 \le L_{Ri} \le 10dB \\ 0 & L_{Ri} > 10dB \end{cases} \tag{14}$$

where $d_i$ is the distance between the wall and the path of propagation; $L_{Ri}$ are losses resulting from reflection, depending on the material of the wall is built; and $\varphi_i$ is the angle between the wall and the path of propagation.

The factor $w(x)$ that represents the partial effects of all $N$ walls in section $x$ specifies the pattern [5]:

$$w(x) = \frac{1}{w_0} \min\left(w_0, \sum_{i=1}^{N} w_i(x)\right) \tag{15}$$

The factor is normalized relative to the $w_0$—maximum value of the conducted wave. Resultant factor wave driving is the superposition of all partial coefficients in the way of propagation [5]:

$$W = \frac{1}{x_R - x_T} \cdot \int_{x=x_T}^{x_R} w(x)dx \tag{16}$$

where $x_R$ is the receiver position and $x_T$-the position of the transmitter.

The value of the coefficient $W$ can range between a value of 0 (the conducting of EM wave phenomenon does not exist) and 1 (the ideal case of the conducting EM wave phenomenon).

The second essential and difficult to model parameter of the D-P model is the attenuation caused by the changing direction of propagation of the angle $\varphi_i$. This parameter is determined as a factor $W$ of the wave driving.

Besides, you should also know the suppression resulting from the transition of the wave by an obstacle and the distance between the transmitter and the receiver. Based on the difficulties in the designation $f(\varphi_i, i)$ and $W$ in the result, this model is used in a small number of computer codes (e.g., WinProp) [5].

**Figure 4** shows a comparison of the simulation results obtained from: (a) only the direct radius (nonlinear of M-W model, (b) the strongest ray (the dominant path D-P model), and (c) the ray tracing, 3D RT, approach (c).

http://dx.doi.org/10.5772/intechopen.75384

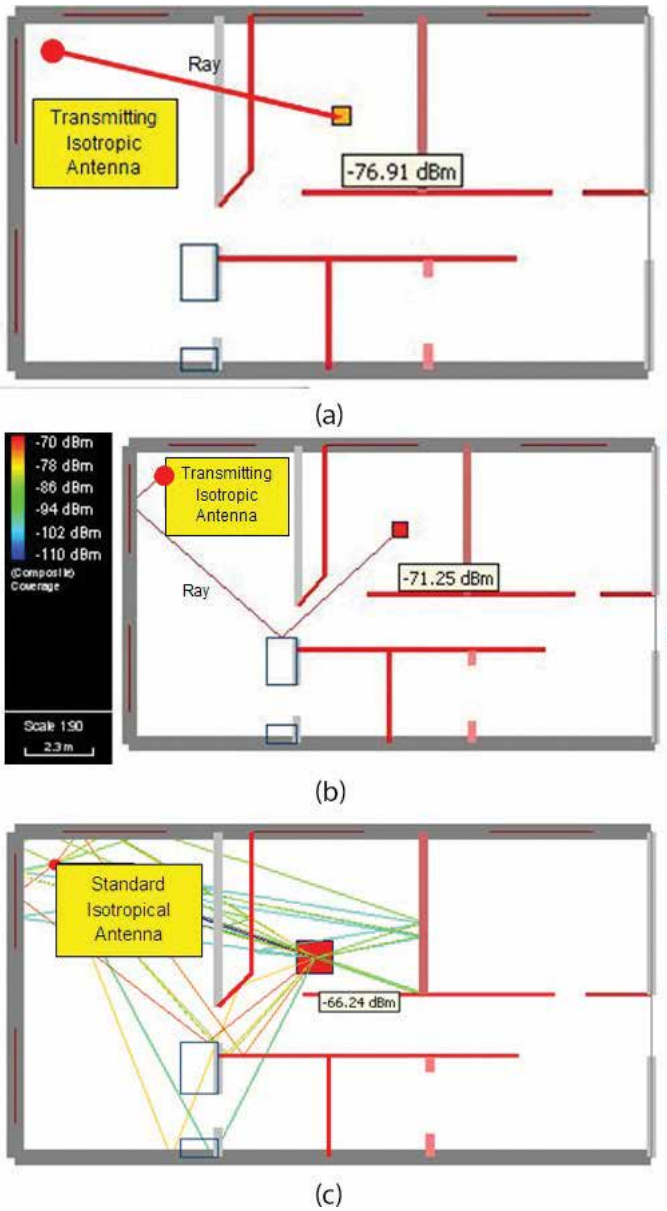


**Figure 4.** Simulation results obtained using: only the direct radius (nonlinear of M-W model) (a), of the strongest ray (the dominant path D-P model) (b), and ray tracing, 3D RT, approach (c).

Both results were obtained by means of ACTIX Analyzer for the transmitter with a power of 10 dBm at frequency of 2.45 GHz [6]. In this example, the direct radius is weaker than the strongest radius of about 5.66 dB, or almost 3.7 times. This result proves the superiority of the D-P model over the M-W model. Unfortunately, the very complex initial calculations make D-P model difficult to implement.

## 4. Deterministic models

Deterministic models are based on physics laws and allow for precise modeling of the propagation of electromagnetic waves. These models take into account the phenomena such as reflection, diffraction, absorption, and wave running, which are essential in the conditions inside buildings as well as in the outdoor area of dense building centers. Unlike the empirical models, the deterministic models are not based on measurements and thus it accuracy does not depend on the similarity of the standard environment and concerned one. To accurately model the phenomenon of propagation of electromagnetic waves, deterministic models require accurate rendering of environment propagation periods. In addition to the level of the model of the environment and on the quality of results, calculation has the effect of repeat accuracy phenomena, which are subject to the electromagnetic waves. The EM waves propagation environments inside buildings are strongly differentiated. Therefore, for these environments, deterministic models are considered to be more accurate in comparison with models of empirical studies.

In order to wave propagation modeling, two concepts were developed. The first is a technique for FDTD (finite-difference time-domain) and the other is a technique GO (geometrical optics) also known under the name of ROM (ray optical method).

### 4.1. FDTD method

The FDTD method is to solve the boundary conditions of the Maxwell's equations for the analyzed area by means of frequency differences method in the time domain. The method requires a transition from continuous space and time distribution of electromagnetic field to a discrete spatially grid that contains in its nodes of the field values in a certain moment of time. The transition from derivatives for odds ratios differential allows you to create an algorithm to calculate the distribution of the field in the next time step of the fields at the time of the previous one. The distribution of the structure given by the material constants is specified in each of the nodes of the grid. This algorithm has been provided by Kane Yee. In accordance with the algorithm EM field value in the node of the grid depends only on the values of the EM field at this point in the previous time step, as well as of the values of other EM fields in the adjacent nodes of the grid, and of the known features of magnetic and electrical sources. FDTD simulation results are more precise relative to GO. It requires a large amount of CPU memory and of the computer microprocessor power for fast calculation of the large Maxwell's equations. For this reason, it is rarely used in computer programs that support design of the wireless networks. An example of such a program is the Wireless InSite of the Remcom Company. The FDTD method is limited in suburban environments, in which the structures are situated close to antennas with complex material properties [7, 23–27].

### 4.2. Method of geometrical optics GO

Deterministic models are based primarily on methods of geometrical optics (ray optical method (RO), or geometrical optics (GO)), which are based on the assumption of rectilinear propagation of electromagnetic waves. Each of the rays carries the part of the radiated power.

If it encounters obstacles, the wave is: reflected, refracted, diffracted, or dispersed. At the beginning, all possible routes between the transmitter and the receiver are determined. In several recent years, the largest popularity won two techniques to determine the possible paths of propagation: method of images (image method, IM) and method of the rays shooting (ray lunching, RL). These methods allow you to recreate the three-dimensional spread of the waves by taking into account of losses on the transmitter-receiver road. The accuracy of the two methods depends largely on the number of phenomena that are included in the models. The more the phenomena will be included, we can get more accurate results.

The image method IM lets you designate all possible routes of the signal propagation between the transmitter and the receiver (the center of the pixel) with regard to the phenomena of reflection and transmission. To find a ray route, the mirrors of transmitter relative to the illuminated surrounding surfaces are created. The intersection of the straight line connecting the virtual source and receiving point of the illuminated plane designates the place of reflection of the rays (**Figure 5a**).

In the case of multiple reflections, the following mirrors of virtual source are generated and the algorithm is repeated. The analysis can be carried out in three dimensions, or separately in the vertical and horizontal planes. Method of images allows you to designate the exact routes of the reflected rays. The direction of the rays invading to the obstacle shall be determined according to the Snell's law. Method of images can be used to find the routes of diffracted rays [8].

In the RL method, the created rays are shooting directly from the source. The azimuth (elevation) angle of rays increases gradually at constant values (**Figure 5b**).

For the 3D model at 1°, discretization of both shooting angles more than 32,000 rays are generated. The route of each of the ray is tracked independently of the other. For each of ray is allocated a part of the sphere forming the wave front (**Figure 6b**).

In the simplest solution, an excerpt of the sphere is approximated by a circle. Then, the circle creates the so-called received sphere (**Figure 6a**), in which the ray for 2D model is expressed by (17), and for the 3D model by (18) [8]:

$$R_S = \frac{\gamma \cdot d}{2} \tag{17}$$

$$R_S = \frac{\gamma \cdot d}{\sqrt{3}} \tag{18}$$

where $\gamma$ is the angle between the directions of launching rays and $d$ is the distance the center of the sphere to the signal source.

This method introduces errors of interpretation arising from the limited geometrical possibility of approximation of a sphere by concentric circles. In order to increase the accuracy, portions of a sphere are approximated by the rectangles (**Figure 6**). The sizes of the $\upsilon_i$ and $\psi_i$ determine the coordinates of the launched ray, and $\Delta\psi_i$ and $\Delta\upsilon_i$ are the sides of the rectangle and are described by [8]:

$$\Delta\psi_i(\vartheta_i) = \frac{\Delta\vartheta}{\sin\vartheta_i} \tag{19}$$

$$\vartheta_i = \frac{\Delta\vartheta}{2} + (i-1)\cdot\Delta\vartheta, \qquad i = 1\ldots N_\vartheta, \qquad \Delta\vartheta = const. \tag{20}$$

The intensity of the electric field at the receiving end is the sum of the intensities of all rays, whose distances from a receiving point are less than $R_S$. The direction of the rays, penetrating

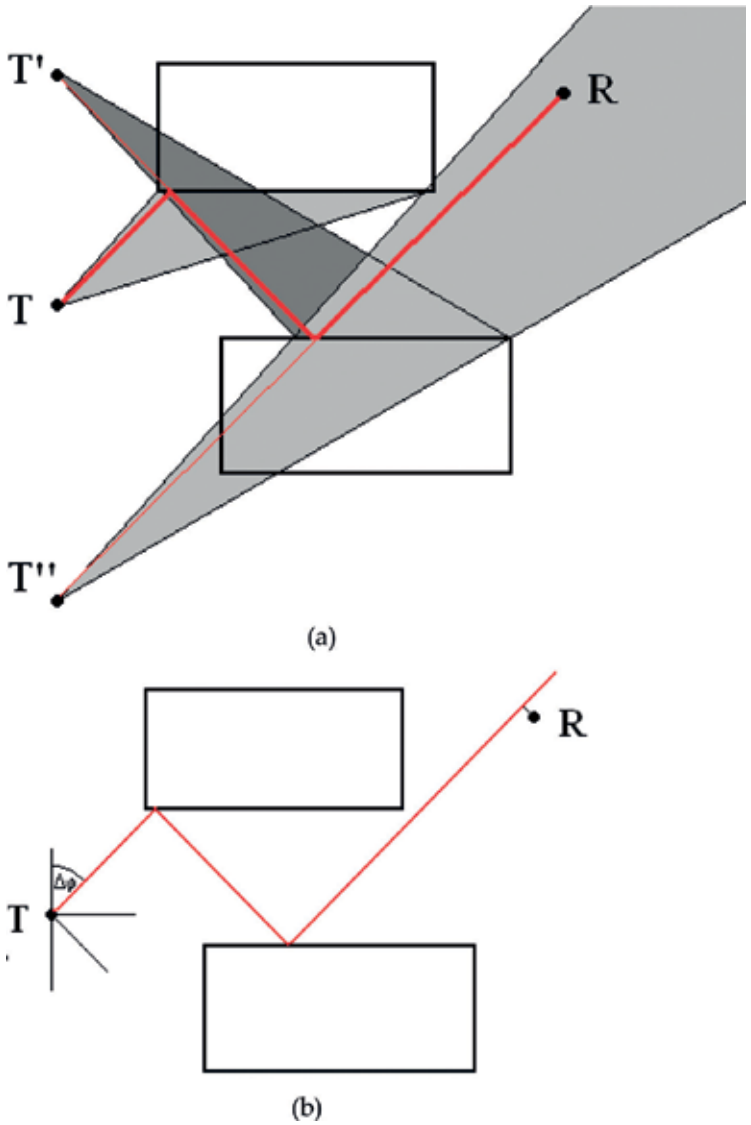


**Figure 5.** Routing of the reflected rays in the method of images IM (a), and routing of the reflected rays in the rays launching R-L method [1].

http://dx.doi.org/10.5772/intechopen.75384

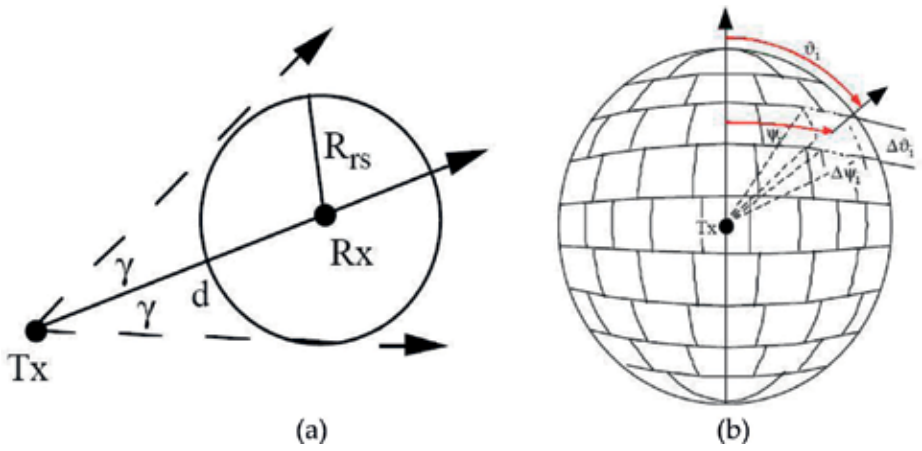


**Figure 6.** Cross-section of the receiving sphere (a) and rays launching method concept (b) [11].

the obstacle shall be determined with the law of Snell. The RL method can be used to find the routes of diffracted rays. The source of diffracted rays may be found when the rectangle (or circle) associated with the ray crosses the diffraction edge [8].

The RL method has a disadvantage in relation to the IM method because it may neglect the very narrow obstacles lying on the extension of transmitter, which can be placed between two rays. To ensure satisfactory resolution of the simulation, the technique of rays splitting RS was introduced, which allows you to split the rays when the radius of the receiving sphere (or side of the rectangle) reaches its maximum size (**Figure 6**).

The RL method is easier to implement with respect to the IM method. It is characterized by the weaker resolution and longer time of computation. Currently, the IM and RL methods are called the ray tracing, RT, method.

In several recent years, research to refine the method of RT has been conducted. Thus the smart method of ray tracing, that is, intelligent ray tracing (IRT) (**Figure 8b**) has been developed. It is based on simple assumptions [10, 14, 15]: (1) only a few rays takes an essential part of the energy of the electromagnetic field, (2) visibility of faces and edges do not depend on the position of the of transmitter antenna, (3) often the bordering receiving points (pixels) are reachable by the rays with a very similar the properties. In accordance with the objectives the calculation were optimized. Pretreatment process of database processing with a collection of information about the obstacles encountered in the model shall be carried out only once. The idea is that each of these obstacles is divided into small pieces called tiles and on the borders in the form of episodes.

Mutual relations of visibility between objects are calculated once and stored in the database. The tiles and the edges are represented only by their center points. The idea of the relationship of visibility center points of the edges or tiles is that if the two center points are in the zone, direct visibility defines the rays from the center of the first tile to the corners of the next one (**Figure 7a**).

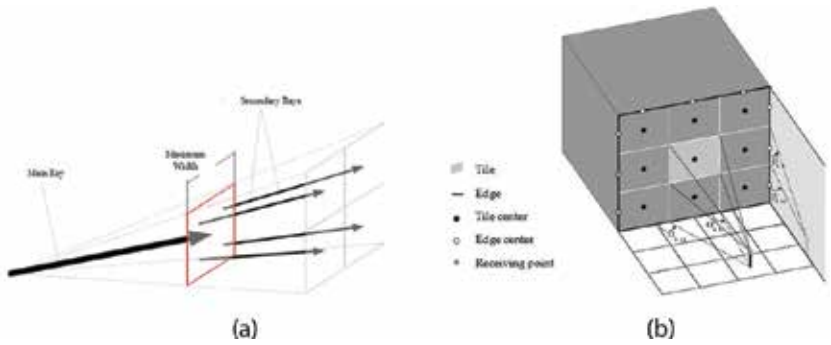


**Figure 7.** The division of the rays in the RT method [12] (a) and the geometry of the inteligent method of ray tracing IRT [10].

These rays and the throw of their angles are data indicating the relationship prevailing between the two center points. Such relationships are created also between edges, as well as in the case of the edge of the tiles. Important are the angles that define the angular distance of possible diffraction and reflection. During the process of routing, the propagation links the information about the relationship of visibility are readily available and you do not need to set dependencies between the obstacles for each ray, which greatly increase the computation speeds [10].

The introduction of the 3D model is associated with the growth of databases and considerable complexity of algorithms. This causes prolongation of the calculation time. To reduce this time, instead of 3D method, the 2 × 2D, so called 2.5D method of modeling has been introduced. In this solution, two independent analyses are carried out: in vertical and horizontal planes [8]. In order to further reduce the calculation time proposed the division of the algorithms in the class due to the number of the relevant phenomena for each of the waves (**Table 2**).

Further increasing the maximum number of, at issue, propagation phenomena takes longer simulation time. In order to reduce calculation time the receiving coverage surface is divided into smaller portions, called the pixels. Each pixel is represented by its center point. The route of the rays is determined only between source and any center point. Increasing the size of the pixels will reduce the resolution of the simulation and the calculation time.

After you specify all the routes between the transmitter and receiver, the components of the electrical field strength $E_i$ at the receiving end originating in from each of the rays are determined [9]:

$$E_i = \frac{\sqrt{Z_0 \cdot P_0 \cdot G_{Ti}(\theta_{Ti}, \varphi_{Ti})}}{4\pi \cdot d_i \cdot L_{Di}(d_i)} \cdot \prod_m D_{mi} \cdot \prod_j R_{ji} \cdot \prod_k T_{ki} \cdot \prod_n e^{-\alpha_{ni} \cdot d_{ni}} \cdot e^{-j\frac{2\pi \cdot d_i}{\lambda}} \tag{21}$$

where $G_{Ti}$ is the energetic gain of receiving antenna for the $i^{th}$ ray, $Z_0$ is the characteristic impedance (≈ 377 Ω), $P_0$ is the power input to the transmitting antenna, $\lambda$ is the of the transmitted wavelength, $d_i$ is the length of the route and of the $i^{th}$ ray, $L_{di}$ is the geometric coefficient depending on the position of the diffraction edge on the route of the $i^{th}$ ray, $D_{mi}$ is the diffraction

| Class of algorithm | Direct ray | Maximum number of reflections in the absence of diffraction | Maximum number of diffraction in the absence of reflections | The maximum number of reflections (o) and diffraction (d) |
|---|---|---|---|---|
| 1 | Yes | — | — | — |
| 2 | Yes | 1 | — | — |
| 3 | Yes | 2 | — | — |
| 4 | Yes | 2 | 1 | — |
| 5 | Yes | 3 | 1 | — |
| 6 | Yes | 3 | 1 | 1 o + 1 d |
| 7 | Yes | 3 | 2 | 1 o + 1 d |
| 8 | Yes | 3 | 2 | 2 o + 1 d |
| 9 | Yes | 4 | 2 | 2 o + 1 d |
| 10 | Yes | 5 | 2 | 2 o + 1 d |
| 11 | Yes | 6 | 2 | 2 o + 1 d |

**Table 2.** Division of algorithms due to the number of the relevant phenomena.

coefficient of $m^{th}$ edge for the $i^{th}$ ray, $R_{ji}$ is reflection coefficient from $j^{th}$ object for the $i^{th}$ ray, $T_{ki}$ is the coefficient for $k^{th}$ border for the $i^{th}$ ray, $\alpha_{ni}$ is attenuation constant of the $n^{th}$ object for the $i^{th}$ ray, and $d_{ni}$ is the length of the route of the $i^{th}$ ray by $n^{th}$ object of attenuation constant of $\alpha_{ni}$.

The intensity of the electric field from the all rays arriving at the receiver is calculated according to the formula [8]:

$$E = \sum_{i=1}^{n} E_i \tag{22}$$

Power $P_R$ delivered by the receiving antenna to receiver depends on the effective area (or the effective length) $A_{SK}$ of the receiving antenna and power density $S$ [8]:

$$P_R = S \cdot A_{SK} = \frac{|E|^2 \cdot A_{SK}}{Z_0} \cdot \sum_i G_{Ri}(\theta_{Ri}, \varphi_{Ri}) \tag{23}$$

where $G_{Ri}$ is a energetic gain of receiving antenna for the $i^{th}$ ray.

The coefficients in the expression (21) are defined by the modeling techniques of propagation phenomena used in the RT method.

In the methods of geometrical optics, GO, reflection phenomenon of reflection of electromagnetic waves describes the Fresnel coefficients, expressing ratios of electromagnetic fields strengths of the reflected (R) and incident (I) waves. The two Fresnel coefficients are different for the EM vectors intensities, namely the parallel and perpendicular components to the plane of incidence. The degree of reflection and transmission of both Fresnel vectors are varying quite different. The plane of incidence is defined as the plane determined by the wave vector of

the incident and the normal to the boundary of separation. **Figure 8** shows the mechanism of the reflection phenomenon [8].

Coefficients of reflection (R) and transmission (T) of both components are expressed by the following expressions [11]:

-the parallel component reflection coefficient

$$R_{II} = \frac{tg\,(\theta_1 - \theta_2)}{tg\,(\theta_1 + \theta_2)} \tag{24}$$

-reflection coefficient of perpendicular component

$$R_{\perp} = -\frac{\sin(\theta_1 - \theta_2)}{\sin(\theta_1 + \theta_2)} \tag{25}$$

-transmission coefficient of the parallel component

$$T_{II} = \frac{2 \cdot \cos(\theta_1) \cdot \sin(\theta_2)}{\sin(\theta_1 + \theta_2) \cdot \cos(\theta_1 - \theta_2)} \tag{26}$$

-coefficient of perpendicular transmission component

$$T_{\perp} = \frac{2 \cdot \cos(\theta_1) \cdot \sin(\theta_2)}{\sin(\theta_1 + \theta_2)} \tag{27}$$

Knowing the material properties of both media: conductivity $\sigma$, permeability $\mu$, and permittivity $\varepsilon$ for an angular frequency $\omega$, we can designate an angle $\theta_2$ using Snell's law [11]:

$$\theta_2 = \arcsin(\sin(\theta_2)) \tag{28}$$

$$\frac{\sin(\theta_1)}{\sin(\theta_2)} = \sqrt{\frac{\mu_2 \cdot \left(\varepsilon_2 - j\frac{\sigma_2}{\omega}\right)}{\mu_1 \cdot \left(\varepsilon_1 - j\frac{\sigma_1}{\omega}\right)}} \tag{29}$$

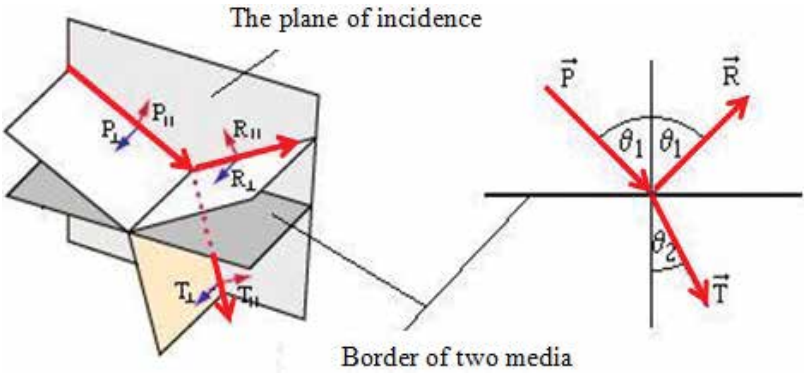


**Figure 8.** The EM wave reflection and transmission phenomenon.

http://dx.doi.org/10.5772/intechopen.75384

In real terms, the walls are constructed of several layers. On each border of the wall layers the wave is splitting on two components, the reflected wave from the surface of layer and transmitted wave to the layer. The result is that the actual coefficients of transmission and reflection depend on the angle of incidence [9].

The incident wave is dissipated as a result of surface roughness. To determine the surface roughness, the criterion of Rayleigh is used [12]:

$$\Delta\varphi = \frac{\pi}{2} \tag{30}$$

where $\Delta\varphi$ is the difference of phase between the two rays as shown in **Figure 9**.

For small angles, the height $H$ of Rayleigh and minimum distance between inequalities $S$ determine the following equations [12]:

$$H = \frac{\lambda}{8 \cdot \theta} \tag{31}$$

$$S = \frac{\lambda}{4 \cdot \theta^2} \tag{32}$$

where $\lambda$ is the length of a scattered wave and $\theta$ is the angle between the incident wave and reflecting plane.

According to the Rayleigh criterion, if the height surface roughness is greater than $H$ and the distance between them is greater than $S$, then consider the surface that causes the dispersion of incident wave [12].

The phenomenon of EM wave scattering can be taken into account by reduction of the reflection coefficients (transmission coefficients are not changed). These coefficients can be multiplied by the value of slightly less than unity, where the exact value depends exponentially on the level of surface roughness calculated in accordance with the theory of Rayleigh:

$$R'_{II,\perp} = R_{II,\perp}\exp\left[-8\left(\frac{\pi \cdot H \cdot \cos\theta}{\lambda}\right)^2\right] \tag{33}$$

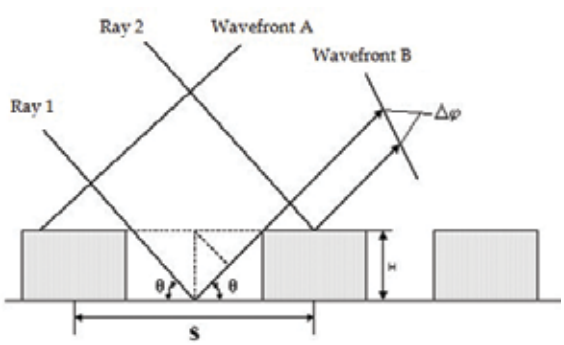


**Figure 9.** Determination of surface roughness [12].

where $R_{II,\perp}$ is the reflection coefficient from the perfectly flat surface, $R'_{II,\perp}$ is the reflection coefficient taking into account the scattering phenomenon, $\lambda$ is the length of the wave, $H$ is the Rayleigh's height, and $\theta$ is the angle of incidence.

Studies have proven that the absorption of the wave by different types of objects (first of all living beings) is very difficult to model. Knowing the obstacle dimensions and material properties: conductivity σ, permeability μ, and ε = ε′- jε″, given the frequency of the EM wave, using a general description of the EM plane wave, we can determine the impact of absorption on changing the wave parameters [11]:

$$U \cdot e^{j\cdot\omega\cdot t} = A \cdot e^{-\alpha\cdot d} \cdot e^{j\left(\omega\cdot t-\beta\cdot d\right)} \tag{34}$$

where $\alpha$ is a attenuation constant, $\beta$ is a phase constant, $U$ is the wave amplitude after absorption, $A$ is the wave amplitude before absorption, $d$ is the dimension of obstacles, and $\omega$ is angular frequency of the wave.

The attenuation constant $\alpha$ and the phase constant $\beta$ are expressed in the following equations [11]:

$$\alpha = \omega \cdot \sqrt{\varepsilon' \cdot \mu'} \cdot \sqrt{\frac{1}{2} \cdot \left[\sqrt{1+\left(\frac{\sigma/\omega + \varepsilon''}{\varepsilon'}\right)^2} - 1\right]} \tag{35}$$

$$\beta = \omega \cdot \sqrt{\varepsilon' \cdot \mu'} \cdot \sqrt{\frac{1}{2} \cdot \left[\sqrt{1+\left(\frac{\sigma/\omega + \varepsilon''}{\varepsilon'}\right)^2} + 1\right]} \tag{36}$$

The ray tracing method RT does not take diffraction into account. In order to model this phenomenon, the deterministic models based on ray tracing method are enhanced with correct techniques. There are several methods for modeling a phenomenon of diffraction: PAW (perfectly absorbing wedge), GTD (geometrical theory of diffraction) and UTD (uniform theory of diffraction). One of the biggest problems of modeling of diffraction is the precise definition of diffraction edges of the buildings and other objects. The most commonly used method is the UTD, which takes into account the wave polarization and the material properties of the diffraction edge. The EM wave coming on the diffraction edge is scattered on a cone whose vertex is at the diffraction point. In **Figure 10a**, the example of a diffraction cone is shown [8].

**Figure 10b** shows the transmission of the ray, which includes the phenomenon of diffraction by means of the UTD method.

The intensity of the electric field at the point of reception can be designated from [13]:

$$E_{UTD} = E_0 \frac{e^{-jks'}}{s'} \cdot D_{II}^{\perp} \cdot \sqrt{\frac{s'}{s+s'}} \cdot e^{-jks} \tag{37}$$

where $E_0$ is the wave field intensity emitted at the transmitting point, $k = \frac{2\cdot\pi}{\lambda}$ is the wave-number, $\sqrt{\frac{s'}{s+s'}}$ sets the geometric relationship necessary for the determination of $L_{Di}$ in an

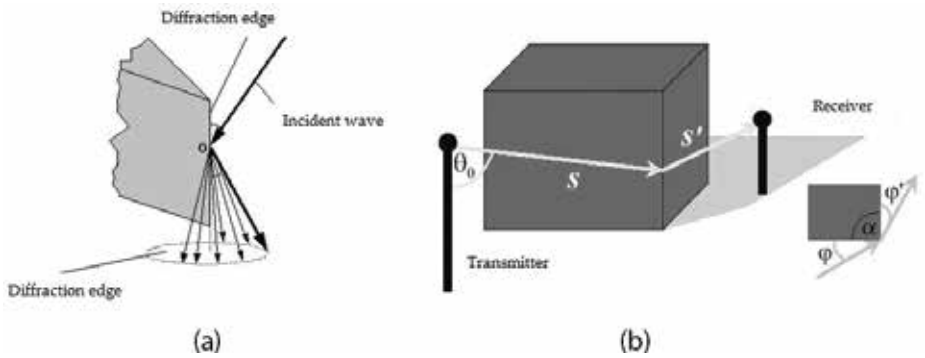


**Figure 10.** Diffraction cone in the UTD method (a) and an example of the radius diffracted on the edge (b) [13].

expression (21), and $D_{II}^{\perp}$ is the diffraction coefficient of the UTD method which is defined as follows [13]:

$$D_{II}^{\perp} = \frac{e^{-j\pi/4}}{2 \cdot n \cdot \sin\theta_0 \cdot \sqrt{2 \cdot \pi \cdot k}} \times (D_1 + D_2 + D_3 + D_4) \tag{38}$$

$$D_1 = \cot\left(\frac{\pi + (\varphi - \varphi')}{2 \cdot n}\right) \cdot F\left(k \cdot L \cdot a^{+}\left(\varphi - \varphi'\right)\right) \tag{39}$$

$$D_2 = \cot\left(\frac{\pi - (\varphi - \varphi')}{2 \cdot n}\right) \cdot F\left(k \cdot L \cdot a^{-}\left(\varphi - \varphi'\right)\right) \tag{40}$$

$$D_3 = R_0^{\perp, II} \cdot \cot\left(\frac{\pi - (\varphi + \varphi')}{2 \cdot n}\right) \cdot F\left(k \cdot L \cdot a^{-}\left(\varphi + \varphi'\right)\right) \tag{41}$$

$$D_4 = R_n^{\perp, II} \cdot \cot\left(\frac{\pi + (\varphi + \varphi')}{2 \cdot n}\right) \cdot F\left(k \cdot L \cdot a^{+}\left(\varphi + \varphi'\right)\right) \tag{42}$$

where $R_n^{\perp, II}$ and $R_0^{\perp, II}$ are the reflection coefficients of sides of diffraction edges at a given EM wave polarization, and $a^{\pm}, \beta^{\pm}, L,$ *and* $F(\cdot)$ (Fresnel transition function) are expressed in the following expressions [13]:

$$a^{\pm}(\beta) = 2 \cdot \cos^2\left(\frac{2 \cdot n \cdot \pi \cdot N^{\pm} - \beta}{2}\right) \tag{43}$$

$$\beta^{\pm} = \varphi \pm \varphi' \tag{44}$$

$$L = \frac{s \cdot s'}{s + s'} \cdot \sin^2\theta_0 \tag{45}$$

$$F(x) = 2 \cdot j \cdot \sqrt{x} \cdot e^{j \cdot x} \int_{\sqrt{x}}^{\infty} e^{-j \cdot \tau^2} \cdot d\tau \tag{46}$$

where $N^{\pm}$ is the integer closest to the fulfillment of the following equations [13]:

$$2 \cdot \pi \cdot n \cdot N^{+} - \left(\varphi \pm \varphi^{'}\right) = \pi \tag{47}$$

$$2 \cdot \pi \cdot n \cdot N^{-} - \left(\varphi \pm \varphi^{'}\right) = -\pi \tag{48}$$

$$n = \frac{2 \cdot \pi - \alpha}{\pi} \tag{49}$$

**Figure 4c** shows the results obtained by RT 3D method. Results were obtained by means of the ACTIX Analyzer computer code [6] for the 10 dBm transmitter power at a frequency of 2.45 GHz.

Method of geometrical optics, GO, is used to model the distribution of electromagnetic fields inside the buildings. On the basis of GO, the computer programs developed are: ACTIX Analyzer (by ACTIX) [6], WinProp (by AWE) [10], WiSE (by Lucent Technologies), Wireless InSite (by Remcom) [33], Cindoor (by Cantaberia University, Spain), Volcano (by Siradel) [28], and SitePlanner (by Motorola), and others for designing the indoor and outdoor wireless communication systems.

## 5. Review of computer programs for wireless networks planning

The EM wave propagation models presented previously have been used in computer programs for planning wireless communication networks. The most commonly used method is the ray tracing RT. Methods based directly on the Maxwell's equations (e.g., FDTD) have not adopted in the design of wireless networks inside buildings, they are rather more attractive for outdoor propagation scenes simulation (e.g., Wireless InSite by Remcom [33]). An empirical model most commonly used in computer programs is a non-linear model of multi-walls MW developed within the framework of the COST 231 project and adopted in the ITU Recommendation. The one slope I-S model is not the exact and therefore rarely used, while the dominant path model (D-P) is difficult to implement. Showcased programs allow you to simulate for the frequency range from 0.05 to about 300 GHz. **Table 3** summarizes the basic characteristics of the mostly used computer programs.

In addition to the presented programs on the market, there are several third-party products. These include, for example, Volcano (Siradel) [28], ADTI ICS online [29], iBWAVE DE [30], TAP™MAPPER [31], SitePlanner (Motorola), EDX Signal Pro (EDX Wireless Technologies) [32], CelPlanner™ [34], etc. The commercial computer solvers of the EM wave propagation models are complemented by the computer tools implemented by academic centers. The examples are the program I-Prop (Technical University of Prague, Czech Republic) [3], Cindoor (University of Cantaberia, Spain), etc.

| | ACTIX Analyzer | Wireless InSite | WiSE | WinProp | I-Prop |
|---|---|---|---|---|---|
| **Firm** | **ACTIX An Amdocs Company** | **Remcom** | **Lucent Technologies** | **AWE Communications** | **Czech Technical University in Prague** |
| Frequency (GHz) | 0.3/300 | 0.05/40 | */ | >0.6 | */ |
| Propagation models | - MW<br>- 2.5D RT<br>- 3D RT | - 2.5D RT<br>- 3D RT | - 2.5D RT<br>- 3D RT | - OS<br>- Linear MW<br>- Non-linear MW<br>- D-P<br>- 3D RT<br>- 3D IRT | - OS<br>- Non-linear MW |
| Modeled phenomenon | - Reflection<br>- Diffraction<br>- Absorption | - Reflection<br>- Diffraction<br>- Absorption<br>- Dispersion | - Reflection<br>- Diffraction<br>- Absorption | - Reflection<br>- Diffraction<br>- Absorption | - Absorption |
| Parameters of materials | - Permittivity ε | - Permittivity ε<br>- Conductivity σ | - Permittivity ε<br>- Conductivity σ | - Permittivity ε<br>- Conductivity σ<br>- Attenuation L (for D-P model) | - Attenuation L |
| Result of the simulation | - The EM power<br>- Delay<br>- The angular span the rays received<br>- Interference<br>- The range of access points | - The EM power<br>- Change of power in time<br>- Delay<br>- The angular span the rays received<br>- Interference<br>- The range of access points | - The EM power<br>- Change of power in time<br>- Delay<br>- The range of access points | - The EM power<br>- Delay<br>- The angular span the rays received<br>- Interference<br>- The range of access points<br>- Transmission speed | - The EM power<br>- The range of access points |
| The characteristics of the codes | - Possibility of introducing the own propagation models<br>- Data base of people and trees models<br>- To take into account the depolarization<br>- Dynamic simulations (of receivers mobility) | - Data base of trees models<br>- Incorporate of phase of received rays<br>- The application of FDTD method (only in urban environments)<br>- Simulation of power changes in time | - Multi-layer structure models | - The applicability of the IRT model<br>- Simulation of the impact of the environment on the system parameters<br>- The ability to compare with the results of the measurements | - The ability to compare with the results of measurements |

*No details.

**Table 3.** Basic characteristics of mostly used the EM wave propagation modeling computer programs.

The EM wave propagation models presented allow you to streamline the process of designing wireless networks of mobile communication systems like WLAN, Bluetooth RFhome, ZigBee, and WPAN inside buildings as well as the outdoor urban environment. Allow you to specify

the most appropriate location of access points and their minimum number of required covering a given area. In the case of a large diversification of the propagation environment (e.g., shopping center) it is recommended that you use the more accurate but at the same time dealing with more time simulation based on deterministic models.

## 6. Planning for wireless communication networks

Planning of the wireless communication systems, for example, LAN and PAN is not simple. Committed design errors can significantly reduce its final performance. Each project is influenced by many factors, which makes the implementation of ready-made scenarios not useful and, as a result, affecting the final result. Due to the complexity of the implementation of projects, short-range wireless networks can be divided into three stages: preparation of the data to the project, the design and implementation of the project and the measurements. Each phase requires the use of an appropriate approach, since errors made in any one of them can undermine efforts in working on the project. **Figure 11** shows the proposed design algorithm [16, 17].

### 6.1. Data preparation for the project

Preparation of the data to the project is an important part of planning wireless networks, because the mistakes made at this stage influence the next steps to the implementation of a wireless network. At the stage of the initial project, you must obtain the following information: range of communication system, number and locations of the supported users (or devices), their mobility, and types of used applications. You need to collect and draw up the technical documentation, the design area and parameters the obstacles which prevent the propagation of electromagnetic waves. Knowledge of the infrastructure of an existing wired network will allow the use of it in a wireless network in the project as a bridge/transition to the users of different communication systems. Based on these data and the financial capacity of the client, we select the appropriate wireless network technology. Most popular solutions for WPAN is the Bluetooth system, and in the case of the WLAN, the IEEE 802.11 standard [16].

### 6.2. Collection and development of technical documentation

The first step in the initial stage is to collect and develop the technical documentation of the design area. On its basis in the design phase, the environment model used in simulations of the EM wave distribution power is built. You must specify the obstacles parameters properties which prevent the propagation of electromagnetic waves, such as location, geometrical shape and dimensions, and material properties (conductivity $\sigma$, permeability $\mu$, and permittivity $\varepsilon$).

### 6.3. Define assumptions of the project

In the initial stage, we need to gather information about the range of the proposed network, estimated the number and location of users (or devices) and their mobility as well as a traffic profile. To do this, you must carry out a survey or environmental interview. In the case of a

http://dx.doi.org/10.5772/intechopen.75384

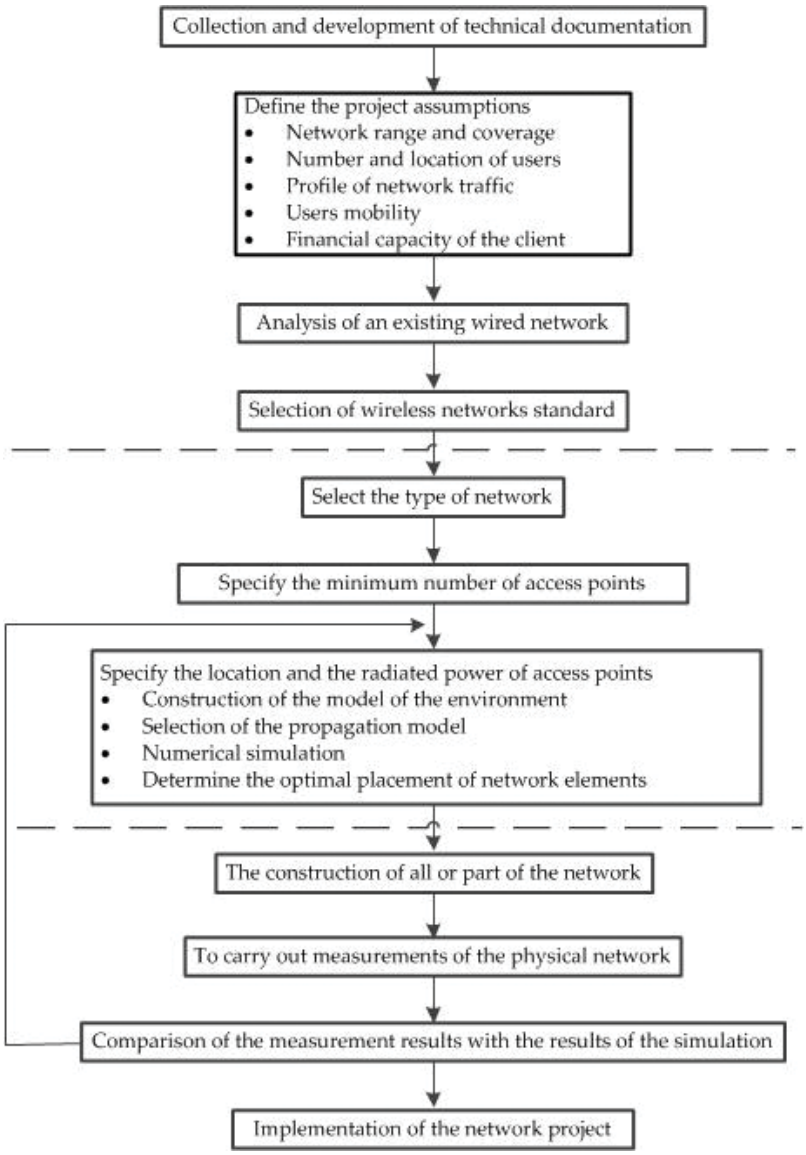


**Figure 11.** Design algorithm of wireless communication networks.

wireless network project such as the alarm system or multimedia communication, you should refer to the specification of a specific system. On the basis of specific requirements and expectations, you must specify the maximum number of simultaneous connections, which is to ensure the proposed network. Fixed number should be greater than the estimated number of calls occurring most of the time (e.g., by 95% of the time within 1 hour). In order to facilitate the analysis and take into account the diversity of needs of all traffic, it is divided into three categories: video a1/a2/a3-duplex services (video conferencing – MPEG4

| Area | Degree of coverage [%] | Number of concurrent connections | | | Mobility | Communication with another network | System selection |
|---|---|---|---|---|---|---|---|
| | | Video $a_1/a_2/a_3$ | Audio $a_4/a_5$ | Data $a_6$ | | | |
| 1 | 90 | 1/2/0 | 8/6 | 34 | + | + | IEEE 802.11 g |
| 2 | 90 | 0/0/0 | 0/2 | 8 | – | + | Bluetooth |
| 3 | 100 | 0/0/0 | 0/0 | 22 | – | – | ZigBee |

**Table 4.** A set of project assumptions of sample wireless communication system [17].

640 × 480 25 frames per sec)/unilateral (streaming MPEG-4, 640 × 480, 25 frames/sec)/ unilateral (streaming-MPEG 2, 720 × 576, 25 frames/sec); audio a4/a5-duplex services (voice chat-g.711)/unilateral (streaming-G. 711), and data a6-FTP, mail, Web, p2p [18]. Mobility users understand the need to move to the area covered by another cell of the network while preserving the connection. This is possible only when both access points are on the same subnet. Often it is not possible to provide coverage of the entire area or associated it with a big financial effort. Therefore, network design requires that you specify the degree of its coverage. In the situation of the area covered with a mesh wireless sensors (e.g., alarm burglar alarm or fire), 100% coverage is required. In the case of the area in which users can easily move (e.g., WLAN at the airport) you can accept less coverage, for example, 90%. It happens that the collected information is not the same throughout the area. This is due to the characteristic features of the area (e.g., conference room or the library of the University). You then need to separately specify the design intent for each of the specific areas.

**Table 4** provides a set of project assumptions sample wireless system for the Bank. The project provides for the 3 areas: (1) area 1 – lobby, corridors, rooms (providing access to the network of the Bank); (2) area 2 – Conference Room (multimedia presentations setup); and (3) area 3-around doors and windows (network sensors of high security locks).

### 6.4. Analysis of exiting wire network

In most cases, wireless networks are designed as an extension to the wired LAN. Then you should be familiar with the topology and the capabilities of the network. It is important to specify the ability to increase her workload resulting from the join of the proposed wireless network, and the ability to support its security mechanisms (e.g., VPN network, IEEE 802.1 X authentication). Analysis of the wired network topology allows you to specify the possible spots to join the proposed network. On the basis of the initial information, we select for each of the areas of wireless technology.

## 7. Network design and simulation

The next step in the process of deploying a wireless network is a design phase. At this stage, on the basis of the information gathered in the initial phase of the project is created. The design phase is discussed on the example of Bluetooth and IEEE 802.11 b/g wireless systems.

http://dx.doi.org/10.5772/intechopen.75384

### 7.1. Selecting the type of network

The first step in the design phase is to select the type of network. There are two main types of network: range coverage and capacitive. Range coverage wireless network designs due to the largest coverage with the fewest number of access points. In this type of networks not optimizes to *QoS* parameters. It is assumed that users will benefit from the services of low-speed of packet transmission (e.g., barcode scanning and database query). These installations are used in warehouses or retail stores for inventory control and purchasing in real time purchases. An example of a range coverage network is a wireless sensors network of anti-theft system. You can deploy the range coverage WLAN networks in small- and medium-sized companies instead of wired Ethernet. When designing the capacitive network to ensure QoS parameters is required, that is, capacity, duration, and variation of delay as well as a bit error rate, *BER*. The sizes of the cells in the capacity networks are smaller, which means that the system must be equipped with a greater number of access points. The size of the cells is determined based on the number of users supported by a single access point. The maximum number of users that are associated with the access point is determined on the basis of the type of services to be available on the network.

### 7.2. Specifying the minimum number of access points

Specifying the minimum number of access points is extremely difficult. The problem is due to complications related to the precision of the estimates of the anticipated traffic generated by the users in the proposed wireless network. This, in turn, makes it difficult to estimate the impact of the number of users on the access point load, and thus the determination of areas of coverage. The Bluetooth system is designed for the implementation of broadcast audio and data. It provides a guarantee of quality of the services offered by granting higher priority connections audio relative to data transmission. Moreover a movement within pico-network is coordinated by the Master device, which eliminates the problem of collisions of packages. Therefore, to ensure the quality of the services offered on the network based on Bluetooth system comes down to minimize the probability of overloading. It is implemented by specifying the maximum number of connections the devices associated with one access point on the basis of the type of generated traffic. For this purpose, referred to in the previous stage of the types of traffic are attributed to the following the weight: audio $w_4/w_5$–2/1, − date $w_6$–1. The sum of the products of consecutive weights by the number of connections does not exceed the value of the $O_B = 7$ for one Master Bluetooth system [19]:

$$\sum_{i=4}^{6} w_i \cdot a_i \leq 7 \tag{50}$$

This value results from the specification of the Bluetooth system (7 slots).

IEEE 802.11 networks analysis is more complicated [20–22]. In the case of this type, the effective capacity decreases with each client connected. The DCF access mechanism provides equitable access to BSS. To ensure the quality of the services offered on the network based on IEEE 802.11 g comes down to minimize the probability of overloading. It is implemented by

specifying the maximum number of connections the devices associated with one access point on the basis of the type of generated traffic. For this purpose, referred to in the previous stage of the types of traffic is attributed to the following weights: video $w_1/w_2/w_3$–7/3.5/10, audio $w_4/w_5$–2/1.5, data $w_6$–1. The sum of the products of consecutive weights by the number of connections does not exceed the value of the $O_I = 22$ for one AP of IEEE 802.11 g network:

$$\sum_{i=1}^{6} w_i \cdot a_i \leq 22 \tag{51}$$

The minimum number of devices needed to cover a given area determines the quotient of the sum of the weights by the numbers subsequent connections in that area by the maximum load of the access point. For the Bluetooth ($L_B$) and WLAN ($L_I$) systems the minimum number of access points is an expression (rounding up):

$$L_{B\,or\,I} = \frac{\sum_{i=4\ or\ 1}^{6} w_i \cdot a_i}{O_{B\ or\ I}} \tag{52}$$

## 8. Implementation of the project

Determination of the optimal location for the deployment of the wireless system access points is a result of the consideration of the position resulting from the numerical simulation of the EM propagation models, as well as taking into account the experimental verification, under real conditions, of the implemented project. In most cases, wireless networks are designed as an extension to the wired LAN. Typically, the access points connect to the LAN network through a combination of their Ethernet cable UTP 5e with the appropriate port of the switch. This combination allows, in addition to access to this network, extension of the existing security in wireless network on the security available in a wired network above all security protocols related to virtual private networks VPN and authentication protocols such as 802.1 X [16, 17].

The information provided has been used to design a wireless network multimedia transmission in the building C-5 Faculty of Electronics the Wroclaw University of Science and Technology (**Figure 12**).

### 8.1. Propagation model selection

Before start of the simulation examined, the usefulness of various propagation models available in the ACTIX ANALYZER computer code [6], in order to select the most suitable for the present environment, compares the results of the propagation models: non-linear multi-wall, MW (COST 231), 2.5D, and 3D models.

**Figure 12** shows the model of the ground floor of the building C-5 of the selected location for the access point, and **Figure 13a–c** – the EM radio wave propagation simulation results using different propagation models for the transmitted power − 10 dBm, and frequency - 2.45 GHz.

http://dx.doi.org/10.5772/intechopen.75384

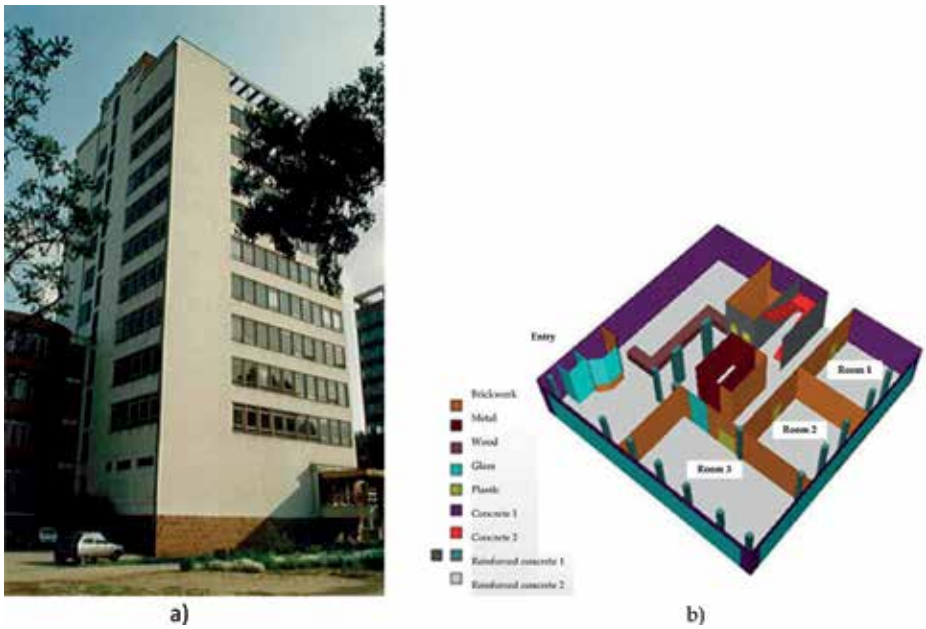


**Figure 12.** Photo of the Wroclaw University of Science and Technology building C-5 (a) and the numerical model of the ground floor with use of defined construction materials an example (b).

Simulations were performed on a computer with an AMD Athlon processor, XP 2000+, and 768 MB of RAM. The duration of the simulation depends on the specific case and propagation model parameters. With the same propagation models parameters settings, the shortest time 1 s of simulation was obtained for MW model, 7 minutes and 14 seconds for the 2.5 RT model, and 16 minutes and 33 seconds for the 3D RT model. The ratio between the durations of the simulation the tested models also depends on the specific example. In the present environment MW model due to metal elevator shaft cannot be used, which is an obstacle for electromagnetic wave (**Figure 13**). In this case, the direct rays of the electromagnetic waves in the MW model are shielded. Comparison of simulation results 2.5D and 3D RT models has shown that theoretically worse 2.5D RT model almost in no way inferior the 3D version, but the computation time is two times longer. In highly complex environments with a large number of obstacles, the 2.5 RT model can be too big simplification, then you must apply the 3D model.

### 8.2. Deployment of network devices

A number of simulation based on 2.5D and 3D RT models, the objective of which was to find the optimal deployment of WLAN AP points in the room 1, and the Bluetooth access points in rooms 2 and 3 implementing the project. The 2.5D RT model used in power distribution simulations on the ground floor. On the basis of simulation, it was found that for the area on one floor you must put only one AP of 10 dBm radiated power, mounted at a height of 3 m. The WLAN AP locations on the ground floor and the simulation results the EM wave power distribution is shown in **Figure 14**.

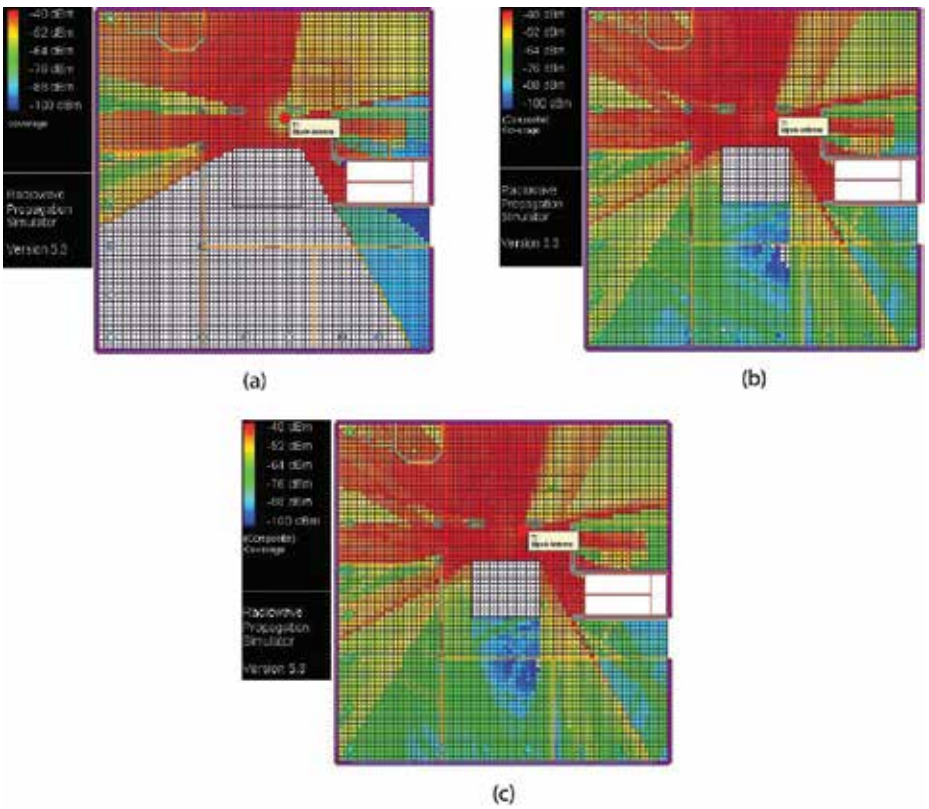


**Figure 13.** The simulation results of signal power distribution in a MW model (a), the 2.5 D RT model (b), and the 3D RT model (c) for radiated power 10 dBm at f = 2.45 GHz on the ground floor of building C-5 of WRUoS&T.

You have selected the points where the power values shown in **Table 5** were read.

Empty areas in the grid of receivers (e.g., inside an elevator shaft) indicate areas where signal strength is lower than the established system sensitivity (−94 dBm for IEEE 802.11 g). Model of a lift shaft turned out to be a screen for electromagnetic waves. Analysis of the simulation results showed that the AP does not cover the whole floor area. AP coverage areas on adjacent floors enough overlap to provide users with the ability to change the AP without losing the connection to the network. Analysis of the results of the simulation of power distribution showed that the vast majority of the coverage area, it is possible to obtain the maximum transmission speed of 54 MB/s.

Bluetooth network simulations were carried out for the room 3 (lecture halls on the ground floor). Assume that the master devices are PCs placed on desks lecture halls at a height of 1 m above the floor. The Bluetooth access point locations in the room 1, on the ground floor, and the simulation results of the EM wave power distribution are shown in **Figure 14b**. The power values selected read at points are shown in **Table 5**. Simulations have shown that full coverage has been achieved already at the radiated power 4 dBm of access points (class 2). Pico networks areas overlap themselves which allows you to combine them to form a distributed

http://dx.doi.org/10.5772/intechopen.75384

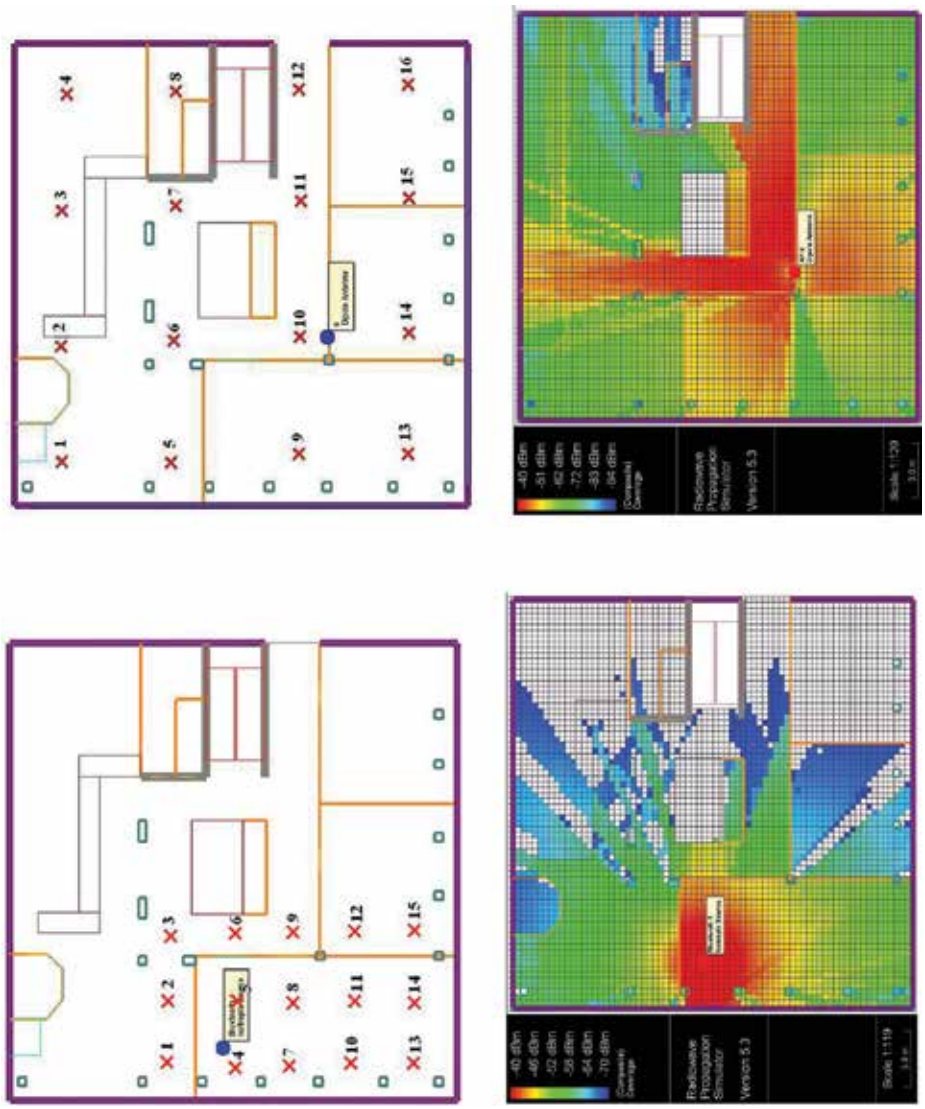

**Figure 14.** Distribution of AP IEEE 802.11 g (a), the simulation results of EM wave power distribution (b), the arrangement of the master point of Bluetooth system (c), and the simulation results for the room 3 on the ground floor of building C-5.

network, which will consist of a device with 3th pico network. Because the area of these networks covers part of the corridor in front of the entrance to each of the rooms, it is possible to move users between meeting rooms without losing the connection.

### 8.3. Calculation of the interference impact

Selected Bluetooth and IEEE 802.11 g systems work in this same frequency 2.4 GHz band ISM (*Industry Scientific Medicine*). In addition, in IEEE 802.11 g are the only three non-overlapping

| Parameter | | Value | Attention |
|---|---|---|---|
| RL | Range of elevation (°) | −90/90 | The full range |
| | Angular resolution in elevation (°) | 1 | |
| | Azimuth angle range (°) | 0/360 | The full range |
| | Angular resolution in azimuth (°) | 1 | |
| | Maximum distance between the rays (m) | 0.1 | |
| Maximum number of reflections | | 2 | |
| Maximum number of penetration | | 2 | |
| Maximum number of diffraction | | 1 | |
| Minimum signal level (dBm) | | −94 | IEEE 802.11 g |
| | | −70 | Bluetooth |
| Maximum number of rays on the route of the transmitter-receiver | | 4 | Negligible impact of the rest of the rays |
| Frequency (GHz) | | 2.45 | |
| Transmitting antenna power gain (dBi) | | 2.2 | Half-wave dipole |
| Receiving antenna power gain (dBi) | | 0 | Isotropic antenna |
| Suspended height of receiving/transmitting antennas (m) | | 1/3 | |
| Size of the receivers grid sets (m) | | 0.3 | |

**Table 5.** The2.5D and 3D RT propagation models parameters applied in the simulation.

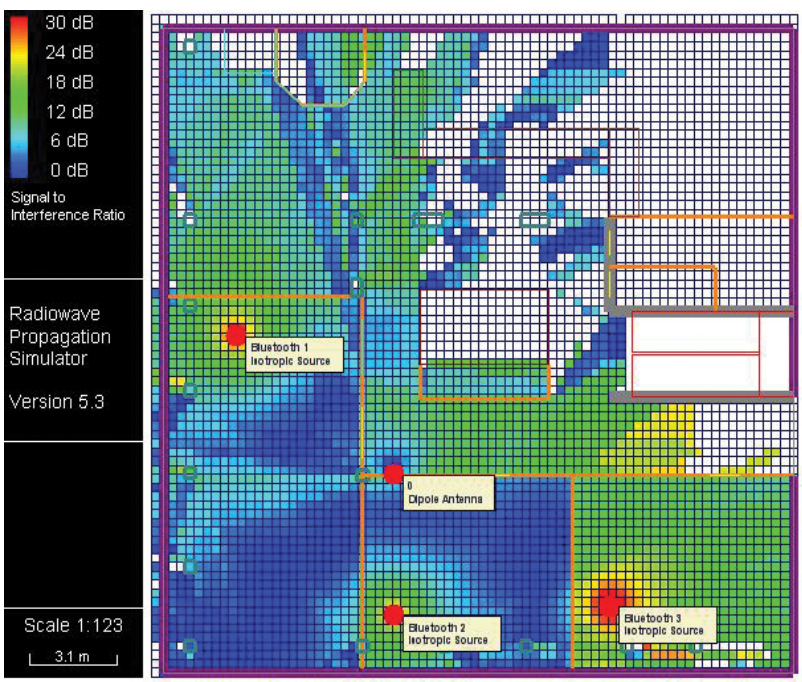


**Figure 15.** Levels of interference between Bluetooth and IEEE 802.11 g systems on the ground floor of the C-5 building.

http://dx.doi.org/10.5772/intechopen.75384

channels. Therefore, in order to evaluate the possibility of the coexistence of Bluetooth and IEEE 802.11 g systems, and the impact of inter-system interference in both systems, a number of simulations were carried out. For 10 WLAN AP in the network, each frequency channel repeats at least three times. For one AP per each floor on the same frequency channels, AP will work every 3rd floor. The ACTIX ANALYZER program allows you to estimate the level of interference on a given area. Selected is the dominant transmitter and then calculated the ratio of the power of its signal to the power of the signals of the other transmitters. The result is expressed in dB. The simulations allowed said there are no significant interference inside the WLAN system for room one.

Interference between Bluetooth and IEEE 802.11 g systems can affect the work of the two systems. **Figure 15** shows the interference between AP (*EIRP* = 10 dBm) located on the ground floor and three Bluetooth master devices (*EIRP* = 4 dBm) forming 3 piconets in the halls 1, 2, and 3.

The analysis of the results indicates a strong interference signal, above all within the hall 2 and 3. In view of the above, the project should examine methods that co-exist in both systems at the same time and space.

### 8.4. Impact of humans in the area of Bluetooth and WLAN systems operation

The ACTIX Analyzer program allows you to simulate taking into account the impact of the people on the EM wave propagation phenomenon. To do this, in the propagation model of the environment are inserted the human models (**Figure 16a**) recognized as the additional obstacles for the EM waves. In ACTIX Analyzer, it is possible to scale the standard human model in order to obtain models representing people of different growth. The man is a complicated living organism and it is difficult to simulate its effects on electromagnetic field. However, studies have shown that the best substance simulating human tissue (a large generalization) is a solution of water with salt in varying degrees of saturation depending on the conditions in question. In the project to simulate human tissue, the solution about the contents of the 4 gram NaCl per liter of water has been chosen. The properties of the substance at frequency 2.4 GHz are $\varepsilon' = 77$ and $\varepsilon'' = 13$ ($\varepsilon = 77\text{-}j13$) [14]. **Figure 16b** shows the arrangement of a dozen models of people on the ground level of building C-5 to simulate their effects on the AP IEEE 802.11 g (area 1) and the Bluetooth master device in the areas 2 and 3. **Figure 16c** shows the results of the simulation taking into account and without taking into account the impact of people on the network coverage in the area 1 with the active AP IEEE 802.11 g networks on the ground floor of the C-5. The AP parameters are set as in previous simulations. The analysis of the results showed that the presence of people on the route of the transmitter-receiver can significantly degrade received power. In order to reduce the impact of humans on the power level of the received signal, install access points so that the route of the transceiver as little as possible was divided by areas with a high concentration of people.

**Figure 16d** shows the results of the simulation, taking into account the impact of people on the network coverage in the area 3 with the active Master device in the Bluetooth system # 3. The analysis of the results shows that the people have a strong effect on the propagation of the signal in the pico-network. In the case of a large number of people in the room radiated power

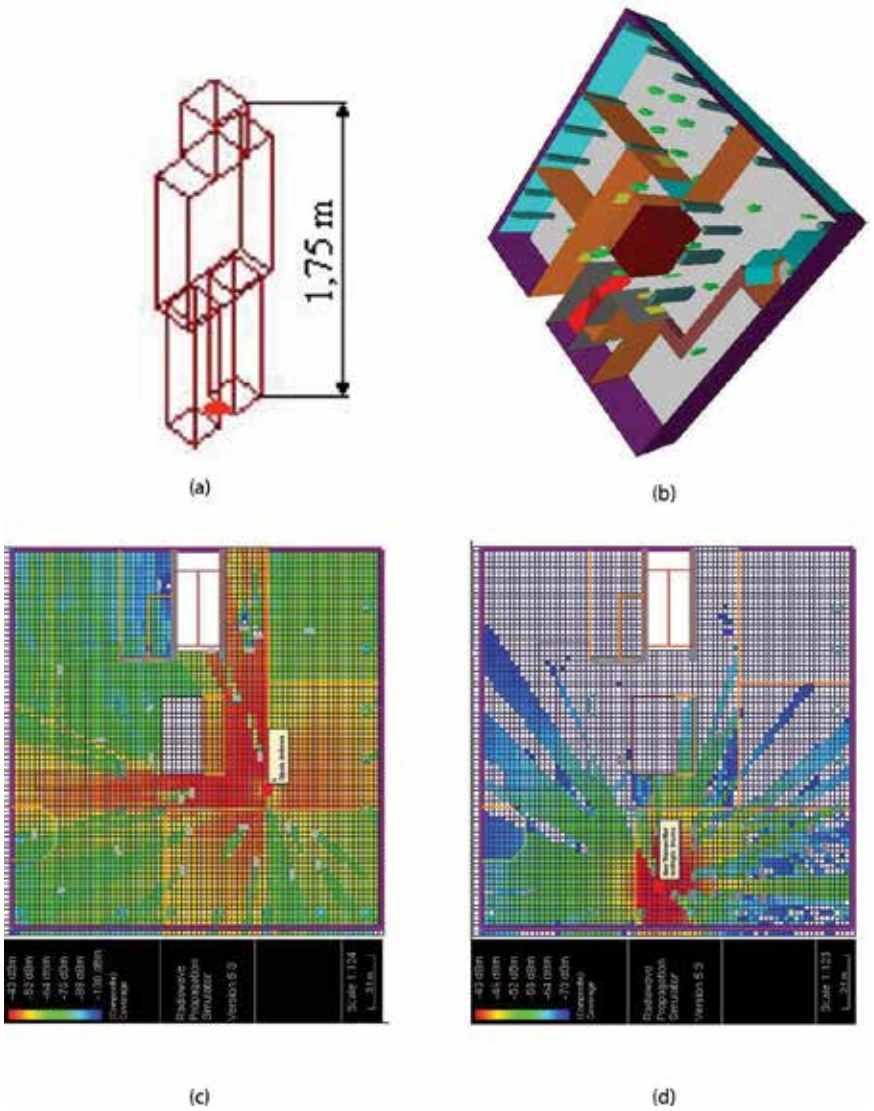


**Figure 16.** The deployment of several human models (a) on the ground floor (b) of the C-5 to simulate their effect on the extent of IEEE 802.11 g (c) and Bluetooth networks (d).

of 4 dBm of master is insufficient to cover the entire area (room 3). Therefore, rooms 2 and 3 are applied the master of first class-Bluetooth system with a higher maximum radiated power.

## 9. Conclusion

The EM wave propagation models presented allow you to streamline the process of designing wireless networks of mobile communication systems like WLAN, Bluetooth RFhome, ZigBee, and WPAN inside buildings as well as the outdoor urban environment. Allow you to specify

the most appropriate location of access points and their minimum number of required covering a given area. In the case of a large diversification of the propagation environment (e.g., shopping center) it is recommended that you use the more accurate but at the same time dealing with more time simulation based on deterministic models.

This chapter presents the concepts, methods, and algorithms that were used to design a wireless system for indoor as well as outdoor mobile communication systems. The project supported simulations carried out using ACTIX Analyzer computer code. Indoor propagation environment is very complex (reflection, diffraction, refraction, etc.) while maintaining high accuracy digital model was built. In most cases, reduce the applied version of computer code that are not influenced significantly on the simulation results. A very interesting option of simulation is possibility taking into account of the impact of humans on the propagation of the signal. Typically, wireless networks are used in places with a high concentration of people (e.g., airports, universities, hotels, libraries, etc.) that is why skipping in simulations of the impact people can turn out to be a very serious mistake.

Designed a network allows users to wireless access in the building of the C-5 to the Internet and Intranet networks of the Wroclaw University of Science and Technology based on the IEEE 802.11g standard. It also allows the implementation of data transfer and audio and video connections with the guarantee of quality of offered services. For conference and lecture-seminar rooms, a separate network of Bluetooth system to ensure that the combination of elements of the multimedia presentations setups is designed. Part of the position includes a host computer, multimedia projectors, cameras, sound system, printers, monitors, wireless microphones, and listeners equipment (e.g., laptops, palmtops, and mobile phones).

## Acknowledgements

It is my pleasure to thank of my former MSc student Piotr Horbatowski for his valuable contribution to the presented topics.

## Author details

Wojciech Jan Krzysztofik

Address all correspondence to: wojciech.krzysztofik@pwr.edu.pl

Department of Telecommunication and Teleinformatics, Faculty of Electronics, Wroclaw University of Science and Technology, Wybrzeze Wyspianskiego, Wroclaw, Poland

## References

[1] Krzysztofik WJ, Horbatowski P. Design of the WLAN and WPAN wireless networks inside buildings - propagation models. Telecommunication Review & Telecommunication News. LXXX, Nr 7/2007:221–231. ISSN 1230–3496

[2] Wesołowski K. Mobile Radio Communication Systems. Warszawa, Poland: WKŁ; 2003

[3] I-Prop Computer Code User Manual [Internet]. 2018. Available from: www.i-prop.cz; https://customer.active24.com/

[4] ITU-R M.1225 Recommendation, Guidelines for Evaluation of Radio Transmission Technologies for IMT-2000, Geneva, Switzerland; 1997

[5] Wölfle G. Propagation Models for Indoor Radio Network Planning Including Tunnels, Millennium Conference on Antennas & Propagation, Davos, Switzerland; 2000

[6] ACTIX ANALYZER, The World's First Multi-Vendor Desktop Analytics Solution for Mobile Networks [Internet]. 2018. Available from http://actix.com/analyzer

[7] Sarkar T, Jl Z, Kim K. A survey of various propagation models for mobile communication. IEEE Antennas and Propagation Magazine. 2003;**45**(3):51-82

[8] Cichon D, Kürner T. COST 231 Final Report, Chapter 4, Propagation Prediction Models; 1996

[9] Staniec K. The indoor radio wave propagation modeling in ISM bands for broadband wireless systems [PhD. Thesis]. Wroclaw, Poland: Wroclaw University of Science and Technology; 2006

[10] WinProp - Propagation Modelling, Method of Optical Rays, Different Scenarios, 2D and 3D Models, Empirical and Ray-Optical, Planning & Simulation, Coverage & Capacity, Cellular & Broadcasting. [Internet] 2018, Available on: https://altairhyperworks.com/product/FEKO/WinProp-Propagation-Modelinghttps://altairhyperworks.com/product/FEKO/WinProp—Indoor-and-Campus

[11] Bansal R, editor. Fundamentals of Engineering Electromagnetics. Boca Raton, FL USA. ISBN-10: 0-8493-7360-3: CRC Press, Taylor & Francis Group; 2006

[12] Popescu I. Neural network applications for radio coverage studies in mobile communication systems [Ph.D. Thesis]. Romania: Polytechnic University Timisoara; 2003

[13] Aryanfar F. Modelling of wireless channels and validation using a scaled MM-wave measurement system [Ph.D. Thesis]. Ann Arbor, USA: University of Michigan; 2004

[14] Krzysztofik W, Horbatowski P. Propagation Models used for WLAN Design Inside Buildings, KKRRiT 2006, The National Conference on Radiocommunication, Radio- and TV-Broadcasting, Poznan, Poland; 2006

[15] Hoppe R, Wertz P, Landstorfer FM, Wolfle G. Advanced ray optical wave propagation modelling for urban and indoor scenarios including wideband properties. Transactions on Emerging Telecommunications Technologies. 2003;**14**(1):61-69

[16] Horbatowski P. The systems of communication and multimedia services in the mobile business and tourism based on wireless access of BLUETOOTH and/or WLAN standards [Thesis]. Wroclaw, Poland: Wroclaw University of Science and Technology; 2006

[17] Krzysztofik WJ, Horbatowski P. Design of the WLAN and WPAN wireless networks inside buildings – examples of realization. Telecommunication Review & Telecommunication News, LXXX, Nr 10/2007:878-895. ISSN 1230–3496

[18] Ganz A, Ganz Z, Wongthavarawat K. Multimedia Wireless Networks-Technologies, Standards and QoS. USA: Prentice Hall PTR; 2003. ISBN-13: 978-0130460998

[19] Bluetooth SIG, Bluetooth Core Specification version 6.0, USA; July 2017

[20] Riverbed Modeler (old name: OPNET Modeler®) Computer Code Users Manual [Internet]. 2018. Available from: www.riverbed.com

[21] Lai Z, Villemaud G, Luo M, Zhang J. Radio propagation modelling, Chapter 2 in book. In: Chu X, Lopez-Perez D, Yang Y, Gunnarsson F, editors. Heterogeneous Cellular Networks - Theory, Simulation, and Deployment. The Edinburgh Building, Cambridge, UK: Cambridge University Press; 2012

[22] Salous S. Radio Propagation and Channel Modelling. River Street Hoboken, NJ, United States: John Wiley & Sons, Ltd. ISBN: 978-1-118-50232-7. DOI: 10.1002/9781118. March 2013, Available online: http://onlinelibrary.wiley.com/book/10.1002/9781118502280

[23] Pagani P, Talom FT, Pajusco P, Uguen B. Ultra-Wideband Radio Propagation Channel: A Practical Approach. River Street Hoboken, NJ, United States: John Wiley & Sons, Ltd. ISBN: 978-1-848-21084-4; Jan. 2009

[24] Primak S, Kontorovich V. Wireless Multi-Antenna Channels: Modeling and Simulation, Wiley Series on Wireless Communication and Mobile Computing. Vol. 28. River Street Hoboken, NJ, United States: John Wiley & Sons, Ltd. ISBN: 978-1-119-96086-7; Oct. 2011

[25] Fontain EP, Espineira PM. Modelling the Wireless Propagation Channel: A Simulation Approach with MATLAB, Wiley Series on Wireless Communication and Mobile Computing. River Street Hoboken, NJ, United States: John Wiley & Sons, Ltd. ISBN: 978-0-470-75173-2; Sep. 2008

[26] Roche G, Alayon-Glazunov A, Allen B. LTE-Advanced and Next Generation Wireless Networks: Channel Modeling and Propagation. River Street Hoboken, NJ, United States: John Wiley & Sons, Ltd. ISBN: 978-1-118-41101-8; Nov. 2012

[27] Yin X, Cheng X. Propagation Channel Characterization, Parameter Estimation, and Modelling for Wireless Communication. River Street Hoboken, NJ, United States: John Wiley & Sons, Ltd., IEEE Press. ISBN: 978-1-118-18826-2; Sep. 2016

[28] Volcano Propagation Model is a Renowned Radio Propagation Modeling Software Available Worldwide in the Leading Commercial Radio Planning Tools, and in SIRADEL's Standalone Platform Smart City Explorer. Available on: https://www.siradel.com/software/

[29] ADTI ICS online Share your Network and Radio Planning [Internet]. Available on: http://www.atdi.com/ics-online/

[30] iBWAVE DE iBwave Design, the Industry Standard for Designing Indoor Wireless Networks. 2018. [Internet], Available on: http://www.ibwave.com/ibwave-design

[31] TAPTMMAPPER, Terrain Analysis package, RF Path Preview and Quick Coverage Analysis, Worldwide Terrain, Land Cover, and Building Data Access, Multi-Site Simulcast and Area Coverage Analysis, [Internet]. 2017. Available on: http://www.softwright.com/

[32] EDX® SignalPro®, is a Comprehensive and Fully Featured RF Planning Software Suite Offering all the Study Types Needed to Design Wireless Networks, Including; Area Studies, Link/Point-to-Point Studies, Point-to-Multipoint and Route Studies [Internet]. 2018, Available on: http://edx.com/products/edx-signalpro/

[33] Wireless InSite® is a Suite of Ray-Tracing Models and High-Fidelity EM Solvers for the Analysis of Site-Specific Radio Wave Propagation and Wireless Communication Systems. The RF Propagation Software Provides Efficient and Accurate Predictions of EM Propagation and Communication Channel Characteristics in Complex Urban, Indoor, Rural and Mixed Path Environments [Internet]. 2018. Available on: https://www.remcom.com/wireless-insite-em-propagation-software/

[34] CelPlanner™, Software for Planning & Designing Wireless Communication Systems. 2018 [Internet]. Available on: http://www.celplan.com/products/celplanner.asp

Chapter 6

# Multi-Elliptical Geometry of Scatterers in Modeling Propagation Effect at Receiver

Jan M. Kelner and Cezary Ziółkowski

Additional information is available at the end of the chapter

http://dx.doi.org/10.5772/intechopen.75142

**Abstract**

In the proposed chapter, the authors present a geometric-statistical propagation model that defines three groups of received signal components, i.e., direct path, delayed scattering, and local scattering components. The multi-elliptical propagation model, which represents the geometry of scatterer locations, is the basis for determining the delayed components. For the generation of the local components, a statistical distribution is used. The basis for this model is a power angular spectrum (PAS) of the received signal, which is closely related to a type of propagation environment and transmitter-receiver spatial positions. Therefore, we have an opportunity to evaluate the influence of the environment type and an object motion direction on the basic characteristics such as envelope distribution, PAS, autocorrelation function, and spectral power density. The multi-elliptical model considers the propagation phenomena occurring in the azimuth plane. In the chapter, we will also show the 3D extension of modeling effects of propagation phenomena.

**Keywords:** radio wave propagation, propagation modeling, channel modeling, geometric-based model, multi-elliptical model, multi-ellipsoidal model, scattering, angular power spectrum, angle spread, angular dispersion, directional antenna pattern, power delay profile, simulation

## 1. Introduction

A development of information and communication systems is characterized by a dynamic increase in demand for the provision of telecommunication services with the participation of wireless networks. A limitation of frequency resources forces the search for new methods of effective spectrum management. One of the solutions to this problem is spatial multiplexing of network access, which minimizes a field strength and increases access area of the network.

IntechOpen

© 2018 The Author(s). Licensee IntechOpen. This chapter is distributed under the terms of the Creative Commons Attribution License (http://creativecommons.org/licenses/by/3.0), which permits unrestricted use, distribution, and reproduction in any medium, provided the original work is properly cited. CC BY

This solution is based on the use of an active phased array antenna (APAA) or massive APAA and is applicable to emerging fifth generation (5G) systems. In these systems, the multiple use of the same frequency bands is qualified by no interference between individual wireless links. Fulfillment of this condition has a large impact on received signals, properties of which significantly depend on a direction of reaching an electromagnetic wave to a reception point. This means that the prediction, modeling, and evaluation of statistical properties of the receipt direction play an important role in assessing internal and external conditions of a compatible operation of wireless networks. This fact justifies the purposefulness of topics presented in this chapter.

The goal of the chapter is to describe the methods for determining the statistical properties of the signal reception angle and its parameters. Particular attention is given to an impact analysis of directional antenna parameters on the statistical parameters and characteristics that describe dispersion of reception angle. The main purpose of this chapter is based on geometric propagation models in which scatterer locations are determined by multi-elliptical curves or multi-ellipsoidal surfaces.

Due to a method of determining the statistical characteristics of a reception angle, propagation models can be divided in accordance with the diagram presented in **Figure 1**.

Measurement data and standard distributions such as the Gaussian, Laplacian, logistic, and von Mises distribution are the basis for empirical models that directly describe a probability density function (PDF) of angle of arrival (AOA) [1–3]. In this case, developing a model consists in such adjustment of distribution parameters that will ensure minimization of approximation error to the measurement data. For the first three models mentioned above, the approximation problem comes down to determining the normalizing constant and parameters that define these distributions [1]. For the von Mises distribution [4], the approximation consists in adjusting a single parameter, which simplifies the procedure of creating the statistical model of the reception angle distribution [1].

In practice, complex empirical models are used. They use standard distributions to describe the statistical properties of individual angular clusters. Examples of such models are defined, i.e., by the WINNER projects [5] and 3rd Generation Partnership Project (3GPP) [6, 7]. The

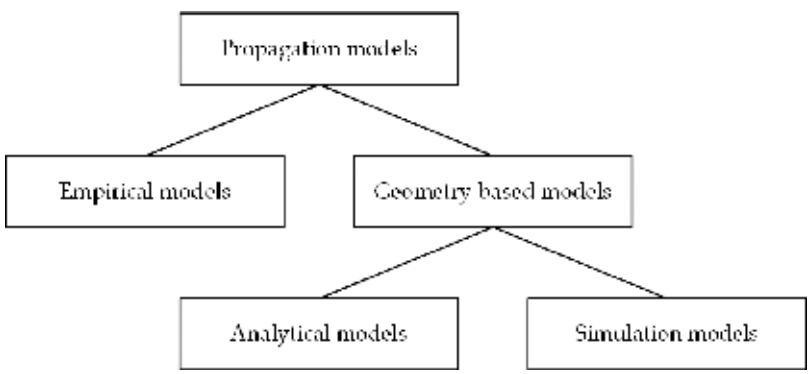


**Figure 1.** Classification of propagation models due to method of determining statistical properties of reception angle.

http://dx.doi.org/10.5772/intechopen.75142

main disadvantages of these models are the lack of consideration of antenna pattern influence and distance between a transmitter (Tx) and receiver (Rx).

These disadvantages do not have geometrical models. These models are defined by geometrical structures that determine positions of elements scattering an electromagnetic wave. Knowledge of propagation environment geometry gives the possibility to determine the signal reception directions. This task can be carried out analytically or through simulation research.

The use of geometrical optics is one of the basic methods of determining AOA, which considers the geometric structure of propagation environment. A ray tracing is practical implementation of this propagation modeling method [8–12]. The accuracy of the obtained results depends to a large extent on the accuracy of mapping electrical properties of all elements forming the electromagnetic environment and the number of generated rays. The difficulty of obtaining environmental data and the complexity of simulation procedures are the reason for limited reliability of the results obtained by this method. A concept of propagation paths [13] gives the possibility of simplifying the ray-tracing method. In this case, the analysis comes down to an evaluation of propagation paths in the presence of scattering elements (scatterers) whose position on the plane (two-dimensional (2D) modeling) or in space (three-dimensional (3D) modeling) maps specific geometric structures.

A shape of scatterer occurrence areas, their position relative to the Tx and Rx locations, and a density distribution are the criteria that differentiate individual models. For the 2D areas, geometric structures such as a circle [5, 6, 14–16], ellipse [15, 16], hollow disk [17], and elliptical disk [18] are most commonly used. In the case of 3D, the scatterer areas represent a sphere [19], semi-spheroid [20, 21], clipping semi-spheroid [22], semi-ellipsoid [23], cylinder [24, 25], and complex solid figures, for example, bounded ellipsoid and elliptical cylinder [26] or sphere and ellipsoid [27].

The density of the scatterers is another criterion that differentiates the individual geometric models. The uniform distribution is most widely used to describe spatial concentration of the scattering elements, especially with regard to limited geometrical structures, e.g., [14, 15, 22, 28–30]. For models where the scatterer occurrence area is unrestricted, the normal distribution is used, e.g. [4, 22, 31].

The area geometry and density of the scatterer occurrence give the possibility to determine the approach directions of the propagation paths to the Rx. However, the practical use of the geometric models to assess the statistical properties of the reception angle is largely hampered. This fact results from the lack of a relationship between the geometry of these models and transmission properties of the propagation environment. These properties are described by a channel impulse response and related characteristics such as a power delay profile (PDP) or power delay spectrum (PDS). Nevertheless, in the set of all models, we can distinguish geometrical structures whose parameters are defined by the channel transmission characteristics. Multi-elliptical and multi-ellipsoidal propagation models are these special cases. Consideration of the relationship between the transmission parameters and geometrical structures ensures minimization of the approximation error between measurement data and modeling results.

This chapter is devoted to the evaluation of the statistical properties of the scattering, a reception angle, and the effects of this phenomenon, which has a significant impact on correlational and spectral properties of the received signals. The multi-elliptical and multi-ellipsoidal propagation models are the basis for the analysis presented in the chapter.

## 2. Environment transmission properties and propagation model geometry

Statistical evaluation of the radio channel transmission properties is based on the energetic measures of the received signals. PDPs and PDSs describe powers and delays of individual components that reach the Rx. An example of PDP, $P(\tau)$, defined by 3GPP [7, Table 7.7.2–2] is shown in **Figure 2**. In this case, the PDP represents non-line-of-sight (NLOS) conditions, urban macro (UMa)-environment type with delay spread, $\sigma_\tau = 363$ ns which is characteristic of the carrier frequency, $f_0 = 2$ GHz.

The PDP graph shows that the received signal is a superposition of component groups that form time clusters with different delays. Measurement results presented in a literature justify the following assumptions:

- Components that undergo single scattering have a dominant energetic significance.
- The probability of the scatterer occurrence seen from the Tx is the same in every direction.
- For each element, the statistical properties of scattering factor module and phase are the same.

Thus, all signal components that arrive at the Rx with the same delay come from the scatterers located on the same ellipsoid. This means that the number of the ellipsoids that represent the scatterer locations is equal to the number of the time clusters. Their foci determine the Tx and Rx positions.

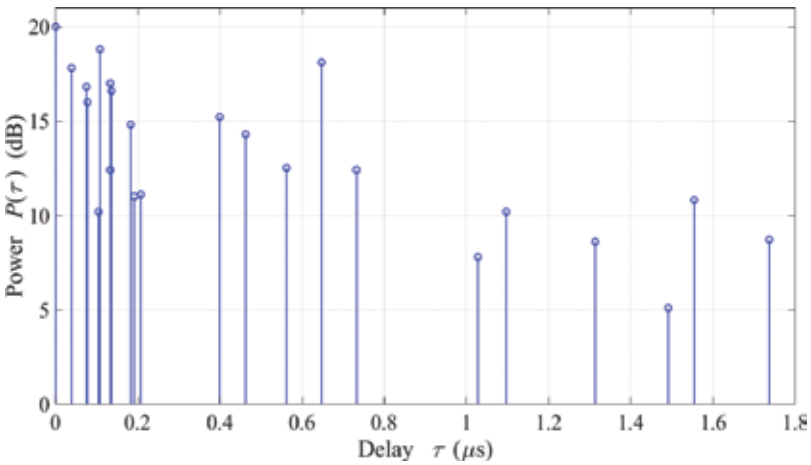


**Figure 2.** Example of PDP for UMa NLOS 2 GHz environment from 3GPP.

http://dx.doi.org/10.5772/intechopen.75142

For majority of wireless links, relations between heights of the Tx ($h_T$)/Rx ($h_R$) antennas and their distance, $D$, meet a condition, $h_T, h_R \ll D$. In the case of ground wave propagation, this condition is the basis for reduction of the scattering areas to semi-ellipsoids. The use of the antennas, whose radiation patterns are narrow in the elevation plane, brings the 3D to 2D modeling. For these conditions, the multi-ellipsoidal model is reduced to the multi-elliptical model of scattering areas, as shown in **Figure 3**.

The delays of the individual time clusters, $\tau_i$ for $i = 1, 2, \ldots, N$, define the parameters of the corresponding semi-ellipsoids. For the $i$th semi-ellipsoid, we have

$$a_i = \frac{1}{2}(D + c\tau_i), \quad b_i = c_i = \frac{1}{2}\sqrt{c\tau_i(2D + c\tau_i)} \tag{1}$$

where $c$ is the speed of light.

Each time cluster is the superposition of the signal components that reach the Rx from the scatterers located on the respective semi-ellipsoids. The reception directions of these components

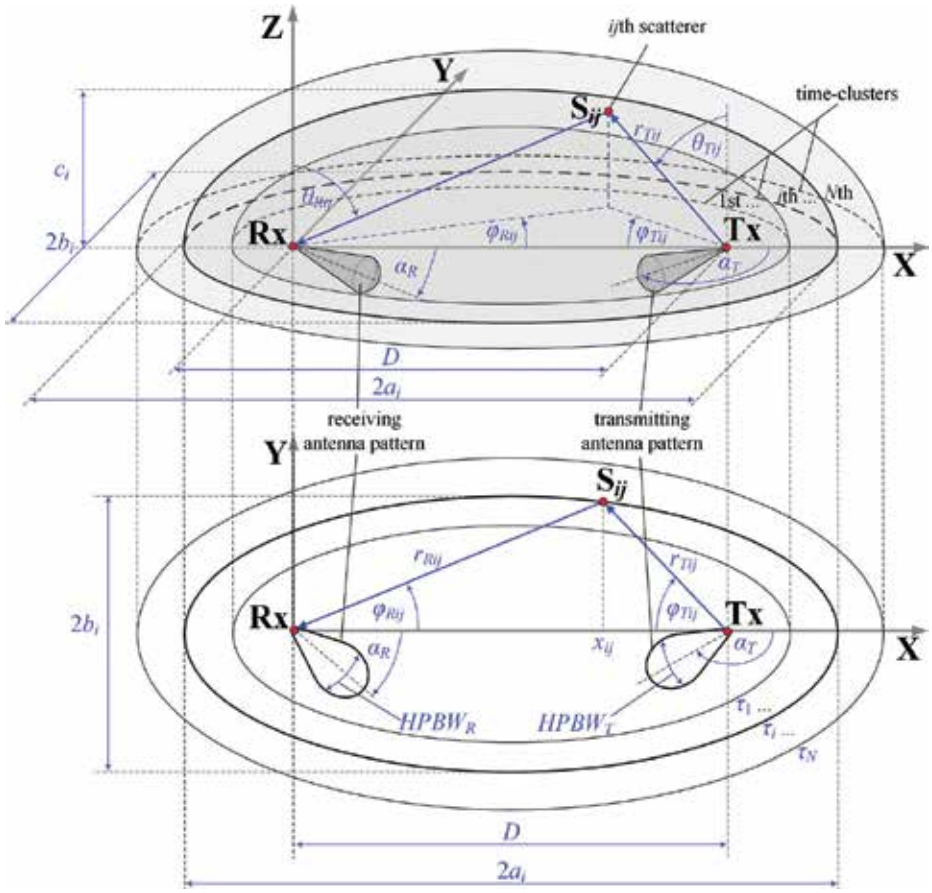


**Figure 3.** 3D and 2D models of scattering areas.

are determined by the shape of the scatterer occurrence surface. This means that the powers of the individual clusters depend on the propagation path direction to the Rx. Differentiation of the cluster delays is the basis for expressing a power angular spectrum (PAS) as a sum of the component powers reaching the Rx with the delays, $P_R(\theta_R, \varphi_R)$, and the component powers, $P_{R0}(\theta_R, \varphi_R)$, whose delays are of the order of a carrier wave period. The first and second groups of components are called the delayed and local scattering components, respectively.

The delayed components are grouped in the time clusters. Therefore,

$$P_R(\theta_R, \varphi_R) = \sum_{i=1}^{N} P_{Ri}(\theta_R, \varphi_R) + P_{R0}(\theta_R, \varphi_R) \tag{2}$$

where $N$ is the number of the time clusters (semi-ellipsoids) and $P_{Ri}(\theta_R, \varphi_R)$ means the PAS of the propagation paths that reach the Rx from the $i$th ellipsoid.

The PAS can be presented as the product of a total power and PDF of AOA [32]. We should also note that $P_{R0}(\theta_R, \varphi_R)$ represents the sum of the powers of the direct path component and the local scattering components. The energy relationship between these components describes the Rice factor, $\kappa$. Thus, we can present the PDF of AOA, $f_R(\theta_R, \varphi_R)$, which describes the statistical properties of the signal reception angle, in the following form:

$$\begin{aligned} f_R(\theta_R, \varphi_R) &= f_d(\theta_R, \varphi_R) + f_l(\theta_R, \varphi_R) + f_{dp}(\theta_R, \varphi_R) \\ &= \sum_{i=1}^{N} \frac{P_i}{P} f_i(\theta_R, \varphi_R) + \frac{\kappa}{1+\kappa} \frac{P_0}{P} f_0(\theta_R, \varphi_R) + \frac{1}{1+\kappa} \frac{P_0}{P} \delta(\theta_R, \varphi_R) \end{aligned} \tag{3}$$

where $f_d(\theta_R, \varphi_R)$, $f_l(\theta_R, \varphi_R)$, and $f_{dp}(\theta_R, \varphi_R)$ represent parts of $f_R(\theta_R, \varphi_R)$ corresponding the delayed scattering components, local scattering components, and direct path component, respectively, $P$ is the total power of the received signal, $P_i$ is the power of the propagation paths reaching the Rx from the $i$th ellipsoids, $f_i(\theta_R, \varphi_R)$ means PDF of AOA for the $i$th ellipsoids, $P_0$ represents the power of the components reaching the Rx with negligible delay, $f_0(\theta_R, \varphi_R)$ is PDF of AOA for the local scattering components, and $\delta(\cdot)$ is the Dirac delta function.

For the delayed components, the multi-ellipsoidal or multi-elliptical structures are the basis for the analytical or simulation determination of individual $f_i(\theta_R, \varphi_R)$, $i = 1, 2, \ldots, N$. In the case of the local scattering, a large diversity of receiving antenna surroundings prevents adoption of a determined geometry of the scatterer positions. To adapt the statistical properties of reception angle, the von Mises distribution is used [4].

Construction of the multi-ellipsoidal or multi-elliptical structures based on PDP/PDS ensures adjustment of the reception angle statistical characteristics to the transmission properties of the propagation environment. In that, these models provide a mapping of the impact of these properties on the correlational and spectral characteristics of the received signals.

The correctness of the adopted model is confirmed by comparative analyses with empirical data presented, among others, in [33–36]. From these analyses, it appears that the multi-elliptical model provides the smallest errors of PAS and PDF of AOA approximation to other geometric and empirical models. The correctness of the adopted model is confirmed by comparative analyses with empirical data presented in, e.g., [37].

## 3. Multi-elliptical propagation model

The use of the antennas with the narrow radiation patterns in the elevation plane limits an environment influence on the received signal properties. Propagation phenomena predominance in the azimuth plane is the premise for reducing the analysis of the reception angle statistical properties to the 2D modeling problem. In this case, the mapping of the propagation phenomena is ensured by the multi-elliptical propagation model. Precursors of this model are Parsons and Bajwa, who presented a multi-elliptical way of modeling the distribution of the propagation paths in [38].

### 3.1. Analysis of reception angle statistical properties for omni-directional antennas

A PDF of AOA analysis for radio links with omni-directional antennas is based on the 2D geometric structure shown in **Figure 3**. In this case, Eq. (3) shows that determining the PDF of AOA for the delayed components comes down to determining $f_i(\varphi_R)$.

Propagation path lengths, i.e., $r_{Tij}$ and $r_{Rij}$ (see **Figure 3**), which describe the distances $\overline{TxS_{ij}}$, respectively, are

$$r_{Tij} = a_i - e_i x_{ij} \quad \text{and} \quad r_{Rij} = a_i + e_i x_{ij} \tag{4}$$

where $e_i = D/(2a_i)$ means the eccentricity of the $i$th ellipse and $x_{ij}$ is coordinate of $S_{ij}$.

But $x_{ij}$ is a function of $\varphi_{Tij}$ and $\varphi_{Rij}$:

$$x_{ij} = r_{Tij}\cos\varphi_{Tij} + \frac{D}{2} \quad \text{and} \quad x_{ij} = r_{Rij}\cos\varphi_{Rij} - \frac{D}{2} \tag{5}$$

Considering that $r_{Tij} + r_{Rij} = 2a_i$ and substituting Eq. (5) to Eq. (4), we can write

$$\frac{1}{1 + e_i\cos\varphi_{Tij}} + \frac{1}{1 - e_i\cos\varphi_{Rij}} = \frac{4a_i}{2a_i - De_i} \tag{6}$$

After transforming Eq. (6), the formula of $\cos\varphi_{Tij}$ versus $\cos\varphi_{Rij}$ has the form [32]:

$$\cos\varphi_{Tij} = \frac{2a_i\cos\varphi_{Rij} + De_i\cos\varphi_{Rij} - 2D}{2a_i + De_i - 2D\cos\varphi_{Rij}} \tag{7}$$

According to the assumptions, the statistical properties of angle of departure (AOD) describe a uniform distribution, i.e., $f_i(\varphi_T) = (2\pi)^{-1}$ for $\varphi_T \in \langle -\pi, \pi)$. Hence, PDF of $\cos\varphi_T$ is

$$f_i(\cos\varphi_T) = f_i(\varphi_T)\left|\frac{\mathrm{d}\varphi_T}{\mathrm{d}(\cos\varphi_T)}\right| = \frac{1}{2\pi}\frac{1}{\sqrt{1-\cos^2\varphi_T}} \quad \text{for} \quad \varphi_T \in \langle -\pi, \pi) \tag{8}$$

Because $\cos\varphi_T$ is a function of $\cos\varphi_R$, so after considering Eq. (7) and Eq. (8), we get [32]:

$$f_i(\cos\varphi_R) = f_i(\cos\varphi_T)\left|\frac{\mathrm{d}(\cos\varphi_T)}{\mathrm{d}(\cos\varphi_R)}\right| = \frac{1}{2\pi}\frac{1}{|\sin\varphi_R|}\frac{\sqrt{(2a_i + De_i)^2 - 4D^2}}{2a_i + De_i - 2D\cos\varphi_R} \quad \text{for} \quad \varphi_R \in \langle -\pi, \pi) \tag{9}$$

Hence, the demanded form of $f_i(\varphi_R)$ is

$$f_i(\varphi_R) = f_i(\cos\varphi_R)\left|\frac{\mathrm{d}(\cos\varphi_R)}{\mathrm{d}\varphi_R}\right| = \frac{1}{2\pi}\frac{1-e_i^2}{1+e_i^2-2e_i\cos\varphi_R} \quad \text{for} \quad \varphi_R \in \langle -\pi, \pi) \tag{10}$$

Eventually, the PDF of AOA for all delayed components, $f_d(\varphi_R)$, takes the form [37]:

$$f_d(\varphi_R) = \sum_{i=1}^{N}\frac{P_i}{P-P_0}f_i(\varphi_R) = \frac{1}{2\pi}\sum_{i=1}^{N}\frac{P_i}{P-P_0}\frac{1-e_i^2}{1+e_i^2-2e_i\cos\varphi_R} \quad \text{for} \quad \varphi_R \in \langle -\pi, \pi) \tag{11}$$

From Eq. (11), it follows that $f_d(\varphi_R)$ depends significantly on $P_i$ and $a_i$, i.e., on the major axis of each ellipse. This means that properties of this function are determined by the power distribution of the individual time clusters, which is closely related to the transmission properties of a given propagation environment.

### 3.2. Reception angle dispersion for directional antennas

For directional antennas used in radio links, the evaluation of the reception angle statistical properties is based on simulation tests. In this case, an input data processing algorithm is the basis for the research procedure, which ensures the determining basic parameters and statistical characteristics of AOA. The purpose of simulation studies is to determine a set of pairs $\left(\varphi_{Rij}, p_{Rij}\right)$ that represent the angles and powers of the individual propagation paths reaching the Rx. The analysis of the obtained set is the basis for the assessment of the AOA statistical properties. The relationship between the multi-elliptical structure of the scatterer positions and the environmental transmission characteristics ensures that the simulation results coincide with empirical results.

A procedure scheme of determining $\varphi_{Rij}$ and $p_{Rij}$ is shown in **Figure 4**.

In the first step of the procedure, the multi-elliptical model parameters are determined based on PDP/PDS. In the next step, the propagation path AODs are generated using the power radiation pattern of the transmitting antenna. For the normalized power pattern, $g_T^2(\varphi_T)$ is

$$\int_{-180^\circ}^{180^\circ} g_T^2(\varphi_T)\,\mathrm{d}\varphi_T = 1 \quad \text{and} \quad g_T^2(\varphi_T) \geq 0 \tag{12}$$

This means that the normalized power radiation pattern meets PDF axioms. Thus, the normalized pattern of the transmitting antenna is used as the PDF of AOD, $f_T(\varphi_T)$:

$$f_T(\varphi_T) = \frac{1}{2\pi} g_T^2(\varphi_T) \quad \text{for} \quad \varphi_T \in \langle -\pi, \pi) \tag{13}$$

For the Gaussian model of the Tx antenna radiation pattern [39]:

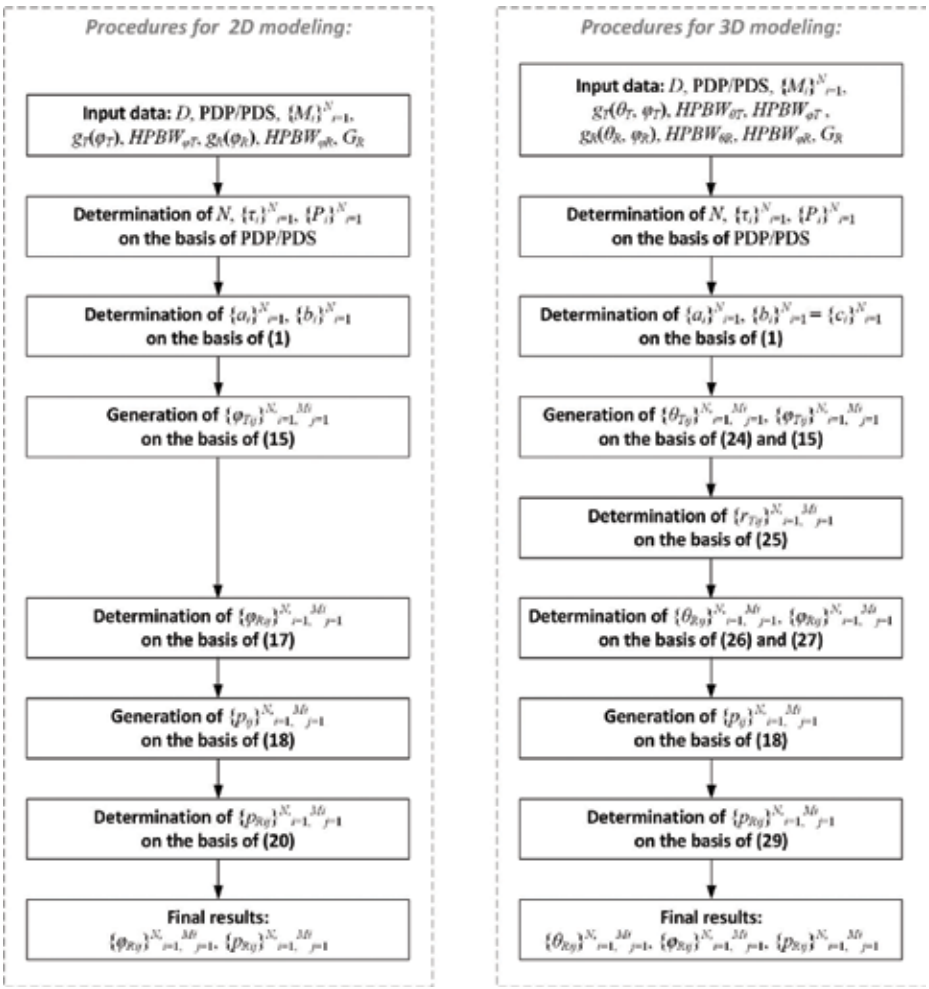


**Figure 4.** Procedure for determining AOAs and powers of propagation paths for multi-elliptical (2D) and multi-ellipsoidal (3D) propagation model.

$$g_T(\varphi_T) = C_0 \exp\left(-\frac{\varphi_T^2}{2\sigma_{T\varphi}}\right) \quad \text{for} \quad \varphi_T \in \langle -\pi, \pi), (C_0 - \text{normalizing constant}) \tag{14}$$

we have

$$f_T(\varphi_T) = C_{T\varphi} \exp\left(-\frac{\varphi_T^2}{\sigma_{T\varphi}}\right) \quad \text{for} \quad \varphi_T \in \langle -\pi, \pi) \tag{15}$$

where $C_{T\varphi} = \left(\int_{-180^\circ}^{180^\circ} f_T(\varphi_T)\mathrm{d}\varphi_T\right)^{-1} = \left(\sqrt{\pi}\sigma_{T\varphi}\mathrm{erf}\left(\pi/\sigma_{T\varphi}\right)\right)^{-1}$, $\sigma_{T\varphi} = HPBW_{T\varphi}/\left(2\sqrt{\ln 2}\right) \cong 0.6$ $HPBW_{T\varphi}$, and $HPBW_{T\varphi}$ is half power beam width (HPBW) of the transmitting antenna in the azimuth plane.

Eq. (15) is the basis for the AOD generation. A relationship between AOD and AOA results from the ellipse properties [32]:

$$\cos\varphi_{Rij} = \frac{2e_i + \left(1 + e_i^2\right)\cos\varphi_{Tij}}{1 + e_i^2 + 2e_i\cos\varphi_{Tij}} \tag{16}$$

Hence [40]:

$$\varphi_{Rij} = \mathrm{sgn}\left(\varphi_{Tij}\right)\arccos\left(\frac{2e_i + \left(1 + e_i^2\right)\cos\varphi_{Tij}}{1 + e_i^2 + 2e_i\cos\varphi_{Tij}}\right) \tag{17}$$

The $j$th propagation path of the $i$th ellipse, i.e., $\varphi_{Rij}$, corresponds to the random power, $p_{ij}$. In the first step, the powers of the delayed components, $p_{ij}$, are generated based on a uniform distribution:

$$f_p\left(p_{ij}\right) = \begin{cases} M_i/(2P_i) & \text{for} \quad p_{ij} \in \langle 0, 2P_i/M_i\rangle \\ 0 & \text{for} \quad p_{ij} \notin \langle 0, 2P_i/M_i\rangle \end{cases} \tag{18}$$

where $M_i$ is the number of the generated paths in the $i$th cluster, $j = 1, 2, \ldots, M_i$, and $P_i$ is the cluster power read from PDP/PDS.

Then, these powers are modified by the power pattern of the receiving antenna, $g_R^2(\varphi_R)$. Let us assume that the main lobe of this pattern is also described using the Gaussian model [39], i.e.,

$$g_R^2(\varphi_R) = G_R \exp\left(-\frac{\varphi_R^2}{\sigma_{R\varphi}}\right) \quad \text{for} \quad \varphi_R \in \langle -\pi, \pi) \tag{19}$$

where $G_R$ is the receiving antenna gain in a linear measure, $\sigma_{R\varphi} = HPBW_{R\varphi}/\left(2\sqrt{\ln 2}\right)$ $\cong 0.6HPBW_{R\varphi}$, and $HPBW_{R\varphi}$ is the receiving antenna HPBW in the azimuth plane.

Therefore, $p_{ij}$ generated using by the uniform distribution, i.e., Eq. (18), should be multiplied by the value of the power pattern which corresponds to the AOA with the same indexes, i.e.,

$$p_{Rij} = p_{ij} g_R^2\left(\varphi_{Rij}\right) \tag{20}$$

where $p_{ij}$ is the so-called power at the reception point and does not consider the receiving antenna pattern, while $p_{Rij}$ is the power seen at the output of the receiving antenna or at the Rx input [41].

If the receiving antenna is isotropic or omni-directional in the azimuth plane, then it should be assumed that $G_R = 1$ and $g_R^2(\varphi_R) = 1$ for $\varphi_R \in \langle -\pi, \pi)$.

## 4. Multi-ellipsoidal propagation model

In the case of using antennas, whose pattern width in the vertical plane exceeds several degrees, the scattering in this plane also determines the direction of reaching the propagation paths. Then, we obtain the multi-ellipsoidal propagation model by extending the multi-elliptical model to 3D space. If the antenna heights meet the conditions of $h_T, h_R \ll D$, then this model is reduced to the set of the semi-ellipsoids. As in the case of the multi-elliptical model, the parameters of the individual semi-ellipsoids, i.e., their semi-axes, are defined by Eq. (1) based on PDP/PDS. The reception angle statistical properties are determined based on simulation studies. In this case, we use a procedure for the 3D modeling shown in **Figure 4**. This procedure also includes the elevation plane.

Similar to the multi-elliptical model, the properties of the normalized power radiation pattern of the transmit antenna, $g_T^2(\theta_T, \varphi_T)$, are used to generate AODs [42]:

$$f_T(\theta_T, \varphi_T) = \frac{1}{4\pi} g_T^2(\theta_T, \varphi_T) \sin\theta_T \quad \text{for} \quad \theta_T \in \langle 0, \pi/2), \varphi_T \in \langle -\pi, \pi) \tag{21}$$

In this case, we use the assumption of the independence of the scatterer position in the azimuth and elevation planes. Hence, we have

$$f_T(\theta_T, \varphi_T) = f_T(\theta_T) \cdot f_T(\varphi_T) \tag{22}$$

where $f_T(\theta_T)$ and $f_T(\varphi_T)$ are the one-dimensional PDFs of AOD in the elevation and azimuth planes, respectively.

Using the Gaussian model [39] for $g_T(\theta_T, \varphi_T)$, we can describe the PDF of AOD for the multi-ellipsoidal model as

$$f_T(\theta_T, \varphi_T) = f_T(\theta_T) \cdot f_T(\varphi_T) = C_{T\theta} \exp\left(-\frac{(\theta_T - \pi/2)^2}{\sigma_{T\theta}}\right) \sin(\theta_T) \cdot C_{T\varphi} \exp\left(-\frac{\varphi_T^2}{\sigma_{T\varphi}}\right) \tag{23}$$

where $\sigma_{T\theta} = HPBW_{T\theta}/\left(2\sqrt{\ln 2}\right) \cong 0.6HPBW_{T\theta}$, $HPBW_{T\theta}$ is the transmitting antenna HPBW in the elevation plane, and $C_{T\theta}$ is a normalizing constant that meets the condition $C_{T\theta} = \left(\int_{0^\circ}^{90^\circ} f_T(\theta_T)\mathrm{d}\theta_T\right)^{-1}$.

Thus, $f_T(\varphi_T)$ is described by Eq. (15), while $f_T(\theta_T)$ is defined as

$$f_T(\theta_T) = C_{T\theta}\exp\left(-\frac{(\theta_T - \pi/2)^2}{\sigma_{T\theta}}\right)\sin\theta_T \quad \text{for} \quad \theta_T \in \langle 0, \pi/2) \tag{24}$$

A generated pair of angles, $\left(\theta_{Rij}, \varphi_{Rij}\right)$, determines the direction of the *ij*th propagation path departing from Tx. This path intersects the *i*th semi-ellipsoid. The intersection point, $S_{ij}$, determines the potential position of the scatterer. In the multi-ellipsoidal model, the method of determining the distance $r_{Tij}$ between Tx and $S_{ij}$ requires considering the elevation plane. Hence [42]:

$$r_{Tij} = -\frac{1}{2a}b_i^2 D\sin\theta_{Tij}\cos\varphi_{Tij} + \frac{1}{2a}\sqrt{\left(b_i^2 D\sin\theta_{Tij}\cos\varphi_{Tij}\right)^2 + 4ab_i^2\left(a_i^2 - \frac{D^2}{4}\right)} \geq 0 \tag{25}$$

where $a = \left(b_i\sin\theta_{Tij}\cos\varphi_{Tij}\right)^2 + a_i^2\left(\cos^2\theta_{Tij} + \left(\sin\theta_{Tij}\sin\varphi_{Tij}\right)^2\right) \geq 0$.

For the 3D modeling, a pair of angles $\left(\theta_{Rij}, \varphi_{Rij}\right)$ representing AOA in the elevation and azimuth planes is determined based on the following formula [42]:

$$\theta_{Rij} = \arctan\frac{\sqrt{\left(r_{Tij}\sin\theta_{Tij}\cos\varphi_{Tij} + D\right)^2 + \left(r_{Tij}\sin\theta_{Tij}\sin\varphi_{Tij}\right)^2}}{r_{Tij}\cos\theta_{Tij}} \tag{26}$$

$$\varphi_{Rij} = \operatorname{sgn}\left(\varphi_{Tij}\right)\arctan\frac{r_{Tij}\sin\theta_{Tij}\sin\varphi_{Tij}}{r_{Tij}\sin\theta_{Tij}\cos\varphi_{Tij} + D} \tag{27}$$

As in the 2D approach, the random power is assigned to each path that reaches the Rx and is defined by AOA. The procedure for determining this power is analogous to the multi-elliptical model and is based on the uniform distribution and the receiving antenna pattern, $g_R(\theta_R, \varphi_R)$. Let us assume that the main lobe of this pattern is also described using the Gaussian model [39], i.e.,

$$g_R^2(\theta_R, \varphi_R) = G_R\exp\left(-\frac{(\theta_R - \pi/2)^2}{\sigma_{R\theta}}\right)\sin(\theta_R)\cdot\exp\left(-\frac{\varphi_R^2}{\sigma_{R\varphi}}\right) \quad \text{for} \quad \theta_T \in \langle 0, \pi/2), \varphi_R \in \langle -\pi, \pi) \tag{28}$$

where $\sigma_{R\theta} = HPBW_{R\theta}/\left(2\sqrt{\ln 2}\right) \cong 0.6HPBW_{R\theta}$ and $HPBW_{R\theta}$ the receiving antenna HPBW in the elevation plane.

Then, $p_{ij}$ generated using the uniform distribution, i.e., Eq. (18), should be multiplied by the value of the pattern corresponding to the elevation and azimuth angles of the same indexes. Hence

$$p_{Rij} = p_{ij} g_R^2\left(\theta_{Rij}, \varphi_{Rij}\right) \tag{29}$$

For an isotropic receiving antenna, we accept $G_R = 1$ and $g_R^2(\theta_R, \varphi_R) = 1$ for $\theta_T \in \langle 0, \pi/2)$, and $\varphi_R \in \langle -\pi, \pi)$.

## 5. Reception angle distribution for local scattering components

Modeling the reception angle statistical properties for the local scattering components is based on the von Mises distribution [1, 4]:

$$f_0(\varphi_R) = \frac{\exp\left(\gamma_\varphi \cos\varphi_R\right)}{2\pi\, \mathrm{I}_0\left(\gamma_\varphi\right)} \quad \text{for} \quad \varphi_R \in \langle -\pi, \pi) \tag{30}$$

where $\mathrm{I}_0(\cdot)$ is the zero-order modified Bessel function and $\gamma_\varphi \geq 0$ is a parameter describing the reception angle dispersion in the azimuth plane.

For the 3D case, considering the independence of the scatterer occurrence in the azimuth and elevation planes, we have [42]:

$$f_0(\theta_R, \varphi_R) = f_0(\theta_R) \cdot f_0(\varphi_R) = C_{M\theta} \frac{\exp\left(\gamma_\theta \cos\left(\frac{\pi}{2} - \theta_R\right)\right)}{2\pi\, \mathrm{I}_0(\gamma_\theta)} \cdot \frac{\exp\left(\gamma_\varphi \cos\varphi_R\right)}{2\pi\, \mathrm{I}_0\left(\gamma_\varphi\right)} \quad \text{for} \quad \theta_R \in \langle 0, \pi/2), \varphi_R \in \langle -\pi, \pi) \tag{31}$$

where $C_{M\theta} = \left(\int_{0^\circ}^{90^\circ} f_0(\theta_R)\mathrm{d}\theta_R\right)^{-1} = 2\pi\, \mathrm{I}_0(\gamma_\theta)\left(\int_{0^\circ}^{90^\circ} \exp\left(\gamma_\theta \cos\left(\frac{\pi}{2} - \theta_R\right)\right)\mathrm{d}\theta_R\right)^{-1}$ and $\gamma_\theta \geq 0$ is a parameter determining the angle dispersion in the elevation plane.

The values of $\gamma_\varphi$ and $\gamma_\theta$ depend on surroundings of the receiving antenna in an analyzed propagation scenario.

For $\gamma_\varphi = \{0, 3, 30\}$, PDFs of AOA for the local scattering components in the azimuth plane are shown in **Figure 5**.

It should be noted that the AOA distribution for the local scattering components is independent of the distance between Tx and Rx, $D$. This PDF depends only on the obstacles in the

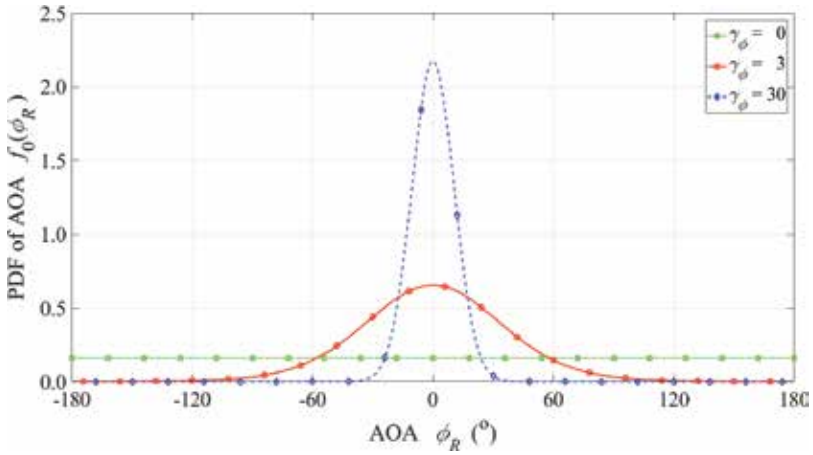


**Figure 5.** PDFs of AOA for local scattering components and selected $\gamma_\varphi$.

immediate vicinity of Rx and the direction of Rx-Tx. For the local scattering components, the random power can also be assigned to each AOA. The generation method of such power is similar to that for the delayed scattering components. However, the power at the reception point, $p_{0j'}$ is determined on the basis of another uniform distribution [42]:

$$f_p\left(p_{0j}\right) = \begin{cases} (\kappa+1)M_0/(2P_0) & \text{for} \quad p_{0j} \in \langle 0, 2P_0/(M_0(\kappa+1))\rangle \\ 0 & \text{for} \quad p_{0j} \notin \langle 0, 2P_0/(M_0(\kappa+1))\rangle \end{cases} \tag{32}$$

where $M_0$ is the number of the generated paths, $j = 1, 2, \ldots, M_0$, and $P_0$ is the value of power read from PDP/PDS for $\tau \cong 0$.

The power at the Rx input, $p_{R0j'}$ is determined as for the delayed scattering components, based on Eq. (20) or Eq. (28) for the 2D or 3D modeling, respectively.

## 6. Sample results of simulation studies

### 6.1. Influence of antenna parameters on reception angle distribution

A result of simulation studies is sets of the propagation path parameters reaching the Rx. In the multi-elliptical model, input data for the analysis of the result PDF of AOA for the delayed and local scattering components are two sets $\mathbf{\Phi} = \left\{\varphi_{Rij}\right\}$ and $\mathbf{P} = \left\{p_{Rij}\right\}$ for $j = 1, 2, \ldots, M_i$ and $i = 0, 1, \ldots, N$. For the multi-ellipsoidal model, a set of elevations is additionally considered, i.e., $\mathbf{\Theta} = \left\{\theta_{Rij}\right\}$. Thus, the *ij*th propagation path is defined by two or three parameters, for 2D or 3D modeling, respectively. The method of determining the estimated PDFs of AOA based on these sets is presented in [41, 42].

Let $\mathbf{O}(\theta_R, \varphi_R) = \left\{(i,j) : \theta_{Rij} \in (\theta_R \pm \varepsilon_\theta) \wedge \varphi_{Rij} \in (\varphi_R \pm \varepsilon_\varphi)\right\}$, where $\varepsilon_\theta$ and $\varepsilon_\varphi$ are the neighborhoods of $\theta_R$ and $\varphi_R$, respectively. Thus, $\sum_{\mathbf{O}(\theta_R,\varphi_R)} p_{Rij}\left(\theta_{Rij}, \varphi_{Rij}\right)$ represents the total power of the signal that arrives at the input of the receiver from $(\theta_R \pm \varepsilon_\theta, \varphi_R \pm \varepsilon_\varphi)$ sector.

An estimator of a joint PDF of AOA for the delayed and local scattering components is defined as [41]:

$$\tilde{f_R}(\theta_R, \varphi_R) = \mathrm{C}_0 \frac{\sum\limits_{\mathbf{O}(\theta_R,\varphi_R)} p_{Rij}\left(\theta_{Rij}, \varphi_{Rij}\right)}{\sum\limits_{i=0}^{N}\sum\limits_{j=1}^{M_i} p_{Rij}\left(\theta_{Rij}, \varphi_{Rij}\right)} \tag{33}$$

where $\mathrm{C}_0$ is a normalizing constant that is associated with $\varepsilon_\theta$ and $\varepsilon_\varphi$ and provides a condition $\lim\limits_{\substack{\varepsilon_\theta \to 0 \\ \varepsilon_\varphi \to 0}} \int\limits_{0}^{90^\circ} \int\limits_{-180^\circ}^{180^\circ} \tilde{f}_R(\theta_R, \varphi_R)\mathrm{d}\theta_R \, \mathrm{d}\varphi_R = 1.$

Eq. (33) is the basis for determining PDFs of AOA in the elevation and azimuth planes. In this case, marginal distribution properties are applied.

Thus, the PDFs of AOA in the elevation and azimuth planes have forms, respectively [41]:

$$\tilde{f_R}(\theta_R) = \mathrm{C}_{R\theta} \frac{\sum\limits_{\mathbf{K}(\theta_R)} p_{Rij}(\theta_{Rij})}{\sum\limits_{i=0}^{N}\sum\limits_{j=1}^{M_i} p_{Rij}(\theta_{Rij})} \text{ and } \tilde{f_R}(\varphi_R) = \mathrm{C}_{R\varphi} \frac{\sum\limits_{\mathbf{L}(\varphi_R)} p_{Rij}\left(\varphi_{Rij}\right)}{\sum\limits_{i=0}^{N}\sum\limits_{j=1}^{M_i} p_{Rij}\left(\varphi_{Rij}\right)} \tag{34}$$

where $\mathbf{K}(\theta_R) = \left\{(i,j) : \theta_{Rij} \in (\theta_R \pm \varepsilon_\theta)\right\}$ and $\mathbf{L}(\varphi_R) = \left\{(i,j) : \varphi_{Rij} \in (\varphi_R \pm \varepsilon_\varphi)\right\}$, whereas $\mathrm{C}_{R\theta}$ and $\mathrm{C}_{R\varphi}$ meet conditions $\lim\limits_{\varepsilon_\theta \to 0} \int\limits_{0}^{90^\circ} \tilde{f}_R(\theta_R)\mathrm{d}\theta_R = 1$ and $\lim\limits_{\varepsilon_\varphi \to 0} \int\limits_{-180^\circ}^{180^\circ} \tilde{f}_R(\varphi_R)\mathrm{d}\varphi_R = 1$, respectively.

For the simulation results presented below, we adopted the following assumptions: the PDP as shown in **Figure 2**, carrier frequency, $f_0 = 2.4$ GHz, $D = 300$ m, and parameters for four antenna types [43]:

- "Corner reflector" (CR): $G_{R-CR} = 23$ dBi, $HPBW_{\theta-CR} = 18^\circ$, and $HPBW_{\varphi-CR} = 58^\circ$
- "Horn antenna" (HA): $G_{R-HA} = 23$ dBi, $HPBW_{\theta-HA} = 40^\circ$, and $HPBW_{\varphi-HA} = 44^\circ$
- "Parabolic grid" (PG): $G_{R-PG} = 46$ dBi, $HPBW_{\theta-PG} = 14^\circ$, and $HPBW_{\varphi-PG} = 10^\circ$
- "Other antenna" (OA): $G_{R-OA} = 23$ dBi and $HPBW_{\theta-OA} = 6^\circ$ and $HPBW_{\varphi-OA} \to 360^\circ$

**Figure 6** shows examples of the PDFs of AOA in the elevation and azimuth planes for the CR-transmitting antenna and OA-receiving antenna. The individual PDFs are presented for selected $\alpha_T$. Whereas, the exemplary marginal PDFs of AOA for the CR receiving antenna and OA transmitting antenna are shown in **Figure 7**. In this case, the PDFs are depicted for selected $\alpha_R$. These graphs show an influence of the directional antenna on the angular dispersion at the transmitting and receiving side, respectively.

The marginal PDFs of AOA for four types of antennas—CR, HA, PG, and OA—are shown in **Figure 8**. In this case, we assume that $\alpha_T = 180^{\circ}$, $\alpha_R = 0$, and the radiation patterns of the transmitting and receiving antennas are the same.

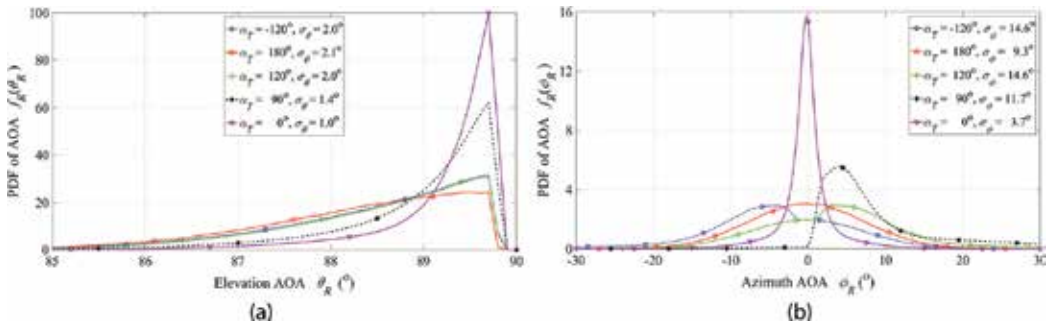


**Figure 6.** PDFs of AOA in (a) elevation and (b) azimuth planes for selected $\alpha_T$.

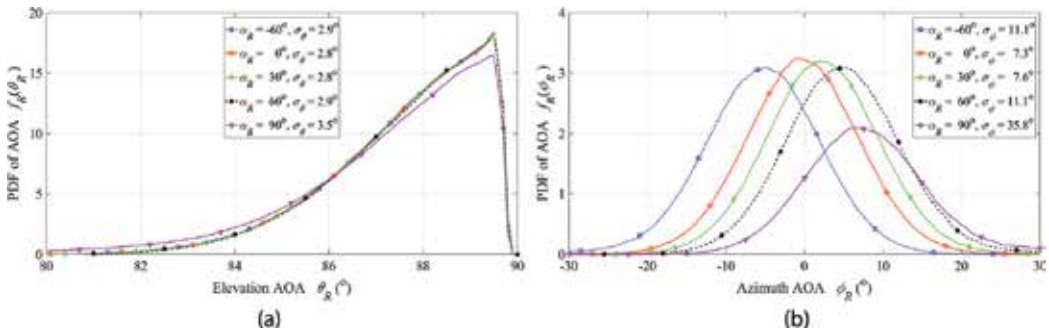


**Figure 7.** PDFs of AOA in (a) elevation and (b) azimuth planes for selected $\alpha_R$.

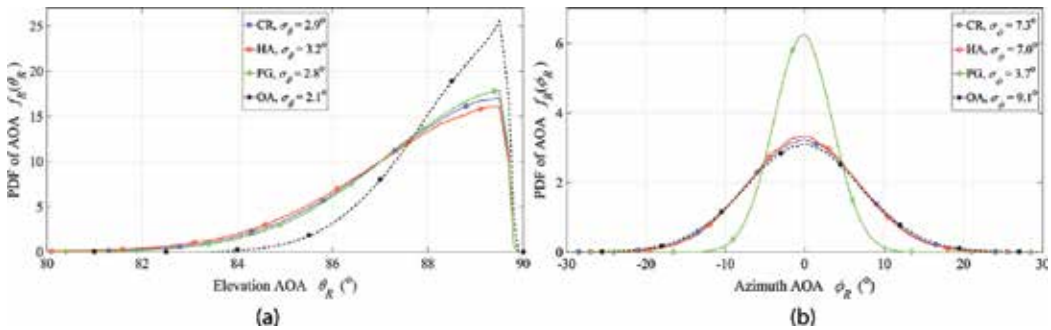


**Figure 8.** PDFs of AOA in (a) elevation and (b) azimuth planes for four antenna types.

http://dx.doi.org/10.5772/intechopen.75142

The PDFs are the basis for assessing the AOA dispersion for different types of propagation environments. A quantitative evaluation of the dispersion is based on the rms angle spread (AS). This measure is defined in the elevation, $\sigma_\theta$, and azimuth, $\sigma_\varphi$, planes, respectively [39]:

$$\sigma_\theta = \sqrt{\int_0^{90^\circ} \theta_R^2 \cdot f_R(\theta_R)\mathrm{d}\theta_R - \left(\int_0^{90^\circ} \theta_R \cdot f_R(\theta_R)\mathrm{d}\theta_R\right)^2} \tag{35}$$

$$\sigma_\varphi = \sqrt{\int_{-180^\circ}^{180^\circ} \varphi_R^2 \cdot f_R(\varphi_R)\mathrm{d}\varphi_R - \left(\int_{-180^\circ}^{180^\circ} \varphi_R \cdot f_R(\varphi_R)\mathrm{d}\varphi_R\right)^2} \tag{36}$$

**Figure 9** shows the relationship between AS and $HPBW_{T\theta} = HPBW_{R\theta}$ for $HPBW_{T\varphi} = HPBW_{R\varphi}$ equal to $HPBW_{\varphi-CR} = 58^\circ$ or $HPBW_{\varphi-PG} = 10^\circ$. ASs versus $HPBW_{T\varphi} = HPBW_{R\varphi}$ for $HPBW_{T\theta} = HPBW_{R\theta}$ equal to $HPBW_{\theta-CR} = 18^\circ$ or $HPBW_{\theta-HA} = 40^\circ$ is presented in **Figure 10**.

In both cases, we assume that the Tx and Rx antennas are oriented toward each other.

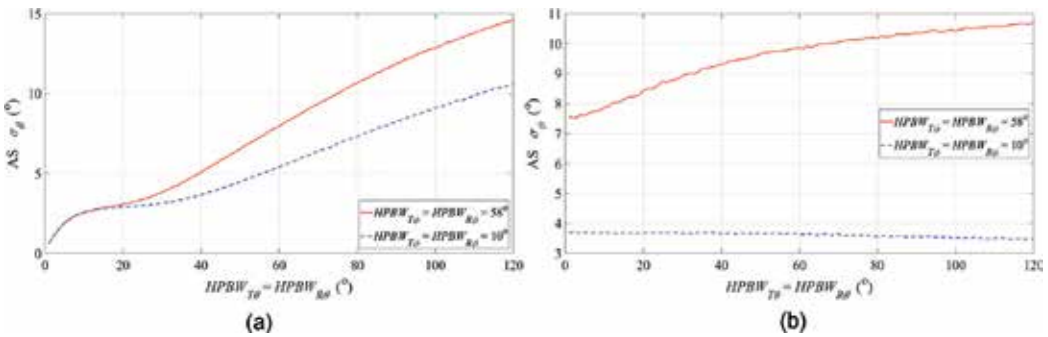


**Figure 9.** ASs in (a) elevation and (b) azimuth planes versus $HPBW_{T\theta} = HPBW_{R\theta}$ for $HPBW_{T\varphi} = HPBW_{R\varphi}$ equal $HPBW_{\varphi-CR} = 58^\circ$ or $HPBW_{\varphi-PG} = 10^\circ$.

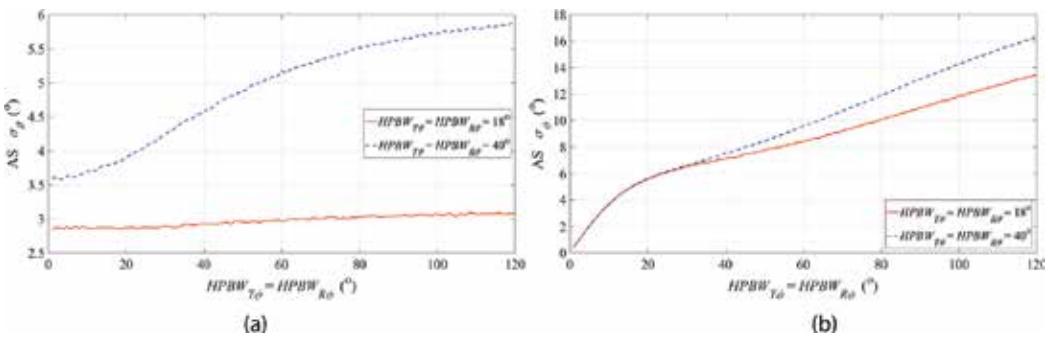


**Figure 10.** ASs in (a) elevation and (b) azimuth planes versus $HPBW_{T\varphi} = HPBW_{R\varphi}$ for $HPBW_{T\theta} = HPBW_{R\theta}$ equal $HPBW_{\theta-CR} = 18^\circ$ or $HPBW_{\theta-HA} = 40^\circ$.

An influence of the radiation/reception direction of the transmitting/receiving antenna on the AS is illustrated in **Figures 11** and **12** for (variable $\alpha_T$, $\alpha_R = 0 = \text{const.}$) and ($\alpha_T = 180^\circ = \text{const.}$, variable $\alpha_R$), respectively. These graphs are obtained for four analyzed antenna types.

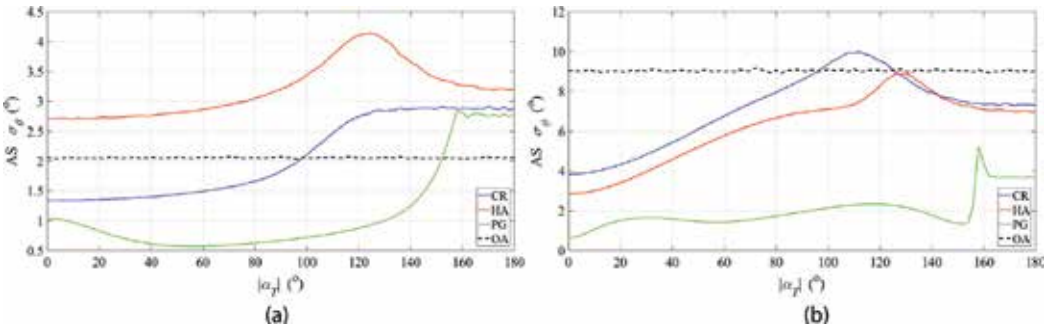


**Figure 11.** ASs in (a) elevation and (b) azimuth planes versus $\alpha_T$.

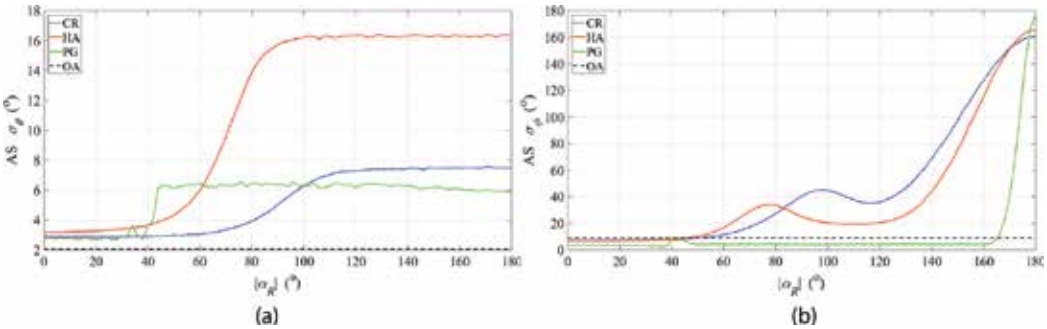


**Figure 12.** ASs in (a) elevation and (b) azimuth planes versus $\alpha_R$.

As a result of scattering phenomenon, the minimum AS occurs when the transmitting antenna radiates in the opposite direction to the Rx location. However, it should be remembered that in this case, the total power of the delayed components is reduced.

The results presented in this chapter are obtained for 2.4 GHz frequency. The evaluation of the AOA statistical properties for other frequency ranges is presented in [32, 37, 40, 42] for 1.8 GHz and in [41] for 28 GHz. The results presented in the chapter and these papers concern the angular distribution. As is shown in ([33], **Figure 8**) and ([2], **Figure 1**), AS is strictly linear correlated with the rms delay spread. Whereas, from ([7], Table 7.7.3-2), we see that the delay spread is reduced with the frequency increase. Therefore, we can conclude that the increase in the frequency brings the decrease in the angular dispersion.

### 6.2. Effects of reception angle dispersion on correlational and spectral properties

Multipath propagation and channel dispersion phenomena as well as an object motion effect have a significant impact on deformation of spectral and correlational structures of the

transmitted signals. Therefore, the assessment of the environment impact on the correlation-spectral properties requires an accurate mapping of these phenomena. For this purpose, we propose the so-called Doppler multi-elliptical channel model (DMCM), which is depicted in [44]. This model describes a procedure for generating the propagation path parameters in simulation studies. In addition to the angular dispersion, DMCM also considers the movement of the objects (Tx/Rx). Obtained simulation results using DMCM give the opportunity to evaluate instantaneous or statistical (averaged) changes of the received signal properties. Additionally in [44], DMCM is verified on the basis of empirical data available in a literature.

The influence analysis of the angular dispersion in DMCM on the correlational and spectral properties is presented in [45, 46]. In this case, the impact of the Rx motion direction on an autocorrelation function (ACF), power density spectrum (PSD), and following parameters—a coherence time, average Doppler frequency, Doppler spread, and asymmetry coefficient—is analyzed.

The basis for assessing the angular dispersion effects on the ACF and PSD is the relationship between the Doppler frequency shift (DFS) and AOA. DFS representing the *ij*th propagation path is determined based on the following formula:

$$f_{Dij} = f_{D\max} \cos\left(\varphi_{Rij} - \beta\right) \tag{37}$$

where $f_{D\max} = f_0 v/\mathrm{c}$ is the maximum DFS, $f_0$ is carrier frequency of the transmitting signal, $v$ is Rx velocity, and $\beta$ is Rx movement direction in relation to the Rx-Tx direction.

Typical assumptions are adopted in the presented analysis. The unmodulated carrier wave signal is used to assess the angular dispersion effects on the correlational and spectral properties. This approach gives an opportunity to simplify an analytical description and provides partial verification and comparison of obtained results with others presented in a literature. In this case, the PSD analyzed in a baseband is called the Doppler spectrum. In addition, the uniform distribution of phase and independence of the signal components are accepted.

Then, an ACF estimator is defined as [47]:

$$\tilde{R}(\tau) = \sum_{i=0}^{N} \sum_{j=1}^{M_i} p_{Rij} \exp\left(\mathrm{i}2\pi f_{Dij}\tau\right) \tag{38}$$

The PSD is obtained based on the Wiener-Khinchin theorem [48, 49]:

$$S(f_D) = \int_{-\infty}^{\infty} R(\tau) \exp\left(-\mathrm{i}2\pi f_D \tau\right) \mathrm{d}\tau \tag{39}$$

To this aim, we use the fast Fourier transform algorithm and smoothing filtering.

An unequivocal assessment of the influence of spatial parameters on the transmission properties of an environment requires normalization of ACF and PSD. Therefore, the results obtained

in the simulation studies are normalized with respect to the average power, $R_x(0)$, of the received signal. So, for the ACF and PSD, we have, respectively [45]:

$$r(\tau) = \frac{R(\tau)}{R(0)} \quad \text{and} \quad s(f_D) = 2f_{D\max}\frac{S(f_D)}{R(0)} \tag{40}$$

Based on these definitions, the properties of the normalized ACF and PSD are $r(0) = 1$ and $\frac{1}{2f_{D\max}}\int_{-f_{D\max}}^{f_{D\max}} s(f_D)\mathrm{d}f_D = 1$.

In the assessment of the AOA dispersion effects on the correlational and spectral properties, a spatial scenario presented in **Figure 13** is analyzed.

In this case, we assume that the Rx moves along a straight road at a constant speed, $v = 50\text{km/h}$. The distance from the route to the Tx is $D_y = 500$ m. The Tx emits the harmonic signal at $f_0 = 2.4$ GHz, so $f_{D\max} \cong 111$ Hz. The antenna patterns are omni-directional. The ACF and PSD evaluations are carried out at four points of the Rx route for specific directions: (A) $\beta = 30^\circ$, (B) $\beta = 60^\circ$, (C) $\beta = 90^\circ$, and (D) $\beta = 120^\circ$. For four analyzed cases, modules of the normalized ACFs and PSDs are presented in **Figure 14**.

A quantitative assessment of the channel dispersion impact on the spectral and correlational properties can be based on the parameter analysis. For the ACF, the coherence time, $T_C$, is determined based on the following condition:

$$|r(T_C)| = \left|\frac{R(T_C)}{R(0)}\right| = \frac{1}{2} \tag{41}$$

However, for the PSD, the average DFS, $F_D$, rms Doppler spread, $\sigma_D$, and asymmetry coefficient, $\mu_D$, [50] are defined, respectively:

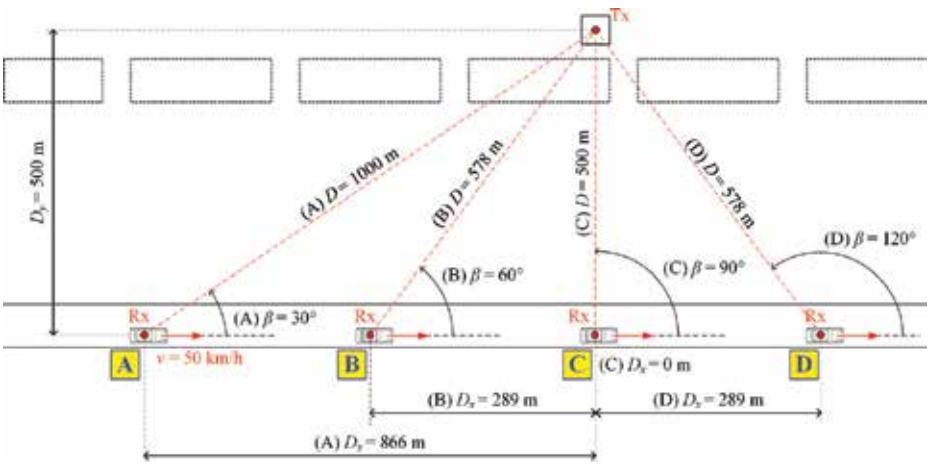


**Figure 13.** Spatial scenario of simulation studies.

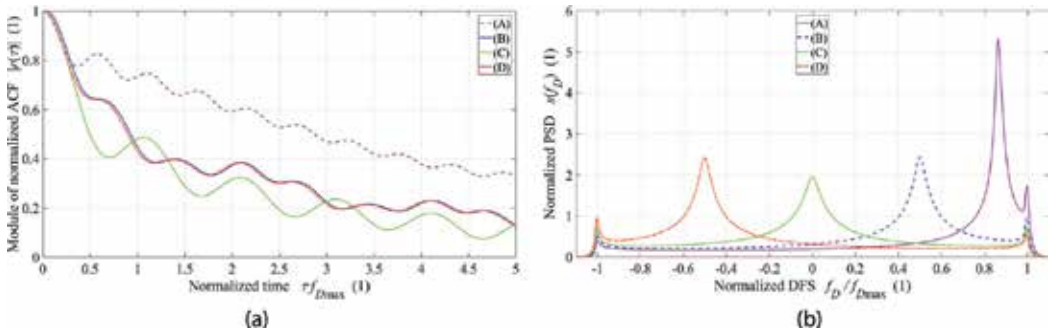


**Figure 14.** Module of normalized ACFs and PSDs for four analyzed points along Rx route.

$$F_D = 2f_{D\max} \int_{-f_{D\max}}^{f_{D\max}} f_D s(f_D) \mathrm{d}f_D \tag{42}$$

$$\sigma_D = \sqrt{2f_{D\max} \int_{-f_{D\max}}^{f_{D\max}} (f_D - F_D)^2 s(f_D) \mathrm{d}f_D} \tag{43}$$

$$\mu_D = \frac{1}{\sqrt{\sigma_D}^3} \sqrt{2f_{D\max} \int_{-f_{D\max}}^{f_{D\max}} (f_D - F_D)^3 s(f_D) \mathrm{d}f_D} \tag{44}$$

To obtain independence of the above metrics from $f_{D\max}$, i.e., from $f_0$ and $v$, we introduce normalized parameters in the following forms: $T_C f_{D\max}$, $F_D/f_{D\max}$, $\sigma_D/f_{D\max}$, and $\mu_D$. Changes of these parameters on the analyzed route are shown in **Figure 15**.

A characteristic feature of the presented PSD graphs is an occurrence of maxima for extreme DFSs and DFS resulted from Eq. (37) for the direct path component. The last frequency is closely related to the angle, $\beta$, between the velocity vector and the Rx-Tx direction. Based on the obtained results presented in **Figures 14** and **15**, we can conclude that close relations exist between the parameters of the analyzed characteristics and the spatial parameters of the simulation scenario. We can conclude that $T_C$, $\sigma_D$, $|F_D|$, and $|\mu_D|$ are decreasing with reduction of the Rx-Tx distance. The results prove that PSDs and ACFs significantly depend not only on the time domain dispersion but also on the angular dispersion and mutual position of the Rx and Tx. A graphical illustration of this fact is shown in **Figure 16**, which shows the PSD changes versus the Rx position.

Based on **Figure 16**, it follows that channels in mobile radiocommunications are spatially anisotropic due to their correlation-spectral properties. This means that the analysis of the ACF and PSD requires not only knowledge of the transmission properties of an environment but also knowledge about the Rx-Tx mutual position and movement parameters of the

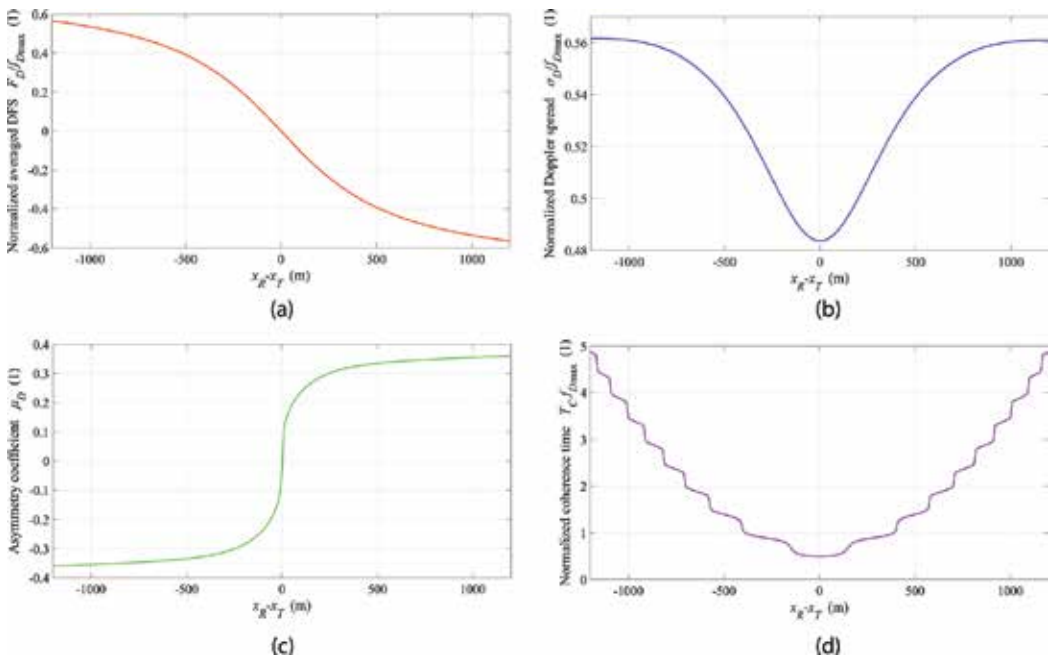


**Figure 15.** Changes of normalized parameters on Rx route: (a) average Doppler, (b) Doppler spread, (c) asymmetry coefficient, and (d) coherence time.

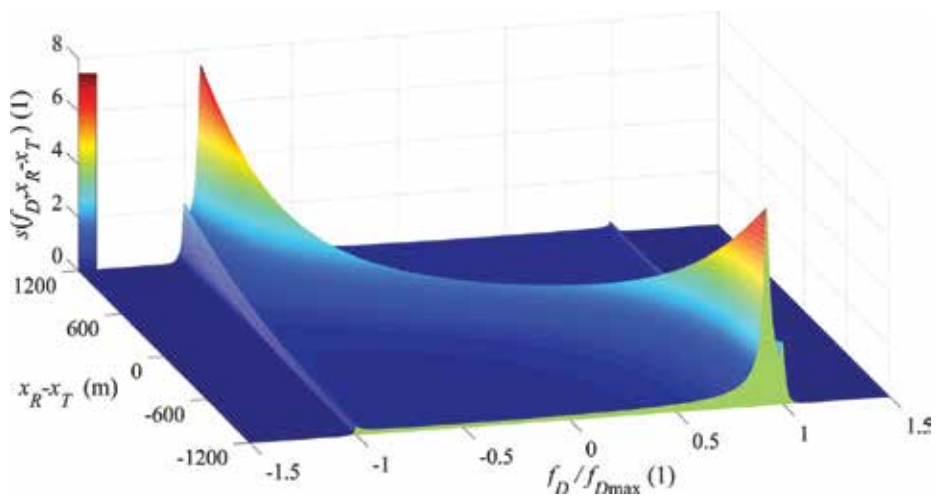


**Figure 16.** Averaged PSD versus Rx position.

elements of communication system. It follows that the set of parameters qualifying correctness of the PSD and ACF analysis, in addition to the characteristics related to the channel impulse response (PDP/PDS), should include the Tx and Rx positions, spatial location of movement trajectory, direction, and value of the velocity vector of the moving object. Therefore, the

channel transmission characteristics (PDP/PDS) condition the nature of the angular dispersion of the received signal in multipath propagation environments.

## 7. Conclusion

The chapter is devoted to the problem of the multipath propagation phenomenon modeling and its impact on changes of the received signal properties. The main focus is on the method of determining the PDF of AOA, which has the significant impact on changes in the correlational and spectral properties. In contrast to the empirical models, using the geometry-based models gives the opportunity to consider in the modeling process the spatial structure of a propagation environment. Linking the environment transmission properties with the position geometry of the scatterers is the main problem of using the geometric models. The use of the multi-elliptical or multi-ellipsoidal models is a solution to this problem. In this case, the geometrical structure of the scatterer locations in the form of the set of the confocal ellipses or semi-ellipsoids is created on the basis of the transmission characteristics of a propagation environment. This ensures adapting the geometrical structure to the analyzed or modeled propagation environment. The use of the multi-ellipsoidal or multi-elliptical models gives the possibility to consider the effect of the antenna radiation patterns on the PDF of AOA. This plays a significant role in the analysis of the compatible operating of coexistent wireless systems. PDF of AOA is the basis for assessing the impact of a propagation environment on the correlational and spectral properties of the transmitted signals. The use of the geometric models presented in this chapter provides mapping of the motion effects, which cause changes in the ACFs and PSDs versus changes of the object positions. The ability to adapt to the environment transmission properties and the assessment of changes in the correlation-spectral characteristics as a function of the object locations significantly distinguishes the models described in this chapter, among those presented so far in a literature.

## Author details

Jan M. Kelner* and Cezary Ziółkowski

*Address all correspondence to: jan.kelner@wat.edu.pl

Military University of Technology, Faculty of Electronics, Institute of Telecommunications, Warsaw, Poland

## References

[1] Ziółkowski C, Kelner JM. Empirical models of the azimuthal reception angle—Part I: Comparative analysis of empirical models for different propagation environments. Wireless Personal Communications. 2016;**91**(2):771-791. DOI: 10.1007/s11277-016-3496-1

[2] Ziółkowski C, Kelner JM. Empirical models of the azimuthal reception angle—Part II: Adaptation of the empirical models in analytical and simulation studies. Wireless Personal Communications. 2016;**91**(3):1285-1296. DOI: 10.1007/s11277-016-3528-x

[3] Sieskul BT, Kupferschmidt C, Kaiser T. Spatial fading correlation for local scattering: A condition of angular distribution. IEEE Transactions on Vehicular Technology. 2011;**60**(3): 1271-1278. DOI: 10.1109/TVT.2010.2103370

[4] Abdi A, Barger JA, Kaveh M. A parametric model for the distribution of the angle of arrival and the associated correlation function and power spectrum at the mobile station. IEEE Transactions on Vehicular Technology. 2002;**51**(3):425-434. DOI: 10.1109/TVT.2002.1002493

[5] WINNER II Channel Models. IST-WINNER II. Tech. Rep. Deliverable 1.1.2 v.1.2. 2007

[6] 3GPP TR 25.996 v13.1.0 (2016-12). Spatial Channel Model for Multiple Input Multiple Output (MIMO) Simulations (Release 13). Tech. Rep. 3GPP TR 25.996 v13.1.0. Valbonne, France. 3rd Generation Partnership Project (3GPP), Technical Specification Group Radio Access Network; 2016

[7] 3GPP TR 38.901 V14.2.0 (2017-09). Study on channel model for frequencies from 0.5 to 100 GHz (Release 14). Tech. Rep. 3GPP TR 38.901 V14.2.0. Valbonne, France. 3rd Generation Partnership Project (3GPP), Technical Specification Group Radio Access Network; 2017

[8] Yun Z, Iskander MF. Ray tracing for radio propagation modeling: Principles and applications. IEEE Access. 2015;**3**:1089-1100. DOI: 10.1109/ACCESS.2015.2453991

[9] Fuschini F, Vitucci EM, Barbiroli M, Falciasecca G, Degli-Esposti V. Ray tracing propagation modeling for future small-cell and indoor applications: A review of current techniques. Radio Science. 2015;**50**(6):2015RS005659. DOI: 10.1002/2015RS005659

[10] Corucci A, Usai P, Monorchio A, Manara G. Wireless propagation modeling by using ray-tracing. In: Mittra R. editor. Computational Electromagnetics. Recent Advances and Engineering Applications. New York, NY, USA: Springer; 2014. pp. 575-618. DOI: 10.1007/978-1-4614-4382-7_17

[11] Lim SY, Yun Z, Iskander MF. Radio propagation modeling: A unified view of the ray-tracing image method across emerging indoor and outdoor environments. In: Lakhtakia A, Furse CM, editors. The World of Applied Electromagnetics. In Appreciation of Magdy Fahmy Iskander. Cham, Switzerland: Springer; 2018. pp. 301-328. DOI: 10.1007/978-3-319-58403-4_13

[12] Yun Z, Iskander MF. Radio propagation modeling and simulation using ray tracing. In: Lakhtakia A, Furse CM, editors. The World of Applied Electromagnetics. In Appreciation of Magdy Fahmy Iskander. Cham, Switzerland: Springer; 2018. pp. 275-299. DOI: 10.1007/978-3-319-58403-4_12

[13] Lee WCY. Estimate of local average power of a mobile radio signal. IEEE Transactions on Vehicular Technology. 1985;**34**(1):22-27. DOI: 10.1109/T-VT.1985.24030

[14] Janaswamy R. Angle and time of arrival statistics for the Gaussian scatter density model. IEEE Transactions on Wireless Communications. 2002;**1**(3):488-497. DOI: 10.1109/TWC.2002.800547

[15] Jiang L, Tan SY. Geometrically Based Statistical Channel Models for Outdoor and Indoor Propagation Environments. IEEE Transactions on Vehicular Technology. 2007;**56**(6):3587-3593. DOI: 10.1109/TVT.2007.901055

[16] Le KN. On angle-of-arrival and time-of-arrival statistics of geometric scattering channels. IEEE Transactions on Vehicular Technology. 2009;**58**(8):4257-4264. DOI: 10.1109/TVT.2009.2023255

[17] Olenko AY, Wong KT, EH-O N. Analytically derived TOA-DOA statistics of uplink/downlink wireless multipaths arisen from scatterers on a hollow-disc around the mobile. IEEE Antennas and Wireless Propagation Letters. 2003;**2**(1):345-348. DOI: 10.1109/LAWP.2004.824174

[18] Baltzis KB. A generalized elliptical scattering model for the spatial characteristics of mobile channels. Wireless Personal Communications. 2011;**67**(4):971-984. DOI: 10.1007/s11277-011-0434-0

[19] Zhang J, Pan C, Pei F, Liu G, Cheng X. Three-dimensional fading channel models: A survey of elevation angle research. IEEE Communications Magazine. 2014;**52**(6):218-226. DOI: 10.1109/MCOM.2014.6829967

[20] Janaswamy R. Angle of arrival statistics for a 3-D spheroid model. IEEE Transactions on Vehicular Technology. 2002;**51**(5):1242-1247. DOI: 10.1109/TVT.2002.801756

[21] Olenko AY, Wong KT, Qasmi SA, Ahmadi-Shokouh J. Analytically derived uplink/downlink TOA and 2-D-DOA distributions with scatterers in a 3-D hemispheroid surrounding the mobile. IEEE Transactions on Antennas and Propagation. 2006;**54**(9):2446-2454. DOI: 10.1109/TAP.2006.880661

[22] Nawaz SJ, Khan NM, Patwary MN, Moniri M. Effect of directional antenna on the Doppler spectrum in 3-D mobile radio propagation environment. IEEE Transactions on Vehicular Technology. 2011;**60**(7):2895-2903. DOI: 10.1109/TVT.2011.2161788

[23] Nawaz SJ, Riaz M, Khan NM, Wyne S. Temporal analysis of a 3D ellipsoid channel model for the vehicle-to-vehicle communication environments. Wireless Personal Communications. 2015;**82**(3):1337-1350. DOI: 10.1007/s11277-015-2286-5

[24] Zajic AG, Stüber GL. Three-dimensional modeling, simulation, and capacity analysis of space-time correlated mobile-to-mobile channels. IEEE Transactions on Vehicular Technology. 2008;**57**(4):2042-2054. DOI: 10.1109/TVT.2007.912150

[25] Olenko AY, Wong KT, Qasmi SA. Distribution of the uplink multipaths' arrival delay and azimuth-elevation arrival angle because of 'bad urban' scatterers distributed cylindrically above the mobile. Transactions on Emerging Telecommunications Technologies. 2013; **24**(2):113-132. DOI: 10.1002/ett.2530

[26] Ahmed A, Nawaz SJ, Gulfam SM. A 3-D propagation model for emerging land mobile radio cellular environments. PLoS One. 2015;**10**(8):e0132555. DOI: 10.1371/journal.pone.0132555

[27] Nawaz SJ, Wyne S, Baltzis KB, Gulfam SM, Cumanan K. A tunable 3-D statistical channel model for spatio-temporal characteristics of wireless communication networks. Transactions on Emerging Telecommunications Technologies. 2017;**28**(12):e3213. DOI: 10.1002/ett.3213

[28] Jiang L, Tan SY. Simple geometrical-based AOA model for mobile communication systems. Electronics Letters. 2004;**40**(19):1203-1205. DOI: 10.1049/el:20045599

[29] Petrus P, Reed JH, Rappaport TS. Geometrical-based statistical macrocell channel model for mobile environments. IEEE Transactions on Communications. 2002;**50**(3):495-502. DOI: 10.1109/26.990911

[30] Ertel RB, Reed JH. Angle and time of arrival statistics for circular and elliptical scattering models. IEEE Journal on Selected Areas in Communications. 1999;**17**(11):1829-1840. DOI: 10.1109/49.806814

[31] Khan NM, Simsim MT, Rapajic PB. A generalized model for the spatial characteristics of the cellular mobile channel. IEEE Transactions on Vehicular Technology. 2008;**57**(1):22-37. DOI: 10.1109/TVT.2007.904532

[32] Ziółkowski C. Statistical model of the angular power distribution for wireless multipath environments. IET Microwaves, Antennas & Propagation. 2015;**9**(3):281-289. DOI: 10.1049/iet-map.2014.0099

[33] Pedersen KI, Mogensen PE, Fleury BH. A stochastic model of the temporal and azimuthal dispersion seen at the base station in outdoor propagation environments. IEEE Transactions on Vehicular Technology. 2000;**49**(2):437-447. DOI: 10.1109/25.832975

[34] Pedersen KI, Mogensen PE, Fleury BH. Spatial channel characteristics in outdoor environments and their impact on BS antenna system performance. In: Proceedings of the 1998 48th IEEE Vehicular Technology Conference (VTC); 18-21 may 1998; Ottawa, Canada: IEEE; 1998. vol. 2; p. 719-723. DOI: 10.1109/VETEC.1998.683676

[35] Mogensen PE, Pedersen KI, Leth-Espensen P, Fleury BH, Frederiksen F, Olesen K, Larsen SL .Preliminary measurement results from an adaptive antenna array testbed for GSM/UMTS. In: Proceedings of the 1997 47th IEEE Vehicular Technology Conference (VTC); 4-7 May 1997; Phoenix, AZ, USA: IEEE; 1997. vol. 3; p. 1592-1596. DOI: 10.1109/VETEC.1997.605826

[36] Fleury BH, Tschudin M, Heddergott R, Dahlhaus D, Pedersen KI. Channel parameter estimation in mobile radio environments using the SAGE algorithm. IEEE Journal on Selected Areas in Communications. 1999;**17**(3):434-450. DOI: 10.1109/49.753729

[37] Ziółkowski C, Kelner JM. Estimation of the reception angle distribution based on the power delay spectrum or profile. International Journal of Antennas and Propagation. 2015;**2015**:e936406. DOI: 10.1155/2015/936406

[38] Parsons JD, Bajwa AS. Wideband characterisation of fading mobile radio channels. IEE Proceedings F Communications, Radar and Signal Processing. 1982;**129**(2):95-101. DOI: 10.1049/ip-f-1:19820016

[39] Vaughan R, Bach Andersen J. Channels, Propagation and Antennas for Mobile Communications. London, UK: Institution of Engineering and Technology; 2003

[40] Ziółkowski C, Kelner JM, Nowosielski L, Wnuk M. Modeling the distribution of the arrival angle based on transmitter antenna pattern. In: Proceedings of the 2017 11th European Conference on Antennas and Propagation (EUCAP); 19-24 March 2017; Paris, France: IEEE; 2017. p. 1582-1586. DOI: 10.23919/EuCAP.2017.7928823

[41] Ziółkowski C, Kelner JM. Statistical evaluation of the azimuth and elevation angles seen at the output of the receiving antenna. IEEE Transactions on Antennas and Propagation. 2018;**66**. DOI: 10.1109/TAP.2018.2796719

[42] Ziółkowski C, Kelner JM. Antenna pattern in three-dimensional modelling of the arrival angle in simulation studies of wireless channels. IET Microwaves, Antennas & Propagation. 2017;**11**(6):898-906. DOI: 10.1049/iet-map.2016.0591

[43] Azevedo JA, Santos FE, Sousa TA, Agrela JM. Impact of the antenna directivity on path loss for different propagation environments. IET Microwaves, Antennas & Propagation. 2015;**9**(13):1392-1398. DOI: 10.1049/iet-map.2015.0194

[44] Ziółkowski C, Kelner JM. Geometry-based statistical model for the temporal, spectral, and spatial characteristics of the land mobile channel. Wireless Personal Communications. 2015;**83**(1):631-652. DOI: 10.1007/s11277-015-2413-3

[45] Ziółkowski C, Kelner JM. Influence of receiver/transmitter motion direction on the correlational and spectral signal properties. In: Proceedings of the 2016 10th European Conference on Antennas and Propagation (EuCAP); 10–15 April 2016; Davos, Switzerland: IEEE; 2016. pp. 1-4. DOI: 10.1109/EuCAP.2016.7481225

[46] Kelner JM, Ziółkowski C. Influence of receiver/transmitter motion direction on the correlational and spectral characteristics – Simulation analysis. In: Proceedings of the 2016 10th International Conference on Signal Processing and Communication Systems (ICSPCS); 19-21 December 2016; Gold Coast, Australia: IEEE; 2016. p. 1-6. DOI: 10.1109/ICSPCS.2016.7843381

[47] Stüber GL. Principles of Mobile Communication. 3rd ed. New York, NY, USA: Springer; 2011

[48] Wiener N. Generalized harmonic analysis. Acta Math. 1930;**55**(1):117-258. DOI: 10.1007/BF02546511

[49] Khintchine AY. Korrelationstheorie der stationären stochastischen Prozesse. Mathematische Annalen. 1934;**109**(1):604-615. DOI: 10.1007/BF01449156

[50] Beckmann P. Probability in Communication Engineering. New York, NY, USA: Harcourt, Brace & World; 1967

Chapter 7

# Ultra Wideband Transient Scattering and Its Applications to Automated Target Recognition

Hoi-Shun Lui, Faisal Aldhubaib, Stuart Crozier and Nicholas V. Shuley

Additional information is available at the end of the chapter

http://dx.doi.org/10.5772/intechopen.75059

**Abstract**

Reliable radar target recognition has long been the holy grail of electromagnetic sensors. Target recognition based on the singularity expansion method (SEM) uses a time-domain electromagnetic signature and has been well studied over the last few decades. The SEM describes the late time period of the transient target signature as a sum of damped exponentials with natural resonant frequencies (NRFs). The aspect-independent and purely target geometry and material-dependent nature of the NRF set make it an excellent feature set for target characterization. In this chapter, we aim to review the background and the state of the art of resonance-based target recognition. The theoretical framework of SEM is introduced, followed by signal processing techniques that retrieve the target-dependent NRFs embedded in the transient electromagnetic target signatures. The extinction pulse, a well-known target recognition technique, is discussed. This chapter covers recent developments in using a polarimetric signature for target recognition, as well as using NRFs for subsurface sensing applications. The chapter concludes with some highlights of the ongoing challenges in the field.

**Keywords:** radar target recognition, ultra wideband radar, transient electromagnetic scattering, singularity expansion method

## 1. Introduction

The need to quickly and accurately identify enemies in confrontational situations is essential to most defense applications. Such decisions often rely upon radar target recognition. The two primary functions of radar are inherent in the acronym, whose letters stand for radio detection and ranging. There are two main categories of radar target recognition techniques: imaging

IntechOpen

© 2018 The Author(s). Licensee IntechOpen. This chapter is distributed under the terms of the Creative Commons Attribution License (http://creativecommons.org/licenses/by/3.0), which permits unrestricted use, distribution, and reproduction in any medium, provided the original work is properly cited.

and what is termed signature recognition. Imaging radars provide a visualization of the target using techniques such as focus spot scanning and inverse synthetic aperture [1]. Signature recognition radar extracts some characteristics or a feature set that characterizes the target. Some of the techniques, such as radar cross section (RCS) [2], polarization techniques [3], high-resolution range profiles (HRRP) [4], scattering centers [5], and multiple frequency measurements [6], are all under this category. The main drawback of these techniques is that the extracted parameters usually vary with incident aspect. For most radar target recognition problems, usually, the incident aspect angles of the target are not known a priori. It is, therefore, preferable to implement a technique that is purely dependent on the target itself and independent of its aspect to the radar.

One of the methods that overcome the aspet-dependent limitation is termed resonance-based target recognition [7]. As the name states, resonance-based target recognition essentially characterizes the radar target based on the natural resonant frequencies (NRFs) embedded in the target response. These NRFs are purely dependent on the physical attributes of the radar target, i.e., its dielectric properties and physical geometry, and these parameters are independent on the incident aspect [7] and incident polarization states [8]. Provided of course the resonances are well excited, the feasibility of using the NRFs for target recognition has been successfully demonstrated in the literature [9–11].

This chapter aims to provide an overview of the fundamentals and the development of resonance-based target recognition. We commence the chapter with a short discussion on RCS—a well-known frequency-domain method on how electromagnetic scattering is characterized at microwave frequencies. The singularity expansion method (SEM), which is the theoretical framework for resonance-based target recognition, provides the physical description of the transient scattering phenomena in time and frequency domains. Technical solutions for retrieving the target-dependent NRFs from the transient target signatures and automated target recognition (ATR) algorithms will be covered. The recent development including the prospect of using full polarimetric signatures, as well as the potential use of the techniques in other sensing applications, is also discussed. Comments and suggestions for future development are considered in conclusion.

## 2. Resonance-based target recognition

RCS is a well-known technique to characterize target from 3 MHz up to 300 MHz (HF to mm) [2]. Attempts have also been made to perform RCS measurement in the terahertz frequency region [12, 13]. RCS is a measure of the power that is returned or scattered in a given direction, normalized with respect to the power of the incident field. Mathematically, the RCS ($\sigma$) of a target is defined as [2]

$$\sigma = 4\pi \lim_{R\to\infty} R^2 \frac{|\mathbf{E_s}|}{|\mathbf{E_i}|}, \tag{1}$$

where $R$ is the range from the radar to the target and $E_i$ and $E_s$ are the amplitudes of the incident electric field from the radar transmitter and the scattered electric field from the target,

respectively. The scattered field and thus the RCS of a definitive target, in general, vary as a function of incident aspects, receiving aspects, and excitation frequency. In the resonant regime which the wavelength of illumination ($\lambda$) and the target size ($L$) are comparable ($0.4\lambda \leq L \leq 10\lambda$), every part of the target affects every other parts. The total field of any part of the target is the vectorial sum of the incident and scattered field due to every part of the scattering body. This collective interaction determines the overall electromagnetic current induced on the target, which explains why the induced current at resonant frequencies is dependent on the physical attributes of the target.

Resonance-based target recognition is based on the resonating electromagnetic current induced on the target such that the ratio of excitation wavelength ($\lambda$) and the target size ($L$) has to be within the resonance scattering regime. The induced current serves as a secondary source and reradiates such that the resonant modes are embedded in the scattered target response. Rather than a frequency-domain characterization using RCS, one can also illuminate the target at a particular aspect in the time domain through a short-pulse excitation, measure the corresponding transient response at the same position (monostatic) or any another aspect (bistatic), and obtain the impulse response of the target. If one applies a Fourier transform to the target impulse response, this is the same as obtaining the frequency-domain "transfer function" of the target, thus evaluating the frequency dependency of the RCS at a particular transmit-receive configuration. Indeed, we assume that the bandwidth of the pulse is wide enough such that it covers at least the first few dominant resonant frequencies of the target.

### 2.1. Singularity expansion method

In the context of linear time-invariant (LTI) systems, the impulse response characterizes the behavior of the system and circuit. In the mid-1960s, Kennaugh and Moffatt [14] extended the concept of the impulse response and applied it to transient electromagnetic scattering from definitive targets. In the early 1970s, Baum [7] introduced the SEM that describes transient scattering phenomena. According to SEM, the entire transient target signature can be divided into two parts, namely, the early time and the late time period. Conceptually, the early time period is defined as the period from when the electromagnetic pulse initially strikes the target until the target is fully illuminated, while the commencement of the late time period is the time when global resonance has been fully established and the excitation is no longer present.

In the early time, the target is partly illuminated such that the majority of the scattering events originate locally from different parts of the target: specular reflections, diffraction from non-planar surfaces, edges, and corners. The occurrence of these events depends on when the pulse strikes on these edges and corners, and thus these early events are local, aspect dependent, and polarization dependent. They can be individually treated as scattering centers [5] or more generally using a wavefront description [15]. In the time domain, these scattering events correspond to impulse-like components, and they are time-varying (nonstationary) and can be modeled in a circuit context using an entire function [7, 16, 17].

In contrast, the commencement of the late time period is the time when the target is fully illuminated such that resonant modes at distinct frequencies are fully established. As previously mentioned the total field at any part of the target is a collective interaction of the incident

and scattered field from every single part of the target. At particular frequencies, the induced current on the target is freely resonating, and resonant modes are established. These resonant modes, known as natural resonance frequencies (NRFs), are theoretically dependent only on the physical attributes of the target and are independent of the aspect [7] and polarization [8]. This allows them to be an excellent candidate to be used as a feature set for target classification. Mathematically, the late time target signature can be modeled as a sum of damped exponentials with constant residues, i.e.,

$$r(t) = \sum_{n=1}^{N} \left[ A_n e^{s_n t} + A_n^* e^{s_n^* t} \right], \quad t > T_l \tag{2}$$

where $N$ is the modal order of the signal—the number of modes embedded in the late time response. It is assumed that only $N$ modes are excited given that the pulse excitation is band-limited. $T_l$ is the onset of the late time and * denotes the complex conjugate. $A_n$ is the aspect-dependent residues. $s_n = \sigma_n \pm j\omega_n$ is the complex NRF. $\sigma_n (< 0)$and $\omega_n$ are the damping coefficients and resonant frequencies of the $n^{\text{th}}$ mode, respectively.

### 2.2. Resonance extractions for target classification

Target classification and recognition rely on accurate extraction of the target-dependent NRFs. There are two main approaches to extract these NRFs. The first one is based on the mathematical formulation of the scattering problem. Through a Fourier transform, the short-pulse excitation corresponds to a broadband of frequencies in the frequency domain. If we formulate the entire scattering problem at a particular frequency via an integral equation formulation, the integral equation relationship can be written in a matrix form and solved via moment methods [18]. In general, this can be written as

$$[\mathbf{Z}][\mathbf{I}] = [\mathbf{V}], \tag{3}$$

where $[\mathbf{Z}]$ is an impedance-like matrix corresponding to the target geometry and $[\mathbf{I}]$ and $[\mathbf{V}]$ are column vectors corresponding to the unknown current induced on the target and the excitation, respectively. The natural resonant modes of the target, $s_n = \sigma_n \pm j\omega_n$, are those such that the homogenous version of Eq. (3) has a nontrivial solution. This implies that the solution exists when the determinant of the $[\mathbf{Z}]$ matrix equals zero, thus establishing the singularities of the $[\mathbf{Z}]$ matrix. These singularities can be extracted using a typical (complex) root searching method such as Muller's method [7]. The $[\mathbf{Z}]$ matrix is constructed based solely on the geometry and dielectric properties of the target. The NRFs are therefore totally independent of the incident aspect angle. A major limitation is that the entire physical problem needs to be modeled using moment method, and each $[\mathbf{Z}]$ corresponds to only one frequency. This means that one needs to repeat the entire root searching process for all the frequency points, which requires extensive computation. Another limitation is that this method cannot be applied directly to measured data.

Shortly after the proposition of SEM by Baum, Van Blaricum and Mittra [19] proposed using Prony's method which directly retrieves the NRFs and residues from the late time response in

http://dx.doi.org/10.5772/intechopen.75059

a computationally affordable manner. Prony's method addresses the above limitations, and it has drawn significant attention in the field. However, the primary drawback of Prony's method is that the accuracies of the extracted parameters are highly sensitive to noise and the estimated modal order of the signal. Since then, many techniques have been proposed which can accurately retrieve the modal order, NRFs, and residues with noisy target signatures. To date, direct extraction of NRFs from late time target signature has become the principal approach in this context, and matrix pencil methods (MPM) developed by Sarkar and Pereira [20] have become the main tool for this purpose.

To illustrate how NRFs can be used for target classification, as well as the aspect dependency nature of the resides, an example of a 1 m wire target illuminated under different excitation aspect angles $\theta$ shown in **Figure 1** is considered [21]. The wire target of length ($\ell$) and radius ($a$) ratio $\ell/a = 200$ is excited by a plane wave with the electric field in the plane of the wire. The transient target responses are obtained using the indirect time-domain method [22]—the scattering problem is first solved in the frequency domain at a large number of discrete frequency points, followed by Gaussian windowing to model a Gaussian pulse excitation [23] and an inverse Fourier transform. Here, the electromagnetic problem is solved using the moment method solver FEKO [24] from 4.39 MHz to 9 GHz with 2048 equally spaced samples. Given the target and incident aspect angles to the target, the late time can be approximated by

$$T_l = T_b + T_p + 2T_{tr}, \tag{4}$$

where $T_{tr}$ is the maximal transit time of the target, $T_p$ is the effective pulse duration, and $T_b$ is the estimated edge when the pulse strikes the leading edge of the target [11]. The Gaussian pulse commences at $T_b = 10ns$ with $T_p = 0.22ns$. According to the geometry of **Figure 1**, $T_{tr} = \ell\cos\theta/c$ where $c = 3 \times 10^8 m/s$, and the excitation angles of $\theta = 15^\circ$, $45^\circ$ and $75^\circ$ are considered, resulting in $T_l \approx 16.6$ns, 14.92ns and 11.9ns, respectively. The NRFs are extracted using the MPM [20] with late time samples from 17 to 140 ns. The first ten dominant extracted NRFs are listed in **Table 1** and are compared with the ground truth—NRFs extracted using a root searching procedure of the [**Z**] matrix [25].

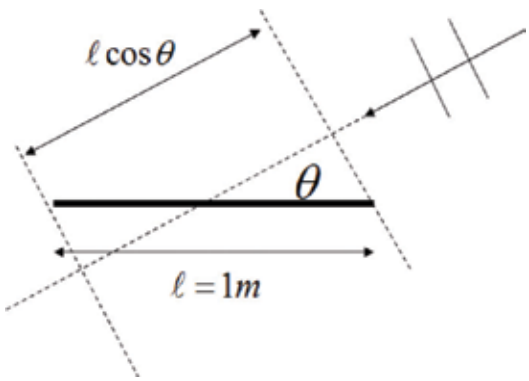


**Figure 1.** The wire scatterer with plane wave incidence (reprinted from [21] with permission from IEEE).

The results show that all the first ten dominant resonant modes can be extracted only at $\theta = 15^{\circ}$, while some modes cannot be retrieved at $\theta = 45^{\circ}$ and $\theta = 75^{\circ}$. To investigate of what is happening as the incidence angle varies, we transform the transient signatures to the joint time-frequency (TF) domain such that the existence and occurrences of the NRFs and scattering phenomena are clearly observed. Of all the time-frequency distributions (TFDs) in the Cohen class and the reassigned TFDs [26, 27], the Smooth Pseudo Wigner-Ville Distribution (SPWVD) gives reasonable TF resolutions without introducing uninterpretable artifacts [28–30].

The SPWVD, together with the corresponding time and frequency responses of the three signals, is shown in **Figure 2(a)–(c)**. At $\theta = 15^{\circ}$, all the ten modes are identified in the joint TF domain. In **Figure 2(b)**, modes 1 to 5 and mode 9 are observed when the incident angle is changed to $45^{\circ}$. Mode 6 is not observed due to its small residue. Two resonant modes at about 1.2 and 1.5 GHz are also found in the figure. They have similar frequencies to modes 8 and 10 but with higher damping factors (marked with ^ in **Table 1**), which could probably be the higher layer NRFs [31]. As the incident angle changes to $75^{\circ}$, only modes 1 to 4, 6, 7, and 9 are excited, and they are be found correspondingly to those frequencies in **Figure 2(c)**. In addition to the TF results, the NRFs also appear as peaks in the frequency response. As shown in both TF and frequency domains, it is apparent that the strength of the resonant modes, i.e., the residues, changes as the incident aspect varies, which validates the aspect dependency nature of the residues.

### 2.3. Extinction pulse technique

The target-dependent nature of the NRFs implies that the NRF patterns appearing in the S-plane are unique for a given target. Target recognition can thus be easily achieved by visually inspecting the patterns of the NRFs in the S-plane [32]. To automate the identification

| $n$ | f (MHz) | [**Z**] [25] | Matrix pencil method [20] | | |
|---|---|---|---|---|---|
| | | $s_nL/c$ | $15^{\circ}$, $s_nL/c$ | $45^{\circ}$, $s_nL/c$ | $75^{\circ}$, $s_nL/c$ |
| 1 | 138 | $-0.260 \pm j2.91$ | $-0.252 \pm j2.87$ | $-0.253 \pm j2.87$ | $-0.252 \pm j2.87$ |
| 2 | 286 | $-0.381 \pm j6.01$ | $-0.372 \pm j5.93$ | $-0.370 \pm j5.93$ | $-0.373 \pm j5.93$ |
| 3 | 432 | $-0.468 \pm j9.06$ | $-0.455 \pm j9.01$ | $-0.458 \pm j9.01$ | $-0.444 \pm j9.05$ |
| 4 | 583 | $-0.538 \pm j12.2$ | $-0.525 \pm j12.1$ | $-0.512 \pm j12.1$ | $-0.545 \pm j12.1$ |
| 5 | 730 | $-0.600 \pm j15.3$ | $-0.585 \pm j15.2$ | $-0.609 \pm j15.2$ | |
| 6 | 879 | $-0.654 \pm j18.4$ | $-0.637 \pm j18.3$ | $-0.833 \pm j18.4$ | $-0.881 \pm j17.6$ |
| 7 | 1027 | $-0.704 \pm j21.5$ | $-0.692 \pm j21.4$ | | $-0.850 \pm j21.6$ |
| 8 | 1175 | $-0.749 \pm j24.6$ | $-0.733 \pm j24.6$ | $-1.043 \pm j24.5$^ | |
| 9 | 1323 | $-0.792 \pm j27.7$ | $-0.785 \pm j27.7$ | $-0.732 \pm j27.9$ | $-1.005 \pm j28.6$ |
| 10 | 1471 | $-0.832 \pm j30.8$ | $-0.817 \pm j30.8$ | $-1.294 \pm j30.9$^ | |

**Table 1.** Comparison between the extracted NRFs ($s_nL/c$) using [**Z**] matrix and MPM (reprinted from [21] with permission from IEEE).

http://dx.doi.org/10.5772/intechopen.75059

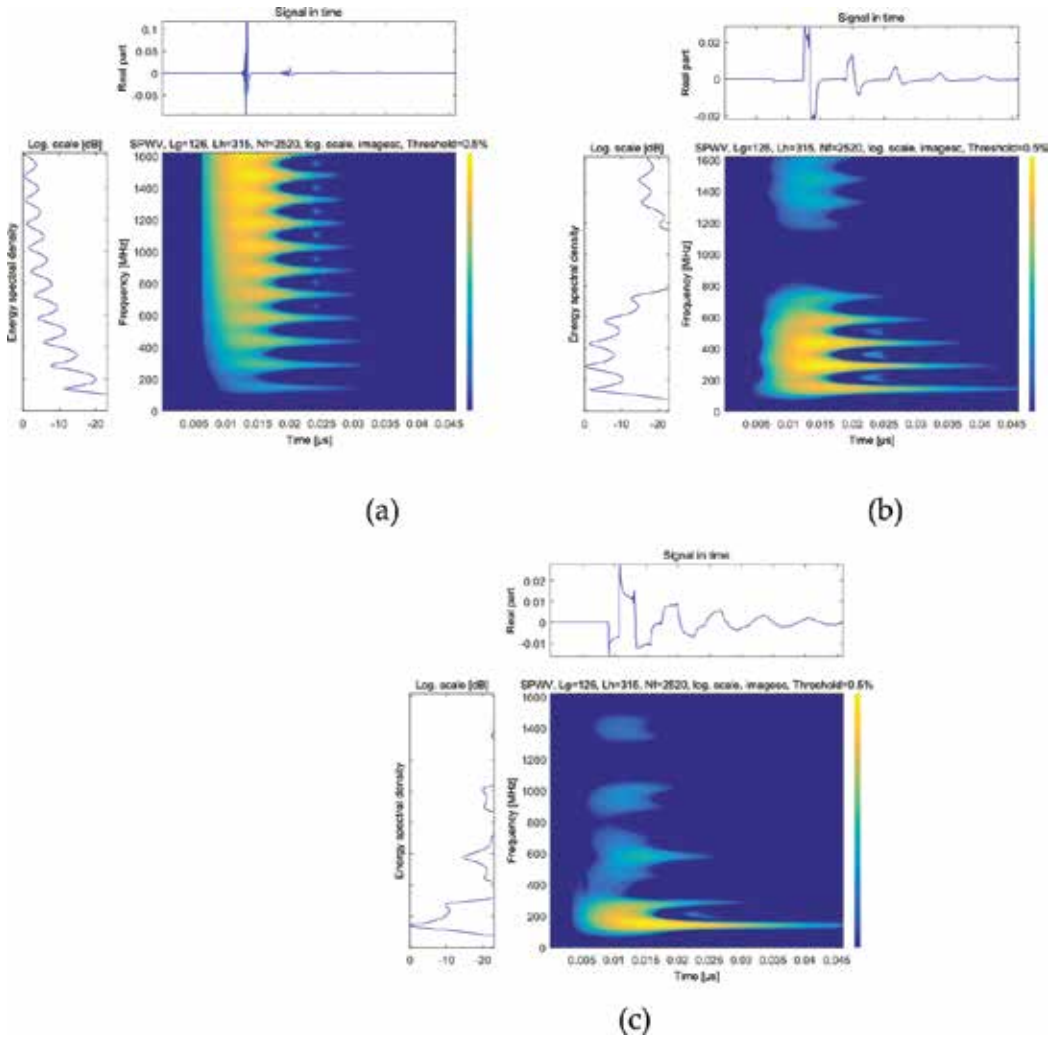


**Figure 2.** SPWVD of the wire scatterer with plane wave incidence at (a) $\theta = 15^{\circ}$, (b) $\theta = 45^{\circ}$, and (c)$\theta = 75^{\circ}$ (reprinted from [21] with permission from IEEE).

procedure, Rothwell [9–11] proposed that target recognition can be performed by convolving the target signatures with a special type of filter, known as the "extinction pulse" or the "E-pulse," in the time domain. The E-pulse is specially designed such that it will annul all the NRFs embedded in the late time response only if it is convolved with the response from the "true target." Mathematically, the E-pulse, $e(t)$, can be defined as [9–11]

$$c(t) = \int_0^{T_E} e(\tau) r(t-\tau) d\tau = 0 \quad \text{for} \quad t > T_L = T_l + T_E, \tag{5}$$

where $r(t)$ is the late time target signature defined in Eq. (2), $T_l$ is the commencement of the late time period, and $T_E$ is the duration of $e(t)$.

To illustrate how E-pulse operates, an ATR scenario is shown in **Figure 3** [11]. The goal here is to identify the target given a measured target signature $v(t)$ from an unknown target [11]. In the target library, a number of E-pulses corresponding to different targets are stored. To perform ATR, $v(t)$ is convolved with each of the E-pulses independently. According to Eq. (5), the one with a null response or smallest signal strength corresponds to the "true" target. Target identification is thus performed by monitoring the output of the convolution and picks up the one with the small energy level. To automate the process, the output is quantified using E-pulse discrimination number, *EDN*, and the E-pulse discrimination ratio, *EDR*, which are defined as follows [11]:

$$EDN = \left[\int_{T_L}^{T_L+W} (e(t)^* v(t))^2 dt\right]\left[\int_0^{T_e} e^2(t)dt\right]^{-1} \tag{6}$$

$$EDR = 10\log_{10}\left[\frac{EDN}{\min\{EDN\}}\right] \tag{7}$$

Therefore, the target signature yielding the smallest *EDN* and 0 dB *EDR* is the one corresponding to the target of interest. This forms the basis for E-pulse ATR.

In most of our studies, we know a priori which one is the "right" target, and our goal is to determine if E-pulse is capable of discriminating the targets in new applications; for instance, the "banded" E-pulse technique that better discriminates between similar targets [33], a novel technique for subsurface target detection [34], and ATR using polarimetric signatures (Section 3.1). **Figure 4** shows the flowchart of how we validate the E-pulse technique. For the case of three targets, there are three target signatures and three E-pulses, resulting in nine convolutions. Instead of using *EDN* and *EDR* in Eqs. (6) and (7), we modify them and introduce $EDN_{p,q}$ and discrimination ratio, $DR_{p,q}$, to quantify and convolution outcome and discrimination performance. They are given as follows [33, 35]:

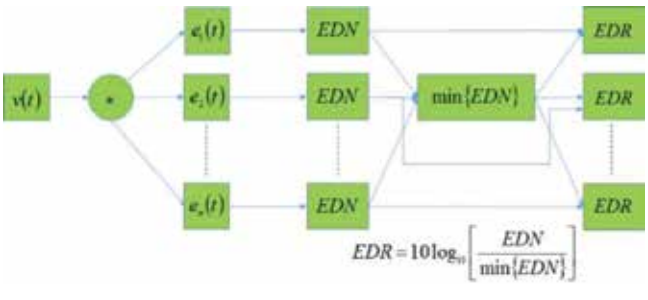


**Figure 3.** Automated target recognition using the E-pulse technique [11]. The goal is to determine which target does the unknown target signature $v(t)$ correspond to. $v(t)$ is convolved with all the E-pulses in the target library, and the corresponding EDN and EDR values are computed. the E-pulse that results in minimum value of EDN or equivalently 0 dB of EDR indicates the E-pulse "matches" with $v(t)$—The true target is thus the one that generate this E-pulse.

http://dx.doi.org/10.5772/intechopen.75059

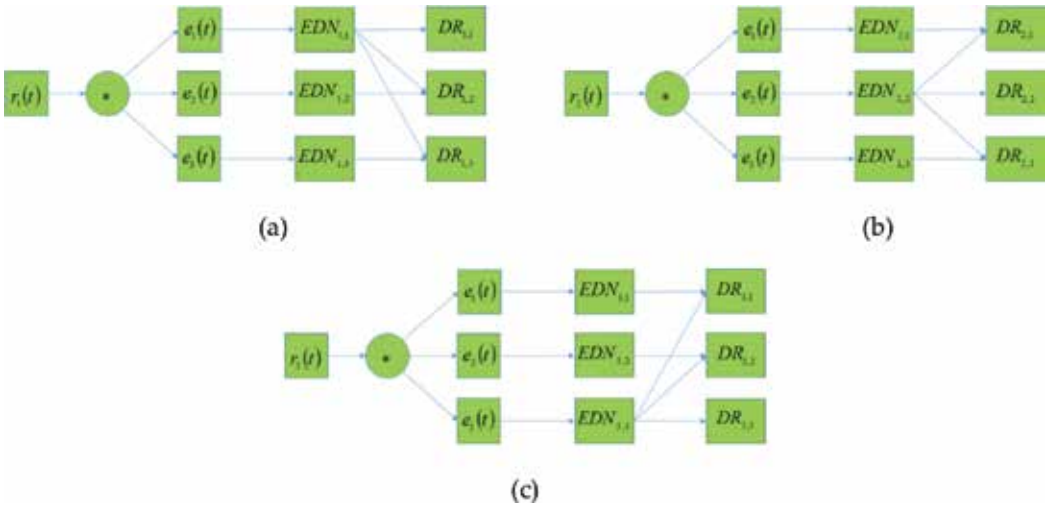


**Figure 4.** Validation of the E-pulse technique for new applications with known targets: (a) to (c) illustrate how the $EDN_{p,q}$ and $DR_{p,q}$ values are computed for the case of three known targets with target signatures ($r_1(t)$, $r_2(t)$, $r_3(t)$) and E-pulses ($e_1(t)$,$e_2(t)$,$e_3(t)$). As we know a priori of the "true" target, our goal is to test if we could obtain positive $DR_{p,q}$ ($p \neq q$) values.

$$EDN_{p,q} = \frac{\left[\int_{T_L}^{T_L+W} \left(e_q(t)^* r_p(t)\right)^2 dt\right]}{\left[\int_0^{T_e} e_q^2(t)dt\right]\left[\int_{T_L}^{T_L+W} r_p^2(t)dt\right]} \tag{8}$$

$$DR_{p,q} = 10\log_{10}\left[\frac{EDN_{p,q}}{EDN_{p,p}}\right] \tag{9}$$

$EDN_{p,p}$ is the case when the E-pulse and target response are from the same target, while $EDN_{p,q}$ is the case which the E-pulse and target returns are from different targets. A positive value of $DR_{p,q}$ implies that $EDN_{p,q}$ is greater than $EDN_{p,p}$ and thus a successful target recognition. As we have a priori knowledge of correct targets, positive $DR_{p,q}$ values are simply a validation of the success of E-pulse ATR or detection in the aforementioned new applications.

In practice, the E-pulse of a target can be obtained by numerically solving the convolution integral in Eq. (5) given the target signature [36] or using the formulation in [10] given the NRFs of the target. The E-pulses used in our studies (e.g., [33–35]) are constructed using the formulation in [10] together with the NRFs extracted from MPM.

## 3. Recent developments

Upon the introduction of SEM in the 1970s until the mid-1990s, research has mainly concentrated on three directions: theoretical studies with better modeling and description of early

time scattering phenomena [15–16], signal processing solutions to better retrieve SEM parameters for target characterization [17, 19–20, 36–39], and development of E-pulse and other ATR solutions for target recognition [11, 33, 40–44]. Most studies focused on ATR for targets in free space. The E-pulse proposed by Rothwell et al. [9–11, 36, 42] and the MPM algorithm by Sarkar and Pereira [20] have become the benchmark for filter-based ATR techniques and NRF extraction in this context. Since the 2000s, research activities have shifted toward applying the techniques developed in resonance-based target recognition for different applications. These include subsurface target detection, nondestructive evaluation, and medical diagnosis. Instead of using the linearly polarized electromagnetic wave to excite the target, the prospect of using fully polarimetric target signatures for ATR has also been investigated.

In this section, we first discuss the use of full polarimetric measurement and its impact on resonance-based target recognition. The merit of using polarimetric transient signatures is demonstrated through numerical examples. Then, different strategies for handling the *multiple-aspect multiple-polarization* data sets in multi-static scenarios are evaluated. Toward the end of the section, research activities on applying the E-pulse technique for different applications will be covered.

### 3.1. ATR using polarimetric signatures

The aspect dependency, as demonstrated in the above wire scattering example, as well as the polarization dependency of the residues, would limit the reliability and performance of ATR as it is uncertain whether all the dominant NRFs are well excited because the target orientation is usually not known a priori. In the mid-2000s, Shuley et al. [9] studied the residues retrieved from a target at 18 linear polarization angles at the same aspect and found that the residues of some NRFs could be so small at some polarization angles such that these NRFs are not retrieved. This was the first instance where polarization dependency of the residues is demonstrated. If we evaluate the RCS of the target at the resonant frequencies, the amplitudes of the scattered field, in general, vary as the observation aspects and polarization. This explains the aspect and polarization dependencies of the residues.

To accurately characterize a target using NRFs extracted from measured target signatures, it is important to incorporate more than one target signature obtained from different aspects and polarization states. Lui and Shuley [45] investigated different ways to process target signatures obtained from a number of polarization angles at a single aspect. Our results show that using the modified MPM [39] that allows extraction of one set of NRFs from multiple target signatures is preferred as it does not corrupt the original time-domain information and the risk of ignoring dominant modes is eliminated [45]. The major drawback is that the computational load grows as the number of target signatures (aspects and polarization angles) is increased. Also, when linear polarization is used, it is not trivial to decide how many polarization angles are sufficient. To better understand the impact of using the different polarimetric response for ATR, examples of some simple wire targets will first be presented. Then, different ways to handle data set obtained from *multiple-aspect multiple polarization* measurements for target classification will be presented.

In polarimetry, the Sinclair scattering matrices [46] in the linear and circular polarization bases are given by

$$[S(H,V)] = \begin{bmatrix} S_{HH} & S_{HV} \\ S_{VH} & S_{VV} \end{bmatrix} \quad \text{and} \quad [S(L,R)] = \begin{bmatrix} S_{LL} & S_{LR} \\ S_{RL} & S_{RR} \end{bmatrix}. \tag{10}$$

Here, the subscripts denote the polarization channels (sets of transmit-receive polarization), where $V$, $H$, $L$, and $R$ correspond to vertical, horizontal, left-hand, and right-hand circular polarization, respectively. The scattering matrices relate the incident and scattered electric field of the target under different polarization bases at a particular frequency. The first and second subscripts in each of the term inside the Sinclair scattering matrix correspond to the polarization state from the transmitting and receiving antennas. For instance, $S_{VH}$ corresponds to the case where the target is illuminated using vertically polarized plane wave and the horizontally polarized scattered field is measured. Once the Sinclair scattering matrix is measured in an orthogonal basis, all the polarization states (linear, circular, and elliptical) can be synthesized such that it is not necessary to illuminate the target with a large number of linear polarization angles from the same aspect [9, 45]. Only four target signatures (three for monostatic) are required which considerably reduces the amount of data to be processed.

To investigate the impact of the excitation and receiving states to the performance of ATR, numerical examples of three wire targets shown in **Figure 5** were studied [47]. The targets are made up of two wire segments—a vertical wire segment (main body) of 1 m and a horizontal wire segment of 0.3 m (Target 1 and Target 3) and 0.2 m (Target 2) located at the center (Target 1 and Target 2) and at 0.2 m away from the end of the main body (Target 3), respectively. The scattering problems of these targets are solved in the frequency domain using FEKO [24] with 512 equally spaced frequency samples from 3.9 MHz to 2 GHz. The polarimetric transient signatures, or equivalently the scattering matrices in the time domain, i.e.,

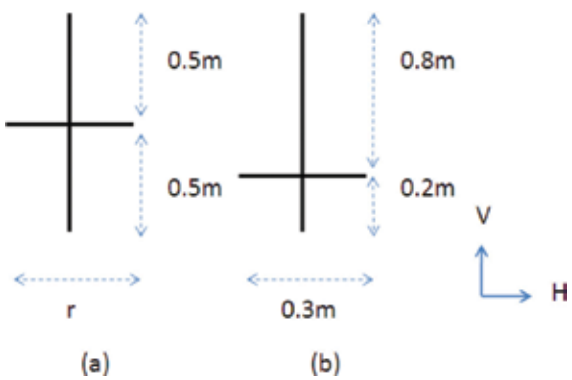


**Figure 5.** Wire targets and corresponding excitation polarization references. (a) Target 1: $r = 0.3m$, target 2: $r = 0.2m$, and (b) target 3 (reprinted from [47] with permission from IEEE).

$$\left[S_{(H,V)}(t)\right] = \begin{bmatrix} S_{HH}(t) & S_{HV}(t) \\ S_{VH}(t) & S_{VV}(t) \end{bmatrix} \quad \text{and} \quad \left[S_{(L,R)}(t)\right] = \begin{bmatrix} S_{LL}(t) & S_{LR}(t) \\ S_{RL}(t) & S_{RR}(t) \end{bmatrix}, \tag{11}$$

are determined using the aforementioned indirect time-domain method [22]. For each target, the NRFs from each target signature is extracted using MPM [20] resulting eight sets of NRFs and residues. At each polarization state, the E-pulses for each of the three targets (denoted as target $q$) are constructed using the extracted NRFs [10]. To evaluate the E-pulse ATR performance, the E-pulse validation procedures shown in **Figure 4** are applied. The E-pulse of each target (denoted as target $q$) is convolved with the target signatures from different targets (denoted as target $p$) but with the same polarization state. Before the convolution, both the E-pulses and target signatures are resampled as usually the sampling rate of the E-pulse and the target signatures are not the same [35]. The $EDN_{p,q}$ and $DR_{p,q}$ are computed, resulting in nine sets of $EDN_{p,q}$s and $DR_{p,q}$s for each polarization state. The corresponding results are tabulated in **Table 2**.

Under vertical excitation, the main body is excited but not the horizontal wire segment. Theoretically, the cross polarized response should be zero in this case and vice versa for horizontal polarization excitation, and thus we only consider the co-polarized components. As tabulated in **Table 2**, the E-pulse technique fails to recognize between Target 1 and Target 2 for the case of $S_{VV}(t)$, with $DR_{1,2}$ and $DR_{2,1}$ values near to 0 dB as only the NRFs corresponding to the main body are excited. For the case of $S_{HH}(t)$, the horizontal wire segments of the two targets are well excited, and $DR_{1,2}$ and $DR_{2,1}$ values of 46.6 and 126.2 dB are obtained, which indicates successful target recognition. However, almost 0 dB of $DR_{1,3}$ and $DR_{3,1}$ values result. This is because the length of the horizontal wire segment of Target 1 and Target 3 is identical and the transient responses are strongly dominated by the horizontal wire segments. Under vertical polarization, the current distributions of the two targets are different due to different positions of the horizontal wire segments. The $DR_{1,3}$ and $DR_{3,1}$ values of 42.9 and 65.4 dB

| $DR_{p,q}$(dB) | (a) $S_{VV}(t)$ | | | (b) $S_{HH}(t)$ | | |
|---|---|---|---|---|---|---|
| | $p=1$ | $p=2$ | $p=3$ | $p=1$ | $p=2$ | $p=3$ |
| $q=1$ | 0 | 0.01 | 42.9 | 0 | 46.6 | 0.002 |
| $q=2$ | −0.01 | 0 | 42.9 | 126.2 | 0 | 126.2 |
| $q=3$ | 65.4 | 65.4 | 0 | −0.002 | 53.9 | 0 |
| $DR_{p,q}$(dB) | (c) $S_{LL}(t)$ | | | (d) $S_{LR}(t)$ | | |
| | $p=1$ | $p=2$ | $p=3$ | $p=1$ | $p=2$ | $p=3$ |
| $q=1$ | 0 | 31.4 | 36.0 | 0 | 38.9 | 42.9 |
| $q=2$ | 27.0 | 0 | 43.8 | 26.7 | 0 | 44.6 |
| $q=3$ | 48.4 | 53.1 | 0 | 43.6 | 49.3 | 0 |

**Table 2.** ATR using target signatures under different polarization bases using E-pulse technique with the corresponding $DR_{p,q}$ (dB) values (reprinted from [47] with permission from IEEE).

result which indicate the E-pulses successfully distinguish between Target 1 and Target 3. With different positions and length of the horizontal wire segments, the E-pulse is capable of distinguishing between Target 2 and Target 3 for both $S_{VV}(t)$ and $S_{HH}(t)$. Under monostatic configuration and circularly polarized illumination, $S_{LL}(t) = S_{RR}(t)$ and $S_{LR}(t) = S_{RL}(t)$, and thus we only need to consider $S_{LL}(t)$ and $S_{LR}(t)$. $DR_{p,q}$values ($p \neq q$) of at least 26 dB result in all cases. Such results indicate that using circularly polarized target signatures can successfully discriminate the three targets.

In this example, ATR performance under different polarization states is studied. When the target is illuminated under linear polarization, only the main body or the horizontal wire segment is excited (details of the extracted NRFs can be found in [47]). The E-pulses are constructed using the incomplete set of NRFs. The target is poorly characterized and is not fully illuminated—these are the two main causes of the inconsistency in ATR performance. An example of the inconsistency in ATR performance due to aspect dependencies of the NRFs is reported in [48]. When the target is illuminated under circular polarization, the NRFs of both wire segments are adequately excited. The constructed E-pulse contains the domain NRFs of the entire target. The target is well characterized and well illuminated under circular polarization. The consistent ATR performance originates from the fact that the NRFs of both wire segments of the targets are well excited. The findings from this example demonstrated the importance of including all the dominant NRFs (including both the global and partial/substructure resonances [30]) for target classification, as well as the importance of exciting all the dominant NRFs, especially when a library of similar targets is considered [33].

### 3.2. Target classification using *multiple-aspect multiple-polarization* data set

Owing to the aspect and polarization dependencies of the residues, it is unlikely that the entire set of dominant NRFs can be excited from only one target signature. As shown above, target signatures obtained from different aspects and polarization states excite a different subset of dominant NRFs. Certainly, the use of multiple target signatures obtained from multiple aspect and polarization states for target characterization allows us to retrieve at least a larger subset of dominant NRFs within the frequency bandwidth. The *multiple-aspect multiple-polarization* data set [49], a data set that consists of transient target signatures obtained with different transmit-receive configurations and polarization basis, is thus required. There are a number of possible ways to illuminate the target and post-process these target signatures, and we want to identify an efficient way to handle the data. To illustrate the different possible ways to handle such large data sets, an example of a simple human breast model shown in **Figure 6 (a)** and **(b)**, a lossless dielectric hemisphere with a small different dielectric spheres embedded, that mimics the breast cancer detection scenario [50–53] is used. The radius of the lossless hemisphere is 60 mm with the relative permittivity of 5 (fat infiltrated tissue at ~3 GHz [54]). A 10 mm radius lossless dielectric sphere with a relative permittivity of 50 (taken from the Debye model [55] for <3 GHz) embedded inside the hemisphere is used to model the tumor. The target is illuminated using plane wave at six different aspects ($\theta = 105^\circ$ and $\phi = 30^\circ,\ 60^\circ,\ 90^\circ,\ 120^\circ,\ 150^\circ$ and $180^\circ$, where $\theta$ is measured from the positive $z$-axis, while

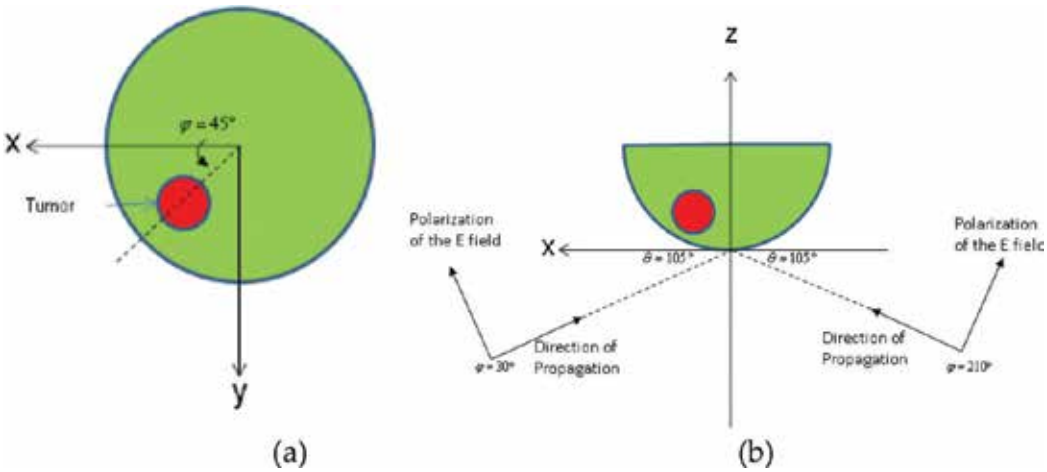


**Figure 6.** (a) Cross-sectional views (x-y plane) of the target. (b) Cross-sectional view ($\phi = 30^{\circ}, \theta = 105^{\circ}$) of the breast volume under plane wave illuminations from $\theta_t = 105^{\circ}$, $\phi_t = 30^{\circ}$, and $\phi_t = 210^{\circ}$, respectively. (reprinted from [49] with permission from IEEE).

$\phi$ is measured from the positive *x*-axis), resulted in 36 transmit-receive combinations (6 are monostatic, and 30 are bistatic) and 8 polarization states, i.e., 288 target signatures. It is apparent that the amount of data is tremendously increased when both aspect and polarization domains are considered. Efficient methods to handle the data are thus required.

First, extraction results of the entire *multiple-aspect multiple-polarization* data sets with 288 target signatures (Case 1: 6 × 6aspects and eight polarizations) are tabulated in column 2 of **Table 3**. Six dominant resonant modes are extracted. This result is treated as a *ground truth* as the extraction has taken all the data into account. Next, we consider NRF extractions in linear and circular polarization bases separately with 144 target signatures (Case 2: 36 aspects and four polarization states) in each basis. All the six resonant modes are retrieved in both bases, and the corresponding boxes in columns 3 and 4 in **Table 3** are shaded. The results indicate that both bases should give similar results in the NRF extraction process once all the four components in the Sinclair matrix are utilized.

Lastly, we perform NRF extraction on the multiple-aspect-only data at each of the eight polarization states (Case 3: 36 aspects and one polarization states). When *HH* data is used, five out of six resonant modes were extracted. When *VV*, *HV*, and *VH* data is used, only four modes were retrieved. When any one of the circularly polarized target signatures is used, all the six modes are accurately retrieved in all the co- and cross polarized results. The results show that we can retrieve all the dominant NRFs when only one of the four circularly polarized target signatures is used in the extraction process.

In summary, it is essential to include multiple-aspect data for target characterization because the NRF can be poorly excited at specific transmit-receive configurations [39, 48]. If all the four components in the scattering matrix are utilized for resonance extraction, both linear and circular polarization bases should give similar results. If only one out of the four components

| **Aspects** | **Case 1 All (6 × 6)** | **Case 2 All (6 × 6)** | | **Case 3 All (6 × 6)** | | | | | | | |
|---|---|---|---|---|---|---|---|---|---|---|---|
| **Pol.** | **Linear + circular (4 + 4)** | **Linear (4)** | **Circular (4)** | ***VV*** | ***HH*** | ***HV*** | ***VH*** | ***LL*** | ***RR*** | ***RL*** | ***LR*** |
| ***P*** | 288 | 144 | 144 | 36 | 36 | 36 | 36 | 36 | 36 | 36 | 36 |
| **NRFs** $\frac{\sigma \pm j\omega}{c}$ | $-3.48 \pm j27.97^{1}$ | | | | | | | | | | |
| | $-4.52 \pm j32.93^{2}$ | | | | | | | | | | |
| | $-2.13 \pm j41.59^{3}$ | | | | | | | | | | |
| | $-3.14 \pm j45.27^{4}$ | | | | | | | | | | |
| | $-3.27 \pm j52.66^{5}$ | | | | | | | | | | |
| | $-4.16 \pm j57.63^{6}$ | | | | | | | | | | |

The shaded boxes indicate the NRF is properly retrieved in the extraction process (***P***, total number of target signatures; Reprinted from [49] with permission from IEEE)

**Table 3.** Comparison of the extracted natural resonance frequencies (NRFs) using *multiple-aspect multiple-polarization* data.

in the polarization matrix is utilized (regardless single or multiple aspects), circularly polarized components are preferred over linearly polarized components as some of the dominant modes may not be retrieved in certain linear polarization states. Compared to previous studies that require a large number of target signatures from multiple linear polarization angles (6 [45] and 18 [9]), the computational load is reduced to the maximum of four or even one without deteriorating the accuracies of the extracted NRF when polarimetric signature is utilized to handle the polarization dependency of the residues. The findings presented here provide us with guidelines on how we should illuminate the targets and process the *multiple-aspect multiple-polarization* data set to extract a set of NRF that includes all the dominant NRFs for target characterization. With the "completed" set of NRF, the E-pulse is constructed and then used for ATR. In most ATR scenarios in which only one target signature from the target is measured, the traditional E-pulse technique using the "completed" E-pulse should be able to effectively distinguish the correct targets from the others. In situations, where more than one target signatures from a target are considered for ATR, e.g., the situation of multidirectional E-pulse presented in [48], novel ATR procedures will be required to effectively utilize the "completed" set of NRF with the extensive data set.

### 3.3. Subsurface target detection

Other than target recognition problems with the target in free space, research activities have also focused on subsurface target detection—where the target is located at a particular depth below an interface. The motivation of subsurface target detection first originated from unexploded ordinance (UXO) detection using ground-penetrating radar [56–60] and later detection of tumors inside a breast volume [49, 51, 55, 61] as well as detection of small changes in hip prostheses [62–64].

In the subsurface target detection problem, usually the excitation and the measured field points are located in one medium, and the target is located in another medium. The scattered response is no longer solely dependent on the target itself but also interactions between the target and the interface. These interactions vary as the dielectric contrast between the two media, the depth and the orientation of the target [56–60], as well as the interactions between the heterogeneity of the medium and the target. In [65], a transient scattering of metallic targets sited below lossless and lossy half space is studied using joint TF analysis. All the interactions of the target and the dielectric interface, as well as attenuation phenomena due to the non-zero conductivity of the half space, are clearly observed in the joint TF domain. Considering a relatively simple situation where both media are homogeneous, studies have demonstrated that there are two types of resonances associated with the entire scattering problem—a target resonance and an image resonance. A target resonance is the NRF associated with the target attributes (geometry and the dielectric properties) and the dielectric properties of the medium in which the target is embedded [56–60]. An image resonance is the NRF that corresponds to the target depth—the distance between the target and the interface of the two media [56, 57]. For target detection and recognition applications, the target NRF is of interest. Studies [56–58, 63] showed that the target NRFs forms a spiral trajectory in the S-plane as the target depth changes. The spiral trajectory surrounds the target NRF within a homogeneous environment—the case where the target is fully immersed in the environment without a dielectric interface.

Other than the characterization of the target resonances for the subsurface target, attempts have also been made to apply the E-pulse for monitoring depth changes [64, 66] and geometrical changes [67] of a hip prosthesis model sited below a half space of tissue. Results show that the E-pulse technique is capable of detecting both depth changes and physical changes of the target. A subsurface target detection technique is proposed in which the E-pulse is constructed using the NRFs for a target inside a homogenous environment [60] to approximate the target NRFs for subsurface targets. This E-pulse is convolved with target signatures from the subsurface target and shows that this approximate technique can distinguish between different targets [34, 68, 69].

### 3.4. Other applications

A critical issue that affects the accuracies of the extracted NRFs is the commencement of the late time or the turn-on time of the resonant modes [30]. The damped exponential model given by Eq. (2) is strictly only valid during the late time period. The early time consists of high-frequency scattering centers that are mainly local scattering events, which can be modeled using the entire functions (e.g., a Gaussian [17]). The inclusion of the early time period into the NRF extraction process will undoubtedly degrade the accuracies of the retrieved NRFs. Automated detection of the commencement of late time without a priori knowledge of the target geometry or orientation becomes crucial for ATR. Hargrave et al. [70] proposed a method to estimate the commencement of the late time based on intrinsic differences between the full-rank Hankel matrix generated from the early time data and the rank-deficient late time matrix generated by discrete resonant components. Rezaiesarlak and Manteghi [71, 72] propose the short-time matrix pencil method (STMPM), which mostly applies the MPM for NRF extraction

within a time window with a proper direction. The time window is moved by small time steps, and the extraction process is repeated until the entire signal is covered. The STMPM was first applied to chipless radio-frequency identification (RFID) application [71–74]. Data is encoded as NRFs of the RFID tagged by incorporating notches in the structure such that each RFID tag has different NRFs [73, 74].

In addition to the applications above, the concept of late time resonances has also been applied to sensing applications in other disciplines. This includes monitoring the deployment of arterial stents [75], nondestructive evaluation of the maturity of fruit [76], automated detection of objects fallen on railway tracks [77], nondestructive evaluation of layered materials [78, 79], and detection of concealed handguns [80].

## 4. Conclusions and ongoing challenges

The fundamentals and development of resonance-based target recognition over the last 40 years have been briefly reviewed. Prospects of using polarimetric transient signatures for target classification and recognition have been demonstrated through numerical examples. Results show that the use of polarimetric signatures will undoubtedly enhance the ATR performance while reducing the amount of data to process.

Other than using a linear polarization basis to synthesize the circularly polarized target signature, the challenges for designing circularly polarized time-domain antennas [81] that directly generate circularly polarized pulses are an ongoing research topic for antenna engineers. In situations where the targets under test are very similar, the resonance-based target recognition would perform poorly and probably fails. Recent results in [51, 82, 83] have shown that incorporating polarimetric features, e.g., characteristic polarization states (CPS) of the resonance modes, can solve the problem. Development of novel target recognition schemes that utilize these novel feature sets would be of practical interest to the radar community.

In addition to defense and security applications, recent studies have been looking into the potential of applying the technology to nondestructive evaluations, medical diagnosis, RFID, and agricultural applications. Compared to radar applications where the target is isolated (e.g., aircrafts in the sky) and located in the far-field region and direct signal path from transmitting and receiving antennas exists higher-order interactions between the targets and antennas as well as scattering from surrounding objects become significant especially when the target is located in the near-field region in medical diagnosis [52, 53] and aforementioned RFID applications. Novel calibration procedures [84, 85] and signal processing solutions for NRF extractions of multiple targets [86–88] are still ongoing research topics for researchers to explore. Regarding subsurface target detection, our results demonstrate that the E-pulse is capable of detecting changes of the NRFs of subsurface targets due to depth [64, 66] and geometrical changes [67]. In conjunction with target NRF, other features embedded in the target signature, such as the "turn-on" time of the resonance [65], could also be used for these applications. Rather than solely relies on NRF for ATR, the trend of having a "combined" feature set with

other parameters (e.g., CPS, turn-on time) will become the fashion for further development in this context.

## Author details

Hoi-Shun Lui[1]*, Faisal Aldhubaib[2], Stuart Crozier[1] and Nicholas V. Shuley[1]

*Address all correspondence to: h.lui@uq.edu.au

1 School of Information Technology and Electrical Engineering, The University of Queensland, St. Lucia, Queensland, Australia

2 Electronics Department, College of Technological Studies, Public Authority for Applied Education, Kuwait

## References

[1] Sullivan RJ. Radar Foundations for Imaging and Advanced Concepts. Raleigh: Scitech Publishing; 2004

[2] Knott EF, Shaeffer JF, Tuley MT. Radar Cross Section: Its Predication, Measurement and Reduction. Dedham, MA: Artech house; 1985

[3] Copeland JR. Radar target classification by polarization properties. Proceedings of the IRE. 1960;**48**:1290-1296

[4] Li HJ, Yang SH. Using range profiles as feature vectors to identify aerospace objects. IEEE Transactions on Antennas and Propagation. 1993;**41**:261-268

[5] Hurst M, Mittra R. Scattering center analysis via Prony's method. IEEE Transactions on Antennas and Propagation. 1987;**35**:986-988

[6] Lin H, Ksienski AA. Optimum frequencies for aircraft classification. IEEE Transactions on Aerospaces Electronic Systems. 1981;**17**:656-665

[7] Baum CE. The singularity expansion method. In: Felsen LB, editor. Transient Electromagnetic Fields. 1st ed. Vol. 10. Berlin; New York: Springer-Verlag; 1976. pp. 129-176

[8] Shuley N, Longstaff D. Role of polarisation in automatic target recognition using resonance descriptions. Electronics Letters. 2004;**40**:268-270

[9] Rothwell E, Nyquist D, Chen KM, Drachman B. Radar target discrimination using the extinction-pulse technique. IEEE Transactions on Antennas and Propagation. 1985;**33**:929-937

[10] Rothwell E, Chen KM, Nyquist DP, Sun W. Frequency domain E-pulse synthesis and target discrimination. IEEE Transactions on Antennas and Propagation. April, 1987;**35**(4): 426-434

[11] Ilavarasan P, Ross JE, Rothwell EJ, Chen KM, Nyquist DP. Performance of an automated radar target pulse discrimination scheme using E pulses and S pulses. IEEE Transactions on Antennas and Propagation. May, 1993;**41**(5):582-588

[12] Iwaszczuk K, Heiselberg H, Jepsen PU. Terahertz radar cross section measurements. Optics Express. 2010;**18**(25):26399-26408. DOI: 10.1364/OE.18.026399

[13] Lui HS, Taimre T, Lim YL, Bertling K, Dean P, Khanna SP, Lachab M, Valavanis A, Indjin D, Linfield EH, Davies AG, Rakic AD. Terahertz radar cross section characterization using self-mixing interferometry with a quantum Cascade laser. Electronics Letters. 22nd Oct. 2015;**51**(22):1774-1776

[14] Kennaugh EM, Moffatt DL. Transient and impulse response approximations. Proceedings of the IEEE. 1965;**53**:893-901

[15] Heyman E, Felsen L. A wavefront interpretation of the singularity expansion method. IEEE Transactions on Antennas and Propagation. 1985;**33**:706-718

[16] Felsen L. Comments on early time SEM. IEEE Transactions on Antennas and Propagation. 1985;**33**:118-119

[17] Jang S, Choi W, Sarkar TK, Salazar-Palma M, Kyungjung K, Baum CE. Exploiting early time response using the fractional Fourier transform for analyzing transient radar returns. IEEE Transactions on Antennas and Propagation. 2004;**52**:3109-3121

[18] Harrington R. Field computation by the moment method. 2nd ed. USA: IEEE Press; 1993

[19] Van Blaricum M, Mittra R. A technique for extracting the poles and residues of a system directly from its transient response. IEEE Transactions on Antennas and Propagation. 1975;**23**:777-781

[20] Sarkar TK, Pereira O. Using the matrix pencil method to estimate the parameters of a sum of complex exponentials. IEEE Antennas and Propagation Magazine. Feb, 1995;**37**(1):48-55

[21] Lui HS, Shuley N. On the analysis of electromagnetic transients from radar targets using smooth pseudo Wigner-Ville distribution (SPWVD). Proc. IEEE Antenna Propag. Society Int. Symp., pp. 5701-5704, Honolulu, HI, Jun. 10–15, 2007

[22] Lui HS, Shuley NV. On the modelling of transient scattering under ultra wideband sources. Asia Pacific Symp. Electromag. Compat., Beijing, China. 12–16 April 2010. pp. 854-857

[23] Rao SM. Time Domain Electromagnetics. San Diego: Academic Press; 1999

[24] FEKO, 32 Techno Lane, Technopark, Stellenbosch, 7600, South Africa: EM Software and System S.A., (pty) Ltd

[25] Rothwell EJ, Chen KM, Nyquist DP. Approximate natural response of an arbitrarily shaped thin wire Scatterer. IEEE Transactions on Antennas Propagation. Oct 1991;**39**(10): 1457-1462

[26] Cohen L. Time-Frequency Analysis. Englewood Cliffs, NJ: Prentice Hall; 1995

[27] Auger F, Flandrin P, Goncalves P, Lemoine O. Time-Frequency Toolbox – For Use with MATLAB. CNRS (France) and Rice University (USA; 1996)

[28] Lui HS, Shuley NV, Longstaff ID. Time-frequency analysis of late time electromagnetic transients from radar targets. Proc. IET Radar 2007, Pp. 1-5, the Edinburgh International Conference Centre, UK. 15–18 Oct., 2007

[29] Lui HS, Shuley NV. Joint time-frequency analysis on UWB radar signals. Proc. Int.l Conf. Signal Process. Comm. Sys., Gold Coast, Australia, 17–19 Dec. 2007

[30] Lui HS, Shuley NVZ. Evolutions of partial and global resonances in transient electromagnetic scattering. IEEE Antennas on Wireless Propagation Letters. 2008;**7**:435-439

[31] Tesche FM. On the analysis of scattering and antenna problems using the singularity expansion technique. IEEE Transactions on Antennas and Propagation. Jan., 1973;**21**(1): 53-62

[32] Van Blaricum M, Pearson L, Mittra R. An efficient scheme for radar target recognition based on the complex natural resonances of the target. IEEE Antennas and Propagation Society International Symposium. 1975;**13**:416-419

[33] Lui HS, Shuley NVZ. Radar target identification using a "banded" E-pulse technique. IEEE Transactions on Antennas and Propagation. Dec., 2006;**54**(12):3874-3881

[34] Lui HS, Shuley NVZ, Rakic AD. A novel, fast, approximate target detection technique for metallic target below a frequency dependent Lossy Halfspace. IEEE Transactions on Antennas and Propagation. May 2010;**58**(5):1699-1710

[35] Lui HS, Shuley NVZ. Sampling procedures in resonance based radar target identification. IEEE Transactions on Antennas and Propagation. May 2008;**56**(5):1487-1491

[36] Rothwell E, Kun-Mu C, Nyquist D. Extraction of the natural frequencies of a radar target from a measured response using E-pulse techniques. IEEE Transactions on Antennas and Propagation. 1987;**35**:715-720

[37] Gallego A, Medouri A, Carmen Carrion M. Estimation of number of natural resonances of transient signal using E-pulse technique. Electronics Letters. 1991;**27**:2253-2256

[38] Ruiz DP, Carrion MC, Gallego A, Medouri A. Parameter estimation of exponentially damped sinusoids using a higher order correlation-based approach. IEEE Transactions on Signal Processing. Nov. 1995;**43**(11):2665-2677

[39] Sarkar TK, Park S, Koh J, Rao SM. Application of the matrix pencil method for estimating the SEM (singularity expansion method ) poles of source-free transient responses from multiple look directions. IEEE Transactions on Antennas and Propagation. April, 2000; **48**(4):612-618

[40] Kennaugh E. The K-pulse concept. IEEE Transactions on Antennas and Propagation. 1981;**29**:327-331

[41] Chen KM, Nyquist D, Rothwell E, Webb L, Drachman B. Radar target discrimination by convolution of radar return with extinction-pulses and single-mode extraction signals. IEEE Transactions on Antennas and Propagation. 1986;**34**:896-904

[42] Rothwell EJ, Chen KM. A hybrid E-pulse/least squares technique for natural resonance extraction. Proceedings of the IEEE. 1988;**76**:296-298

[43] Carrion MC, Gallego A, Porti J, Ruiz DP. Subsectional-polynomial E-pulse synthesis and application to radar target discrimination. IEEE Transactions on Antennas and Propagation. 1993;**41**:1204-1211

[44] Blanco D, Ruiz DP, Alameda E, Carrion MC. An asymptotically unbiased E-pulse-based scheme for radar target discrimination. IEEE Transactions on Antennas and Propagation. 2004;**52**:1348-1350

[45] Lui HS, Shuley N. Resonance Based Radar Target Detection with Multiple Polarisations. Proc. IEEE Antennas Propag. Soc. Int. Symp. USNC/URSI National Radio Science Meeting. 9–14 July, 2006, Albuquerque, New Mexico, USA. pp. 3259-3262

[46] Mott H. Remote Sensing with Polarimetric Radar. New Jersey: Wiley; 2007

[47] Lui HS, Shuley NVZ. Resonance based target recognition using ultra-wideband Polarimetric signatures. IEEE Transactions on Antennas and Propagation, New Jersey. August 2012;**60**(8):3985-3988

[48] Zhang H, Fan Z, Ding D, Chen R. Radar target recognition based on multi-directional E-pulse technique. IEEE Transactions on Antennas and Propagation. Nov. 2013;**61**(11):5838-5843

[49] Lui HS. Characterization of radar target using multiple transient responses. IEEE Antennas on Wireless Propagation Letters. Sept. 2015;**14**:1750-1753

[50] Lui HS, Fhager A, Persson M. On the forward scattering of microwave breast imaging. International Journal of Biomedical Imaging, 15 Pages. May 2012

[51] Lui HS, Fhager A, Yang J, Persson M. Characterization and detection of breast cancer using ultra wideband Polarimetric transients. European Conference on Antennas and Propagation. Gothenburg, Sweden, 8–11 April 2013. pp. 2909-2913

[52] Lui HS, Fhager A, Persson M. Preliminary Investigations of Three-Dimensional Microwave Tomography Using Different Data Sets. European Conference on Antennas and Propagation, Prague, Czech Republic. 26–30 March 2012

[53] Lui HS, Fhager A, Persson M. Antenna Configurations of Microwave Breast Imaging. Asia Pacific Microwave Conference, 5–8 Nov., 2013, Seoul, Korea

[54] Gabriel S, Lau RW, Gabriel C. The dielectric properties of biological tissues: III. Parametric models for the dielectric spectrum of tissues. Physics in Medicine and Biology. Nov. 1996;**41**(11):2271-2293

[55] Huo Y, Bansal R, Zhu Q. Modeling of noninvasive microwave characterization of breast tumors. IEEE Transactions on Biomedical Engineering. 2004;**51**:1089-1094

[56] Vitebskiy S, Carin L. Moment-method modeling of short-pulse scattering from and the resonances of a wire buried inside a lossy, dispersive half-space. IEEE Transactions on Antennas and Propagation. 1995;**43**:1303-1312

[57] Geng N, Jackson DR, Carin L. On the resonances of a dielectric BOR buried in a dispersive layered medium. IEEE Transactions on Antennas and Propagation. 1999;**47**:1305-1313

[58] Wang Y, Longstaff ID, Leat CJ, Shuley NV. Complex natural resonances of conducting planar objects buried in a dielectric half-space. IEEE Transactions on Geoscience Remote Sensing. 2001;**39**:1183-1189

[59] Chen C-C, Peters L Jr. Buried unexploded ordnance identification via complex natural resonances. IEEE Transactions on Antennas and Propagation. 1997;**45**:1645-1654

[60] Baum CE. Detection and Identification of Visually Obscured Targets. Philadelphia: Taylor & Francis; 1999

[61] Lui HS, Li BK, Shuley N, Crozier S. Preliminary Investigation of Breast Tumor Detection Using the E-Pulse Technique. Proc. IEEE Antenna Propag. Soc. Int. Symp. USNC/URSI National Radio Science Meeting, pp. 283-286, 9–14 July. 2006. Albuquerque, New Mexico, USA

[62] Lui HS, Shuley N, Crozier S. A Concept for Hip Prosthesis Identification Using Ultra Wideband Radar. Proc. 26th Annual Int. Conf. of the IEEE Engineering in Medicine and Biology Society. pp. 1439-1442, 1–5 Sept. 2004, San Francisco, CA, USA

[63] Lui HS, Shuley N, Crozier S. Hip Prosthesis Detection Based on Complex Natural Resonances. Proc. 27th Annual Int.l Conf. of the IEEE Engineering in Medicine and Biology Society, 1–5 Sept. 2005. Shanghai, China. pp. 1571-1574

[64] Lui HS, Shuley N, Padhi SK, Crozier S. Detection of hip prosthesis depth changes using an E-pulse technique. Topical Meeting on Biomedical Electromagnetics. 17th International Zurich Symposium on Electromagnetic Compatibility. 27 February to 3 march 2006, Singapore. pp. 81-84

[65] Lui HS, Shuley N, Persson M. Joint time-frequency analysis of transient electromagnetic scattering from a subsurface target. IEEE Antennas and Propagation Magazine. Oct. 2012; **54**(5):109-130

[66] Lui HS, Shuley NVZ. Detection of depth changes of a metallic target buried inside a Lossy Halfspace using the E-pulse technique. IEEE Transactions on Electromagnetic Compatibility. November 2007;**49**(4):868-875

[67] Lui HS, Aldhubaib F, Shuley NVZ, Hui HT. Subsurface target recognition based on transient electromagnetic scattering. IEEE Transactions on Antennas and Propagation. October 2009;**57**(10):3398-3401

[68] Lui HS, Shuley N. Subsurface target recognition using an approximated method. Asia Pacific Microw. Conf. Singapore, 7–10 Dec. 2009. pp. 2216-2219

[69] Lui HS, Shuley NV. Performance evaluation of subsurface target recognition based on ultra-wideband short pulse excitation. IEEE Int. Symp. Antennas Propag., pp. 1-4, Toronto, Ontario, Canada, July 11–17, 2010

[70] Hargrave CO, Clarkson IVL, Lui HS. Late-time estimation for resonance-based radar target identification. IEEE Transactions on Antennas and Propagation. Nov., 2014;**62**(11): 5865-5871

[71] Rezaiesarlak R, Manteghi M. Short-time matrix pencil method for Chipless RFID detection applications. IEEE Transactions on Antennas Propagation. May 2013;**61**(5):2801-2806

[72] Rezaiesarlak R, Manteghi M. On the application of short-time matrix pencil method for wideband scattering from resonant structures. IEEE Transactions on Antennas Propagation. Jan. 2015;**63**(1):328-335

[73] Blischak AT, Manteghi M. Embedded singularity Chipless RFID tags. IEEE Transactions on Antennas Propagation. Nov 2011;**59**(11):3961-3968

[74] Rezaiesarlak R, Manteghi M. Complex-natural-resonance-based Design of Chipless RFID tag for high-density data. IEEE Transactions on Antennas Propagation. Feb 2014;**62**(2): 898-904

[75] Manteghi M, Cooperand DB, Vlachos PP. Application of singularity expansion method for monitoring the deployment of arterial stents. Microwave and Optical Technology Letters. 2012;**54**(10):2241-2246

[76] Tantisopharak T, Moon H, Youryon P, Bunya-Athichart K, Krairiksh M, Sarkar TK. Nondestructive determination of the maturity of the durian fruit in the frequency domain using the change in the natural frequency. IEEE Transactions on Antennas Propagation. Feb 2016;**64**(5):1779-1787

[77] Mroué A, Heddebaut M, Elbahhar F, Rivenq A, Rouvaen J-M. Automatic radar target recognition of objects falling on railway tracks. Measurement Science and Technology. Jan. 2012;**23**(2). DOI: 10.1088/0957-0233/23/2/025401

[78] Stenholm G, Rothwell EJ, Nyquist DP, Kempel LC, Frasch LL. E-pulse diagnostics of simple layered materials. IEEE Transactions on Antennas and Propagation. Dec. 2003; **51**(12):3221-3227

[79] Wierzba JF, Rothwell EJ. E-pulse diagnostics of curved coated conductors with varying thickness and curvature. IEEE Transactions on Antennas and Propagation. September 2006;**54**(9):2672-2676

[80] Harmer SW, Andrews DA, Rezgui ND, Bowring NJ. Detection of handguns by their complex natural resonant frequencies. IET Microwaves, Antennas and Propagation. 2010, 2010;**4**(9):1182-1190. DOI: 10.1049/iet-map.2009.0382

[81] Shlivinski A. Time domain circularly polarized antenna. IEEE Transactions on Antennas and Propagation. June 2009;**57**(6):1606-1611

[82] Aldhubaib F, Shuley NVZ, Lui HS. Characteristic polarization states in an ultra-wideband context based on singularity expansion method. IEEE Geoscience and Remote Sensing Letters. Oct. 2009;**6**(4):792-796

[83] Lui HS, Persson M. Characterization of radar targets based on ultra wideband Polarimetric transient signatures. XXX URSI General Assembly and Scientific Symposium of International Union of Radio Science. pp. 1-4. Istanbul, Turkey. 13–20 Aug. 2011

[84] Sarkar TK, Tseng FI, Rao SM, Dianat SA, Hollmann BZ. Deconvolution of impulse response from time-limited input and output: Theory and experiment. IEEE Transactions on Instrumentation and Measurement. 1985;**34**:541-546

[85] Bannawata L, Boonpoongaa A, Burintramartb S, Akkaraekthalina P. On the resolution improvement of radar target identification with filtering antenna effects. International Journal of Antennas Propagation. accepted for publication, Dec 2017

[86] Rezaiesarlak R, Manteghi M. A space–time–frequency Anticollision algorithm for identifying chipless RFID. IEEE Transactions on Antennas Propagation. Mar 2014;**62**(3):1425-1432

[87] Lee W, Sarkar TK, Moon H, Salazar-Palma M. Identification of multiple objects using their natural resonant frequencies. IEEE Antennas and Wireless Propagation Letters. 2013;**12**:54-57

[88] Lee JH, Jeong SH, Park GS, Lee YC, Cho SW. Performance analysis of natural frequency-based multiple radar target recognition for multiple-input–multiple-output radar application. IET Radar, Sonar and Navigation. June 2014;**8**(5):457-464

Chapter 8

# Anisotropic Propagation of Electromagnetic Waves

Gregory Mitchell

Additional information is available at the end of the chapter

http://dx.doi.org/10.5772/intechopen.75123

**Abstract**

This chapter will analyze the properties of electromagnetic wave propagation in anisotropic media. Of particular interest are positive index, anisotropic, and magneto-dielectric media. Engineered anisotropic media provide unique electromagnetic properties including a higher effective refractive index, high permeability with relatively low magnetic loss tangent at microwave frequencies, and lower density and weight than traditional media. This chapter presents research including plane wave solutions to propagation in anisotropic media, a mathematical derivation of birefringence in anisotropic media, modal decomposition of rectangular waveguides filled with anisotropic media, and the full derivation of anisotropic transverse resonance in a partially loaded waveguide. These are fundamental theories in the area of electromagnetic wave propagation that have been reformulated for fully anisotropic magneto-dielectric media. The ensuing results will aide interested parties in understanding wave behavior for anisotropic media to enhance designs for radio frequency devices based on anisotropic and magnetic media.

**Keywords:** anisotropic, wave propagation, dispersion, birefringence, waveguides, transverse resonance

## 1. Introduction

Recently engineered materials have come to play a dominant role in the design and implementation of electromagnetic devices and especially antennas. Metamaterials, ferrites, and magneto-dielectrics have all come to play a crucial role in advances made both in the functionality and characterization of such devices. In fact, a movement towards utilizing customized material properties to replace the functionality of traditional radio frequency (RF) components such as broadband matching circuitry, ground planes, and directive elements is apparent in the literature and not just replacement of traditional substrates and superstrates with engineered

IntechOpen

© 2018 The Author(s). Licensee IntechOpen. This chapter is distributed under the terms of the Creative Commons Attribution License (http://creativecommons.org/licenses/by/3.0), which permits unrestricted use, distribution, and reproduction in any medium, provided the original work is properly cited. CC BY

structures. A firm theoretical understanding of the electromagnetic properties of these materials is necessary for both design and simulation of new and improved RF devices.

Inherently, many of these engineered materials have anisotropic properties. Previously, the study of anisotropy had been limited mostly to the realm of optical frequencies where the phenomenon occurs naturally in substances such as liquid crystals and plasmas. However, the recent development of the aforementioned engineered materials has encouraged the study of electromagnetic anisotropy for applications at megahertz (MHz) and gigahertz (GHz) frequencies.

For the purposes of this chapter, an anisotropic electromagnetic medium defines permittivity ($\underline{\underline{\varepsilon_r}}$) and permeability $\underline{\underline{\mu_r}}$ as separate tensors where the values differ in all three Cartesian directions ($\varepsilon_x \neq \varepsilon_y \neq \varepsilon_z$ and $\mu_x \neq \mu_y \neq \mu_z$). This is known as the biaxial definition of anisotropic material which is more encompassing than the uniaxial definition which makes the simplifying assumption that $\varepsilon_x = \varepsilon_y = \varepsilon_t$ and $\mu_x = \mu_y = \mu_t$. The anisotropic definition also differs from the traditional isotropic definition where $\varepsilon_r$ and $\mu_r$ are the same in all three Cartesian directions defining each by a single value. For the definition of the tensor equations see Section 3.1. Anisotropic media yield characteristics such as conformal surfaces, focusing and refraction of electromagnetic waves as they propagate through a material, high impedance surfaces for artificial magnetic conductors as well as high index, low loss, and lightweight ferrite materials. The following sections aim to discuss in more detail some RF applications directly impacted by the incorporation of anisotropic media and also give a firm understanding of electromagnetic wave propagation as it applies to anisotropic media for different RF applications.

## 2. Applications of anisotropy in radio frequency devices

Traditionally, the study of anisotropic properties was limited to a narrow application space where traditional ferrites, which exhibit natural anisotropy were the enabling technology. These types of applications included isolators, absorbers, circulators and phase shifters [1]. Traditional ferrites are generally very heavy and very lossy at microwave frequencies which are the two main limiting factors narrowing their use in RF devices; however, propagation loss is an important asset to devices such as absorbers. Anisotropy itself leads to propagation of an RF signal in different directions, which is important in devices such as circulators and isolators [1]. For phase shifters and other control devices the microwave signal is controlled by changing the bias field across the ferrite [1, 2]. However, newer versions of some of these devices, utilizing FETs and diodes in the case of phase shifters, rely on isotropic media to enable higher efficiency devices.

As early as 1958, Collin showed that at microwave frequencies, where the wavelength is larger, it is possible to fabricate artificial dielectric media having anisotropic properties [3]. This has led some to investigate known theoretical solutions to typical RF problems, such as a microstrip patch antenna, and extend them utilizing anisotropic wave propagation in dielectric media [4, 5]. The anisotropic dielectric antenna shows interesting features of basic antenna applications featuring anisotropic substrates. While these solutions establish a framework for electromagnetic wave propagation in anisotropic media, they simplify the problem by necessarily setting $\mu_r$ to 1 and only focusing on dielectric phenomena of anisotropy.

The concept of artificial media is also exemplified by the proliferation of metamaterials research over the last few decades. Metamaterials incorporate the use of artificial microstructures made of subwavelength inclusions that are usually implemented with periodic and/or multilayered structures known as unit cells [6]. These devices operate where the wavelength is much larger than the characteristic dimensions of the unit cell elements. One characteristic feature of some types of metamaterials is wave propagation anisotropy [7]. Anisotropic metamaterials are used in applications such as directive lensing [8, 9], cloaking [10], electronic beam steering [11], and metasurfaces [12] among others.

Finally, a class of engineered materials exists that exhibits positive refractive index, anisotropy, and magneto-dielectric properties with reduced propagation loss at microwave frequencies compared to traditional ferrites. These materials show the unique ability to provide broadband impedance matches for very low profile antennas by exploiting the inherent anisotropy to redirect surface waves thus improving the impedance match of the antenna when very close to a ground plane. Antenna profile on the orders of a twentieth and a fortieth of a wavelength have been demonstrated using these materials with over an octave of bandwidth and positive realized gain [13, 14].

## 3. Plane wave solutions in an anisotropic medium

The recent development of low loss anisotropic magneto-dielectrics greatly expands the current antenna design space. Here we present a rigorous derivation of the wave equation and dispersion relationships for anisotropic magneto-dielectric media. All results agree with those presented by Meng et al. [15, 16]. Furthermore, setting $\underline{\underline{\mu_r}} = \underline{\underline{I}}$, where $\underline{\underline{I}}$ is the identity matrix, yields results that agree with those presented by Pozar and Graham for anisotropic dielectric media [4, 5]. This section and the following section expand on the results presented by Meng et al., Pozar and Graham. Incorporating a fully developed derivation of anisotropic properties of both $\underline{\underline{\varepsilon_r}}$ and $\underline{\underline{\mu_r}}$ expands upon the simplification imposed by both Pozar and Graham that uses an isotropic value of $\mu_r = 1$. An expansion on the results of Meng et al. given in Section 4 develops the waveguide theory including a full modal decomposition utilizing the biaxial definition of anisotropy versus their simplified uniaxial definition. The derivation of anisotropic cavity resonance in Section 4 differs from that of Meng et al. by addressing the separate issue of how the direct relationship of an arbitrary volume of anisotropic material will distort the geometry of a cavity to maintain resonance at a given frequency. This property is especially important for the design of conformal cavity backed antennas for ground and air-based vehicle mobile vehicular platforms. Furthermore, the analysis of anisotropic properties is not restricted to double negative (DNG) materials, which is the case for both of the Meng et al. studies.

### 3.1. Source free anisotropic wave equation

In order to solve for the propagation constants, we will need to formulate the dispersion relationship from the anisotropic wave equation. This allows us to solve for the propagation constant in the normal direction of the anisotropic medium. We start with the anisotropic, time harmonic form of Maxwell's source free equations for the electric and magnetic fields $\underline{E}$ and $\underline{H}$

$$\nabla x\underline{E} = j\omega\mu_o\underline{\underline{\mu_r}} \cdot \underline{H}, \tag{1}$$

$$\nabla x\underline{H} = -j\omega\varepsilon_o\underline{\underline{\varepsilon_r}} \cdot \underline{E}, \tag{2}$$

where $\omega$ is the frequency in radians, $\varepsilon_o$ is the permittivity of free space, $\mu_o$ is the permeability of free space, $\underline{E} = \underline{x}_o E_x + \underline{y}_o E_y + \underline{z}_o E_z$ and $\underline{H} = \underline{x}_o H_x + \underline{y}_o H_y + \underline{z}_o H_z$. We define $\underline{\underline{\mu_r}}$ and $\underline{\underline{\varepsilon_r}}$ as

$$\underline{\underline{\varepsilon_r}} = \begin{bmatrix} \varepsilon_x & 0 & 0 \\ 0 & \varepsilon_y & 0 \\ 0 & 0 & \varepsilon_z \end{bmatrix}, \tag{3}$$

$$\underline{\underline{\mu_r}} = \begin{bmatrix} \mu_x & 0 & 0 \\ 0 & \mu_y & 0 \\ 0 & 0 & \mu_z \end{bmatrix}. \tag{4}$$

Applying Eqs. (3) and (4) to Eqs. (1) and (2) yields the following

$$\underline{x}_o\left(\frac{dE_Z}{dy} - \frac{dE_Y}{dz}\right) + \underline{y}_o\left(\frac{dE_X}{dz} - \frac{dE_Z}{dx}\right) + \underline{z}_o\left(\frac{dE_Y}{dx} - \frac{dE_X}{dy}\right) = -j\omega\mu_o\left(\mu_x H_X\underline{x}_o + \mu_y H_Y\underline{y}_o + \mu_z H_Z\underline{z}_o\right), \tag{5}$$

$$\underline{x}_o\left(\frac{dH_Z}{dy} - \frac{dH_Y}{dz}\right) + \underline{y}_o\left(\frac{dH_X}{dz} - \frac{dH_Z}{dx}\right) + \underline{z}_o\left(\frac{dH_Y}{dx} - \frac{dH_X}{dy}\right) = j\omega\varepsilon_o\left(\varepsilon_x E_X\underline{x}_o + \varepsilon_y E_Y\underline{y}_o + \varepsilon_z E_Z\underline{z}_o\right). \tag{6}$$

Using the radiation condition, we assume a solution of $\underline{E}(x, y, z) = \underline{E}(x, y)e^{-jk_z z}$ [17]. Now isolate the individual components of (5) by taking the dot product with $\underline{x}_o$, $\underline{y}_o$, and $\underline{z}_o$ respectively. This operation yields the following equations

$$(d/dy)E_z - jk_z E_y = -j\omega\mu_o\mu_x H_x, \tag{7}$$

$$jk_z E_x - (d/dx)E_z = -j\omega\mu_o\mu_y H_y, \tag{8}$$

$$(d/dx)E_y - (d/dy)E_x = -j\omega\mu_o\mu_z H_z. \tag{9}$$

Assuming a solution of $\underline{H}(x, y, z) = \underline{H}(x, y)e^{-jk_z z}$ for (6), the same procedure yields [17]

$$(d/dy)H_z - jk_z H_y = j\omega\varepsilon_o\varepsilon_x E_x, \tag{10}$$

$$jk_z H_x - (d/dx)H_z = j\omega\varepsilon_o\varepsilon_y E_y, \tag{11}$$

$$(d/dx)H_y - (d/dy)H_x = -j\omega\mu_o\mu_z H_z. \tag{12}$$

Using (7)–(12) allows for the transverse field components of the electric and magnetic fields in terms of the derivatives of $H_z$ and $E_z$ as

$$E_x = -\frac{j}{k_o^2\mu_y\varepsilon_x - k_z^2}\left(\omega\mu_o\mu_y(d/dy)H_z + k_z(d/dx)E_z\right), \tag{13}$$

$$E_y = \frac{j}{k_o^2\mu_x\varepsilon_y - k_z^2}\left(\omega\mu_o\mu_x(d/dx)H_z - k_z(d/dy)E_z\right), \tag{14}$$

$$H_x = \frac{j}{k_o^2\mu_x\varepsilon_y - k_z^2}\left(\omega\varepsilon_o\varepsilon_y(d/dy)E_z - k_z(d/dx)H_z\right), \tag{15}$$

$$H_y = -\frac{j}{k_o^2\mu_y\varepsilon_x - k_z^2}(\omega\varepsilon_o\varepsilon_x(d/dx)E_z + k_z(d/dy)H_z). \tag{16}$$

The relationships for the transverse field components, applied to (1) and (2), yield the following solutions for $\underline{\boldsymbol{H}}$ and $\underline{\boldsymbol{E}}$, respectively

$$\underline{H} = -\left(\underline{\underline{\mu_r}}^{-1}/j\omega\varepsilon_o\right)\cdot(\nabla x\underline{E}), \tag{17}$$

$$\underline{E} = \left(\underline{\underline{\varepsilon_r}}^{-1}/j\omega\varepsilon_o\right)\cdot(\nabla x\underline{H}). \tag{18}$$

Taking the cross product of both sides and substituting (1) and (2) for the right hand side of (17) and (18) yields

$$\nabla x\underline{\underline{\varepsilon_r}}^{-1}\cdot(\nabla x\underline{H}) = k_o^2\underline{\underline{\mu_r}}\cdot\underline{H}, \tag{19}$$

$$\nabla x\underline{\underline{\mu_r}}^{-1}\cdot(\nabla x\underline{E}) = -k_o^2\underline{\underline{\varepsilon_r}}\cdot\underline{E}. \tag{20}$$

Equations (19) and (20) represent the vector wave equations in an anisotropic medium [12].

### 3.2. Dispersion equation for $H_z$

We expand (19) in terms of (13)–(16)

$$\nabla x\left\{\frac{\underline{x}_o}{\varepsilon_x}\left[(d/dy)H_Z - (d/dz)H_y\right] + \frac{\underline{y}_o}{\varepsilon_y}\left[(d/dz)H_x - (d/dx)H_z\right] + \frac{\underline{z}_o}{\varepsilon_z}\left[(d/dx)H_y - (d/dy)H_x\right]\right\} = k_o^2\underline{\underline{\mu_r}}\cdot\underline{H}, \tag{21}$$

Evaluating the remaining cross product of (21) yields the final form of the expanded wave equation

$$\underline{x}_o\Pi_x + \underline{y}_o\Pi_y + \underline{z}_o\Pi_z = k_o^2\underline{\underline{\mu_r}}\cdot\underline{H}, \tag{22}$$

$$\Pi_x = \left[\left(d^2/dxdy\right)H_y - \left(d^2/dy^2\right)H_x\right]/\varepsilon_z - \left[\left(d^2/dz^2\right)H_x - \left(d^2/dxdz\right)H_z\right]/\varepsilon_y, \tag{23}$$

$$\Pi_y = \left[\left(d^2/dydz\right)H_z - \left(d^2/dz^2\right)H_y\right]/\varepsilon_x - \left[\left(d^2/dx^2\right)H_y - \left(d^2/dxdy\right)H_x\right]/\varepsilon_z, \tag{24}$$

$$\Pi_z = \left[\left(d^2/dxdz\right)H_x - \left(d^2/dx^2\right)H_z\right]/\varepsilon_y - \left[\left(d^2/dy^2\right)H_z - \left(d^2/dxdy\right)H_x\right]/\varepsilon_x. \tag{25}$$

Taking the dot product of (22) with $\underline{z}_o$ allows the isolation of $H_z$ on the right hand side of the equation in terms of (265 on the left hand side

$$\left[\left(d^2/dydz\right)H_y - \left(d^2/dy^2\right)H_z\right]/\varepsilon_x - \left[\left(d^2/dx^2\right)H_z + \left(d^2/dxdz\right)H_x\right]/\varepsilon_y = k_o^2\mu_z H_z, \tag{26}$$

By keeping in mind that $d/dz = -jk_z$, setting $E_z = 0$, and differentiating (15) and (16) by $d^2/dxdz$ and $d^2/dydz$, produces the following result

$$\left[\frac{k_z^2}{\varepsilon_y\left(k_z^2 - k_o^2\varepsilon_y\mu_x\right)} - \frac{1}{\varepsilon_y}\right]\left(d^2/dx^2\right)H_z + \left[\frac{k_z^2}{\varepsilon_x\left(k_z^2 - k_o^2\varepsilon_x\mu_y\right)} - \frac{1}{\varepsilon_x}\right]\left(d^2/dy^2\right)H_z = k_o^2\mu_z H_z. \tag{27}$$

Combining the $d^2H_z/dx^2$ and $d^2H_z/dy^2$ terms in (27) gives the following second order differential dispersion equation for $H_z$

$$\frac{k_o^2\mu_x}{k_o^2\mu_x\varepsilon_y - k_z^2}\left(d^2/dx^2\right)H_z + \frac{k_o^2\mu_y}{k_o^2\mu_y\varepsilon_x - k_z^2}\left(d^2/dy^2\right)H_z + k_o^2\mu_z H_z = 0. \tag{28}$$

### 3.3. Dispersion equation for $E_z$

Expanding the $\nabla x\underline{E}$ term of (18) in terms of (13)–(16) yields

$$\begin{aligned}\nabla x\Big\{&\underline{x}_o[(d/dy)E_Z - (d/dz)E_Y]/\mu_x + \underline{y}_o[(d/dz)E_X - (d/dx)E_Z]/\mu_y \\ &+\underline{z}_o[(d/dx)E_Y - (d/dy)E_X]/\mu_z\Big\} = k_o^2\underline{\varepsilon}_r\cdot\underline{E}.\end{aligned} \tag{29}$$

Evaluating the remaining cross product of (29) gives the final form of the expanded wave equation

$$\underline{x}_o\xi_x + \underline{y}_o\xi_y + \underline{z}_o\xi_z = k_o^2\underline{\varepsilon}_r\cdot\underline{E}, \tag{30}$$

$$\xi_x = \left[\left(d^2/dxdy\right)E_Y - \left(d^2/dy^2\right)E_x\right]/\mu_z - \left[\left(d^2/dz^2\right)E_x - \left(d^2/dxdz\right)E_z\right]/\mu_y, \tag{31}$$

$$\xi_y = \left[\left(d^2/dydz\right)E_z - \left(d^2/dz^2\right)E_y\right]/\mu_x - \left[\left(d^2/dx^2\right)E_y - \left(d^2/dxdy\right)E_x\right]/\mu_z, \tag{32}$$

$$\xi_z = \left[\left(d^2/dxdz\right)E_x - \left(d^2/dx^2\right)E_z\right]/\mu_y - \left[\left(d^2/dy^2\right)E_z - \left(d^2/dydz\right)E_y\right]/\mu_x. \tag{33}$$

Taking the dot product of (30) with $\underline{z}_o$ allows isolation of the $E_z$ component on the right hand side of the equation in terms of (33) on the left hand side

$$\left[\left(d^2/dxdz\right)E_x - \left(d^2/dx^2\right)E_z\right]/\mu_y + \left[\left(d^2/dydz\right)E_y - \left(d^2/dy^2\right)E_z\right]/\mu_x = k_o^2\varepsilon_z E_z, \tag{34}$$

Keeping in mind that $d/dz = -jk_z$, setting $H_z = 0$, and differentiating (15) and (16) by $d^2/dxdz$ and $d^2/dydz$ produces the following result

$$\left[\frac{k_z^2}{\mu_y\left(k_z^2-k_o^2\mu_y\varepsilon_x\right)}-\frac{1}{\mu_y}\right]\left(d^2/dx^2\right)E_z+\left[\frac{k_z^2}{\mu_x\left(k_z^2-k_o^2\mu_x\varepsilon_y\right)}-\frac{1}{\mu_x}\right]\left(d^2/dy^2\right)E_z=k_o^2\varepsilon_z E_z. \tag{35}$$

Combining the $d^2E_z/dx^2$ and $d^2E_z/dy^2$ terms in (35) gives the following second order differential dispersion equation for $E_z$

$$\frac{k_o^2\varepsilon_x}{k_o^2\mu_y\varepsilon_x-k_z^2}\left(d^2/dx^2\right)E_z+\frac{k_o^2\varepsilon_y}{k_o^2\mu_x\varepsilon_y-k_z^2}\left(d^2/dy^2\right)E_z+k_o^2\varepsilon_z E_z=0. \tag{36}$$

### 3.4. Transmission and reflection from an anisotropic half-space

Birefringence is a characteristic of anisotropic media where a single incident wave entering the boundary of an anisotropic medium gives rise to two refracted waves as shown in **Figure 1** or a single incident wave leaving gives rise to two reflected waves as shown in **Figure 2**. We call these two waves the ordinary wave and the extraordinary wave. To see how the anisotropy of a medium gives rise to the birefringence phenomenon, Eqs. (28) and (36) will yield a solution for $k_z$ in the medium.

Equations (28) and (36) yield the following solutions in unbounded anisotropic media restricted by the radiation condition in all three dimensions

$$E_z(x,y,z)=E_o e^{-j\left(k_x x+k_y y+k_z z\right)}, \tag{37}$$

$$H_z(x,y,z)=H_o e^{-j\left(k_x x+k_y y+k_z z\right)}. \tag{38}$$

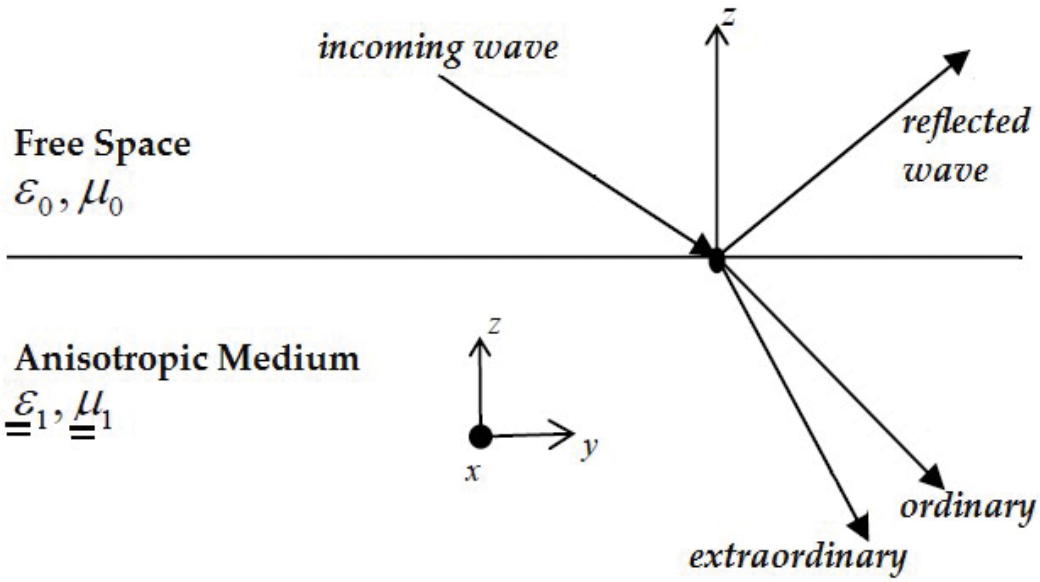


**Figure 1.** A plane wave incident from free space on an anisotropic boundary.

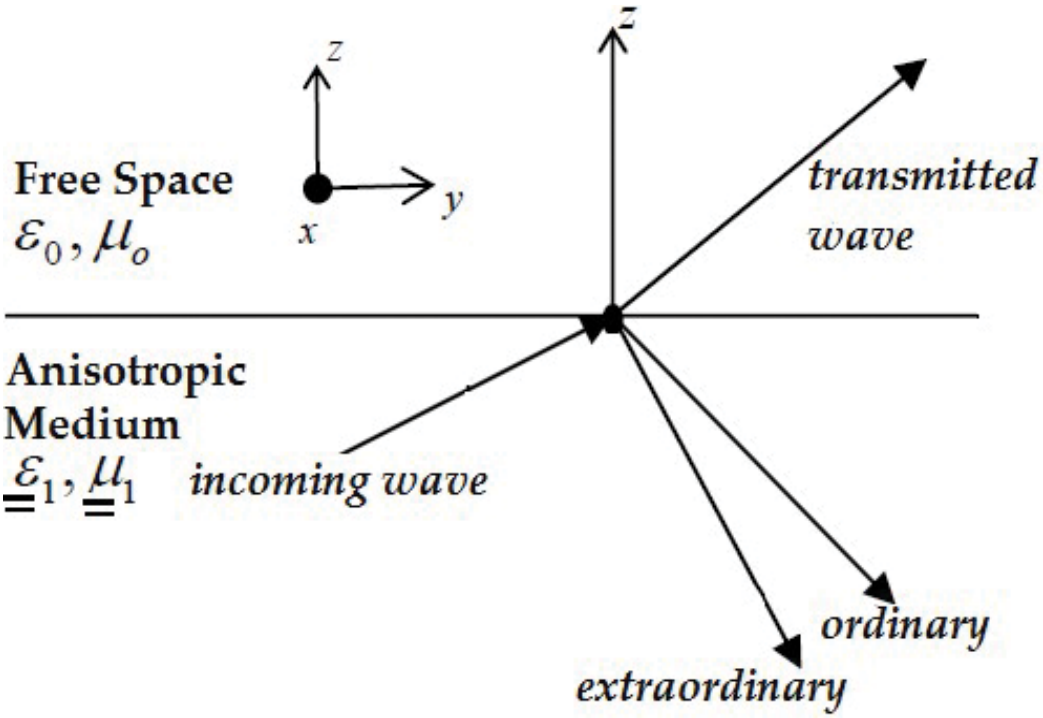


**Figure 2.** A plane wave incident from an anisotropic medium on a free space boundary.

Plugging (37) into (36) (equivocally we could substitute (38) into (19)) allows the generation of a polynomial equation whose solutions give the values of $k_z$ in the anisotropic medium. Noting that $d^2/dx^2 = -k_x^2$ and $d^2/dy^2 = -k_y^2$, (36) simplifies as

$$k_o^2 k_x^2 \varepsilon_x E_z / \left(k_o^2 \mu_y \varepsilon_x - k_z^2\right) + k_o^2 \varepsilon_y k_y^2 E_z / \left(k_o^2 \mu_x \varepsilon_y - k_z^2\right) - k_o^2 \varepsilon_z E_z = 0. \tag{39}$$

Dividing out the $k_o^2 E_z$term and multiplying through by both denominators gives us the following factored polynomial

$$\left(k_o^2 \mu_y \varepsilon_x - k_z^2\right)\left(k_o^2 \mu_x \varepsilon_y - k_z^2\right)\varepsilon_z - k_x^2 \varepsilon_x \left(k_o^2 \mu_x \varepsilon_y - k_z^2\right) - \varepsilon_y k_y^2 \left(k_o^2 \mu_y \varepsilon_x - k_z^2\right) = 0. \tag{40}$$

Finally, multiplying out (40) yields a fourth order polynomial whose roots yield the four values of $k_z$ describing the ordinary wave and extraordinary wave in the positive and negative propagation directions

$$k_z^4 \mu_z + \left[k_x^2 \mu_x + k_y^2 \mu_y - \left(\varepsilon_x \mu_y + \varepsilon_y \mu_x\right) k_o^2 \mu_z\right] k_z^2 + \left[k_o^4 \varepsilon_x \varepsilon_y \mu_x \mu_y \mu_z - k_o^2 k_x \varepsilon_x \mu_y \mu_x - k_o^2 \varepsilon_y k_y \mu_x \mu_y\right] = 0. \tag{41}$$

Equation (41) is directly responsible for the existence of the extraordinary wave that is characteristic of the birefringence phenomenon. In an isotropic medium, the resulting polynomial for

$k_z$ is a second order polynomial, which yields only the values for the positive and negative propagation of the single ordinary wave.

## 4. Anisotropic rectangular waveguide

Electromagnetic wave behavior of waveguides is well understood in the literature. The mode within a waveguide that are based on the voltage and current distributions within the waveguide make up the basis for the electric and magnetic field calculations. This section derives similar formulations for a rectangular waveguide uniformly filled with an anisotropic medium as shown in **Figure 3**. **Figure 3** shows propagation in the $\underline{z}_o$-direction along the length of the waveguide. Rectangular waveguides are most commonly used for material measurement and characterization, and therefore understanding how electromagnetic waves propagate in an anisotropic waveguide is important for material characterization purposes. Furthermore, this section shows how the anisotropic derivation of waveguide behavior parallels that of a typical waveguide, and therefore how anisotropy may be applied to other waveguide geometries.

### 4.1. Anisotropic mode functions

Assume source free Maxwell's equations in the same form as (1) and (2). Then the transverse electromagnetic fields are defined

$$\underline{E}_{Tv}(x,y,z) = \sum_m \sum_n \left[V'_v(z)\underline{e}'_v(x,y) + V''_v(z)\underline{e}''_v(x,y)\right], \tag{42}$$

$$\underline{H}_{Tv}(x,y,z) = \sum_m \sum_n \left[I'_v(z)\underline{h}'_v(x,y) + I''_v(z)\underline{h}''_v(x,y)\right], \tag{43}$$

$$V_v(z) = V_o e^{-jk_z z}, \tag{44}$$

$$I_v(z) = I_o e^{-jk_z z}, \tag{45}$$

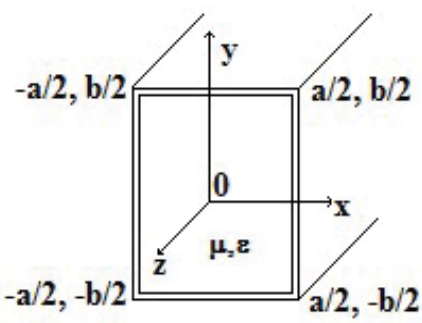


**Figure 3.** Cross section of a closed rectangular waveguide filled with anisotropic metamaterial and surrounded by PEC walls.

where $\underline{E}_T$ and $\underline{H}_T$ are the transverse electric and magnetic fields, $V(z)$ and $I(z)$ are the voltage and current at point $z$, $e$ and $h$ are the waveguide mode equations, and $\upsilon \in [m, n]$ is the mode number defined by the two indices $m$ and $n$.

### *4.1.1. Incident TE mode*

Assuming only a TE type mode in the waveguide sets $E_z = 0$. Then (13)–(16) become

$$E''_{x\upsilon} = -j\omega\mu_o\mu_y(d/dy)\,H''_{z\upsilon}/\left(k_o^2\mu_y\varepsilon_x - k_{z\upsilon}^2\right), \tag{46}$$

$$E''_{y\upsilon} = j\omega\mu_o\mu_x(d/dx)\,H''_{z\upsilon}/\left(k_o^2\mu_x\varepsilon_y - k_{z\upsilon}^2\right), \tag{47}$$

$$H''_{y\upsilon} = -jk_{z\upsilon}^2(d/dx)\,H''_{z\upsilon}/\left(k_o^2\mu_x\varepsilon_y - k_{z\upsilon}^2\right), \tag{48}$$

$$H''_{y\upsilon} = -jk_{z\upsilon}^2(d/dy)\,H''_{z\upsilon}/\left(k_o^2\mu_y\varepsilon_x - k_{z\upsilon}^2\right). \tag{49}$$

To solve for $H''_{z\upsilon}$ we formulate the anisotropic wave equation from (1) and (2) where (52) resembles (19)

$$\nabla\times\nabla\times\underline{H} = j\omega\varepsilon_o\underline{\underline{\varepsilon_r}}\cdot\left(-j\omega\mu_o\underline{\underline{\mu_r}}\cdot\underline{H}\right), \tag{50}$$

$$\nabla\times\nabla\times\underline{H} = j\omega\varepsilon_o\underline{\underline{\varepsilon_r}}\cdot(\nabla\times\underline{E}), \tag{51}$$

$$\nabla\times\underline{\underline{\varepsilon_r}}^{-1}\cdot(\nabla\times\underline{H}) = k_o^2\underline{\underline{\mu_r}}\cdot\underline{H}. \tag{52}$$

Expanding the curl of (52)

$$\begin{bmatrix} \frac{1}{\varepsilon_z}\frac{d\chi''_{z\upsilon}}{dy} - \frac{1}{\varepsilon_y}\frac{d\chi''_{y\upsilon}}{dz} & 0 & 0 \\ 0 & \frac{1}{\varepsilon_x}\frac{d\chi''_{x\upsilon}}{dz} - \frac{1}{\varepsilon_z}\frac{d\chi''_{z\upsilon}}{dx} & 0 \\ 0 & 0 & \frac{1}{\varepsilon_y}\frac{d\chi''_{y\upsilon}}{dx} - \frac{1}{\varepsilon_x}\frac{d\chi''_{x\upsilon}}{dy} \end{bmatrix}\begin{bmatrix}1\\1\\1\end{bmatrix} = k_o^2\begin{bmatrix}\mu_x H''_{x\upsilon}\\ \mu_y H''_{y\upsilon}\\ \mu_z H''_{z\upsilon}\end{bmatrix}, \tag{53}$$

$$\chi''_{x\upsilon} = (d/dy)H''_{z\upsilon} - (d/dz)H''_{y\upsilon}, \tag{54}$$

$$\chi''_{y\upsilon} = (d/dz)H''_{x\upsilon} - (d/dx)H''_{z\upsilon}, \tag{55}$$

$$\chi''_{z\upsilon} = (d/dx)H''_{y\upsilon} - (d/dy)H''_{x\upsilon}. \tag{56}$$

Isolating the $\underline{z}_o$-component of (53) gives the following relationship for $H''_{z\upsilon}$

$$\left[\left(d^2/dxdz\right)H''_{x\upsilon} - \left(d^2/dx^2\right)H''_{z\upsilon}\right]/\varepsilon_y + \left(\left(d^2/dydz\right)H''_{y\upsilon} - \left(d^2/dy^2\right)H''_{z\upsilon}\right)/\varepsilon_x - k_o^2\mu_z H''_{z\upsilon} = 0, \tag{57}$$

and substituting (48) and (49) for $H_{xv}^{''}$ and $H_{yv}^{''}$ yields the following differential equation that can be solved for $H_{zv}^{''}$

$$k_o^2\mu_x\left(d^2/dx^2\right)H_{zv}''/\left(k_o^2\mu_x\varepsilon_y - k_{zv}^2\right) + k_o^2\mu_y\left(d^2/dy^2\right)H_{zv}''/\left(k_o^2\mu_y\varepsilon_x - k_{zv}^2\right) + k_o^2\mu_z H_{zv}'' = 0. \tag{58}$$

Assuming a solution of the form

$$H_{zv}'' = H_o\cos(k_{xv}x)\cos\left(k_{yv}y\right)e^{-jk_{zv}z}, \tag{59}$$

$$k_{xv} = m\pi/a, \tag{60}$$

$$k_{yv} = n\pi/b, \tag{61}$$

which meets the boundary conditions at the PEC walls of the waveguide, then plugging (58) into (53) imposes the following restriction on the values of the tensors in (3) and (4)

$$\mu_x k_{xv}^2/\left(k_o^2\mu_x\varepsilon_y - k_{zv}^2\right) + \mu_y k_{yv}^2/\left(k_o^2\mu_y\varepsilon_x - k_{zv}^2\right) = \mu_z. \tag{62}$$

Solving (62) for $k_{zv}$ gives the following equation which yields four solutions to the propagation constant for the ordinary and extraordinary waves described in Section 3.4

$$\begin{aligned} k_{zv}^2 = \Big\{ & k_o^2\left(\mu_x\varepsilon_y + \mu_y\varepsilon_x\right) - k_{xv}^2\mu_x/\mu_z - k_{yv}^2\mu_y/\mu_z \\ & \pm\sqrt{4k_{xv}^2k_{yv}^2\mu_x\mu_y/\mu_z^2 + \left[k_o^2\left(\mu_x\varepsilon_y - \mu_y\varepsilon_x\right) - k_{xv}^2\mu_x/\mu_z + k_{yv}^2\mu_y/\mu_z\right]^2}\Big\}\Big/2. \end{aligned} \tag{63}$$

Equations (62) and (63) provide the criteria for determining the cutoff frequency for the propagation of modes inside the waveguide. Plugging (59) into (46)–(49) yields the following equations for the TE mode vectors in (42) and (43)

$$\begin{aligned} \underline{e}_v''(x,y) = j\omega\mu_o H_o\Big[ & \underline{x}_o\mu_y k_{yv}\cos(k_{xv}x)\sin\left(k_{yv}y\right)/\left(k_o^2\mu_y\varepsilon_x - k_{zv}^2\right) \\ & -\underline{y}_o\mu_x k_{xv}\sin(k_{xv}x)\cos\left(k_{yv}y\right)/\left(k_o^2\mu_x\varepsilon_y - k_{zv}^2\right)\Big], \end{aligned} \tag{64}$$

$$\begin{aligned} \underline{h}_v''(x,y) = jk_{zv}H_o\big[ & \underline{x}_o k_{xv}\sin(k_{xv}x)\cos\left(k_{yv}y\right)/\left(k_o^2\mu_x\varepsilon_y - k_{zv}^2\right) \\ & +\underline{y}_o k_{yv}\cos(k_{xv}x)\sin\left(k_{yv}y\right)/\left(k_o^2\mu_y\varepsilon_x - k_{zv}^2\right)\Big]. \end{aligned} \tag{65}$$

*4.1.2. Incident TM mode*

Assuming only a TM type mode in the waveguide sets $H_z = 0$. Then (13)–(16) become

$$E_{xv}' = -jk_{zv}(d/dx)E_{zv}'/\left(k_o^2\mu_y\varepsilon_x - k_{zv}^2\right), \tag{66}$$

$$E_{yv}' = -jk_{zv}(d/dy)E_{zv}'/\left(k_o^2\mu_x\varepsilon_y - k_{zv}^2\right), \tag{67}$$

$$H_{xv}^{'} = j\omega\varepsilon_o\varepsilon_y(d/dy)E_{zv}^{'}/\left(k_o^2\mu_x\varepsilon_y - k_{zv}^2\right), \tag{68}$$

$$H_{yv}^{'} = -j\omega\varepsilon_o\varepsilon_x(d/dx)E_{zv}^{'}/\left(k_o^2\mu_y\varepsilon_x - k_{zv}^2\right). \tag{69}$$

Solving (66)–(69) for $E_z$ and substituting (1) for $\nabla \times \underline{H}$ formulates the anisotropic wave equation for $\underline{E}$ where (72) resembles (20)

$$\nabla \times \nabla \times \underline{E} = -j\omega\mu_o\underline{\underline{\mu_r}} \cdot (\nabla \times \underline{H}), \tag{70}$$

$$\nabla \times \nabla \times \underline{E} = -j\omega\mu_o\underline{\underline{\mu_r}} \cdot \left(j\omega\varepsilon_o\underline{\underline{\varepsilon_r}} \cdot \underline{E}\right), \tag{71}$$

$$\nabla \times \underline{\underline{\mu_r}}^{-1} \cdot (\nabla \times \underline{E}) = k_o^2\underline{\underline{\varepsilon_r}} \cdot \underline{E}. \tag{72}$$

Equation (72) represents the anisotropic wave equation for the time harmonic electric field. Expanding the curl of (72) and isolating the $\underline{z}_o$ component as we did for $H_z$ in Section 4.1.1 yields the following solution for the $E_z$ component

$$E_{zv}^{'} = E_o\sin(k_{xv}x)\sin\left(k_{yv}y\right)e^{-jk_{zv}z}. \tag{73}$$

Plugging (73) into (66)–(69) yields the following equations for the TM mode vectors in (42) and (43)

$$\underline{e}_v^{'}(x,y) = -jk_{zv}E_o\left[\underline{x}_o k_{xv}\cos(k_{xv}x)\sin\left(k_{yv}y\right)/\left(k_o^2\mu_y\varepsilon_x - k_{zv}^2\right) + \underline{y}_o\sin(k_{xv}x)\cos\left(k_{yv}y\right)/\left(k_o^2\mu_y\varepsilon_x - k_{zv}^2\right)\right], \tag{74}$$

$$\underline{h}_v^{'}(x,y) = j\omega\varepsilon_o E_o\left[\underline{x}_o\varepsilon_y k_{yv}\sin(k_{xv}x)\cos\left(k_{yv}y\right)/\left(k_o^2\mu_x\varepsilon_y - k_{zv}^2\right) - \underline{y}_o\varepsilon_x k_{xv}\cos(k_{xv}x)\sin\left(k_{yv}y\right)/k_o^2\mu_y\varepsilon_x - k_{zv}^2\right]. \tag{75}$$

### 4.2. Anisotropic transverse resonance

This section describes the derivation of an anisotropic transverse resonance condition established between resonant walls of a rectangular waveguide. Assume an infinite rectangular waveguide partially loaded with an anisotropic medium, then $w(z)$ represents the width of the anisotropic medium at any point $z$ along the direction of propagation as shown in **Figure 4**.

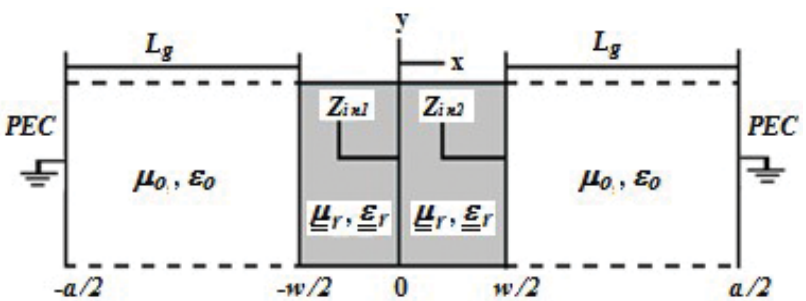


**Figure 4.** Symmetrically loaded transmission line model with a short at either end.

At any length $z$ along the waveguide, the assumption that the horizontal distance between two resonant walls represented as a partially filled parallel plate waveguide is a valid presumption. We can calculate $L_g(z)$ as the unknown distance between the edge of the anisotropic medium and the cavity wall based on a transverse resonance condition in the $\underline{x}_o$-direction. However, we first need to derive the characteristic impedance of the anisotropic region in the transmission line model.

#### *4.2.1. Electromagnetic fields in free space regions*

Calculating the fields in the free space region of the waveguide begins with Maxwell's source free Eqs. (1) and (2) and the equations for the individual vector components of the electromagnetic fields (13)–(16). Using the standard derivation of the wave equation for $H_z$ in free space from (1) and (2) shows

$$\nabla_T \times \nabla_T \times \underline{H}_v = j\omega\varepsilon_o\left(\nabla_T \times \underline{E}_v\right) = \nabla_T(\nabla_T \cdot \underline{H}_v) - \nabla_T^2 H_{zv}, \tag{76}$$

$$j\omega\varepsilon_o\left(-j\omega\mu_o H_{zv}\right) + \nabla_T^2 H_{zv} = 0, \tag{77}$$

$$\left[\left(d^2/dx^2\right) + \left(d^2/dy^2\right) + k_o^2\right]H_{zv} = 0. \tag{78}$$

Utilizing (52) and setting $k_{zo} = 0$ due to the assumption of the transverse resonance condition in the free space region of the waveguide will lead to the solution to $H_z$. Assuming the dominate mode to be $TE_{10}$ because $a \geq 2b$, then $k_{yo} = 0$ for the first resonance at cutoff [1]. With $k_{yo} = 0$ no variation of the fields in the $\underline{y}_o$ direction and $(d^2/dy^2)H_z = 0$ then (78) becomes

$$\left(d^2/dx^2 + k_o^2\right)H_z = 0. \tag{79}$$

Equation (80) is a standard differential equation with a known solution [17]

$$H_{zv} = Ae^{-jk_o x} + Be^{+jk_o x}, \tag{80}$$

where $A$ and $B$ are yet to be determined coefficients. Substituting (80) into (13)–(16) yields the expression for $E_y$

$$E_y = k_o\omega\mu_o\left(Ae^{-jk_o x} - Be^{+jk_o x}\right)/k_o^2 = Z_o\left(Ae^{-jk_o x} - Be^{+jk_o x}\right). \tag{81}$$

Accounting for the restrictions imposed by the transverse resonance conditions on $E_z$, $k_{zo}$ and $k_{yo}$, then $E_x = 0$, $H_x = 0$ and $H_y = 0$ as well.

#### *4.2.2. Electromagnetic fields in anisotropic region*

Starting with (1) and (2) for the source free Maxwell's equations in an anisotropic medium, the vector components (13)–(16) led to the derivation of the dispersion Eqs. (26) and (38) for $H_z$ and $E_z$, respectively.

The cutoff frequency or resonance of a rectangular waveguide is determined when the propagation constant in the direction of resonance, in the case the $\underline{x}_o$-direction, is 0 [1]. By definition, when the waveguide's dominant mode $\upsilon = 1$ propagates, then $k_{x1} > 0$ and the guide is resonant whereas when the mode attenuates then $k_{x1} < 0$ and there is no resonance. Therefore, the resonance first manifests itself when $k_{x1} = 0$. For the dominate mode to be $TE_{10}$ then $a \geq 2b$ and $d^2H_z/dy^2 = 0$. Simplifying (28) with these substitutions produces a simpler form to solve for $H_z$

$$\left[\left(d^2/dx^2\right) + k_o^2\mu_z\varepsilon_y\right]H_z = 0, \tag{82}$$

$$\beta = k_o\sqrt{\mu_z\varepsilon_y}. \tag{83}$$

Solving (82) for $H_z$ and plugging the result into (13)–(16) yields

$$H_z = Ce^{-j\beta x} + De^{+j\beta x}, \tag{84}$$

$$E_y = Z_o\beta\left(Ce^{-j\beta x} - De^{+j\beta x}\right)/k_o\varepsilon_y = Z_o\sqrt{\mu_z/\varepsilon_y}\left(Ce^{-j\beta x} - De^{+j\beta x}\right), \tag{85}$$

We can see from (13)–(16) that based on our resonance conditions on $E_z$, $k_{z1}$ and $k_{y1}$ that $E_x = 0$, $H_x = 0$ and $H_y = 0$.

*4.2.3. Characteristic impedances of the two regions*

The first boundary condition exists at the perfect electric conductor (PEC) boundary when $x = -a/2$ and $\underline{E}(x, y, z) = 0$

$$E_y\big|_{x=-a/2} = 0 \rightarrow Ae^{jk_oa/2} = Be^{-jk_oa/2}, \tag{86}$$

$$A = Be^{-jk_oa}. \tag{87}$$

Plugging (87) into (80) and (81) yields

$$E_y = Z_oBe^{-jk_oa/2}\left[e^{-jk_o(x+a/2)} - e^{+jk_o(x+a/2)}\right], \tag{88}$$

$$E_y = -2Z_oBe^{-jk_oa/2}\sin[k_o(x + a/2)]. \tag{89}$$

Similarly,

$$H_z = 2Be^{-jk_oa/2}\cos[k_o(x + a/2)]. \tag{90}$$

Equations (89) and (90) solve for the impedance of the free space region as $Z = -E_y/H_z$

$$Z_o = -E_y/H_z = jZ_o\tan[k_o(x + a/2)], \tag{91}$$

within the region $0 \leq (x + a/2) \leq (a-w)/2$. The second boundary condition exists at $x = -w/2$ where the tangential fields at the boundary are equal. In this case, there are two tangential fields in $E_y$ and $H_z$. At the boundary, we have the following three conditions

$$E_y^-\Big|_{x=-w/2} = E_y^+\Big|_{x=-w/2}, \tag{92}$$

$$H_z^-\Big|_{x=-w/2} = H_z^+\Big|_{x=-w/2}, \tag{93}$$

$$Z_o\big|_{x=-w/2}^- = Z_1\big|_{x=-w/2}^+. \tag{94}$$

Plugging Eqs. (80) and (81) into (92) and (93) yields the following set of equations

$$-2jBe^{-jk_o(a/2)}\sin[k_o(a-w)/2] = \sqrt{(\mu_z/\varepsilon_y)}\left(Ce^{-j\beta_1(w/2)} - De^{+j\beta_1(w/2)}\right), \tag{95}$$

$$2Be^{-jk_o(a/2)}\cos[k_o(a-w)/2] = Ce^{-j\beta_1(w/2)} - De^{+j\beta_1(w/2)}. \tag{96}$$

Equations (95) and (96) give two equations to solve for three unknowns. Match equation (91) to the impedance in the anisotropic region at $x = -w/2$ to solve for the third unknown. Now solve for $Z = -E_y/H_z$ from (89) and (90)

$$\begin{aligned} Z_1 &= Z_o\sqrt{(\mu_z/\varepsilon_y)}\left[\left(De^{+j\beta_1 x} - Ce^{-j\beta_1 x}\right)/\left(De^{+j\beta_1 x} + Ce^{-j\beta_1 x}\right)\right] \\ &= Z_o\sqrt{(\mu_z/\varepsilon_y)}\left[\left(1-\rho e^{-j2\beta_1 x}\right)/\left(1+\rho e^{-j2\beta_1 x}\right)\right], \end{aligned} \tag{97}$$

$$|Z_1| = Z_o\sqrt{(\mu_z/\varepsilon_y)}, \tag{98}$$

where $\rho = C/D$. Now apply boundary condition (94) to (91) and (97) in order to yield an expression for $\rho$

$$Z_o\sqrt{(\mu_z/\varepsilon_y)}\left[\left(1-\rho e^{j\beta_1 w}\right)/1+\rho e^{j\beta_1 w}\right] = jZ_o\tan[k_o(a-w)/2], \tag{99}$$

$$\left(1-\rho e^{j\beta_1 w}\right)/1+\rho e^{j\beta_1 w} = j\sqrt{(\varepsilon_y/\mu_z)}\tan[k_o(a-w)/2] = j\Psi, \tag{100}$$

$$\rho = e^{-j\beta_1 w}(1-j\Psi)/(1+j\Psi). \tag{101}$$

Substituting (101) into (97) yields the last equation along with (95) and (96) to solve for $B$, $C$ and $D$.

#### *4.2.4. Anisotropic transverse resonance condition*

To simplify the calculation, consider **Figure 4** as slice of **Figure 3** in only one direction that is partially filled with an anisotropic medium. **Figure 4** represents a transmission line representation that allows for a solution to $L_g$ in terms of $w$ for a given wavelength. Now use standard transmission line theory to calculate the input impedance $Z_{in}$ at $x = 0$ from both directions. Transmission line theory says that as we approach the same point in a transmission line from either direction the input impedances should be equal. Then by symmetry the transverse resonance condition simplifies to $Z_{in} = 0$ from either direction.

Starting with the short located at $x = a/2$, calculate $Z_{in2}$ at $x = w/2$ as

$$Z_{in2} = jZ_o \tan\left(k_o L_g\right). \tag{102}$$

Now calculate $Z_{in1}$ at $x = 0$ as

$$Z_{in1} = Z_1\left[Z_{in2} + jZ_1 \tan\left(\beta_1 w/2\right)\right]/\left[Z_1 + jZ_{in2}\tan\left(\beta_1 w/2\right)\right]. \tag{103}$$

The symmetric transverse resonance condition simplifies (103) to

$$Z_1 + jZ_{in2}\tan\left(\beta_1 w/2\right) = 0. \tag{104}$$

Plugging (98) and (101) into (104) yields the following equation for $L_g$ [14]

$$L_g = \lambda \tan^{-1}\left[\sqrt{\left(\mu_z/\varepsilon_y\right)}/\tan\left(\pi w\sqrt{\mu_z\varepsilon_y}/\lambda\right)\right]/(2\pi). \tag{105}$$

where $\lambda$ is wavelength. Importantly, the solution of (105) shows that the transverse resonance only depends on two of the six $\underline{\underline{\varepsilon_r}}$ and $\underline{\underline{\mu_r}}$ components. This means that maintaining a constant resonance in a waveguide or cavity relies on the clever engineering of $\varepsilon_y$ and $\mu_z$ and leaves designers free to adjust the other components as they see fit to enhance performance in other ways. Furthermore, if $\varepsilon_y = \mu_z = 1$ then the resonance in the $\underline{x}_o$ direction will see the anisotropic substrate as air, while other tensor elements can be utilized to achieve performance attributed to materials with an arbitrarily high refractive index.

#### *4.2.5. Suppression of birefringence in a rectangular waveguide*

Section 3.4 discusses the phenomenon of birefringence in an unbounded anisotropic half-space by deriving the existence of a fourth order polynomial for the wavenumber in the propagation direction. However, for low order resonances, a rectangular waveguide suppresses the birefringence inherent to anisotropic media by suppressing propagation in the vertical direction of the waveguide. In other words, $k_y = 0$ and $d^2/dy^2 = 0$ assuming the horizontal dimension of the waveguide is at least twice the size of the vertical dimension or $a \geq 2b$ in **Figure 1** [3]. The bound on the waveguide geometry simplifies (39), the dispersion equation for $E_z$ in an anisotropic waveguide, to

$$k_o^2 k_x^2 \varepsilon_x E_z / \left(k_o^2 \mu_y \varepsilon_x - k_z^2\right) - k_o^2 \varepsilon_z E_z = 0, \tag{106}$$

and results in the following second order polynomial for $k_z$

$$k_z^2 = \varepsilon_x\left(k_o^2 \mu_y - k_x^2/\varepsilon_z\right). \tag{107}$$

The suppression of the $k_y$ term in (39) yields a second order differential equation for the wave number in the propagation direction, thereby eliminating the property of birefringence for this case.

## 5. Conclusions

Recently engineered materials have come to play an important role in state of the art designs electromagnetic devices and especially antennas. Many of these engineered materials have inherent anisotropic properties. Anisotropic media yield characteristics such as conformal surfaces, focusing and refraction of electromagnetic waves as they propagate through a material, high impedance surfaces for artificial magnetic conductors as well as high index, low loss, and lightweight ferrite materials. This chapter analyzes the properties of electromagnetic wave propagation in anisotropic media, and presents research including plane wave solutions to propagation in anisotropic media, a mathematical derivation of birefringence in anisotropic media, modal decomposition of rectangular waveguides filled with anisotropic media, and the full derivation of anisotropic transverse resonance in a partially loaded waveguide.

## Author details

Gregory Mitchell

Address all correspondence to: gregory.a.mitchell1.civ@mail.mil

U.S. Army Research Laboratory, Adelphi, USA

## References

[1] Pozar DM. Microwave Engineering. 3rd ed. New York: John Wiley and Sons; 2005. pp. 106-117

[2] Ince WJ, Stern E. Mint: Non-reciprocal remanence phase shifters in rectangular waveguide. IEEE Transactions on Microwave Theory and Techniques. 1967;**MTT-15**(2):87-95

[3] Collin R. Mint: A simple artificial anisotropic medium. IRE Transactions on Microwave Theory and Techniques. 1958;**6**:206-209

[4] Pozar D. Mint: Radiation and scattering from a microstrip patch on a uniaxial substrate. IEEE Transactions on Antennas and Propagation. 1987;**AP-35**(6):613-621

[5] Graham J. Arbitrarily Oriented Biaxlly Anisotropic Media: Wave Behvaior and Microstrip Antennas [thesis]. Syracuse: University of Syracuse; 2012

[6] Torrent D, Sanchez-Dehesa J. Radial wave crystals: Radially periodic structures from anisotropic metamaterials for engineering acoustic or electromagnetic waves. Physics Review Letters. 2009;**103**

[7] Sanchez-Dehesa J, Torrent D, Carbonell J. Anisotropic metamaterials as sensing devices in acoustics and electromagnetism. In: The Proceedings of the International Society for Optics and Photonics (SPIE). 2012; San Diego, California. Washington: SPIE

[8] Ma YG, Wang P, Chen X, Ong CK. Mint: Near-field plane-wave-like beam emitting antenna fabricated by anisotropic metamaterial. Applied Physics Letters. 2009;**94**

[9] Cheng Q. Directive radiation of electromagnetic waves based on anisotropic metamaterials. In: The Proceedings of IEEE Asia-Pacific Conference on Antennas and Propagation. Singapore. New York: IEEE; 27–29 August 2012

[10] Schurig D, Mock JJ, Justice BJ, Cummer SA, Pendry JB, Starr AF, Smith DR. Metamaterial electromagnetic cloak at microwave frequencies. Science. 2006;**314**:977-980

[11] Wong J, Balmain K. A beam-steerable antenna based on the spatial filtering property of hyperbolically anisotropic metamaterials. In: The Proceedings of IEEE International Symposium of the Antennas and Propagation Society. Honolulu. New York: IEEE; 9–15 June 2007

[12] Cai T, Wang GM. Polarization-controlled bifunctional antenna based on 2-D anisotropic gradient metasurface. In: The Proceedings of IEEE Conference on Microwave and Millimeter Wave Technology. Beijing. New York: IEEE; 5–8 June 2016

[13] Mitchell G, Weiss S. An overview of ARL's low profile antenna work utilizing anisotropic metaferrites. In: The Proceedings of the IEEE International Symposium on Phased Array Systems and Technology. Waltham. New York: IEEE; 18–21 October 2016

[14] Mitchell G, Wasylkiwskyj W. Mint: Theoretical anisotropic resonance technique for the design of low-profile wideband antennas. IET Microwaves, Antennas & Propagation. 2016;**10**:487-493

[15] Meng FY, Wu Q, Li LW. Mint: Transmission characteristics of wave modes in a rectangular waveguide filled with anisotropic Metamaterial. Applied Physics A: Materials Science and Processing. 2009;**94**:747-753

[16] Meng FY, Wu Q, Fu JH. Mint: Miniaturized rectangular cavity resonator based on anisotropic metamaterials bilayer. Microwave and Optical Technology Letters. 2008;**50**:2016-2020

[17] Boyce WE, DiPrima RC. Elementary Differential Equations. 7th ed. New York: John Wiley and Sons; 2001

Chapter 9

# Magnetic Line Source Diffraction by a PEMC Step in Lossy Medium

Saeed Ahmed and Mona Lisa

Additional information is available at the end of the chapter

http://dx.doi.org/10.5772/intechopen.74938

**Abstract**

In this chapter, we investigate a magnetic line source diffraction problem concerned with a step. To study the diffraction problem in lossy medium, we follow the Wiener-Hopf technique and steepest decent method to solve it for impedance step. By equating the impedances of the step to zero, the solution reduces for magnetic line source diffraction by PEC step. Then we transform the obtained solution for PEMC step by using duality transformation. Perfect electromagnetic conductor (PEMC) theory is novel idea developed by Lindell and Sihvola. This media is interlinked with two conductors namely perfect electric conductor (PEC) and perfect magnetic conductor (PMC). Both PEC and PMC are the limiting cases of perfect electromagnetic conductor (PEMC). We study the magnetic line source diffraction by PEMC step placed in different soils (i) gravel sand (ii) sand and (iii) clay. By using the permittivity, permeability and conductivity of these lossy mediums we predict the loss effect on the diffracted field. Such kind of study is very useful in antenna and wave propagation for subsurface targets and to investigate antenna radiation patterns.

**Keywords:** Wiener-Hopf technique, Fourier transform, Green function, impedance, diffraction, line source, step, PEMC, PMC, PEC, Lossy medium, permeability, conductivity, permittivity

## 1. Introduction

In this chapter, we have studied the diffraction problem precisely and investigated the magnetic line source diffraction by a perfect electromagnetic conductor (PEMC) step [1–3] for the lossy medium. PEMC step is assumed to be placed in lossy medium. Discontinuity in diffraction theory is relevant to many engineering applications. The physical significance of the step

IntechOpen

© 2018 The Author(s). Licensee IntechOpen. This chapter is distributed under the terms of the Creative Commons Attribution License (http://creativecommons.org/licenses/by/3.0), which permits unrestricted use, distribution, and reproduction in any medium, provided the original work is properly cited.

problem regarding engineering application is due to the fact that it is used in many electronic devices such as solder pad which have many applications in them which are interconnected through a step like circuit, microwave oven etc. This configuration is significant for predicting the scattering caused by an abrupt change in the material as well as in the geometrical properties of a surface. This problem is concerned with the diffraction of plane, cylindrical and surface waves by different impedance step discontinuities, such as step discontinuities made of plasmonic materials. Specially diffraction by a step in a perfectly conducting plane makes a canonical problem for the geometrical theory of diffraction (GTD) analysis of scattering by metallic tapes on paneled compact range reflectors [4]. The scattering of surface waves by the junction of two semi-infinite planes joined together by a step was first introduced by Johansen [5] in the case where both the half planes and the step are characterized by the same surface impedances. This problem is solved by using Wiener-Hopf technique, Green function and steepest descent method. The diffracted far field is investigated by the method of steepest descent. Some of the other researchers like Büyükaksoy and Birbir, Büyükaksoy and Tayyar, Büyükaksoy and Tayyar, Aksoy and Alkumru [6–16] have been investigated the scattering problems which can also be considered for the diffraction of plane, cylindrical and surface waves by different impedance step discontinuities, such as step discontinuities made of plasmonic materials.

The importance of present work stems from the facts that: (a) the scattering properties of a surface are functions of both its geometrical and material properties. (b) The edge scattering by dihedral structures whose surfaces can be modeled by the impedance boundary condition has been the focus of attention of many scientists for both acoustic and electromagnetic waves [17]. (c) The step geometry constitutes a canonical problem for scattering because a step geometry is used as an interconnection circuit of many electronic devices such as solder pad, microwave oven and frequency selective surface etc. [18]. A diffraction problem due to a magnetic line source is considered as better substitute than the plane waves. It is pertinent to mention here that the problem of diffraction of plane or line source diffraction of electromagnetic waves from a step is both mathematically difficult and physically important because the solution of the problem involves determination of $n$ unknowns which in turn requires the solution of system of $n$ linear equations.

It is clear that in the case of the line source incidence, the results of plane wave diffraction by impedance step are modified by a multiplicative factor of the form $\left(\frac{2\pi}{k\rho_0}\right)^{\frac{1}{2}}\exp\left(ik\rho_0 + i\frac{\pi}{4}\right)$, which agrees with the results already known [19, 20]. In far zone, the solution of magnetic line source diffraction reduces to plane wave as $k\rho \to \infty$. Using the method described in [16], the concerned problem "magnetic line source diffraction by an impedance step" is first reduced to a modified Wiener-Hopf equation of the second kind whose solution contains infinitely many constants satisfying an infinite system of linear algebraic equations. From this far field solution we obtain analytical solution for magnetic line source diffraction by perfect electric conductor (PEC) step, by taking the surface impedances $\eta_1$ and $\eta_2$ equal to zero. Next, we apply the duality transformation introduced by Lindell and Sihvola. Transformations have been made from the diffracted fields by a PEC step plane to PEMC step. Numerical solution of this system is obtained for various values of parameter $M$ with

http://dx.doi.org/10.5772/intechopen.74938

step height $a = \lambda/4$, from which the effects of these parameters on the diffraction phenomenon are studied and compared with the PEMC analytical theory [3]. Next we study the solution magnetic line source diffraction by PEMC step. PEMC is novel metamaterial developed by Lindell and Sihvola [21, 22]. Its constitutive relations and salient features are given below:

$$(i)\ \ \mathbf{D} = M\mathbf{B}$$

and

$$(ii)\ \ \mathbf{H} = -M\mathbf{E}$$

PEMC behaves as an example of an ideal boundary. As a check, we obtain the PMC and PEC boundary conditions as the two limiting case of PEMC:

$$M \rightarrow 0\ (PMC) : \mathbf{n} \times \mathbf{H} = 0,\ \ \mathbf{n}.\mathbf{D} = 0$$

and

$$M \rightarrow \pm\infty(PEC) : \mathbf{n} \times \mathbf{E} = 0,\ \ \mathbf{n} \cdot B = 0.$$

This medium is characterized by a scalar parameter M known as admittance of the surface. PEMC is a generalization of both perfect electric conductor (PEC) and perfect magnetic conductor (PMC) media. Therefore, the medium is known as PEMC. Defining a certain class of duality transformations, this medium corresponds to PEC or PMC media. PEMC medium allows some nonzero fields, it rejects electromagnetic field propagation and acts as a boundary to electromagnetic waves just like the PEC and PMC media. Denoting the unit normal between air and PEMC by, from the continuity of tangential component, the electric field **E** and the magnetic field **H** satisfy the equation

$$\mathbf{H} + M\mathbf{E} = 0$$

It is also continuous through the PEMC air interface, because this vanishes in the PEMC medium, and the boundary condition becomes

$$\mathbf{n} \times (\mathbf{H} + M\mathbf{E}) = 0$$

Similarly, the normal component of the field satisfies

$$\mathbf{D} - M\mathbf{B} = 0$$

and is continuous across the boundary for

$$\mathbf{n} \cdot (\mathbf{D} - M\mathbf{B}) = 0.$$

Because the normal component of the Poynting vector at the PEMC boundary vanishes and is nonreciprocal, except in the PMC and PEC limiting cases $M = 0,\ \pm\infty$ respectively. PEMC

is truly isotropic, but due to the cross-components in addition to the co-components in the scattered field, it is bi-isotropic. Due to its particular property of short-circuiting a linear combination of the tangential electric and magnetic fields, the PEMC media can be exploited in microwave engineering applications. Some examples of such are, e.g., ground planes for low-profile antennas, field pattern purifiers for aperture antennas, polarization transformers, radar reflectors, and generalized high-impedance surfaces. PEMC medium can be artificially constructed by building a structure which forces the boundary conditions on the surface of a sample to be the same as those of PEMC. Many authors have worked on PEMC and metamaterial [21–47]. Next we will study the magnetic line diffraction by PEMC step in lossy medium and the fields are obtained analytically for more general solution.

We extend the problem reported by [3] for the lossy background medium. Several canonical objects in lossy media has been investigated over the years by many authors [44–56] by applying approximate values of electric conductivity and dielectric constants of various materials. The concept of subsurface scattering of EM waves for detecting the cavities and targets buried in soil has important applications in the areas of nonproliferation of weapons, environmental monitoring, hazardous-waste site location and assessment, and even archeology. To have information about this potential, it is first essential to understand the behavior of the soil by applying EM wave, and how the targets within the soil give response. We analyze the response of the soil to an EM wave by using complex dielectric permittivity of the soil in finding radar range resolution. This leads to a concept of an optimum frequency and bandwidth for imaging in a particular soil. The radar cross section of several canonical objects in lossy media is derived, and examples are given for several objects like scattering of buried PEC sphere, PEC cylinder, and PEC plate [44] and similarly scattering by PEMC plate [54], PEMC strip [55] and PEMC cylinder [56]. Furthermore, we can study the diffraction by PEC and PEMC half plane [39] and step is also made by semi-infinite half planes with a step height a, so they can also be investigated for diffraction by using the electric parameters of soils. Also characteristics of radar cross section can be further studied with different objects for PEC, PMC and PEMC cases in lossy medium. In addition to RCS of various PEC, PMC and PEMC objects [59] in lossy medium can also be investigated in future.

The objective of this chapter is to determine the diffracted field by PEMC step excited by a line source in lossy medium and to investigate surface and borehole techniques for detecting and mapping subsurface cavities, targets and to evaluate the results of surface and borehole radar probings performed at the test sites. Detection of subsurface cavities is concerned with ground-probing radar. A number of factors that control the velocity, absorption and attenuation characteristics of a radar wave and plane EM wave propagating through a dielectric as well as lossy medium like the earth. The imaging of objects buried in soil has potentially valuable applications in many diverse areas, such as nonproliferation of weapons, environmental monitoring, hazardous-waste site location and assessment, and even archeology. We study the magnetic line source diffraction by PEMC step placed in different soils (i) gravel sand (ii) sand and (iii) clay. By using the approximate value of permittivity, permeability and conductivity of these lossy mediums, we predict and analyze the loss effect on the diffracted field.

## 2. Mathematical model

Consider the diffraction due to a magnetic line source located at $(x_0, y_0)$, illuminated by two half planes $S_1 = \{x < 0,\ y = a,\ z \in (-\infty, \infty)\}$ and $S_2 = \{x > 0,\ y = 0,\ z \in (-\infty, \infty)\}$ with relative surface impedance $\eta_1$ joined together by a step of height $''a''$ with relative surface impedance $\eta_2$. The geometry of the line source diffraction is shown in **Figure 1**.

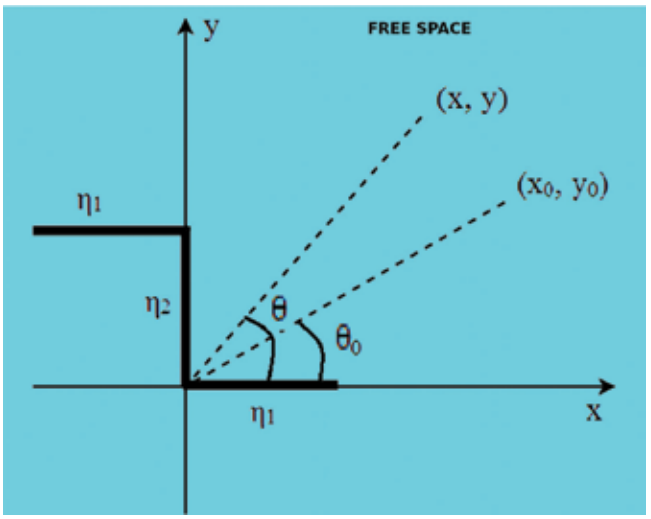


**Figure 1.** Geometry of problem: a line source located at $(x_0, y_0)$ making an angle $\theta_0$ with the horizontal, is incident upon impedance step of surface impedances $\eta_1$ and $\eta_2$, respectively, as shown. Here, $(x, y)$ is the observation point at an angle $\theta$ with the horizontal.

The time dependence $e^{-i\omega t}$, is suppressed throughout the solution.

The Helmholtz equation concerned with the diffraction problem is given below

$$\left(\frac{\partial^2}{\partial x^2} + \frac{\partial^2}{\partial y^2} + k^2\right) u^T(x, y) = \delta(x - x_0)\delta(y - y_0), \tag{1}$$

subject to the boundary conditions at two half planes and a step given by:

## 3. Boundary conditions

$$\left[1 + \frac{\eta_1}{ik}\frac{\partial}{\partial y}\right] u^T(x, a) = 0, \quad x < 0 \tag{2}$$

$$\left[1 + \frac{\eta_2}{ik}\frac{\partial}{\partial x}\right] u^T(0, y) = 0, \quad 0 < y < a \tag{3}$$

and

$$\left[1+\frac{\eta_1}{ik}\frac{\partial}{\partial y}\right]u^T(x,0)=0,\quad x>0 \tag{4}$$

with continuity equations:

$$u^T(x,a^-)=u^T(x,a^+) \tag{5}$$

and

$$\frac{\partial u^T(x,a^-)}{\partial y}=\frac{\partial u^T(x,a^+)}{\partial y} \tag{6}$$

where $u^T$ is the total field. For the mathematical analysis purpose, it is easy to express the total field $u^T(x,y)$ as follows:

$$u^T(x,y)=\begin{cases}u_i(x,y)+u_1^r(x,y)+u_1(x,y), & y>a,\\ u_2(x,y), 0<y<a,\end{cases} \tag{7}$$

Here, $k=\omega/c$ is the wave number and supposed to have positive imaginary part. The lossless case can be obtained by making $Imk\to 0$ in the final expressions. By substituting Eq. (7) in Eqs. (1)–(6), we arrive at

$$\left(\frac{\partial^2}{\partial x^2}+\frac{\partial^2}{\partial y^2}+k^2\right)u^i(x,y)=\delta(x-x_0)\delta\big(y-y_0\big). \tag{8}$$

and

$$\left(\frac{\partial^2}{\partial x^2}+\frac{\partial^2}{\partial y^2}+k^2\right)u_1^r(x,y)=\delta(x-x_0)\delta\big(y+y_0\big). \tag{9}$$

The solution of the incident field and reflected field from [11] can be written as

$$u^i(x,y)=be^{-ik\left[x\cos\phi_0+y\sin\theta_0\right]}$$

$$u_1^r(x,y)=b\frac{\eta_1\sin\phi_0-1}{\eta_1\sin\theta_0+1}e^{-ik\left[x\cos\phi_0+(y-2a)\sin\phi_0\right]}$$

where

$$b=-\frac{1}{4i}\sqrt{\frac{2}{\pi kr_0}}e^{i(kr_0-\pi/4)}$$

The diffracted field $u_1(x,y)$ and $u_2(x,y)$ satisfy the Helmholtz equations

$$\left(\frac{\partial^2}{\partial x^2}+\frac{\partial^2}{\partial y^2}+k^2\right)u_1(x,y)=0, \qquad x\in(-\infty,\infty). \tag{10}$$

$$\left(\frac{\partial^2}{\partial x^2}+\frac{\partial^2}{\partial y^2}+k^2\right)u_2(x,y)=0, \qquad x\in(0,\infty). \tag{11}$$

$$\left[1+\frac{\eta_1}{ik}\frac{\partial}{\partial y}\right]u_1(x,a)=0, \quad x<0 \tag{12}$$

$$\left[1+\frac{\eta_2}{ik}\frac{\partial}{\partial x}\right]u_2(0,y)=0, \quad 0<y<a \tag{13}$$

and

$$\left[1+\frac{\eta_1}{ik}\frac{\partial}{\partial y}\right]u_2(x,0)=0, \quad x>0 \tag{14}$$

$$u_1(x,a^+)+\frac{2b\eta_1\sin\phi_0}{\eta_1\sin\phi_0+1}e^{-ik\left[x\cos\phi_0+a\sin\phi_0\right]}=u_2(x,a^-) \tag{15}$$

and

$$\frac{\partial u_1(x,a^+)}{\partial y}-\frac{2bik\eta_1\sin\phi_0}{\eta_1\sin\phi_0+1}e^{-ik\left[x\cos\phi_0+a\sin\phi_0\right]}=\frac{\partial u_2(x,a^-)}{\partial y} \tag{16}$$

where

$$b=-\frac{1}{4i}\sqrt{\frac{2}{\pi kr_0}}e^{i(kr_0-\pi/4)}$$

## 4. Fourier transform

Taking Fourier transform of the Eq. (10) such that:

$$\Phi(\alpha,y)=\frac{1}{\sqrt{2\pi}}\int_{-\infty}^{\infty}u_1(x,y)e^{i\alpha x}dx,$$

and

$$u_1(x,y)=\frac{1}{\sqrt{2\pi}}\int_{-\infty}^{\infty}\Phi(\alpha,y)e^{-i\alpha x}d\alpha,$$

where

$$\Phi(\alpha, y) = \Phi_-(\alpha, y) + \Phi_+(\alpha, y)$$

$$\Phi_+(\alpha, y) = \frac{1}{\sqrt{2\pi}} \int_0^\infty u_1(x, y) e^{i\alpha x} dx,$$

$$\Phi_-(\alpha, y) = \frac{1}{\sqrt{2\pi}} \int_{-\infty}^0 u_1(x, y) e^{i\alpha x} dx,$$

and Eq. (10) reduce to

$$\frac{d^2\phi}{dy^2} + \gamma^2 \phi(\alpha, y) = 0, \tag{17}$$

where $\gamma(\alpha) = \sqrt{k^2 - \alpha^2}$ and $\alpha$ is a complex transform variable.

Apply half range Fourier transforms to the Eq. (11)

$$\left[\frac{\partial^2}{\partial x^2} + \frac{\partial^2}{\partial y^2} + k^2\right] \Psi_+(\alpha, y) = 0, \quad 0 < y < a. \tag{18}$$

where

$$\Psi_+(\alpha, y) = \frac{1}{\sqrt{2\pi}} \int_0^\infty u_2(x, y) e^{i\alpha x} dx$$

Fourier transforms of the Eqs. (12)–(16) can be written as

$$\left[1 + \frac{\eta_1}{ik} \frac{\partial}{\partial y}\right] \Phi_-(\alpha, a) = 0, \quad x < 0 \tag{19}$$

$$\left[1 + \frac{\eta_2}{ik} \frac{\partial}{\partial x}\right] \Psi_+(\alpha, a) = 0, \quad 0 < y < a \tag{20}$$

and

$$\left[1 + \frac{\eta_1}{ik} \frac{\partial}{\partial y}\right] \Psi_+(\alpha, 0) = 0, \quad x > 0 \tag{21}$$

$$\Phi_-(\alpha, a^+) - \frac{H_0}{\alpha - k\cos\phi_0} = \Psi_+(x, a^-) \tag{22}$$

and

$$\frac{\partial \Phi_-(\alpha, a^+)}{\partial y} + \frac{ik}{\eta_1} \frac{H_0}{\alpha - k\cos\phi_0} = \frac{\partial \Psi_+(x, a^-)}{\partial y} \tag{23}$$

where

$$H_0 = \frac{1}{8\pi^2}\frac{2\eta_1 \sin\phi_0}{\eta_1 \sin\phi_0 + 1} e^{-ika\sin\phi_0}\frac{2\pi}{\sqrt{kr_0}} e^{i(kr_0-\pi/4)}.$$

The solution of Eq. (17) satisfying the radiation condition for $y > a$ can be written as:

$$\Phi(\alpha, y) = B(\alpha) e^{i\gamma(\alpha)|y-a|}, \tag{24}$$

where $B(\alpha)$ is the unknown coefficient to be determined by substituting $y = a$ in the following expression $\Phi_+(\alpha, y) + \Phi_-(\alpha, y)$ and $\frac{\partial\Phi_+(\alpha,y)}{\partial y} + \frac{\partial\Phi_-(\alpha,y)}{\partial y}$, and with the help of boundary condition;

$$\Phi_-(\alpha, a) + \frac{\eta_1}{ik}\Phi_-'(\alpha, a) = 0, \tag{25}$$

where prime denotes differentiation with respect to $y$.

$$R_+(\alpha) = B(\alpha)\left(1 + \frac{\eta_1}{k}\gamma(\alpha)\right), \tag{26}$$

where

$$R_+(\alpha) = \Phi_+(\alpha, a) + \frac{\eta_1}{ik}\Phi_+'(\alpha, a). \tag{27}$$

From the Eqs (22), (23), (26) and (27), we obtain the following Wiener-Hopf functional equations

$$\frac{\partial\Psi_+(x,a)}{\partial y} = \frac{R_+(\alpha) i\gamma(\alpha)}{\left(1 + \frac{\eta_1}{k}\gamma(\alpha) + \frac{ik}{\eta_1}\Phi_-(\alpha, a) + \frac{ik}{\eta_1}\frac{F_0}{\alpha - k\cos\phi_0}\right.} \tag{28}$$

The corrected solution of Wiener-Hopf equation [2] in case of line source can be expressed as

$$\begin{aligned}
&\frac{R_+(\alpha)}{(\alpha + T)G_+(\alpha)} \\
&= F_0\frac{i\eta_1}{k}\frac{(k\cos\theta_0 - T)G_-(k\cos\theta_0)}{\alpha - k\cos\theta_0} \\
&\quad + \frac{k}{\eta_1}\frac{\left(\frac{k}{\eta_2} - T\right)G_+(T)R_+(T)e^{-\frac{ika}{\eta_1}}}{\left(\frac{k}{\eta_2} + T\right)\sin\left(\frac{ka}{\eta_1}\right)(\alpha + T)} \\
&\quad + \sum_{n=1}^{\infty}\frac{\left(\frac{k}{\eta_2} - \alpha_n\right)G_+(\alpha_n)R_+(\alpha_n)\left(\frac{n\pi}{a}\right)^2}{\left(\frac{k}{\eta_2} + \alpha_n\right)a\alpha_n(T - \alpha_n)(\alpha + \alpha_n)},
\end{aligned}$$

where

$$F_0 = \frac{i}{8\pi^2}\frac{2\eta_1 \sin\theta_0}{1+\eta_1 \sin\theta_0} e^{-ika\sin\theta_0}\frac{2\pi}{\sqrt{kr_0}} e^{-i\left(kr_0-\frac{\pi}{4}\right)}.$$

and $\alpha_n, G(\alpha)$ and $G_+(\alpha)$ are defined in [11]. The function $R_+(\alpha)$ depends upon the unknown series of constants $R_+(T),\ R_+(\alpha_1),\ R_+(\alpha_2),\ R_+(\alpha_3)\ldots$. To find an approximate value for $R_+(\alpha)$, substitute $\alpha = T, \alpha_1, \alpha_{2,\ldots,}\alpha_m$ in Eq. (29) to get $m+1$ equations in $m+1$ unknowns. The simultaneous solution of these equations yields approximate solutions for $R_+(T),\ R_+(\alpha_1),\ R_+(\alpha_2), \ldots R_+(\alpha_m)$.

## 5. Far zone solution

The unknown constant $B(\alpha)$ can be obtained by taking inverse Fourier transform of Eq. (24), the final expression for the diffracted field is written as

$$u_1(x,y) = \frac{1}{\sqrt{2\pi}}\int_L \frac{R_+(\alpha)}{\left(1+\frac{\eta_1}{k}\gamma(\alpha)\right)} e^{i\gamma(\alpha)(y-a)} e^{-i\alpha x} d\alpha, \tag{29}$$

where $L$ is a straight line parallel to the real axis, lying in the strip $Im[k\cos\theta_0] < Im[\alpha] < Im[k]$. To determine the far field behavior of the scattered field, introducing the following substitutions $x = r\cos\theta, y - a = r\sin\theta$ and $\alpha = -k\cos(\theta + it)$, where $t$ is real. The contour of integration over $\alpha$ in Eq. (30) goes into the branch of hyperbola around $-ik$ if $\frac{\pi}{2} < \theta < \pi$. We further observe that in deforming the contour into a hyperbola the pole $\alpha = \xi$ may be crossed. If we make another transformation $\xi = k\cos(\theta_0 + it_1)$ the contour over $\xi$ also goes into a hyperbola. The two hyperbolae will not cross each other if $\theta < \theta_0$. However, if the inequality is reversed there will be a contribution from pole which, in fact, cancels the incident wave in the shadow region in [11]. Simply the asymptotic evaluation of the integral in Eq. (30) using the method of steepest descent, we find the following solution for far field diffracted by an impedance step due to a line source at a large distance from the edge:

$$u_1\left(r,\phi\right) e^{-i\pi/4} k\sin\phi R + (\alpha)\frac{e^{ikr}}{\sqrt{kr}} \tag{30}$$

## 6. Magnetic line source diffraction by PEC step

The asymptotic solution for the field diffracted by perfect electric conductor (PEC) step is obtained by equating $\left(\eta_1 = \eta_2 = 0\right)$ as

$$u_1\left(r,\phi\right) = e^{-i\pi/4} k\sin\phi\Phi_+\left(-k\cos\phi, a\right)\frac{e^{ikr}}{\sqrt{kr}} \tag{31}$$

where

$$\Phi_+(\alpha,a)=G_+(\alpha)\left[i\sin\phi_0\frac{e^{i\left(kr_0-\frac{\pi}{4}\right)}}{4\pi\sqrt{kr_0}}\frac{G_-\left(k\cos\phi_0\right)}{\alpha-k\cos\phi_0}+\sum_{n=1}^{\infty}\frac{G_+(\alpha_n)\left(\frac{n\pi}{a}\right)^2}{a\alpha_n(\alpha_n+\alpha)}\Phi_+(\alpha_n,a)\right] \tag{32}$$

and

$$G_+(\alpha)=\sqrt{a}e^{[\gamma a/\pi\ln(\alpha+i\gamma)/k]}e^{[i\alpha a/\pi(1-C+\ln(2\pi)/ka+i\pi/2)]}$$
$$\times\prod_{n=1}^{\infty}\left[1-\left(\frac{ka}{n\pi}\right)^2-\frac{i\alpha a}{n\pi}\right]e^{\frac{i\alpha a}{n\pi}} \tag{33}$$

such that

$$G_-(\alpha)=G_+(-\alpha)$$

Next we transform magnetic line source diffracted field from PEC to PEMC step under the duality transformations in the [21]. The field diffracted by perfectly electric conducting (PEC) step can be transformed.

## 7. Magnetic line source diffraction by PEMC step

We obtain a solution for magnetic line source diffraction by PEMC step by applying a transformation introduced by Lindell and Sihvola, that is known as duality transformation [21]:

$$\begin{pmatrix}E_d^s\\H_d^s\end{pmatrix}=\begin{pmatrix}M\eta_0 & \eta_0\\ \dfrac{-1}{\eta_0} & M\eta_0\end{pmatrix}\begin{pmatrix}E^s\\H^s\end{pmatrix}, \tag{34}$$

$$E_d^s=M\eta_0E^s+\eta_0H^s \tag{35}$$

$$H_d^s=-\frac{1}{\eta_0}E^s+M\eta_0H^s \tag{36}$$

where $E^s$ and $H^s$ are the diffracted fields and $E_d^s$ and $H_d^s$ are the intermediate fields obtained from the PEC step by satisfy the condition,

$$\eta_oH_d^s=-u_z\times E_d^s. \tag{37}$$

Moreover, the transformation

$$\begin{pmatrix}E\\H\end{pmatrix}=\frac{1}{\left(M\eta_0\right)^2+1}\begin{pmatrix}M\eta_0 & -\eta_0\\ \dfrac{1}{\eta_0} & M\eta_0\end{pmatrix}\begin{pmatrix}E_d^s\\H_d^s\end{pmatrix} \tag{38}$$

gives

$$E = \frac{1}{\left(M\eta_0\right)^2 + 1}\left[\left(\left(M\eta_0\right)^2 - 1\right)E^s - 2M\eta_0 E^s\right] \tag{39}$$

$$H = \frac{1}{\left(M\eta_0\right)^2 + 1}\left[\left(\left(M\eta_0\right)^2 - 1\right)H^s - 2M\eta_0 H^s\right] \tag{40}$$

where $E$ and $H$ are the fields diffracted (scattered) by the PEMC step which is written as

$$E = \frac{1}{\left(M\eta_0\right)^2 + 1}\left[\left(\left(M\eta_0\right)^2 - 1\right)E^s - 2M\eta_0 E^s\right] \tag{41}$$

and

$$E^s = e^{-i\pi/4}k\sin\phi\Phi_+\left(-k\cos\phi, a\right)\frac{e^{ikr}}{\sqrt{kr}} \tag{42}$$

where

$$\Phi_+(\alpha, a) = G_+(\alpha)\left[ik\sin\phi_0\frac{e^{i\left(kr_0-\frac{\pi}{4}\right)}}{4\pi\sqrt{kr_0}}\frac{G_-\left(k\cos\phi_0\right)}{\alpha - k\cos\phi_0} + \sum_{n=1}^{\infty}\frac{G_+(\alpha_n)\left(\frac{n\pi}{a}\right)^2}{a\alpha_n(\alpha_n+\alpha)}\Phi_+(\alpha_n, a)\right] \tag{43}$$

## 8. Magnetic line source diffraction by PEMC step in lossy medium

When we study magnetic line source diffraction by PEMC step in lossy medium, we just replace free-space wave number k by $\gamma$, then the solution obtained from the PEMC step for the lossy medium can be expressed such that (**Figure 2**)

$$E = \frac{1}{\left(M\eta_0\right)^2 + 1}\left[\left(\left(M\eta_0\right)^2 - 1\right)E^s - 2M\eta_0 E^s\right] \tag{44}$$

and

$$E^s = e^{-i\pi/4}\gamma\sin\phi\Phi_+\left(-\gamma\cos\phi, a\right)\frac{e^{i\gamma r}}{\sqrt{\gamma r}} \tag{45}$$

where

$$\Phi_+(\alpha, a) = G_+(\alpha)\left[i\gamma\sin\phi_0\frac{e^{i\left(\gamma r_0-\frac{\pi}{4}\right)}}{4\pi\sqrt{\gamma r_0}}\frac{G_-\left(\gamma\cos\phi_0\right)}{\alpha - \gamma\cos\phi_0} + \sum_{n=1}^{\infty}\frac{G_+(\alpha_n)\left(\frac{n\pi}{a}\right)^2}{a\alpha_n(\alpha_n+\alpha)}\Phi_+(\alpha_n, a)\right] \tag{46}$$

where $\gamma = \beta - \alpha$, here $\alpha$ is attenuation factor and $\beta$ is propagation constant defined as in [57].

$$\alpha = \omega\sqrt{\varepsilon_0\mu_0}\sqrt{\frac{\varepsilon_r}{2}}\left[\sqrt{1+\left(\frac{18\sigma}{\omega\varepsilon_r\varepsilon_0}\right)^2}-1\right]^{1/2}$$

$$\beta = \omega\sqrt{\varepsilon_0\mu_0}\sqrt{\frac{\varepsilon_r}{2}}\left[\sqrt{1+\left(\frac{18\sigma}{\omega\varepsilon_r\varepsilon_0}\right)^2}+1\right]^{1/2}$$

where $\varepsilon_0$ and $\mu_0$ are the permittivity and the permeability of free space. For the hosted medium, we use three type of soil models [58] namely: (i) gravel sand having its conductivity $\sigma = 0.001$ mho/m and its relative permittivity $\varepsilon_r = 10.5\varepsilon_0$; (ii) sand: $\sigma = 0.0001$ mho/m and $\varepsilon_r = 8\varepsilon_0$ and (iii) clay: $\sigma = 0.01$ mho/m and $\varepsilon_r = 7\varepsilon_0$, respectively.

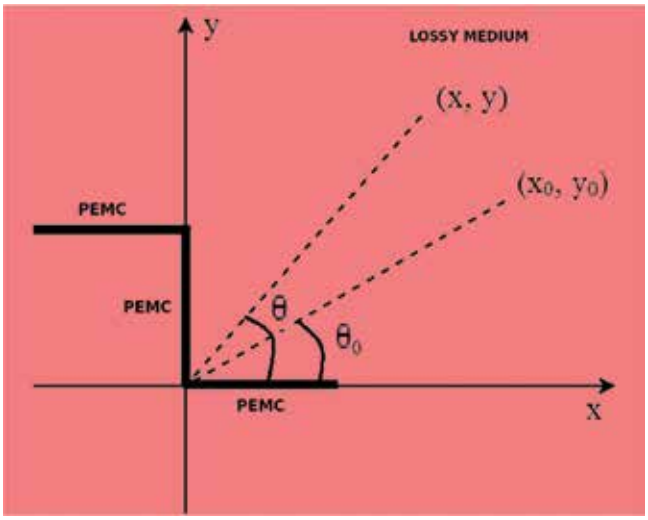


**Figure 2.** Geometry of the diffraction problem: a line source located at $(x_0, y_0)$ making an angle $\theta_0$ with the horizontal, is incident upon PEMC step surrounded by lossy medium, as illustrated in this figure. Here, $(x, y)$ is the observation point at an angle $\theta$ with the horizontal.

## 9. Results and discussion

In this section we discuss some graphical results which have been presented in [3] to predict the effects of the admittance parameters $M$ and step height $a$ and line source parameter $r_0$ on the diffraction phenomenon. It can be observed from [3] that the amplitude of the diffracted field increases with increase in step height. The graphs show that the amplitude of the diffracted field decreases as the source is taken away from the origin, which is a natural phenomenon and verifying the results. Through Mathematica software we have reproduced the results given by Lindell and Sihvola [21] and the results have retrieved. Here, an attempt is made to develop the theoretical results for lossy medium using the analytical solution for magnetic line source diffraction by PEMC step. As the step is assumed to be surrounded by different soils (i) gravel sand

(ii) sand and (iii) clay. By using the permittivity, permeability and conductivity of these lossy mediums we predict the loss effect on the diffracted field. The computed fields are obtained analytically for more general solution. The said problem is first reduced to a modified Wiener-Hopf equation of second kind whose solution contains an infinite set of constants satisfying an infinite system of linear algebraic equations. A numerical solution of this system is obtained for various values of admittance parameter $M$ and the height of the step a versus observation angle. Further, the effect of these parameters on the diffraction phenomenon is studied. It is observed that if the source is shifted to a large distance these results differ from those of by a multiplicative factor to the part of the scattered field containing the effects of incident and reflected waves. The diffraction analysis of magnetic line source by a PEMC step provides explicit formulas for electric and magnetic field amplitude and the polarization. Here, it is interesting to note that the co-polarized and the cross-polarized fields depend on the parameter $M$.

## 10. Conclusion

It is concluded that the both coupled electric and magnetic fields excitation can be observed analytically for PEMC theory that leads to a most general case for the magnetic line source diffraction by step embedded in lossy medium. The lossy medium is assumed to be made of three different soils (i) gravel sand, (ii) sand and (iii) clay. We see from their respective electric parameters namely permittivity, permeability and conductivity, as the loss increases the amplitude of the diffracted field decreases. By applying this technique to detect the subsurface targets, we can use various soil models. Further, in this chapter at a time we studied diffraction by step using PEMC theory and loss effect on the field patterns. Here, we can predict the behavior of the fields diffracted by magnetic line source. This is the most general solution and is more useful rather a plane wave solution. In far zone, we can obtain a solution for the diffraction of a plane wave by PEMC step placed in lossy medium under the condition $k\rho \to \infty$. It is also concluded that the parameter $M$ plays a significant role in PEMC theory to interlink the PEC and PMC media. The cross-polarized scattered fields vanish in the presence of PEC and PMC cases and they are maximal for $M\eta_0 = \pm 1$. If $M = \pm\infty$, correspond to PEC case and $M = 0$, correspond to a PMC case. The impulse response of the soil is important in investigating the best operating frequency and bandwidth for a subsurface-imaging SAR. Due to dispersion and loss in the soil, the impulse response deviated from the free-space impulse response. The following conclusions can be drawn from examination of the soil's impulse response: (i) an optimum bandwidth exists; (ii) loss increases as bandwidth increases; (iii) very large bandwidths are not useful for imaging objects at large depths; (iv) vertical polarization is best for large angles of incidence and (v) lower frequencies seem best.

## Acknowledgements

The author Dr. Saeed Ahmed acknowledges the financial support from the Department of Earth Sciences, Quaid-i-Azam University, Islamabad, Pakistan, during the Post Doctoral studies for the year (20 January, 2017–19 January, 2018).

## Author details

Saeed Ahmed* and Mona Lisa

*Address all correspondence to: saeedqau@gmail.com

Department of Earth Sciences, Quaid-i-Azam University, Islamabad, Pakistan

## References

[1] Ayub M, Ramzan M, Mann AB. Magnetic line source diffraction by an impedance step. IEEE Transactions on Antennas and Propagation. 2009;**57**(4):1289-1293

[2] Ahmed S. Comments on magnetic line source diffraction by an impedance step. IEEE. 2015;**PP**(99):1

[3] Ahmed S. Magnetic line source diffraction of a plane wave by a perfectly electromagnetic conducting (PEMC) step. Journal of Modern Optics. 2014;**62**(3):175-178

[4] Sommers GA, Pathak PH. GTD solution for the diffraction by metallic tapes on paneled compact range reflectors. Proceedings of the Institution of Electrical Engineers. 1992; **139**(3):291-305

[5] Johansen E. Surface wave scattering by a step. IEEE Transactions on Antennas and Propagation. 1967;**15**(3):442-448

[6] Jamid HA, Al-Bader SJ. Reflection and transmission of surface Plasmon mode at a step discontinuity. IEEE Photonics Technology Letters. February 1997;**9**(2):220-222

[7] Valagiannopoulos CA, Uzunoglu NK. Rigorous analysis of a metallic circular post in a rectangular waveguide with step discontinuity of sidewalls. IEEE Transactions on Microwave Theory and Techniques. August 2007;**55**(8):1673-1684

[8] Yang H-Y, Alexopoulos NG. Characterization of the finline step discontinuity on anisotropic substrates. IEEE Transactions on Microwave Theory and Techniques. November 1987;**MTF35**(11):956-963

[9] Valagiannopoulos CA. High selectivity and controllability of a parallel-plate component with a filled rectangular ridge. Progress in Electromagnetics Research. 2011;**119**:497-511

[10] Pannon W, Uslenghi PLE. Exact and asymptotic scattering by a step discontinuity in an impedance plane, antennas and Propagation Society International Symposium, Houston, TX, USA. 1983; **21**. pp.13-17

[11] Büyükaksoy A, Birbir F. Plane wave diffraction by an impedance step. IEEE Transactions on Antennas and Propagation. 1993;**41**(8):1160-1164

[12] Büyükaksoy A, Birbir F. Correction to plane wave diffraction by an impedance step. IEEE Transactions on Antennas and Propagation. Mar. 1996;**44**(3):422-422

[13] Büyükaksoy A, Birbir F. Plane wave diffraction by a reactive step. International Journal of Engineering Science. 1997;**35**:311-319

[14] Büyükaksoy A, Tayyar IH. High frequency diffraction by a rectangular impedance cylinder on an impedance plane. IEE Proceedings–Science, Measurement and Technology. 2002;**149**:49-59

[15] Tayyar IH, Aksoy S, Alkumru A. Surface wave scattering by a rectangular impedance cylinder located on a reactive plane. Mathematical Methods in the Applied Sciences. 2005; **28**:525-549

[16] Noble B. Methods Based on Wiener Hopf Techniques. New York: Pergamon; 1958

[17] Rojas RG. Wiener-Hopf analysis of the EM diffraction by an impedance discontinuity in a planar surface and by an impedance half-plane. IEEE Transactions on Antennas and Propagation. 1988;**36**(1):71-83

[18] Clavel E, Schanen L, Roudet J, Arechal YM. Influence of an impedance step in interconnection inductance calculation. IEEE Transactions on Magnetics. May 1996;**32**(3)

[19] Jones DS. The Theory of Electromagnetism. London: Pergamon Press; 1964

[20] Hohmann GW. Electromagnetic scattering by conductors in the earth near a line source of current. Geophysics. 1971;**36**(1):101-131

[21] Lindell IV, Sihvola AH. Transformation method for problems involving perfect electromagnetic conductor (PEMC) structures. IEEE Transactions on Antennas and Propagation. 2005;**53**(9):3005-3011

[22] Lindell IV, Sihvola AH. Perfect electromagnetic conductor. Journal of Electromagnetic Waves and Applications. 2005;**19**:861-869

[23] Lindell IV. Electromagnetic fields in self-dual media in differential-form representation. Progress in Electromagnetics Research, PIER. 2006;**58**:319-333

[24] Ruppin R. Scattering of electromagnetic radiation by a perfect electromagnetic conductor cylinder. Journal of Electromagnetic Waves and Applications. 2006;**20**(13):1853-1860

[25] Lindell IV, Sihvola AH. Reflection and transmission of waves at the interface of perfect electromagnetic conductor (PEMC). Progress in Electromagnetics Research B. 2008;**5**: 169-183

[26] Lindell IV, Sihvola AH. Realization of the PEMC boundary. IEEE Transactions on Antennas and Propagation. 2005;**53**:3012-3018

[27] Lindell IV. Differential Forms in Electromagnetics. New York: Wiley and IEEE Press; 2004

[28] Lindell IV, Sihvola AH. Losses in PEMC boundary. IEEE Transactions on Antennas and Propagation. 2006;**54**(9):2553-2558

[29] Jancewicz B. Plane electromagnetic wave in PEMC. Journal of Electromagnetic Waves and Applications. 2006;**20**(5):647-659

[30] Lindell IV, Ruotanen LH. Duality transformations and Green dyadics for bi-anisotropic media. Journal of Electromagnetic Waves and Applications. 1998;**12**:1131-1152

[31] Lindell IV, Olyslager F. Duality in electromagnetics. Journal of Communications Technology and Electronics. 2000;**45**(2):S260-S268

[32] Ahmed S, Akbar M, Shafiq M. Diffraction by a perfectly electromagnetic conducting (PEMC) step. Journal of Modern Optics. 2013;**60**:637-640

[33] Ahmed S, Mehmood I. Diffraction of a plane wave by a perfectly electromagnetic conducting (PEMC) slot. Journal of Modern Optics. 2014;**61**:335-338

[34] Ahmed S, Manan F. Scattering by randomly placed line source in the presence of perfectly electromagnetic conducting plane. American International Journal of Contemporary Research. November 2011;**1**(3):168-172

[35] Ahmed S, Manan F. Scattering by randomly placed perfectly electromagnetic conducting half plane. International Journal of Applied Science and Technology. November 2011;**1**(6): 311-317

[36] Ahmed S, Manan F. Scattering by perfectly electromagnetic conducting random grating. American International Journal of Contemporary Research. November 2011;**1**(3):66-71

[37] Ahmed S, Manan F. Scattering by perfectly electromagnetic conducting random width strip. American International Journal of Contemporary Research. November 2011;**1**(6): 305-310

[38] Ahmed S, Manan F. Scattering by randomly placed perfectly electromagnetic conducting random width strip. International Journal of Applied Science and Technology. November 2011;**1**(6):300-304

[39] Ahmed S. Diffraction by perfect electromagnetic conductor (PEMC) half plane. International Journal of Electronics Letters. January 2017;**5**(3):255-260

[40] Ahmed S, Mann AB, Nawaz R, Tiwana MH. Diffraction of electromagnetic plane wave by a slit in a homogeneous bi-isotropic medium. Waves in Random and Complex Media. 2017;**27**(2):325-338

[41] Ahmed S. Comments on electromagnetic scattering from chiral coated nihility cylinder. Progress In Electromagnetics Research Letters. 2015;**53**:123

[42] Ahmed S. Comments on electromagnetic scattering from a chiral coated PEMC cylinder. Progress in Electromagnetics Research Letters. 2015;**53**:101

[43] Ahmed S. Comments on electromagnetic response of a circular DB cylinder in the presence of chiral and chiral nihility metamaterials. Progress in Electromagnetics Research Letters. 2015;**54**:1

[44] Brock BC, Sorensen KW. Electromagnetic Scattering from Buried Objects. Sandia National Laboratories, SAND94-2361; September 1994

[45] Kuloglu M, Chen H-C. Ground penetrating radar for tunnel detection. Geoscience and Remote Sensing Symposium (IGARSS), IEEE International, 2010;4314-4317

[46] Brock BC, Patitz WE. Optimum Frequency for Subsurface-Imaging Synthetic Aperture Radar, SAND93-0815. Springfield, USA: National Technical Information Service, US Department of Commerce; May 1993

[47] Doerry AW. A Model for Forming Airborne Synthetic Aperture Radar Images of Underground Targets, SAND94-0139. Albuquerque, New Mexico: Sandia National Laboratories; January 1994

[48] Von Hippel AR, editor. Dielectric Materials and Applications. New York: The Technology Press of M.I.T., and John Wiley & Sons, Inc.; 1954

[49] Radzevicius SJ, Daniels JJ. Ground penetrating radar polarization and scattering from cylinders. Journal of Applied Geophysics. 2000;**45**:111-125

[50] Frezza F, Pajewski L, Ponti C, Schettini G, Tedeschi N. Cylindrical-wave approach for electromagnetic scattering by subsurface metallic targets in a lossy medium. Journal of Applied Geophysics. 2013;**97**:55-59

[51] Armin WD. A Model for Forming Airborne Synthetic Aperture Radar Images of Underground Targets, Synthetic Aperture Radar Department, 2345, Sandia National Laboratories Albuquerque, NM 87185-0529, Technical Report; January 1994

[52] Bradford JH. Frequency-dependent attenuation analysis of ground-penetrating radar data. Geophysics. May–June 2007;**72**(3)

[53] Zhenhua M. Advanced Feature Based Techniques for Landmine Detection Using Ground Penetrating Radar, MS Thesis, University of Missouri-Columbia; 2007

[54] Ahmed S, Khan MK, ur Rehman A. Scattering by a perfect electromagnetic conductor plate embedded in lossy medium. International Journal of Electronics. 2015;**103**(07):1228-1235

[55] Ahmed S. The study of the radar cross section of perfect electromagnetic conductor strip. Optik. 2015;**126**(23):4191-4194

[56] Ahmed S, Rehaman AU, Zain Iftekhar M, Lisa M. Scattering by a PEMC cylinder embedded in lossy medium. Optik. 2016;**127**(19):8011-8018

[57] Ballard RB Jr. Electromagnetic (RADAR) Techniques Applied to Cavity Detection, Technical Report No. 5, Geotechnical Laboratory, P.O. BOX 631, Vicksburg, Miss. 39180; 1983

[58] Carcione JM. Ground-radar numerical modelling applied to engineering problems. European Journal of Environmental and Engineering Geophysics. 1996;**1**:65-81

[59] Rajyalakshmi P, Raju GSN. Characteristics of radar cross section with different objects. International Journal of Electronics and Communication Engineering. 2011;**4**(2):205-216

*Edited by Pedro Pinho*

Antennas and radio propagation are continuously and rapidly evolving and new challenges arise every day. As a result of these rapid changes the need for up-to-date texts that address this growing field from an interdisciplinary perspective persists. This book, organized into nine chapters, presents new antenna designs and materials that will be used in the future, due to the trend for higher frequencies, as well as a bird's eye view of some aspects related to radio propagation channel modeling. The book covers the theory but also the practical aspects of technology implementation in a way that is suitable for undergraduate and graduate-level students, as well as researchers and professional engineers.

Published in London, UK
© 2018 IntechOpen
© Panuwat Sikham / iStock

IntechOpen

ISBN 978-1-83881-530-1